PhD Thesis

Optimal control of a motor-integrated hybrid powertrain for a two-wheeled vehicle suitable for personal transportation

Himadri Bhushan Das

Supervisor: Dr. Simos A Evangelou

Department of Electrical and Electronic Engineering

Imperial College London

20th June 2018

Preface

Nahi gyanena sadrusham pavitramiha vidyate

Tatswayam yogamsiddhaha kalenatmani vindati

One of the verses of Bhagavad Gita says, there is nothing in this world which is as pure and pious as ***Gyaan*** (knowledge). Lord Krishna says a yogi (A person who has breached the boundaries of the physical and have the ability to touch and experience everything in the universe) will find the real knowledge or wisdom in himself in due season.

While I went searching for the scholastic wisdom wishing for joy in seeking through my PhD research, it was absolute necessary for a perfect ***Guru*** to guide me through this pursuit.

Guru brahma guru Vishnu Guru devo maheshwaraha

Guru sakshayat parambrahmaha tasami shree guruwe namaha

A Guru or a teacher is a person who is above all the Gods. Therefore, I bow to that Guru who made this journey possible. Thanks to my supervisor Dr Simos A Evangelou and my mentor Dr Samraj J Dhinagar for all their guidance and time.

Having the desire to seek education and being blessed by a Guru may not allow one to complete his journey.

Kanchanena karya siddhhi

Financial resource is very essential for this research. I am thankful to the Commonwealth Scholarship Commission UK, my employer TVS Motor Company India and Imperial College London for all the financial supports.

Shaktihi krupayuktham jeevanamasthi

Kutumbam jeevanam mama

The real strength of a person is his family, who are besides his in thick and thin. I am extremely grateful to the almighty for having given me such a strength in form of a graceful life and family.

Declaration

I declare that the submitted work in the thesis is original and I certify that, to the best of my knowledge, my thesis does not infringe upon anyones copyright nor violate any proprietary rights and that any ideas, techniques, quotations, or any other material from the work of other people included in my thesis, published or otherwise, are fully acknowledged in accordance with the standard referencing practices.

Himadri Bhushan Das

Copyright Declaration

The copyright of this thesis rests with the author and is made available under a Creative Commons Attribution Non-Commercial No Derivatives licence. Researchers are free to copy, distribute or transmit the thesis on the condition that they attribute it, that they do not use it for commercial purposes and that they do not alter, transform or build upon it. For any reuse or redistribution, researchers must make clear to others the licence terms of this work.

Abstract

The present research aims to propose an optimized configuration of the motor integrated power-train with an optimal controller suitable for small power-train based two wheeler automobile which can increase the system level efficiency without affecting drivability. This work will be the foundation for realizing the system in a production ready vehicle for the two wheeler OEM TVS Motor Company in India. A detailed power-train model is developed (from first principles) for the scooter vehicle, which is powered by a 110 cc spark ignition (SI) engine and coupled with two types of transmission, a continuous variable transmission (CVT) and a 4-speed manual transmission (MT). Both models are capable of simulating torque and NOx emission output of the SI engine and dynamic response of the full power-train. The torque production and emission outputs of the model are compared with experimental results available from TVS Motor Company. The CVT gear ratio model is developed using an indirect method and an analytical model. Both types of powertrain models are applied to perform a simulated study of fuel consumption, NOx emission and drivability study for a particular vehicle platform. In the next stage of work, the mathematical model for a brush-less direct current machine (BLDC) with the drive system and Li-Ion battery are developed. The models are verified and calibrated with the experimental results from TVS Motor Company. The BLDC machine is integrated with both the CVT and MT powertrain models in parallel hybrid configurations and a drive cycle simulation is conducted for different static assist levels by the electrical machines. The initial test confirms the need of optimal sizing of the powertrain components as well as an optimal control system. The detailed model of the powertrain is converted to a control-oriented model which is suitable for optimal control. This is followed by multi-objective optimization of different com-

ponents of the motor-integrated powertrain using a single function as well as Pareto-Optimal methods. The objective function for the multi-objective optimization is proposed to reduce the fuel consumption with battery charge sustainability with least impact on the increase of financial cost and weight of the vehicle. The optimization is conducted by a nested methodology that involves Particle Swarm Optimization and a Non-dominated sorting genetic algorithm where, concurrently, a global optimal control is developed corresponding to the multi-objective design. The global optimal controller is designed using dynamic programming. The research is concluded with an optimal controller developed using the hp-collocation method. The objective function of the dynamic programming method and hp-collocation method is proposed to reduce fuel consumption with battery charge sustainability.

Contents

Abstract 4

Publications and Patents 5

List of Publications 5

List of Poster presented 6

List of Applied Patents 6

1 Introduction **7**

1.1 Original Contributions 11

1.2 Assessment of Research Achievements 12

1.3 Overview of each chapter 12

2 Literature Review **15**

2.1 Review on powertrain modeling 15

2.2 Review on vehicle drivability 16

2.3 Review on optimal control of hybrid powertrain 17

3 Mathematical model of the powertrain **29**

3.1 Introduction 29

3.2 Dynamic model of SI engine 31

3.2.1 Inlet manifold model 33

3.2.2 In-cylinder combustion dynamics 36

3.2.3 Crankshaft dynamics 40

3.2.4 Verification Results 45

3.3 NOx emission model for SI engine 46

3.3.1 NO kinetic model . . . 47
3.3.2 Molar fraction calculation for combustion products . . . 49
3.3.3 Dynamic simulation of kinetic NO model . . . 50
3.3.4 Simulation results of kinetic NO model . . . 51
3.4 Dynamic model for the Continuous Variable Transmission . . . 54
3.4.1 Driven pulley system . . . 55
3.4.2 Drive pulley system . . . 58
3.4.3 Dynamic model for power transfer . . . 62
3.4.4 Simulation results . . . 63
3.5 Dynamic model for the Manual Transmission (MT) . . . 65
3.6 Conclusions . . . 66

4 Objective analysis of the CVT and MT powertrain 68
4.1 Introduction . . . 68
4.2 Simulation of the complete powertrain model for CVT vehicle . . . 69
4.3 Simulation of the complete powertrain model for manual transmission-based vehicle 73
4.4 Drive cycle simulation results . . . 73
4.5 Conclusions . . . 77

5 Drivability characteristics assessment 79
5.1 Introduction . . . 79
5.2 Drivability characteristics . . . 80
5.3 Transmission model . . . 82
5.3.1 CVT transmission with centrifugal clutch . . . 84
5.3.2 MT transmission with clutch . . . 86
5.4 Simulation results . . . 87
5.4.1 Tip in simulation for significant engine operating zones . . . 87
5.4.2 Tip in simulation for significant vehicle operating zones . . . 91
5.4.3 Vehicle launch test . . . 94

5.5 Conclusions 95

6 Mathematical model of the electric machine and battery 96

6.1 Introduction 96

6.2 BLDC motor drive 97

6.2.1 Mathematical model of the BLDC motor 98

6.2.2 Inverter 100

6.2.3 Simulation 100

6.3 Li-Ion Battery 101

6.3.1 Mathematical model 103

6.3.2 Expressions for Li-Ion battery model 103

6.3.3 Simulation results 104

6.4 Conclusions 105

7 Integrated simulation for parallel hybrid configuration 106

7.1 Introduction 106

7.2 Parallel hybrid configurations with CVT and MT powertrains 107

7.3 Simulations of the CVT powertrain 109

7.4 Simulations of the MT powertrain 112

7.5 Conclusions 114

8 Control-oriented model for optimal control 115

8.1 Introduction 115

8.2 Dynamic model for the vehicle powertrain 115

8.2.1 Battery 117

8.2.2 IC Engine 117

8.2.3 Reference vehicle speed 118

8.2.4 Gear shift and engine speed 119

8.3 State and Control vector for optimal control problem formulation 120

8.4 Conclusions 123

9 Single function multi-objective optimization for component sizing 124

9.1 Introduction . . . 124

9.2 Multi-objective optimization . . . 125

9.3 Particle Swarm Optimization algorithm . . . 126

9.4 Deterministic dynamic programming algorithm . . . 128

9.5 Nested methodology for optimal sizing using PSO and DP . . . 130

9.6 Optimal design problem formulation . . . 131

9.7 Results for optimal design and control . . . 134

9.8 Conclusions . . . 140

10 Pareto-optimal multi-objective optimization for component sizing 141

10.1 Introduction . . . 141

10.2 Multi-objective optimization algorithm for Pareto-optimal solution . . . 143

10.3 Nested methodology for fitness function evaluation . . . 144

10.4 Optimal control problem formulation . . . 147

10.5 Results and discussion . . . 148

10.6 Conclusions . . . 154

11 Optimal controller for the motor-integrated transmission using hp-adaptive collocation 155

11.1 Introduction . . . 155

11.2 Numerical methods for Optimal Control . . . 156

11.3 Optimal control problem formulation . . . 162

11.4 Mathematical tools for hp-adaptive collocation method and dynamic programming . . . 163

11.5 Results and discussion . . . 163

11.6 Conclusions . . . 174

12 Conclusions and Future Work 176

Publications and Patents

List of Publications

The following publications are based on the research work :

1. Himadri B Das, Simos A Evangelou, and Samraj J Dhinagar, *"An Objective evaluation of characterisation matrix for two wheeler powertrain with Control oriented mathematical model," SAE World Congress* , 2015.

2. Himadri B Das, Simos A Evangelou, and Samraj J Dhinagar, *"An Objective analysis of drivability for two wheeler powertrain with control oriented dynamic model," 4th IFAC Workshop on Engine and Powertrain Control, Simulation and Modeling*, 2015.

3. Himadri B Das, Simos A Evangelou, and Samraj J Dhinagar, *"Multi-objective optimization using Genetic algorithm & Global optimal control for a motor integrated powertrain suitable for 2-wheeler application," Submitted to the Journal of Control Engineering Practice*, 2017.

4. Himadri B Das, Simos A Evangelou, and Samraj J Dhinagar, *"A multi-objective single function based nested methodology for optimal dimensioning & optimal control of a small capacity two-wheeled HEV powertrain," Submitted to the SAE International Journal of Alternative Powertrains*, 2017.

5. Himadri B Das, Simos A Evangelou, and Samraj J Dhinagar, *"hp-collocation based optimal control for a motor integrated hybrid power-train suitable for 2 wheeler application,"*

Submitted to the Journal of Dynamic Systems, Measurement and Control, 2017.

List of Posters presented

Part of this work has been presented as Poster in the following conferences :

1. Himadri B Das, Simos A Evangelou, and Samraj J Dhinagar, *"A methodology for drivability characteristics evaluation of two wheeler powertrain with Control Oriented mathematical model," Future Powertrain Conference,UK,* 2015.

1. Himadri B Das, Simos A Evangelou, and Samraj J Dhinagar, *"Design framework of Hybrid Scooter Power-train with Optimal performance suitable for Personal transportation," Commonwealth Science Conference, Singapore,* 2017.

List of Patents applied for

The following patents are applied for based on the this work :

1. Himadri B. Das and Samraj J. Dhinagar, *"Integrated unit for motor integrated hybrid transmission control and engine control"*, Nov. 14 2013, wO Patent App. PCT/IN2013/000,307. [Online]. Available:http://www.google.com/patents/WO2013168183A1?cl=en

2. Himadri B. Das, Simos A Evangelou and Samraj J. Dhinagar, *"Real time intelligent optimal electronic controller for hybrid vehicle"*, application under process.

3. Himadri B. Das, Simos A Evangelou and Samraj J. Dhinagar, *"Real time intelligent optimal electronic controller for motor integrated powertrain based vehicle"*, application under process.

Chapter 1

Introduction

India, which is one of the leading developing countries has witnessed an annual growth of 11% in vehicle sales [1] for last 8 years. According to the International Council of Clean Transport (ICCT) report (with data from World Road Statistics WRS, 2010) [1], two-wheeled vehicles comprise 80% of the total vehicle sales in India with a very strong annual growth. The strong presence of two-wheeled vehicles in India is evident from the sales data for the last couple of years (Figure 1.1) and (Figure 1.2). The gear-less two wheeler (popular as a scooter type vehicle), which is a major portion of the total two wheeler vehicles has witnessed a growth of 31% (Society of Indian Automotive Manufacturer's industry performance report) [2]. This is the strongest growth among the different categories of two wheelers. The growth of this industry has contributed to the increase of emissions resulting in deteriorating air quality. Any internal combustion engine emits combustion products of air pollutant and carbon monoxide (CO), nitrogen oxides (NOx), particulate matter (PM), hydro carbon (HC) and sulfur oxides (SOx). In India, the share of hydro carbon and carbon monoxide from vehicles with a smaller powertrain is higher than other motor vehicles. According to the ICCT's India Emissions Model, in 2010 the share of HC and CO are 92% and 74%, respectively [1].

A conventional powertrain of a scooter type vehicle consists of an IC engine, a centrifugal clutch system and a rubber-belt driven CVT. The advantages of the system are the smooth drivability due to the powertrain topology and the ability to operate the IC engine in better

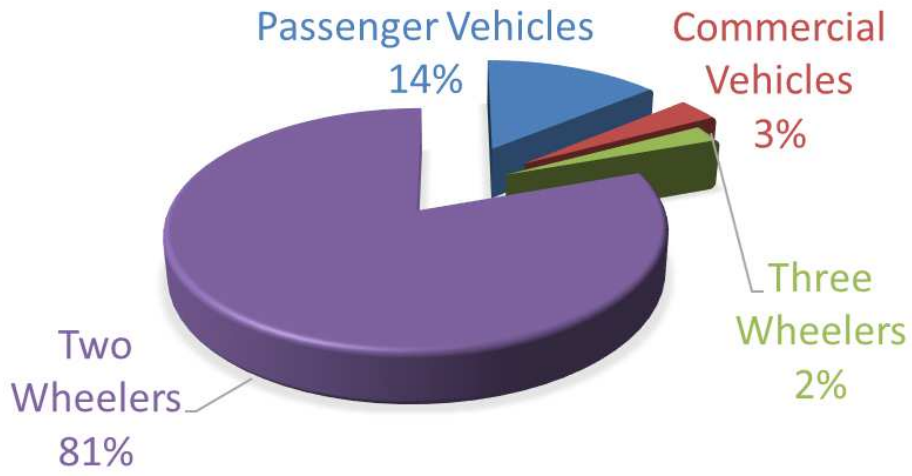


Figure 1.1: Domestic market share of different segments of vehicles in India for the year 2016-2017

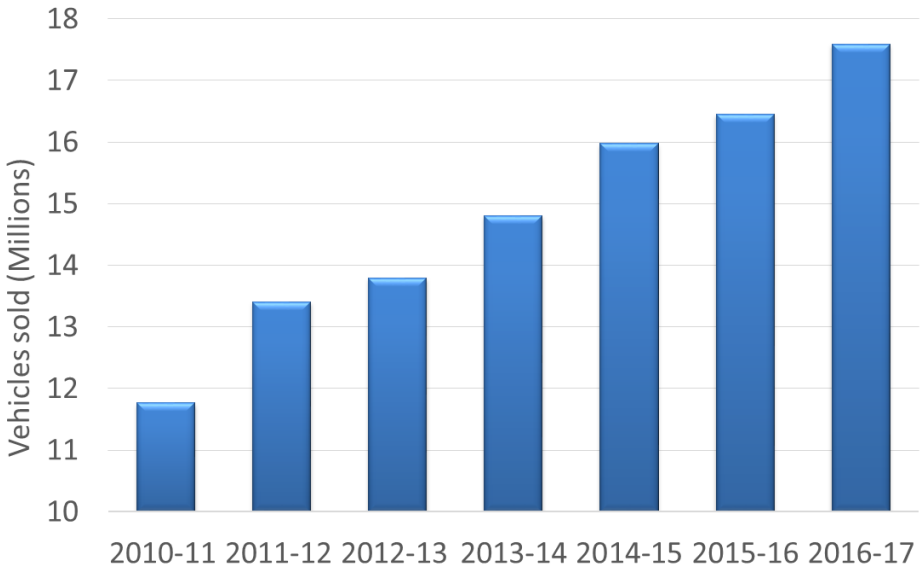


Figure 1.2: Two wheeler vehicle sales growth over the last 7 years in India

operating zone. The main disadvantage of the system is the lower system level efficiency due to high frictional losses in the rubber belt of the CVT. The high frictional loss of the CVT system nullifies the advantage of operating the IC engine in the suitable operating zone. On the other hand, the MT consists of a friction clutch system with step geared powertrain for transferring the engine power to the wheel. It has the advantage of low loss of the transmission. However, the system lacks drivability for transient city driving conditions. Hence it is very much essential to develop technologies suitable for a scooter type vehicle which is capable of emission reduction.

The automotive industry has developed several electric hybrid powertrain technologies, which can reduce the emissions for the vehicle. There are several production hybrid vehicles, which show fuel economy improvement from 10% (for mild hybrids) to 30% (for highly hybridized) [3]. Most of the hybrid vehicles achieve the fuel economy by power split algorithms, based on rules, a static-calibrated map or real-time optimization [3–8]. All such algorithms aim to control the split of power between the IC engine and electric drive to reduce fuel consumption and to maintain the State of Charge (SOC) of the battery in a narrow band during the drive. All of the above-mentioned algorithms need the information about instantaneous power requirement and states of the vehicle. Other than production-ready hybrid vehicles, there are several groups world-wide working in the hybrid vehicle energy management field [3]. Most of the above-mentioned methodologies are aimed for cars for developed nations where the traffic is well-regulated and the cost of the technology is not the prime factor, whereas the challenges are different for the two wheeler industry of India. There are several challenges in terms of packaging, weight and cost of the extra components, which need to be integrated with the existing IC engine-based powertrain to hybridize the powertrain. The traffic condition in India creates extra challenges for the existing algorithms. The drivability aspect for the two wheeler is a very strong influencing factor in calibration and tuning of the current powertrain components. Since the two wheeler is used in dense city traffic conditions, the smooth drivability of the vehicle is a very essential requirement for all the operating points.

The main intention of the research is to design a motor-integrated low-powered powertrain

suitable for two wheeler applications, which guarantees optimal performance as well as optimized sizing, considering the weight and cost impact on the vehicle. The above requirements imply the necessity for proposing a method of multi-objective optimization of the powertrain with an optimal control system. The advancement of modern automotive powertrains leads to different powertrain technologies, which can meet the above-mentioned requirement. However, the advanced powertrain concepts are not suitable for low-powertrain based two wheeler automobiles due to unsuitability of packaging and increase of cost. The powertrain configurations (with control scheme) proposed in this research are flexible to function as a hybrid powertrain if connected with an auxiliary power storage system [9].

In this research, a control-oriented mathematical model for the various powertrain components is developed as it

- provides modular flexibility to develop various powertrain configurations for future work,
- provides a platform to develop a control-oriented model for optimal design,
- provides a platform to perform objective drivability analysis and choose a suitable powertrain.

It was decided to investigate the optimized integration of an electric machine on the engine crank shaft to provide parallel hybrid vehicle functionality with CVT, considering the packaging, weight and cost of the extra components. The investigation is performed by:

- Single function-based multi-objective optimization with a nested global optimal controller
- Pareto-Optimal multi-objective optimization with a nested global optimal controller

The investigation for the optimal controller is performed using:

- Dynamic programming for a global optimal control, which can be used as a benchmark for other optimal controllers
- Global collocation method to evaluate a numerical optimal control method, which can inspire a real-time optimal controller for future work

1.1 Original Contributions

The aim of the research is to develop an optimized motor-integrated powertrain with an optimal controller for a two-wheeled vehicle. The current methods of sizing the powertrain components for two wheeler vehicles are based on static calibration methods. These methods are very much effective for a pure IC engine-based powertrain. However, in the case of a motor-integrated powertrain, the system complexity increases due to multiple sources of energy. Thus the need arises for an optimal control approach with optimization for control of the various components of the powertrain. The powertrain configuration chosen for the research is a parallel hybrid system where the electric machine is connected to the crank shaft of the IC engine and coupled with an electronically controlled CVT. The dynamic models of different sub-systems of the motor-integrated powertrain are created in a phased manner. These are high fidelity models developed from first principles, which ensures design flexibility for future unconventional powertrains. The selection of the suitable transmission system for the powertrain is done using an objective methodology introduced in this research. The control-oriented model for the powertrain is developed based on the detailed high fidelity model. The control-oriented model is suitable for numerical optimal control. The sizes of the powertrain components are optimized with multi-objective optimization method. The multi-objective optimization method is implemented with a single-objective function as well as Pareto-Optimal approach.

The unique work of multi-objective optimization for the motor-integrated powertrain provides a design framework for any further work for future horizontal deployment in any type of automotive powertrain. The optimal controller is developed using a global optimal method as well as with a numerical collocation method. The numerical collocation method provides the foundation for possible future research on real-time model predictive control in the automotive powertrain domain.

1.2 Assessment of Research Achievements

The dynamic model of the existing powertrain was verified with the experimental results of a production-ready vehicle from TVS Motor Company, India. Drive cycle simulation for both the MT and CVT powertrains configurations were performed on the dynamic models. These simulation results were reviewed by the technical experts from TVS Motor Company as well as presented in the SAE World Congress 2015. The drivability analysis of vehicle models with both the powertrains were performed with close collaboration of expert riders from TVS Motor Company. This work was presented in the IFAC Workshop on Engine and Powertrain Control 2015, Simulation and Modeling and FPC 2015 UK. The mathematical models of BLDC motor and Li Ion battery were compared with the results provided from TVS Motor Company. The nested methodology for single function-based multi-objective optimization was submitted to the SAE International Journal of Alternative Powertrains (2017) and it is currently under review. The Pareto-optimal multi-objective optimization work for the motor-integrated powertrain was submitted to the Journal of Control Engineering Practice (2017) and it is currently under review. The optimal controller developed using hp-collocation method was submitted to the IFAC Journal of Dynamic Systems, Measurement and Control (2017) and it is also currently under review. The ideas generated from the research helped to file three patents for TVS Motor Company.

1.3 Overview of each chapter

The work presented in the thesis provides a detailed insight into the optimal control of a motor-integrated hybrid powertrain for two wheeler application. The thesis is divided into 12 Chapters. Chapter 2 provides a literature review on the multi-domain area relevant to the area of research.

Chapter 3 presents dynamic mathematical models of:

- SI engine capable of simulating torque generation, fuel consumption and NOx emission.

- Powertrain transmission capable of simulating gear-less transmission (CVT) and geared transmission (MT).

The control-oriented model consists of a mean value SI engine model capable of simulating in cylinder as well as crankshaft dynamics. The SI engine model is validated and calibrated using available test data for a 110 cc production engine from TVS Motor Company. The transmission model is simulated for dynamic response of the system.

Chapter 4 presents dynamic mathematical models of:

- vehicle with gear-less transmission (CVT) with a low-powered powertrain, integrated with a longitudinal driver
- vehicle with geared transmission (MT) with a low-powered powertrain, integrated with a longitudinal driver

The fuel consumption and NOx emission is simulated for both dynamic models. The vehicle models are useful for the drivability evaluation work presented in the subsequent chapter.

Chapter 5 presents an objective drivability analysis for the two types of existing powertrains presented in Chapter 4 by making use of the model described in Chapters 3 and 4. The CVT and MT based powertrain models are objectively analyzed for tip in and launch operation of the vehicle.

Chapter 6 presents dynamic mathematical models of:

- BLDC motor with inverter, and
- Li-Ion battery.

The above-mentioned models from Chapter 3, Chapter 4 and Chapter 6 are very crucial for optimal control and multi-objective optimization presented in subsequent chapters. Chapter 7 presents simulation results of the integrated models. This simulation provides dynamic response of the motor-integrated powertrain.

Chapter 8 presents control-oriented mathematical models for the motor-integrated powertrain which is coupled with a CVT system. The models are appropriately simplified versions of

the detailed powertrain model developed in previous chapters. The model formulation, which is in discretized form, is useful for numerical optimal control.

In Chapter 9, a nested design methodology of optimal controller development and optimized powertrain component sizing for a parallel hybrid powertrain is proposed and implemented. The optimized sizing of different powertrain components (maximum power of the electric machine, maximum capacity of the Li-Ion battery pack, maximum gear ratio and minimum gear ratio) are determined using the algorithm, which can guarantee global optimal performance of the objective function.

Chapter 10 presents a multi-objective optimization coupled with a numerical optimal method for a motor-integrated hybrid powertrain. The NSGA-II algorithm is suitable for multi-objective optimization due to it's inherent strength. The numerical optimal control method is implemented using dynamic programming and it is used for evaluation of the part of the objective vector. The multi-objective simulation provides a Pareto-Optimal front of possible sizes of different components of the motor-integrated powertrain.

Chapter 11 presents a comprehensive study about different numerical optimal control methods. The hp-adaptive collocation method is chosen in this work due to its advantages over the other numerical optimal control methods. The objective function of the optimal control problem is formulated with equal weightage towards minimizing the fuel consumption and maintaining the battery SOC near a pre-defined level.

The final chapter concludes the thesis with an overview for the future research direction for this work.

Chapter 2

Literature Review

In this research, knowledge from different domains is utilized. Therefore the literature review covers a wide range of topics such as SI engine-based powertrain modeling, electric vehicle powertrain modeling, optimal control with multi-objective optimization etc.

2.1 Review on powertrain modeling

Significant work has already been carried out on the mathematical model development of SI engines. Work in [10] explained the mean value modeling and discrete event modeling for a SI engine. The mean value approach considers all the parameters of the model as functions of time, while discrete event-based models consider the parameters as functions of the crank angle position. The books [11,12] explained the different thermodynamic cycles for an SI engine. The literature of [10–12] discussed the inlet manifold dynamics for an IC engine. The characteristics of carburettor air flow and fuel flow model are described in [11, 13]. Effect of ignition timing on the combustion process is explained in [14–16].

The main contribution of the NO emission is due to kinetics of the chemical reaction for a lean air fuel ratio [11]. The initial kinetic reaction is proposed by Zeldovich in 1946 [17] and modified as Extended Zeldovich Mechanism (EZM) in 1970 [18]. The modeling of NO

emissions is discussed based on EZM [11, 19–21]. The EZM approach has some drawbacks and experimental result shows that the error can be as high as 50% [22]. Ford Motor Company has developed a new reaction scheme for NOx production which has been incorporated into a steady state quasi-dimensional engine combustion simulation [22,23]. The new reaction scheme is called a super-extended Zeldovich mechanism (SEZM). The reaction kinetics includes 67 reactions and 13 chemical species, and assumes equilibrium concentration for all other chemical species [22, 23]. This model reduces the error to 10% ,but it is not a control system oriented model.

BLDC motor modeling and inverter control is covered in detail by [24–27]. The BLDC motor model presented in this thesis is developed based on these literatures. The inverter model used in the thesis is developed using the approach explained in [27]. Significant works have been done for the development of mathematical models for batteries [28–34]. All of these references explain different types of models and based on the particular application a suitable model can be selected. The control-oriented model applied in this work is developed using the work presented in [28, 29].

2.2 Review on vehicle drivability

There are very few references available for subjective assessment of drivability for the two-wheeled vehicle segment. The paper [35] defines drivability as the longitudinal dynamic behaviour of a vehicle in response to driver inputs, in a comprehensive range of driving situations, and the related driver subjective perception of that behaviour. The reference [36] discusses 300 parameters for full subjective drivability analysis for a car. The papers [36–42] discuss how the subjective parameters can be linked to objective parameters such as the delay in response, stumble, oscillations and overshoot for a drivability analysis.

2.3 Review on optimal control of hybrid powertrain

A good overview on optimal control of hybrid vehicles is presented by [43]. The book [43] gives a detail overview about setting up the optimal control problem for the hybrid powertrain. It explains analytical methods, numerical solution and real-time implementation strategies for optimal control. It discusses the importance of control-oriented physical modelling of all the components of a hybrid powertrain and presents the appropriate models. The discussion covers the Willans line model of the IC engine, a piecewise quadratic function-based model for the electric machine and a simplified quadratic function for the battery is suggested. A similar approach for control-oriented modelling is also observed and reported in other literature [44–51]. It provides a formal definition of the optimal control problem with performance criteria. The performance criteria address the fuel consumption with different components of exhaust gas emission as a single-objective function with different weights. The discussion continues with a theoretical introduction to the analytical methods of optimal control, which explains the method of Lagrange multipliers and Pontryagins Minimum Principle with a parallel hybrid topology with the above-mentioned performance criteria. This discussion also explains the origin of the Equivalent Consumption Minimization Strategy w.r.t. the method of Lagrange multipliers. This paper covers basic information about different numerical and real-time approaches for optimal control strategies suitable for hybrid powertrains. The paper [3] is a good starting point for understanding optimal control applications on hybrid vehicles. The general optimal problem is discussed in detail for arriving at global optimal trajectories in [52–55]. Real-time strategies for optimal control in hybrid vehicles are presented in [4, 5, 56]. One of the main requirements for real-time optimal control is prediction of the reference vehicle speed for future horizon. The reference [57] provides a very good overview about the driver model from the past vehicle data.

The papers [44, 46–51] further cover recent trends for development of different control strategies for hybrid vehicles. These references suggests hybrid electric vehicle controllers are divided into two broad groups: 1) rule-based controllers and 2) optimization-based controllers.

Rule-based control strategies are tuned to achieve the best fuel economy, efficiency, performance, and emissions for a specific drive cycle [58–60]. They operate based on a set of criteria defined by the system. The main goal of any rule-based control strategy is to operate the powertrain at its highest efficiency point, by running the engine and the electric machine at their most efficient points, utilizing the extended battery range and maximizing the regenerative potential. Predefined rules are initially set based on desirable outputs and expectations without any prior knowledge of the trip. Flowcharts and state diagrams are commonly used to represent the power flow of a given driving scenario. The rule-based control schemes are sub-divided into two sub-groups 1) deterministic rule-based and 2) fuzzy rule-based [46, 49]. The optimization-based control strategies try to overcome the inherent rigidity of the rule-based controllers by designing an optimal control strategy by minimizing a cost function. The cost function is derived based on the vehicle and component parameters and the performance expectations of the vehicle. Some controllers are optimized for specific drive cycles using past and future (expected) information regarding the trip and components and are therefore termed acausal systems. More advanced control techniques are based on real-time optimization. Also referred to as causal systems, they rely on real-time feedback to optimize a cost function that is developed using past information.

The optimization-based control strategies are further subdivided based on different characteristics of the particular strategies. The first subdivision is based on the capability of the control strategy to determine the global minima or local minima, the second subdivision is based on modes of search algorithm deployed by a particular control strategy (deterministic or stochastic) and the third subdivision is based on use of numerical methods to search the optimal control (gradient and derivative-free). Three different energy management approaches for the control of a parallel hybrid electric sport-utility-vehicle that do not require prior knowledge of the driving cycle are compared with results obtained from dynamic programming in [44]. The considered approaches are: a rule-based control, an adaptive equivalent fuel consumption minimization strategy (A-ECMS) and an H_∞ control method. The comparison shows that the A-ECMS strategy is the best performing strategy. The control-oriented models of IC engine

and electric machine of this paper have the same structure as mentioned in [43]. The objective function consists of the fuel consumption term. The rule-based control technique presented in this paper employs heuristic knowledge to develop a set of event-triggered rules. The presented rule-based control method is very much suitable for real-time implementation, however it can not guarantee an optimal performance as mentioned in other references [44, 46–50, 61]. While the rule-based control technique does not explicitly seek to optimize energy consumption or emissions, the ECMS explicitly formulates a cost function for the equivalent fuel consumption to be optimized, subject to constraints related to charge sustainability, emissions reduction and drivability. The ECMS objective function consists of the fuel consumption term with a penalty function associated with the use of stored electric energy and the equivalent fuel consumption associated with the emissions. The penalty and weights are inspired by the method of Lagrange multipliers. However, the results depend on the form of the penalty function. A real-time sub-optimal energy management strategy for HEVs is proposed in this reference, which modified the existing ECMS framework to the above-mentioned A-ECMS strategy. The main idea is to periodically refresh the control parameters according to the current road load, so that the SOC is maintained within the boundaries and the fuel consumption and pollutant emissions are minimized. In particular, the algorithm identifies the mission that the vehicle is to follow and determines the optimal equivalence factor for the current mission by direct optimization, thus it is able to relate the control parameters to the current velocity profile.

It is essential to review the advancements of control strategies for plug-in hybrid vehicles. Classification and review of control strategies for plug-in hybrid electric vehicles is provided in [45]. This paper argues that the existing control strategies of a hybrid vehicle may not hold true for a plug-in hybrid electric vehicle due to the criteria of electric-only drive capability, additional discharge range due to the larger battery pack and the option of turning the engine off of plug-in hybrid electric vehicles. The paper [46] is the most recent publication which covers the latest progress in the field of optimization-based control development of plug-in hybrid electric vehicles. In contrast to previous references, this paper avoids the classification into groups, which can be sometimes misleading due to possible algorithms modifications and vari-

ous assumptions taken for implementation. Instead, each algorithm is individually introduced and evaluated, highlighting its strengths and weaknesses. The charge sustaining and charge depleting control methods of hybrid powertrains can be extended to plug-in hybrid powertrain controllers [46, 47, 59]. These control methods can be categorised as rule-based [45], which are easy to implement, however they suffer performance degradation due to their inherent rigidity [46, 47, 59, 62, 63]. The blended mode control strategy tends to perform better than the above-mentioned charge sustaining and charge depleting control strategies for known drive cycles. However the performance of this method degrades substantially for general driving conditions [48, 60, 64, 65].

As mentioned above, the optimization-based control strategies tend to perform better in dynamic driving scenarios, however they are also associated with additional implementation issues, e.g. algorithm complexity, high computation effort, robustness and sensitivity to drive cycle information and characteristics which are the main reasons for their slow integration in industry [46, 47]. There are several approaches adopted by researchers to adopt optimization-based algorithms for optimal control of hybrid powertrains. These methods are dynamic programming, equivalent fuel consumption minimization strategy, simulated annealing, genetic algorithm, particle swarm optimization, divided rectangle method, neural networks, game theory, sliding-mode control and convex programming. Dynamic programming is an algorithm able to compute global optimal solutions in general control problems. Dynamic programming divides the problem into sub-problems, which are easier to solve and require less computational cost [46, 66–68]. Sub-problem optimality is guaranteed through the principle of optimality: "Optimal policies have optimal sub-policies". The sub-problems are solved using multiple state decision-making processes, and the possible solutions are studied via selecting only optimal combinations, which reduces the searching space and thus calculation time. Dynamic programming is applicable to varied domains, including non-linear constrained dynamic processes and integer problems, and it can manage several complex constraints applied to states and inputs. However, the dynamic programming algorithm itself is not easily tractable and its computational resource requirements increase exponentially with the number of states and control

variables [46, 66–68].

Simulated annealing is a derivative free method which is inspired by the annealing process of metals. The solution is searched through a stochastic technique that takes the solution candidates that show improvement over the objective function but keeps suboptimal solution candidates which still agree with a defined criterion as well. This characteristic prevents the algorithm from being trapped in local minima and enhances its evolution towards global optimality [46, 69, 70]. Simulated annealing can be combined with other derivative-free optimization algorithms to increase its capabilities [46, 71, 72]. The convergence capabilities of the simulated annealing algorithm is improved by integrating it with genetic algorithm. This integrated algorithm utilizes of the robust global convergence capabilities of genetic algorithm in earlier stages, and reduced the run-time of later phases using the simulated annealing algorithm [46,71]. Similarly, the simulated annealing and particle swarm optimization algorithms convergence deficiencies are compensated by combining both algorithms to form a so-called PSOSA [46, 72].

Genetic algorithm is a stochastic optimization method inspired on natural selection and genetic evolution. It consists of three phases: reproduction, crossover and mutation, which involve randomness to ensure population diversity. In each of the iterations, the solution is coded in simulated "chromosomes". Then, the best candidates are selected according to the value of the objective function (fitness value) and deployed to populate the next set of solutions following the previously listed steps. The process eventually converges to "the best solution", a satisfying trade-off between computational effort and precision. This algorithm provides good performance even when dealing with complex problems and it is compatible with a broad variety of models, such as linear and non-linear models with continuous or discontinuous-time form [46, 51, 69, 73–75]. One of the main strengths of this algorithm, compared with other optimization strategies, is the capacity of parallelism detection between different agents, which is particularly beneficial to computing Pareto-Optimal solutions for multi-objective optimization. As mentioned for the case of the simulated annealing algorithm, the genetic algorithm can be combined with other optimization algorithms like quadratic programming to solve optimal

control problems for a plug-in hybrid vehicle [46, 73].

Particle Swarm Optimization (PSO) is inspired by the behavior of social organism moving together for a food searching exercise, such as swarms, ant colonies, and bird flocking, which share information within the members. PSO is also considered a particular case of evolutionary algorithms, due to the solution population characteristic similar to the crossover mechanism in genetic algorithm. This algorithm populates particles states, position and velocity in each iteration. The particles of the population interact locally between each other with the purpose of interchanging information and can store their last best position and group best solution, with the goal of improving individual objective functions the next iteration [46, 51, 69, 72, 74]. The convergence behaviour depends on previously calculated solutions and particle velocity. PSO is robust to complex objective functions and merely requires a population of two variables per particle (i.e., position and velocity), and iteration. The small number of tuning parameters facilitates its implementation and reduces its sensitivity to initial solutions, when compared with other stochastic optimization algorithms [46, 51, 69, 72, 74].

DIRECT (DIvided RECTangles) is a sampling algorithm, developed by Donald R.Jones [46,51,76,77]. This global optimisation algorithm is a modification of the standard Lipschitzian approach that eliminates the need to specify the Lipschitz constant. The Lipschitz constant is a weighing parameter, which decides the emphasis on the global and the local search. The use of the Lipschitz constant is eliminated by searching all possible values for the Lipschitz constant, thus putting a balanced emphasis on both the global and the local search. The algorithm begins by scaling the design box to an n-dimensional unit hypercube. DIRECT initiates its search by evaluating the objective function at the centre point of the hypercube. It then divides the potentially optimal hyper-rectangles by sampling the longest coordinate directions of the hyper-rectangle. The sampling is done such that each sampled point becomes the centre of its own n-dimensional rectangle or box. This division continues until termination (pre-specified iteration limit is reached) or convergence is achieved [46, 51, 76, 77]. Compared with other stochastic optimization algorithms, DIRECT is relatively simple as it does not require tuning parameters and can handle both equality and inequality constraints. Moreover, it is robust in

the presence of non-linearities and disturbances [46, 51, 61].

Game theory deals with the interaction between decision-makers, also known as players. The players pursue defined objectives and are considered agents with self-interest. Game theory is inspired by the main characteristics describing ordinary games, which typically involve various players, a set of rules, and a number of allowable strategies. These available actions have an associated pay-off, which rates how beneficial or detrimental the "movement" for each player is. The game itself only describes what the players can do, but not the ultimate actions, in the same way the model equations constrain the variables feasible values [46, 78–81]. Every strategy followed by one player generates a benefit for the named agent and a loss for the rest, which is the so called pay-off. It is assumed that each player acts rationally towards the action that maximizes its own pay-off, and the game evolves towards the steady-state case, where no player has any incentive to change its state. This is known as a Nash equilibrium, a non-unique situation usually difficult to reach which does not necessarily represent the fairest outcome for all players. Game theory can be implemented with receding horizon in the same way as model predictive control, however, its computation burden can be comparable to dynamic programming, even when it uses simpler equations. This makes its online implementation difficult in vehicular applications. The papers underlined the fact that game theory requires deep knowledge of the system elements and consequently cannot be extrapolated to other vehicles with different components. This constitutes one of the main drawbacks [46, 78–81].

Sliding mode controller is an inherently robust algorithm to modeling uncertainty and non-linearity, which can efficiently work with system structures that alternatively switch. It is also insensitive to parameters change and disturbances, a salient characteristic that makes it useful for vehicular applications. The complexity and performance of sliding mode controller depends on the sliding surface design. Consequently, the mathematics involved in this algorithm can be relatively complicated, in contrast with most of the above-mentioned algorithms [46, 82, 83].

Convex programming is a generalization of linear programming and quadratic programming. In convex optimisation problems, local optima coincide with global optima, simplifying

extensively the search of solution. Nevertheless, the algorithm can only be applicable when the problem is strictly expressed in convex terms, which requires both the cost function and inequality constraints to be expressed in convex form and affine equality constraints. Convex vehicle models need to be simplified to comply with convexity requirements [10]: 1) eliminate integer decisions, i.e., engine on/off, gear shift etc, 2) equality constraints must be relaxed if they are originally not affine, 3) use new variables to preserve convexity, such as battery energy instead of SoC and 4) problem coding should be implemented in discrete time. The main limitation of this algorithm lies in the formulation of an appropriate vehicle model. For instance, switch decisions cannot be optimized in the convex programming problem, and consequently, the optimal gear shift cannot be easily pursued with high accuracy [46, 84, 85].

In the following part, literature review for different numerical methods of optimal control is presented. The optimal problem can be formulated as

$$J = \Phi\left[\mathbf{x}(t_0), t_0, \mathbf{x}(t_f), t_f; \mathbf{p}\right] + \int_{t_0}^{t_f} \mathcal{L}\left[\mathbf{x}(t), \mathbf{u}(t), t; \mathbf{p}\right] dt \tag{2.1}$$

subject to the dynamic constraints

$$\dot{\mathbf{x}}(t) = f\left[\mathbf{x}(t), \mathbf{u}(t), t; \mathbf{p}\right] \tag{2.2}$$

with path constraints

$$C_{min} \leq C\left[\mathbf{x}(t), \mathbf{u}(t), t, \mathbf{p}\right] \leq C_{max} \tag{2.3}$$

and boundary conditions

$$\phi_{min} \leq \phi\left[\mathbf{x}(t_0), t_0, \mathbf{x}(t_f), t_f; \mathbf{p}\right] \leq \phi_{max} \tag{2.4}$$

where $\mathbf{x}(t)$ is the n dimensional state vector, $\mathbf{u}(t)$ is the m dimensional control vector and $\mathbf{p}$ is the q dimesional vector for static parameters

$$\mathbf{x}(t) = \begin{bmatrix} x_1(t) \\ . \\ . \\ x_n(t) \end{bmatrix}, \mathbf{u}(t) = \begin{bmatrix} u_1(t) \\ . \\ . \\ u_m(t) \end{bmatrix}, \mathbf{p} = \begin{bmatrix} p_1 \\ . \\ . \\ p_q \end{bmatrix} \tag{2.5}$$

The optimal control problem mentioned in (2.1), (2.2), (2.3) and (2.4) can be solved using various numerical methods. Figure 2.1 shows the two major types of numerical optimal control approaches. In an indirect method, the calculus of variations is used to determine the

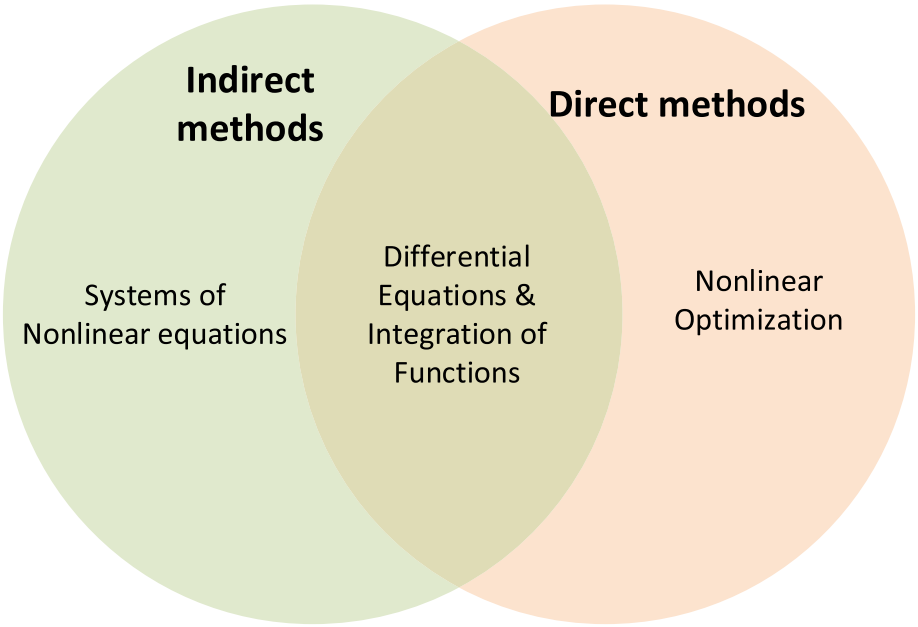


Figure 2.1: Two major approaches of a numerical optimal control

first-order optimality conditions of the original optimal control problem. The indirect approach leads to a multiple-point boundary-value problem that is solved to determine candidate optimal trajectories called extremal. Each of the computed extremal is then examined to see if it is a local minimum, maximum or a saddle point. Among the locally optimizing solutions, the particular extremal with the lowest cost is chosen [86–90]. The direct method (should not be confused with the DIRECT/DIvided RECTangles method, mentioned earlier in this Chapter) is the combination of numerical methods for differential equations with non-linear optimization, whereas the indirect method is the combination of numerical methods for differential equations with numerical solution of systems of non-linear equations.

Figure 2.2 gives a more detailed view of different methods of solving a numerical optimal control problem. There are three numerical approaches which are predominantly used in optimal control research viz dynamic programming, indirect method and direct method [86–90].

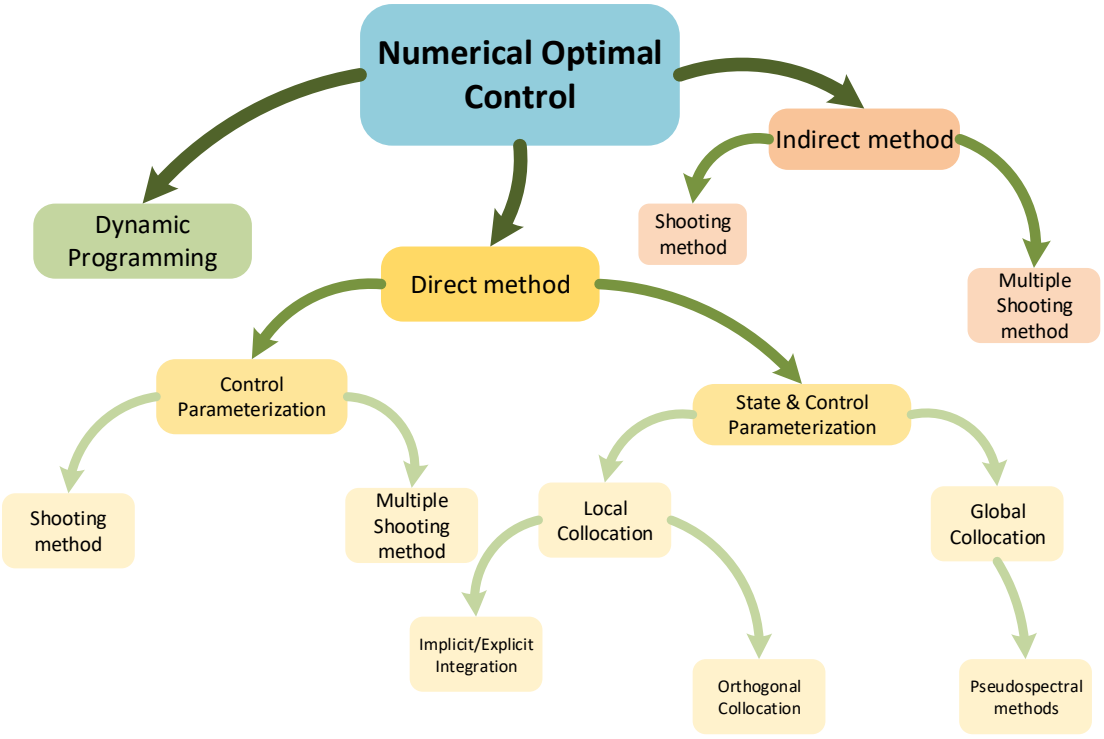


Figure 2.2: Different methods for Numerical Optimal Control

As mentioned previously, dynamic programming uses the principle of optimality of sub-arcs to compute recursively a feedback control for all times [66, 67, 87]. In the continuous time case, this leads to the Hamilton-Jacobi-Bellman (HJB) equation, a partial differential equation in state space. Methods to numerically compute solution approximations exist, but the approach severely suffers from Bellman's "curse of dimensionality" and is restricted to small state dimensions. The most basic direct method for solving optimal control problems is the direct shooting method. The direct shooting method is a control parametrization method where the control is parametrized using a specified functional form [86–89]. In a direct multiple-shooting method, the total time horizon is divided into multiple sub-intervals. The mentioned direct shooting method is then used over each sub-interval with the values of the state at the beginning of each sub-interval and the unknown coefficients in the control parametrization

being unknowns in the optimization [86–90].

Arguably the most powerful methods for solving general optimal control problems are direct collocation methods [86, 89, 91]. A direct collocation method is a state and control parametrization method where the state and control are approximated using a specified functional form. The two most common forms of collocation are local collocation and global collocation [86, 89, 91]. In the context of optimal control, local collocation has been employed using one of two categories of discretization: Runge-Kutta methods and orthogonal collocation methods. In the case of Runge-Kutta, nearly all of the methods used are implicit because the stability properties of implicit Runge-Kutta methods are better than those of explicit methods. The seminal work on orthogonal collocation methods in optimal control is due to Reddien, where Legendre-Gauss points were used together with cubic splines [86, 89, 91]. In recent years pseudospectral methods have increased in popularity. A pseudospectral method is a global form of orthogonal collocation, i.e. in a pseudospectral method the state is approximated using a global polynomial and collocation is performed at chosen points. Thus, as opposed to local collocation, where the degree of the polynomial is fixed and the number of segments (meshes) is varied, in a pseudospectral method the number of meshes is fixed and the degree of the polynomial is varied. As with a local orthogonal collocation method, the basis functions are typically Chebyshev or Lagrange polynomials. Pseudospectral methods were developed originally to solve problems in computational fluid dynamics. The rationale for using a global polynomial with orthogonally collocated points is that the approximation will converge spectrally (i.e., at an exponential rate) as a function of the number of collocation points [86, 89, 91]. Four important computational issues that arise in the numerical solution of optimal control problems are: (a) consistent approximations for the solution of differential equations; (b) the scaling of the optimal control problem; (c) exploitation of sparsity in the non linear programmer; and (d) computation of derivatives of the objective and constraint functions [86, 89, 91]. The manner in which the differential equations are discretized is of great importance because an inconsistent approximation to the differential equations can lead to either non convergence or convergence of the optimization problem to the wrong solution. Scaling and exploitation of sparsity in the

non linear programmer are issues that greatly affect both computational efficiency and convergence of the non linear programmer. Finally, the manner in which derivatives are computed is of great importance because accurate derivatives can greatly improve both computational efficiency and reliability [86, 89, 91].

The above section provides an overview about the appropriateness of the choice of the optimization algorithm for the research objective. The preview does not intend to compare different methods for numerical capabilities. The optimization methods implemented in Chapter 9-11 are chosen based on the above mentioned reason.

Chapter 3

Mathematical model of the powertrain

3.1 Introduction

It is essential to mathematically evaluate the characteristics of gear-less transmission (CVT) and geared transmission (MT) for a low-powered powertrain for certain objectives. Currently, the low-powered powertrain-based automotive industry in India evaluates the characteristics using either experimental methods or simulation-based methods with commercially available software tools. Both of the industry accepted methods have their own limitations for the research of future powertrains. The experimental method requires prototype powertrain building, which may be a time consuming and challenging process. On the other hand, most of the commercially available software use proprietary models for certain modules of the powertrain model. Moreover, the commercial software are mainly developed targeting the automotive car industry. Hence it is very much essential to develop the powertrain models for gear-less transmission (CVT) and geared transmission (MT) for a low-powered powertrain from first principles.

The above-mentioned powertrain models should be able to :

- Simulate the dynamic characteristics of the SI engine including torque generation and fuel consumption.
- Simulate NOx emission of the SI engine. Although HC and CO contribute significant portions of the exhaust gas emissions, the proposed work does not capture the dynamic models of either of these.
- Simulate CVT functionality.
- Simulate MT functionality.

The powertrain models do not include tyre model and vehicle dynamics model. Hence, they are not suitable to simulate the wheel spin and wheel skid phenomenon. Moreover, the research is not focussed on lateral vehicle dynamics. Therefore vehicle dynamics model is not incorporated in the models. Hence, these exclusions would not effect the main objectives of the research. The exclusion of HC and CO emissions in this research work would definitely influence design of optimal controller as well as sizing of the powertrain components. Especially during warming-up phase of a SI engine, it emits considerable amount of HC and CO emissions. However, the research work excludes engine warming up phase, i.e. the cranking and idle operating phases for design of optimal controller as well as sizing of the powertrain components. Current emission norm for low power SI engine excludes exhaust emission testing for the warming-up phase. The powertrain model for warming-up phase would be included in future work, by treating warming-up phase as an independent phase of SI engine. This is necessary, since functionality of the three-way catalyst (it ensures chemical conversions of exhaust emissions to non-harmful emissions) depends on the temperature of the exhaust gas. This approach would result in two separate optimal controllers each for warming-up phase and warm engine for future research work. The proposed powertrain models are integrated with a longitudinal driver model for simulating the Indian Drive Cycle (IDC). The drive cycle simulation provides objective information for different characteristics of the powertrain. The driver model ensures that the powertrain model tracks the reference trajectory of longitudinal vehicle speed as defined by the drive cycle. The model developed in this chapter will be used in Chapter 5, 8-11 for optimal control development of an integrated powertrain control scheme.

The main significance of this work is to develop the simulation platform with traditional power-train components. The engine platform for the research is a 110 cc SI engine with carburettor fuel metering from TVS Motor Company. The detailed technical specifications of the engine could not be provided in this work due to confidentiality restrictions.

3.2 Dynamic model of SI engine

The IC engine is an energy converter that converts chemical energy to mechanical energy. It is broadly classified as Spark Ignition (SI) type and Compression Ignition (CI) engine based on the type of combustion phenomena. There is another type of classification for the IC engine, which is based on the number of rotations per engine cycle. It is classified as four-stroke or two-stroke engine based on this classification. In this research, a four-stroke spark ignition (4S SI) is considered as the main energy source of the vehicle. A carburetor controls the fuel flow for the SI engine. Although fuel injection technology is becoming the norm in bigger capacity engines, in smaller displacement engines (less than 150 cubic centimeters(cc)) fuel metering is controlled by carburetor.

The aim of the model is to simulate the dynamic characteristics of the main energy source. In the model, the mass of air fuel mixture and spark timing are the two primary inputs to the energy source, and crankshaft torque and emission are the primary outputs.

The scopes of the model are:

- To simulate the dynamic crank shaft torque for the operating zone corresponding to the non-idle driving zone for a drive cycle of the SI engine.
- To simulate NOx emission for the full operating zone corresponding to the non-idle driving zone for a drive cycle of the SI engine.

The cranking and idle operating zones are kept out of scope of the work due to following reasons:

- Both the operating zones are unstable operating zone for the SI engine.

- Since vehicle is stationary for both the operating zones, the scope of optimal control to minimize the cost function (for example fuel consumption or/and exhaust emission or/and maintain battery charge sustainability) is negligible.

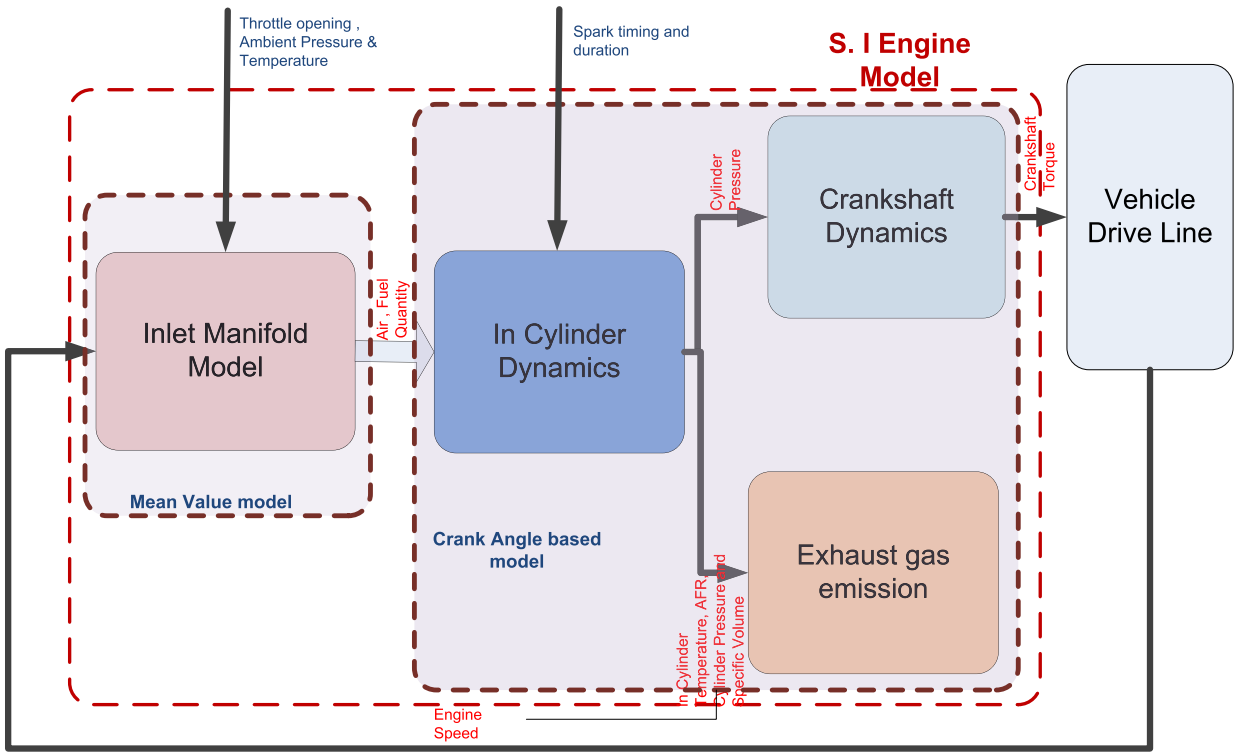


Figure 3.1: Implementation of the spark ignition engine model

The proposed model is a hybrid model which consists of mean value as well as discrete event modeling parts. The inlet manifold dynamics is slower than the combustion dynamics inside the combustion chamber. Figure 3.1 shows the interaction of both types of models in the research. The inlet manifold model is implemented as a mean value model and the in cylinder dynamics is modeled as a discrete event model. The model is structured with four sub models as shown in Figure 3.1 :

- Inlet manifold model
- In-cylinder dynamics
- Crankshaft dynamics

- Exhaust gas emission

The "inlet manifold model" calculates manifold air flow (MAF), fuel flow (FF), manifold air pressure (MAP) and air fuel ratio (AFR). The value of MAF and fuel flow is used in the "In-cylinder dynamics" model. The "In-cylinder dynamics" model calculates the in-cylinder pressure for the "crankshaft dynamics" model and the in-cylinder temperature, in-cylinder pressure and AFR for the "exhaust gas emission" model. In this thesis, only one component of exhaust gas emission is modeled.

3.2.1 Inlet manifold model

As mentioned above, the inlet manifold is modeled as a mean value model. The inlet manifold can be assumed as a receiver where the mass flows from the carburetor to the engine cylinder. The rate of change of mass of the air charge inside the inlet manifold can be expressed as

$$\frac{dm_{manifold}}{dt} = \frac{dm_{carburetor}}{dt} - \frac{dm_{cylinder}}{dt} \tag{3.1}$$

where $m_{manifold}$, $m_{carburetor}$ and $m_{cylinder}$ are the mass of air charge inside the inlet manifold, mass of air charge flowing through the carburetor and mass of air charge flowing to cylinder respectively. The expression for MAP can be derived from (3.1) and the ideal gas equation as

$$\frac{dp_{manifold}}{dt} = \frac{RT_{manifold}}{V_{manifold}} \left(\frac{dm_{carburetor}}{dt} - \frac{dm_{cylinder}}{dt} \right) \tag{3.2}$$

where $p_{manifold}$, R, $T_{manifold}$ and $V_{manifold}$ represent MAP, gas constant, manifold gas temperature and volume of the inlet manifold respectively. The $\frac{dm_{carburetor}}{dt}$ term can be modeled assuming the carburetor as a valve with variable opening:

$$\frac{dm_{carburetor}}{dt} = C_d A_{carburetor}(t) \frac{p_{atm}}{\sqrt{RT_{atm}}} \Psi \left(\frac{p_{atm}}{p_{manifold}} \right) \tag{3.3}$$

where C_d is the coefficient of discharge for the air path of the carburetor, $A_{carburetor}(t)$ is the opening area of the carburetor air path at time t, p_{atm} is the atmospheric pressure, T_{atm} is the

atmospheric temperature and $\Psi(\cdot)$ is the flow function. The $A_{carburetor}(t)$ term is a function of throttle position. The flow function can be defined as

$$\Psi\left(\frac{p_{atm}}{p_{manifold}}\right) \approx \begin{cases} \frac{1}{\sqrt{2}} & p_{manifold} < p_{atm} \\ \sqrt{\frac{2p_{manifold}}{p_{atm}}\left(1 - \frac{p_{manifold}}{p_{atm}}\right)} & p_{manifold} \geq p_{atm} \end{cases} \tag{3.4}$$

As this engine's fuel metering is achieved by a carburetor, it is required to model the fuel flow through the carburetor. The pressure difference between the carburetor inlet and opening of the fuel flow nozzle controls the fuel flow. As the fuel is an incompressible fluid, the fuel flow through the nozzle m_{fuel} can be derived using Bernoullis equation [11], as

$$\frac{dm_{fuel}}{dt} = C_0 A_{nozzle}(t)(2\rho_f \Delta p_f(t)) \tag{3.5}$$

where C_0 is the discharge coefficient of the nozzle, $A_{nozzle}(t)$ is the opening of the nozzle, ρ_f is the density of the fuel and $\Delta p_f(t)$ is the pressure difference across the fuel flow nozzle. The $A_{nozzle}(t)$ is a function of throttle position. The C_0 is a function of the operating point of the engine as well as the geometry of the fuel path. This expression for C_0 can be complicated considering the geometrical configuration of the nozzle. The parameter C_0 is considered as a calibration parameter for tuning the values of m_{fuel} in different operating points of the engine. The $\Delta p_f(t)$ term can be expressed as

$$\Delta p_f(t) = (p_{atm} - p_{manifold}) - \rho_f g h \tag{3.6}$$

where g is the gravitational constant and h is in the order of 10 mm [11]. The $\frac{dm_{cylinder}}{dt}$ term can be modeled assuming engine to be a volumetric pump. In a volumetric pump, the mass flow is approximately proportional to the speed of the pump. The expression for this model

is

$$\frac{dm_{cylinder}}{dt} = \rho_{air}\mu_{volumetric}\frac{V_{cylinder}}{2}\frac{\omega_e}{2\pi} \tag{3.7}$$

where ρ_{air}, $\mu_{volumetric}$, $V_{cylinder}$ and ω_e are gas charge density, volumetric efficiency of the engine, total cylinder volume and engine speed respectively. The AFR can be calculated as the ratio between $m_{cylinder}$ and m_{fuel}.

The above-mentioned model is validated with the available experimental data for a 110 cc capacity engine in TVS Motor Company. The fuel metering for this engine is achieved by a carburetor. The detailed model of inlet manifold involves complex mathematical expressions and can be implemented using computational fluid dynamics. This conflicts the aim of developing a control-oriented model for the powertrain. The discharge coefficients C_0 and C_d can be considered as two calibration parameters due to two reasons, (a) both of the parameters do not change with time (b) both of the parameters are not mechanical dimensional parameters. Therefore both of the parameters are calibrated for different engine operating points to achieve the required AFR ratios. This calibration process of tuning the coefficients is very essential to build the mathematical model which can be validated with available experimental data. The model is simulated for the wide open throttle (WOT) condition in different engine speeds. The following model parameters are validated against the experimental data available from TVS Motor Company:

- Manifold air flow ((MAF)
- Fuel flow (FF)
- Manifold air pressure (MAP)
- Air fuel ratio (AFR)

The above-mentioned parameters are very significant as all of them have a significant influence on the torque and emission outputs of the engine model. Figure 3.2 shows the percentage error for the above-mentioned parameters. The calibration parameters C_0 and C_d are tuned to keep errors within an acceptable limit for WOT condition. The error graphs for MAF and MAP do

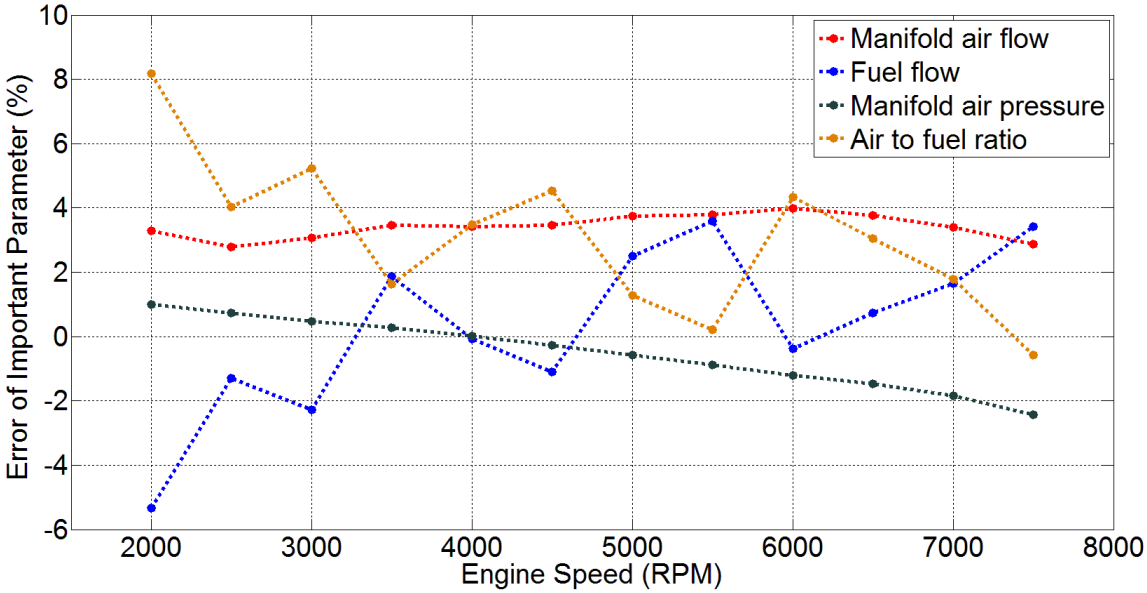


Figure 3.2: Error plot for the manifold model outputs in WOT condition

not change sign, but the same is not true for the other two parameters FF and AFR. The error curves of FF and AFR are symmetrical w.r.t. the X axis. The error of FF can be influenced by the measurement sensitivity.

3.2.2 In-cylinder combustion dynamics

The in-cylinder dynamics is subdivided into five discrete phases according to the internal dynamics of the cylinder, viz intake stroke phase, compression stroke phase, combustion phase, power stroke phase and exhaust stroke phase. There are three important thermodynamic parameters (in-cylinder pressure p, in-cylinder temperature T and dynamic volume of cylinder V), which need to be modeled for each of the different phases. The gas charge inside the cylinder changes its states (p and T) depending on the above-mentioned phases of in-cylinder dynamics. The thermodynamic process corresponding to each of the phases can be subdivided as:

- Intake and and exhaust strokes are assumed to be isochoric heat loss processes ($dV = 0$).
- Compression stroke is isentropic compression ($dq = 0$, where q is the input of thermal energy).
- Combustion phase is an isochoric process with input of thermal energy as the heat release

occurs during relatively small crank angle duration.

- Power stroke is an isentropic expansion.

Compression and Expansion stroke

The in-cylinder states of compression stroke are given by the relations

$$p(\alpha) = p(BDC)\left(\frac{V(BDC)}{V(\alpha)}\right)^{\gamma},\ T(\alpha) = T(BDC)\left(\frac{V(BDC)}{V(\alpha)}\right)^{\gamma-1} \tag{3.8}$$

where $p(BDC), T(BDC), V(BDC)$ correspond to the values of in-cylinder pressure, in-cylinder temperature and cylinder volume at the start of compression stroke, i.e. bottom dead center (BDC) of the cylinder. $p(\alpha)$, $T(\alpha)$, and $V(\alpha)$ correspond to the instantaneous values of the states and they are functions of the crank angle position α of the engine. The expressions for $p(\alpha)$ and $T(\alpha)$ during the expansion stroke are similar to (3.8). γ is defined in the next section.

Combustion phase

The in-cylinder states of the combustion phase need to be expressed in detail as they involve the model for heat release from the cylinder charge. In this work, the single zone heat release model is considered as it gives a good prediction of the heat release rate with less numerical resource [11, 14–16]. The mass fraction burned x_b, from the fuel is expressed as a function of crank angle position with the Wiebe function. Thus x_b can be expressed as

$$x_b = 1 - \exp\left[-a\left(\frac{\alpha - \alpha_{spark}}{\Delta\alpha}\right)^{(m+1)}\right] \tag{3.9}$$

where α_{spark} is the crank angle position for the start of combustion, $\Delta\alpha$ is the combustion duration in crank angle, a and m are curve fitting constants determined as 5 and 2 respectively

[11,14–16]. The Wiebe function can be expressed in the time domain with the expression

$$x_b = \int \left[(1 - x_b) \frac{a(m+1)}{\Delta\alpha} \left(\frac{\alpha - \alpha_{spark}}{\Delta\alpha} \right)^m \omega_e \right] dt. \tag{3.10}$$

The expression for (3.10) is crucial for model implementation. The crank angle domain ($d\alpha$) is converted to time domain (dt) with the engine speed. The following expression can be derived from the ideal gas equation:

$$\ln(p(\alpha)V(\alpha)) = \ln(mRT(\alpha)) \tag{3.11}$$

where m is the mass of the gas and R is the gas constant. Equation 3.11 can be differentiated with respect to crank angle position to get

$$\frac{1}{p(\alpha)} \frac{dp(\alpha)}{d\alpha} + \frac{1}{V(\alpha)} \frac{dV(\alpha)}{d\alpha} = \frac{1}{T(\alpha)} \frac{dT(\alpha)}{d\alpha}. \tag{3.12}$$

The relation between the constants γ (the ratio between specific heat for constant pressure C_p and specific heat for constant volume C_v) and R can be expressed as

$$\gamma = 1 + \frac{R}{C_v}. \tag{3.13}$$

The following equation can be derived using 1^{st} law of thermodynamics and the above expression for γ:

$$mC_v \frac{dT(\alpha)}{d\alpha} = \frac{dQ_{in}(\alpha)}{d\alpha} - \frac{dQ_w}{d\alpha} - p(\alpha) \frac{dV(\alpha)}{d\alpha} \tag{3.14}$$

where Q_{in} is the heat added from the fuel combustion and Q_w is the heat loss through the cylinder wall due to convection. The final expression for $\frac{dp(\alpha)}{d\alpha}$ can be derived using (3.12) and

(3.14):

$$\frac{dp(\alpha)}{d\alpha} = \frac{\gamma - 1}{V(\alpha)} \left(\frac{dQ_{in}(\alpha)}{d\alpha} - \frac{dQ_w}{d\alpha} \right) - p(\alpha) \frac{\gamma}{V(\alpha)} \frac{dV(\alpha)}{d\alpha}. \tag{3.15}$$

Similarly the expression for $\frac{dT(\alpha)}{d\alpha}$ can be derived as

$$\frac{dT(\alpha)}{d\alpha} = T(\alpha) \frac{\gamma - 1}{V(\alpha)} \left[\frac{1}{p(\alpha)} \left(\frac{dQ_{in}(\alpha)}{d\alpha} - \frac{dQ_w}{d\alpha} \right) - \frac{1}{V(\alpha)} \frac{dV(\alpha)}{d\alpha} \right]. \tag{3.16}$$

The expression for $\frac{dQ_{in}(\alpha)}{d\alpha}$ depends on the fuel mass fraction burned as in (3.10), i.e.

$$\frac{dQ_{in}(\alpha)}{d\alpha} = \eta_{combustion} L.H.V \frac{dx_b}{d\alpha} m_f \tag{3.17}$$

where $\eta_{combustion}$ is the combustion efficiency, $L.H.V$ is Lower Heating Value of Petrol (42000 kJule/kg) and m_f is the mass of fuel per engine cycle. The convection heat loss term $\frac{dQ_w(\alpha)}{dt}$ can be expressed using Newton's law of cooling

$$\frac{dQ_w(\alpha)}{d\alpha} = h_w A_w (T(\alpha) - T_{wall}) \tag{3.18}$$

where h_w is the heat transfer coefficient, A_w is the heat transfer wall area and T_{wall} is the cylinder wall temperature. The instantaneous cylinder volume $V(\alpha)$ can be expressed using (3.21), which is introduced in the next section as

$$V(\alpha) = V_c + \frac{\pi B^2}{4} s(\alpha) \tag{3.19}$$

where V_c is the clearance volume of the cylinder and B is the bore of the piston.

Figure 3.3 shows two important outputs of the above model, the mass fraction burnt and the in-cylinder pressure with respect to the crank angle for a particular operating point of the engine. The 360^0 crank angle position is the top dead center (TDC) point. Figure 3.3 shows that the combustion phase terminates at 25^0 after TDC and peak in-cylinder pressure

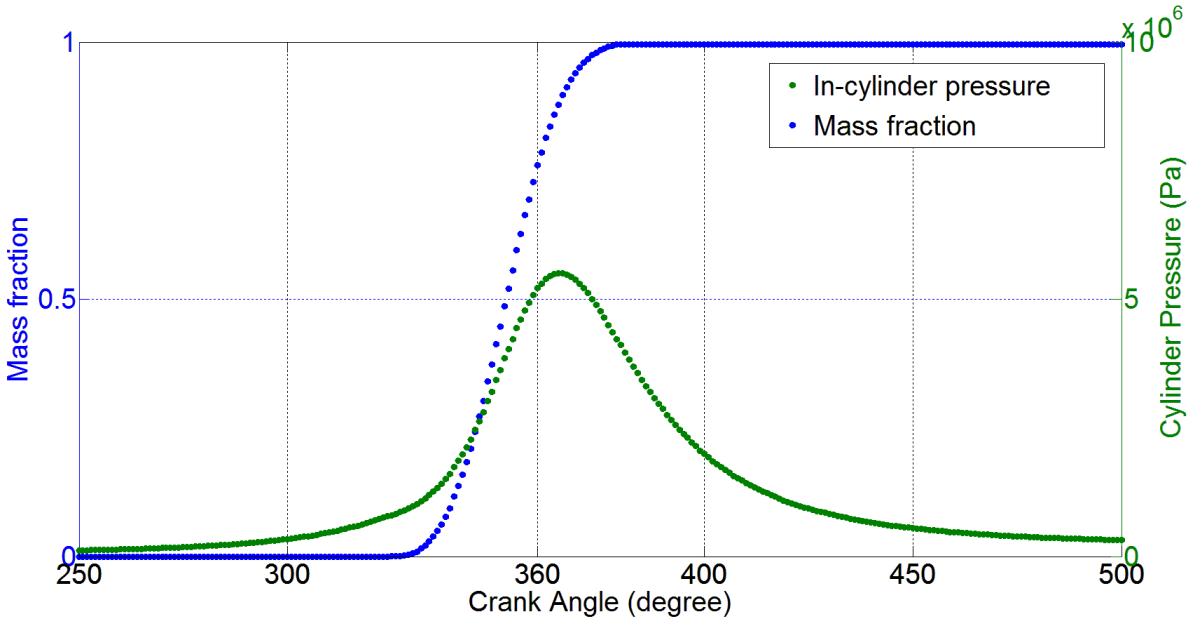


Figure 3.3: Plot for mass fraction burned and in-cylinder pressure

occurs after the TDC point. The starting of the combustion phase is controlled by the ignition timing. The slope of the mass fraction curve in Figure 3.3 depends on the ignition timing. This parameter affects in-cylinder combustion dynamics and which in turn affects the torque and emission output of the engine.

Figure 3.4 shows the effect of ignition timing on in-cylinder pressure and in-cylinder temperature. The peak pressure and temperature decrease with the retardation (i.e. shifting ignition timing towards TDC). The variation of peak pressure affects crankshaft torque output and the variation of peak temperature affects NOx emission. The respective mathematical relations between in-cylinder pressure and in-cylinder temperature with crankshaft torque and NOx emission are discussed in subsequent sections.

3.2.3 Crankshaft dynamics

The crankshaft, piston and connecting rod assembly together convert the force generated by the in-cylinder pressure to output torque. This section discusses the functional relationship between the in-cylinder pressure and the crankshaft torque. The relationship is derived in detail in different references [11, 12]. The piston stroke s (shown in Figure 3.5) is a function of

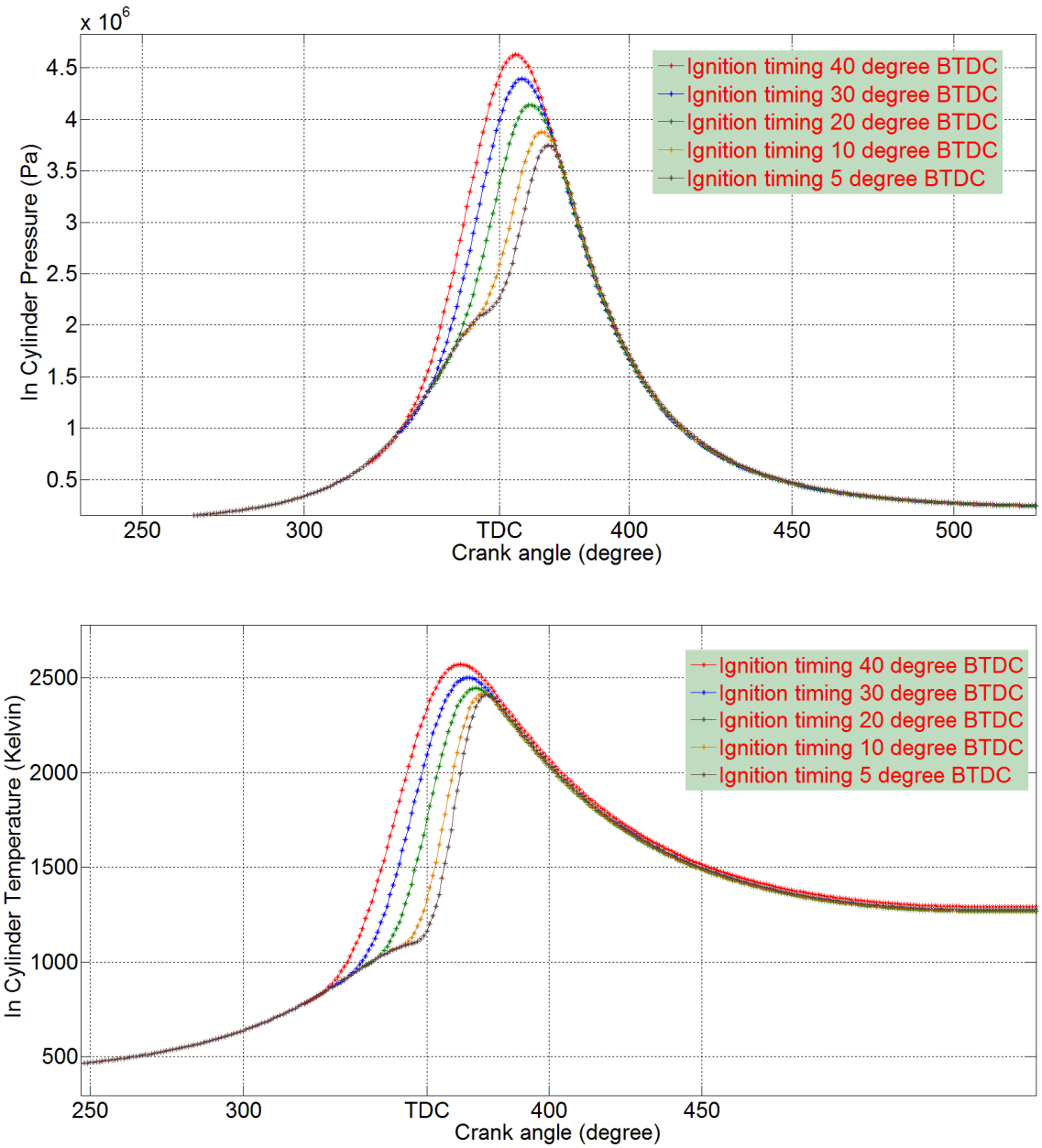


Figure 3.4: (a) Variation of In Cylinder Pressure with Ignition timing (b) Variation of In Cylinder Temperature with Ignition timing

the crank angle α. It can be expressed as

$$s(\alpha) = l(1 - \cos\beta) + r(1 - \cos\alpha) \tag{3.20}$$

where l is the length of the connecting rod, r is the radius of the crankshaft and β is the angle between the center axis and connecting rod. It is assumed that there is no offset between the center of the crankshaft and piston center. Equation 3.20 can be expressed as

$$s(\alpha) = r\left(1 - \cos\alpha + \frac{l}{r}\left(1 - \sqrt{1 - \frac{r^2}{l^2}\sin^2\alpha}\right)\right). \tag{3.21}$$

The mechanical work generated by combustion can be calculated by integrating the pressure-volume (pV) diagram

$$w_i = \oint (p(V) - p_{atm})dV. \tag{3.22}$$

Here p is expressed as a function of V. The in-cylinder pressure and instantaneous cylinder volume are functions of crank angle α (as discussed in the previous section). Therefore (3.22) can be expressed as

$$w_i = \oint ((p(\alpha) - p_{atm})A_p ds) = \oint \left((p(\alpha) - p_{atm})A_p \frac{ds}{d\alpha} d\alpha\right) = \oint (\mathbf{T}_{cylinder} d\alpha) \tag{3.23}$$

where A_p is the surface area of the piston and $\mathbf{T}_{cylinder}$ is the torque generated by the in-cylinder gas pressure. The $\mathbf{T}_{cylinder}$ term can be expressed as a function of $p(\alpha)$ as

$$\mathbf{T}_{cylinder} = (p(\alpha) - p_{atm})A_p \frac{ds}{d\alpha}. \tag{3.24}$$

The expressions for the derivatives of s can be derived from (3.21)

$$\frac{ds(\alpha)}{d\alpha} = r\left(sin\alpha + \frac{r}{l}\frac{sin\alpha cos\alpha}{\sqrt{1 - \frac{r^2}{l^2}sin^2\alpha}}\right) \tag{3.25}$$

and

$$\frac{d^2s(\alpha)}{d\alpha^2} = r\left(cos\alpha + \frac{\frac{r}{l}(cos^2\alpha - sin^2\alpha) + \frac{r^2}{l^2}sin^4\alpha}{\left(\sqrt{1-\frac{r^2}{l^2}sin^2\alpha}\right)^3}\right). \tag{3.26}$$

The derivatives of s are functions of α and both of them are stationary with respect to α. The

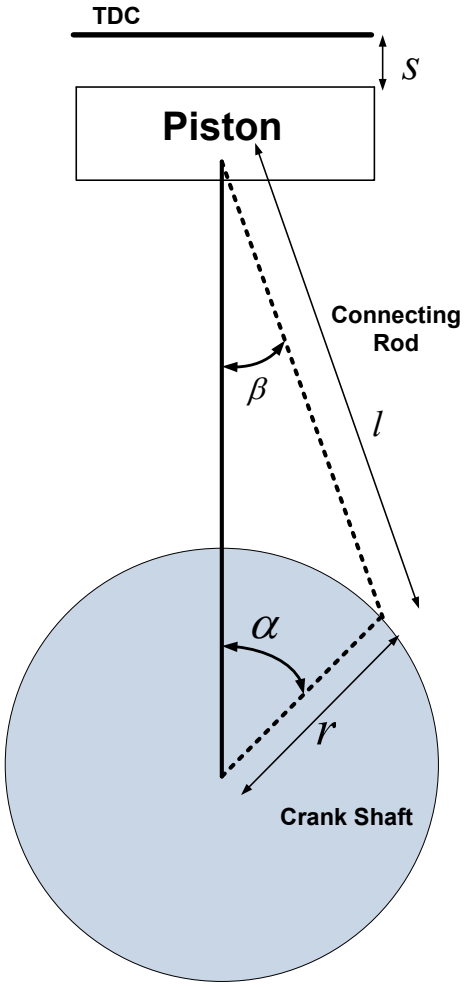


Figure 3.5: Piston and Crankshaft motion

torque balance at the crankshaft is given by

$$\mathbf{T}_{cylinder} - \mathbf{T}_{mass} - \mathbf{T}_{load} - \mathbf{T}_{frictional} = 0 \tag{3.27}$$

where $\mathbf{T}_{mass}$ is the torque generated by the rotating and oscillating masses of the crankshaft, piston and connecting rod assembly. Using the two-mass approach explained in [12], the fol-

lowing expression for (3.27) can be made:

$$(p(\alpha) - p_{atm})A_p\frac{ds(\alpha)}{d\alpha} - \left(m_{rotational}r^2 + m_{oscillating}\left(\frac{ds(\alpha)}{d\alpha}\right)^2\dot{\omega}_e - m_{oscillating}\frac{ds(\alpha)}{d\alpha}\frac{d^2s(\alpha)}{d\alpha^2}\omega_e^2 - \mathbf{T}_{load} - \mathbf{T}_{frictional} = 0 \quad (3.28)$$

where $m_{rotational}$ is the total of rotational mass of the crankshaft with the rotational portion of the connecting rod and $m_{oscillating}$ is the total mass of the piston and oscillating portion of the connecting rod. Equation 3.28 can be rearranged as

$$J(\alpha)\dot{\omega}_e = (p(\alpha) - p_{atm})A_p\frac{ds(\alpha)}{d\alpha} - m_{oscillating}\frac{ds(\alpha)}{d\alpha}\frac{d^2s(\alpha)}{d\alpha^2}\omega_e^2 - \mathbf{T}_{load} - \mathbf{T}_{frictional} \quad (3.29)$$

where $J(\alpha)$ is the moment of the inertia of the crankshaft, piston and connecting rod assembly and is given by

$$J(\alpha) = \left(m_{rotational}r^2 + m_{oscillating}\left(\frac{ds(\alpha)}{d\alpha}\right)^2\right). \quad (3.30)$$

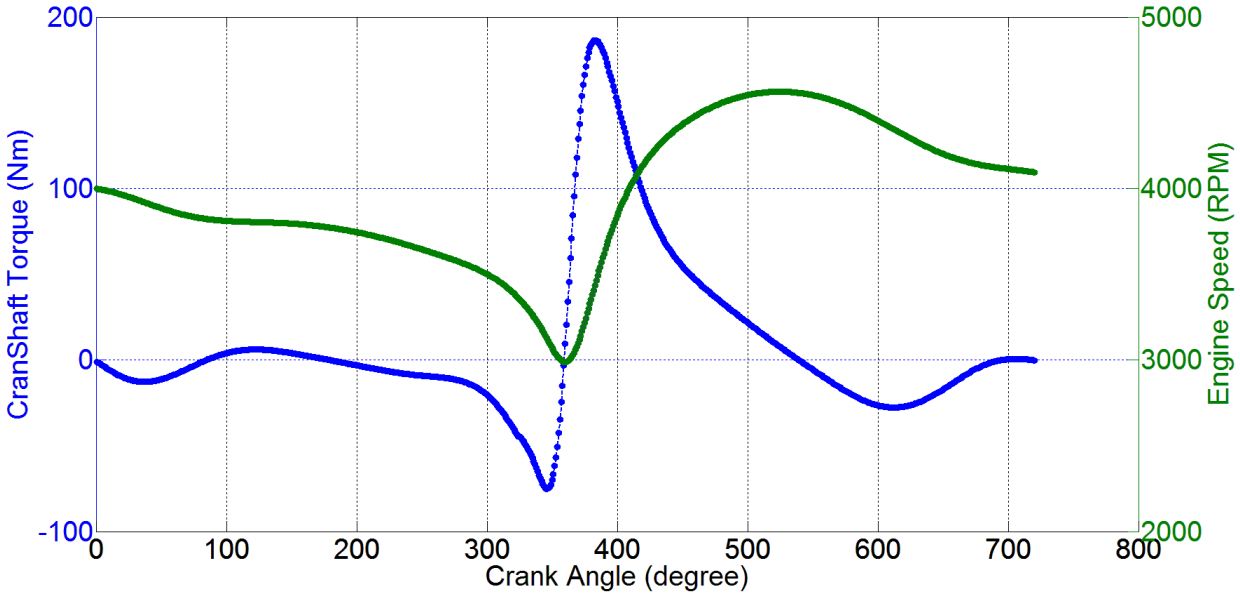


Figure 3.6: Plot for instantaneous Crankshaft torque and speed

Figure 3.6 shows the combined outputs of combustion and crankshaft dynamic models. It

shows the variation of instantaneous speed and torque outputs of the crankshaft as a function of crank angle. The instantaneous speed and torque outputs are marked as engine speed and crankshaft torque in the figure. The dip in both the outputs near 360^0 crank angle is generated by the isentropic compression phase. The crankshaft accelerates during the combustion and power phase of the engine. The crankshaft speed is a 1^{st} order filtered output of the crankshaft torque (as the the contribution of the term with ω_e^2 is negligible). The mean engine speed and mean crankshaft torque are calculated by using a moving average filter with a window of 720^0 crank angle.

3.2.4 Verification Results

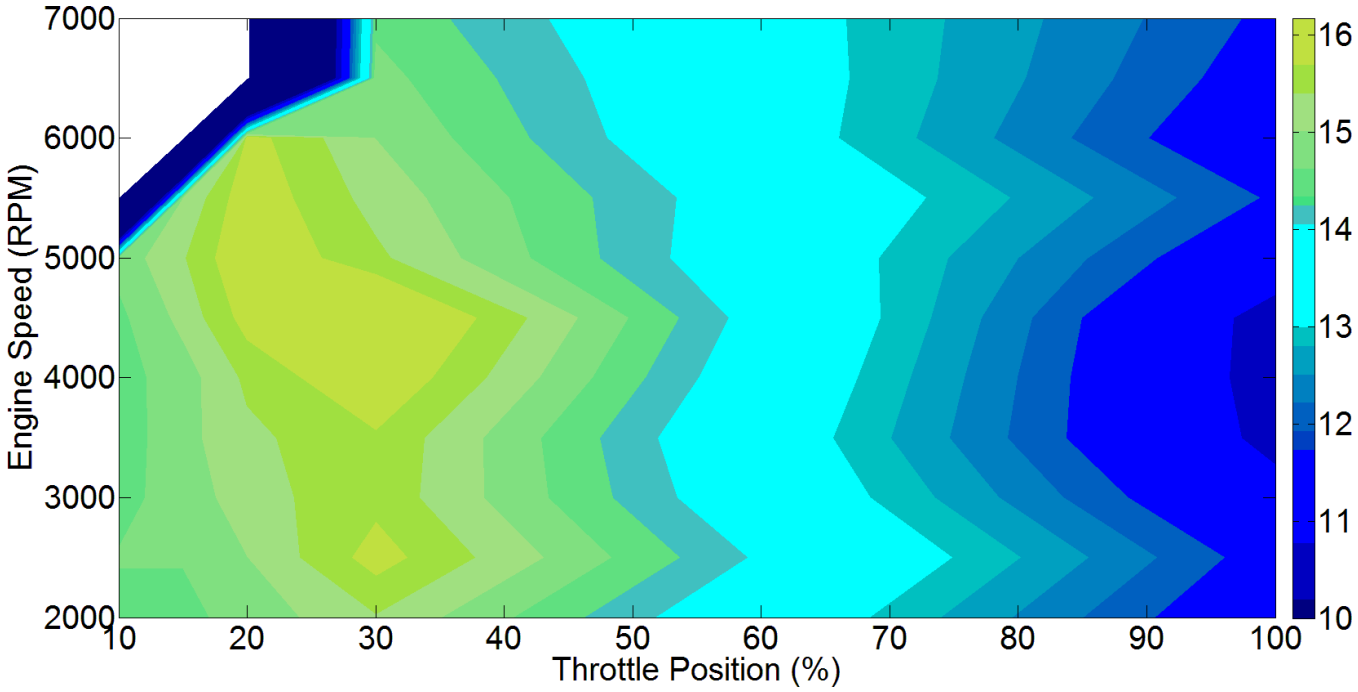


Figure 3.7: Target AFR for full operating zone of the SI engine (derived and proposed by TVS Motor Company)

The combined model of the SI engine is verified with experimental results for the full operating zone of the engine. The model is calibrated with C_0 and C_d for the target air fuel ratio. The target air fuel ratio for the full engine operating zone is shown in Figure 3.7, which was experimentally derived and utilized by TVS Motor Company for a 110 cc SI engine. The values of AFR are influenced by the target vehicle driving characteristics, target fuel consumption and prevention from over heating of engine. The AFR is maintained richer (AFR

< 14.6) with higher throttle value to reduce the cylinder head temperature by the cooling effect of fuel. Figure 3.8 shows the comparison of the simulation result and actual values of mean

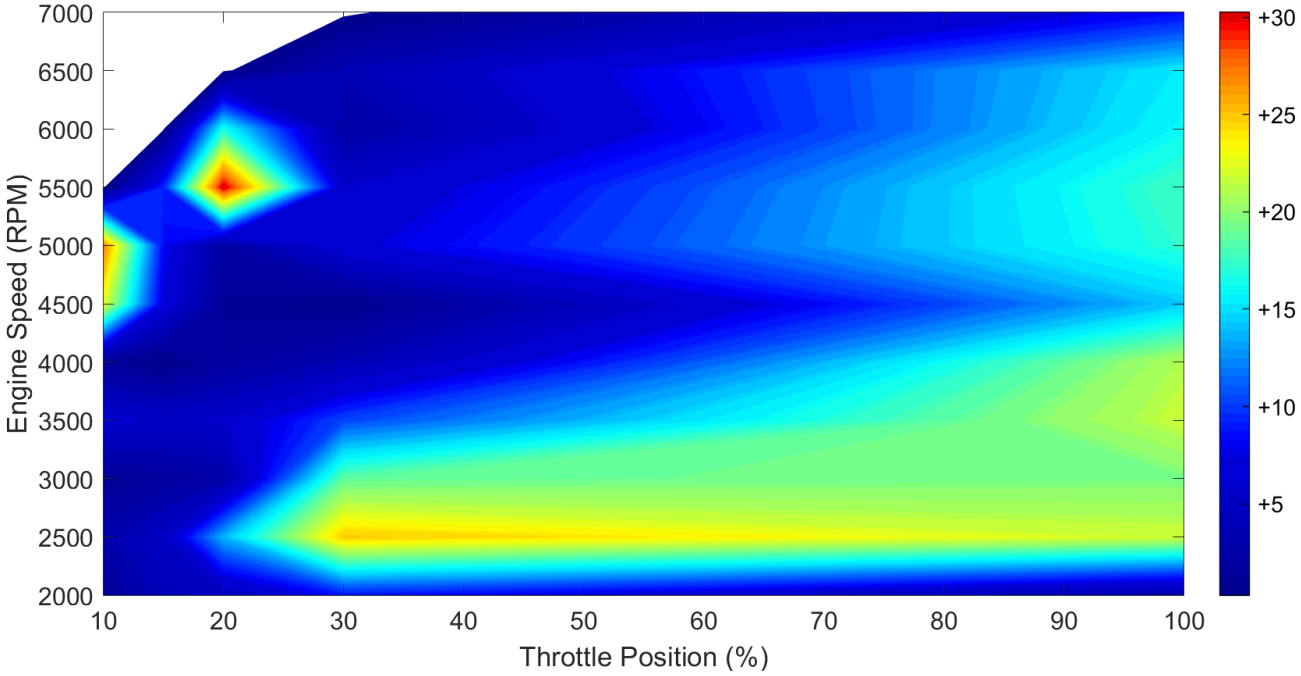


Figure 3.8: Torque output percentage error for full operating zone of the SI engine

crankshaft torque for the full operating zone of the SI engine. The model shows significant errors in two zones.

- Low throttle and high speed operating region.
- Low speed and high throttle operating region.

Both of these two zones are not stable zones for operation and the experimental results are prone to error due to the same reason. The engine does not operate in either of these zones significantly. The rest of the operating zone shows acceptable error result between simulation and experimental data.

3.3 NOx emission model for SI engine

In this work, the effort is put to derive a dynamic model for calculating NOx emissions of SI engine. The exhaust gas of SI engine mainly consists of 3 different components viz NOx

(different oxides of nitrogen), HC and CO. The NOx term includes all the oxides formed during combustion. The percentages of other oxides of nitrogen are significantly lower than NO for an SI engine [11, 17, 19]. In this work, the kinetics of NO formation is captured using the EZM approach with a single zone heat release model.

3.3.1 NO kinetic model

In general, the concentrations of various pollutant species in the exhaust differ from calculated equilibrium values, indicating the importance of chemical kinetics in the pollutant formation process [19]. The NO emission model is a kinetic model based on EZM (Extended Zeldovich Mechanism). In case of lean and near stoichiometric fuel-air mixture, the principle chemical reactions for formation of NO are expressed as

$$O + N_2 \Leftrightarrow NO + N$$

$$N + O_2 \Leftrightarrow NO + O$$

$$N + OH \Leftrightarrow NO + H$$

The experimental observation shows that the kinetic of NO formation is much slower than the combustion process and most of NO is formed after completion of the combustion phase [11,17,19–21,92]. The dynamic rate of formation of NO can be expressed as [11,17,19–21]:

$$\frac{d[NO]}{dt} = k_1^+[O][N_2] + k_2^+[N][O_2] + k_3^+[N][OH] - k_1^-[NO][N] - k_2^-[NO][O] - k_3^-[NO][H].$$

The $[O]$, $[N_2]$ etc., denote species concentration in moles/cm^3 and the values of k_i denote the kinetic rate constants. Two assumptions can be considered due to the slow reaction based on EZM [11, 17]:

- The combustion and NO formation process are decoupled. The C-O-H system is in equilibrium.
- The N atom concentration is much less than the other species concentration.

The second assumption implies that the rate of change of [N] is equal to zero which

means [11, 17, 19–21]

$$\frac{d[N]}{dt} = k_1^+[O][N_2] - k_2^+[N][O_2] - k_3^+[N][OH] - k_1^-[NO][N] + k_2^-[NO][O] + k_3^-[NO][H] = 0.$$

The values of the rate constants are mentioned below. The unit of the rate constants is $cm^3/(mole.sec)$ [11, 17]

$$k_1^+ = 7.6 \times 10^{13} \times e^{(-38000/T)}, k_1^- = 1.6 \times 10^{13}, k_2^+ = 6.4 \times 10^9 \times e^{(-3150/T)},$$

$$k_2^- = 1.5 \times 10^9 \times e^{(-19500/T)}, k_3^+ = 4.1 \times 10^{13}, k_3^- = 2.0 \times 10^{14} \times e^{(-23650/T)}$$

where T is the in-cylinder temperature in Kelvin.

The rate equation for $[NO]$ can be simplified using the above two assumptions. The final expression for $\frac{d[NO]}{dt}$ can be expressed as

$$\frac{d[NO]}{dt} = \frac{2R_1\{1 - ([NO]/[NO]_e)^2\}}{1 + ([NO]/[NO]_e)R_1/(R_2 + R_3)} \tag{3.31}$$

where R_1, R_2 and R_3 are equilibrium products formed by the three principle chemical reactions (for formation of NO) expressed previously. The typical values of $R_1, R_1/(R_2 + R_3)$ are mentioned in Table 3.1 for 10 atm in-cylinder pressure and 2600 Kelvin in-cylinder temperature. The equilibrium concentration of NO is expressed as

$$[NO]_e = (K_{NO}[O_2]_e[N_2]_e)^{\frac{1}{2}} \tag{3.32}$$

where $K_{NO} = 20.3 \times e^{(-21650/T)}$. The expression $\frac{d[NO]}{dt}$ can be analyzed during the start of the reaction when $[NO] << [NO_e]$. In this case, the above-mentioned expression for $\frac{d[NO]}{dt}$ can be expressed as

$$\frac{d[NO]}{dt} = 2R_1 = 2k_1^+[O]_e[N_2]_e.$$

The $[O]_e$ can be expressed as

$$[O]_e = \frac{K_p[O_2]_e^{\frac{1}{2}}}{(RT)^{\frac{1}{2}}}$$

where K_p is the equilibrium constant expressed as

$$K_p = 3.6 \times 10^3 \times e^{\left(\frac{-31090}{T}\right)} \text{ atm}^{\frac{1}{2}}.$$

The final expression of $2R_1$ is

$$2R_1 = \frac{27.36 \times 10^{16}}{T^{\frac{1}{2}}} e^{\left(\frac{-69090}{T}\right)} \text{ atm}^{\frac{1}{2}} [O_2]_e^{\frac{1}{2}} [N_2]_e.$$

The above expression of R_1, which is a function of in-cylinder temperature and in-cylinder pressure, is substituted in the kinetic equation (3.31).

Table 3.1: Typical values of R_1 and $R_1/(R_2 + R_3)$ [11]

AFR	R_1	$R_1/(R_2 + R_3)$
18.25	5.8×10^{-5}	0.33
14.6	2.8×10^{-5}	0.26
12.17	7.6×10^{-6}	0.14

3.3.2 Molar fraction calculation for combustion products

As mentioned above, other combustion products reach equilibrium during the combustion phase and the process is governed by the following chemical equation [11]. The combustion equation for a hydrocarbon fuel of average molar H/C ratio y can be written as

$$\epsilon\phi C + 2(1-\epsilon)\phi H_2 + O_2 + \psi N_2 \rightarrow n_{CO_2} CO_2 + n_{H_2O} H_2O + n_{CO} CO + n_{H_2} H_2 + n_{O_2} O_2 + n_{N_2} N_2$$

where

ψ= the molar N/O ratio (3.773 for air)

$\epsilon = \frac{4}{4+y}$

ϕ = fuel to air equivalence ratio

n_i= molar of species i per mole O_2 reactant

The n_i are determined by the following three assumptions :

- CO and H_2 can be neglected for ($\phi \leq 1$)
- O_2 can be neglected for ($\phi > 1$)
- The water gas reaction $CO_2 + H_2 \rightarrow CO + H_2O$ can be assumed to be in equilibrium with the equilibrium constant being $K(T)$. $K(T)$ can be determined from a curve fit to

JANAF Table data [11]

$$lnK(T) = 2.743 - \frac{1.761\times10^3}{T} - \frac{1.661\times10^6}{T^2} + \frac{0.2803\times10^9}{T^3}$$

where T is the in-cylinder temperature mentioned in the previous section.

The n_i which can be calculated by element balance and the above assumptions is summarized in Table 3.2. The value of c in Table 3.2 can be calculated by solving the following quadratic equation [11]

$$(K-1)c^2 - c\{K[2(\phi-1)+\epsilon\phi] + 2(1-\epsilon\phi)\} + 2K\epsilon\phi(\phi-1) = 0.$$

Table 3.2: Burned gas composition n_i, moles/mole of O_2

Species	$\phi \leq 1$	$\phi > 1$
CO_2	$\epsilon\phi$	$\epsilon\phi - c$
H_2O	$2(1-\epsilon)\phi$	$2(1-\epsilon)\phi + c$
CO	0	c
H_2	0	$2(1-\epsilon)\phi - c$
O_2	$1-\phi$	0
N_2	ψ	ψ

3.3.3 Dynamic simulation of kinetic NO model

The block diagram of the NOx dynamic model is shown in Figure 3.9. The model is implemented in conjunction with the torque generation model of the SI engine. The torque generation model generates the values of air to fuel ratio (AFR), mass of air, in-cylinder temperature, in-cylinder pressure and in-cylinder volume per engine cycle for the NOx generation model. Equation 3.32 explains that, the value of $[NO]_e$ is a function of crank angle (as K_{NO} is a function of in-cylinder temperature). Therefore it is very much essential to convert (3.31) to the crank angle domain. Equation 3.31 needs to be solved numerically for each crank angle to calculate the values of $[NO]$. As the time duration for each crank angle is a function of the rotational speed of the engine, the time duration for the integration dt is calculated based on

$$dt = \frac{\pi}{180} \cdot \frac{1}{\omega_e} \tag{3.33}$$

where ω_e is the engine speed. In the initial stage shown in Figure 3.9, the molar concentrations

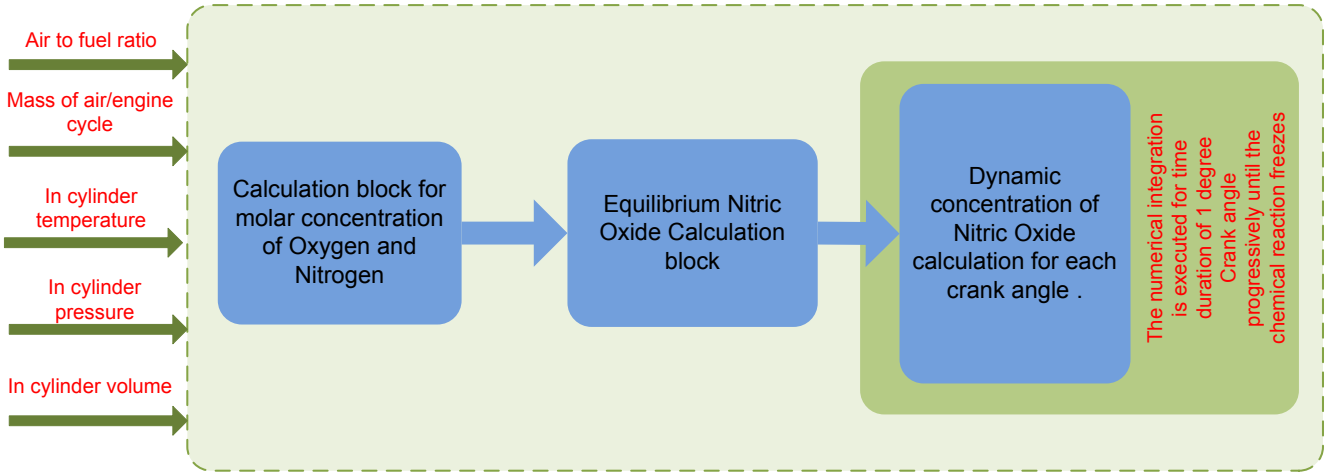


Figure 3.9: Block diagram for NOx model implementation

of $[O_2]$ and $[N_2]$ are calculated based on the Table 3.2. The values of molar concentrations are used for the calculation of the equilibrium concentration $[NO]_e$. In the final stage, $[NO]$ is calculated for each crank angle based on the above discussion.

3.3.4 Simulation results of kinetic NO model

The simulation results of the kinetic model are shown in Figure 3.10. The first plot of Figure 3.10 shows the variation of $[NO]_e$ and $[NO]$ in the crank angle domain with 360^0 as TDC of the engine. The second plot shows the variation of $[NO]$ with in-cylinder temperature. The simulation results are identical to the results discussed in [17] and [11]. The simulation assumes that the burned gases mix rapidly and thus uniformly. This assumption allows to consider the in-cylinder temperature to be uniform. This assumption may not be valid for a high cubic capacity engine. A second assumption is that there is no exhaust gas mixing during the valve overlap of exhaust and intake stroke. Figure 3.10 shows that initial concentration of produced NO is less, since it is assumed that there is no residual gas due to valve overlap. The rate controlled concentration rise lags behind the equilibrium levels, then crosses the equilibrium level and freezes the reaction at around an in-cylinder temperature of 2000 Kelvin. The value of $[NO]$ is much higher than $[NO]_e$ as the kinetic constants of the chemical reactions involved

are faster than the kinetic constant of the equilibrium equation. The reaction freezing is shown in the second plot. The concentration of NO during this point corresponds to the exhaust emission concentration of NO.

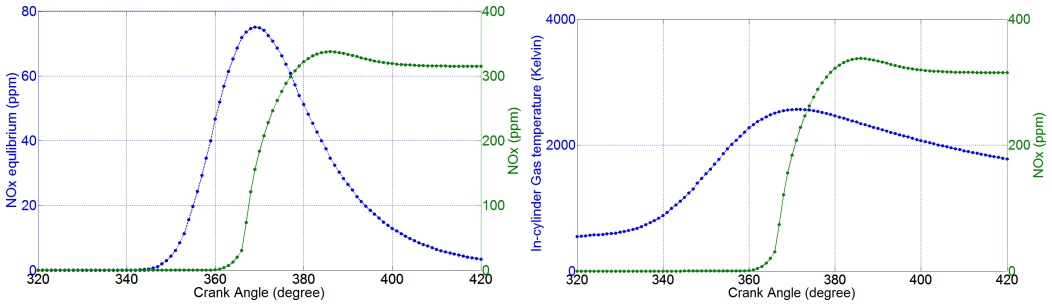


Figure 3.10: (a) NOx equilibrium vs actual produced NOx (b) NOx production with in-cylinder temperature

The first plot of Figure 3.11 shows the comparison of the simulation results with engine dynamometer test for WOT condition. This error can be caused by the above-mentioned two assumptions and inherent limitations of the EZM approach. The result shows that the error is very high at 2000 rpm. The engine dynamometer experimental result shows that the actual $[NO]$ at 2000 rpm is 4 times higher than the $[NO]$ at 2500 rpm. The explanation of kinetic NO formation shows that $[NO]$ depends on the mass of air, in-cylinder temperature and time available for each crank angle duration. The mass of air and time available for each crank angle duration for both the operating points (WOT and 2000 rpm and 2500 rpm) do not change significantly. Therefore the formation of high $[NO]$ at 2000 rpm, WOT operating point can be attributed to the very high in-cylinder temperature (approximately around 2750 Kelvin). In the next section, it is shown that the operating engine speed range lies in between 3000 rpm and 6000 rpm. The $[NO]$ model error is acceptable in this operating region. The model is further tested for variation of AFR and spark timing for a particular engine operating point. The results are shown in the second and the third plots of Figure 3.11. The $[NO]$ is maximum for the AFR of 15 which is in concurrence with [11] and [17]. The reason for the particular shape is explained in above-mentioned reference. The gas mixture reaches maximum temperature for richer mixture, but the $[O_2]$ is less. The gas temperature reduces as the mixture is leaned out. As the mixture is leaned, increasing of $[O_2]$ initially offsets the falling gas temperature and $[NO]$ peaks at around AFR=15. The third plot shows that $[NO]$ decreases with the retardation

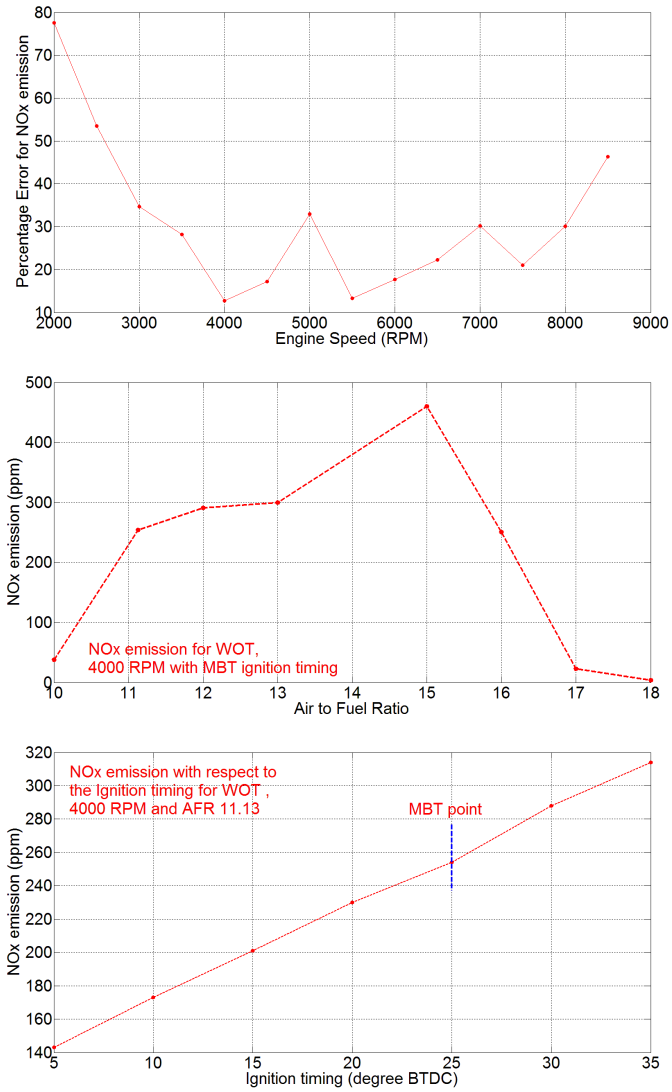


Figure 3.11: (a) Error for NOx at WOT condition (b) NOx variation w.r.t AFR (c) NOx variation w.r.t Ignition timing

of spark timing assuming stability of the combustion is not effected by the retardation. The simulation results agree with the findings of [11] and [17]. The model can be accepted for the further work on control development as it behaves correctly with variation of AFR and Spark timing.

3.4 Dynamic model for the Continuous Variable Transmission

The CVT system consists of a pair of pulleys with rubber belt, pulley actuation system and a centrifugal clutch system. The radius of the drive pulley is controlled by the force balance between the rubber belt and centrifugal masses placed on the actuation system. The crank shaft is directly connected to the drive pulley without any gear reduction. The force balance equation between the axial forces is expressed in [93–97]. This system is termed as a speed sensing system. The driven pulley diameter is controlled by the spring with a mechanical cam based system [93–97] which is termed as a torque sensing system. The force balance equations are not included in the dynamic model of the CVT. The force balance equations are analytically used to generate the static relation between engine speed, road load and CVT ratio.

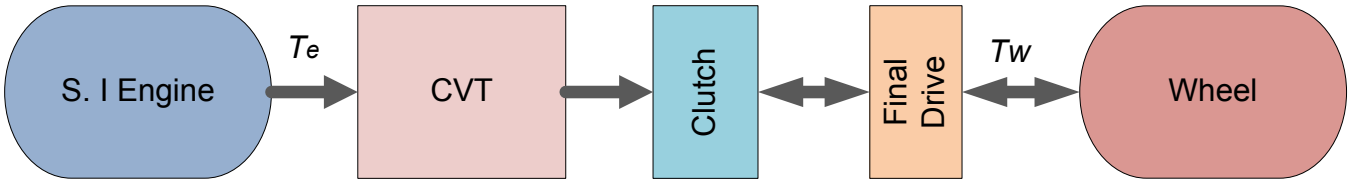


Figure 3.12: CVT system schematic

The schematic diagram of the powertrain with CVT transmission is shown in Figure 3.12. The mean torque T_e is calculated from the dynamic torque model of the SI engine mentioned in the above section. The system can be expressed by

$$J_e\dot{\omega}_e + B_e\omega_e = T_e - \frac{T_w}{(R_N R_f \eta_N \eta_f)} \tag{3.34}$$

where J_e is the engine inertia (this is same as $J(\alpha)$ as mentioned in (3.30)), ω_e is the mean speed of the engine, B_e is the damping constant, T_w is the road load and R_N is the CVT gear ratio. R_f is the final gear ratio, η_N is the efficiency of the CVT and η_f is the efficiency of the final ratio. The road load T_w (which is same as $\mathbf{T}_{wheel}$ as introduced in Chapter 5) is expressed

$$m\dot{v} = \frac{T_w}{R_w} - C_n v^2 - \mu_r mg\cos(\theta) - mg\sin(\theta) - F_b \tag{3.35}$$

where m is the mass of the vehicle, v is the linear velocity of the vehicle, R_w is the dynamic radius of the wheel, C_n is the equivalent air drag term, μ_r is the rolling friction coefficient, g is the acceleration constant, θ is the road inclination and F_b is the braking force. The gear ratio R_N of the CVT can be determined uniquely for a particular operating point of the powertrain. Since this model is a control-oriented model, it is unnecessary to derive the dynamic equation based on the force balance relation derived in [93–97]. The dynamic model for the CVT gear ratio selection can be derived by testing the vehicle on the chassis dynamometer [98]. In this work, the testing could not be carried out due to limitation of resources and it was decided to generate the steady state operating points map mentioned in [98] by using an analytical method based on the force balance relation of [93–97].

3.4.1 Driven pulley system

The driven pulley mechanism is explained in Figure 3.13. This is a movable flange which can slide axially along the driven shaft. The helical cam converts the road load to an axial force on the belt. The axial force F_{vn} on the driven pulley can be expressed as the total of force acting by the helical cam (due to road load) and the torsion compression spring :

$$F_{vn} = \frac{D_n}{D_a} \times \frac{F_1 - F_2}{2} \times \frac{\cos\beta - \mu_a \sin\beta}{\sin\beta + \mu_a \cos\beta} + F_p + K_n(D_{no} - D_n)\tan(\alpha_g/2) \tag{3.36}$$

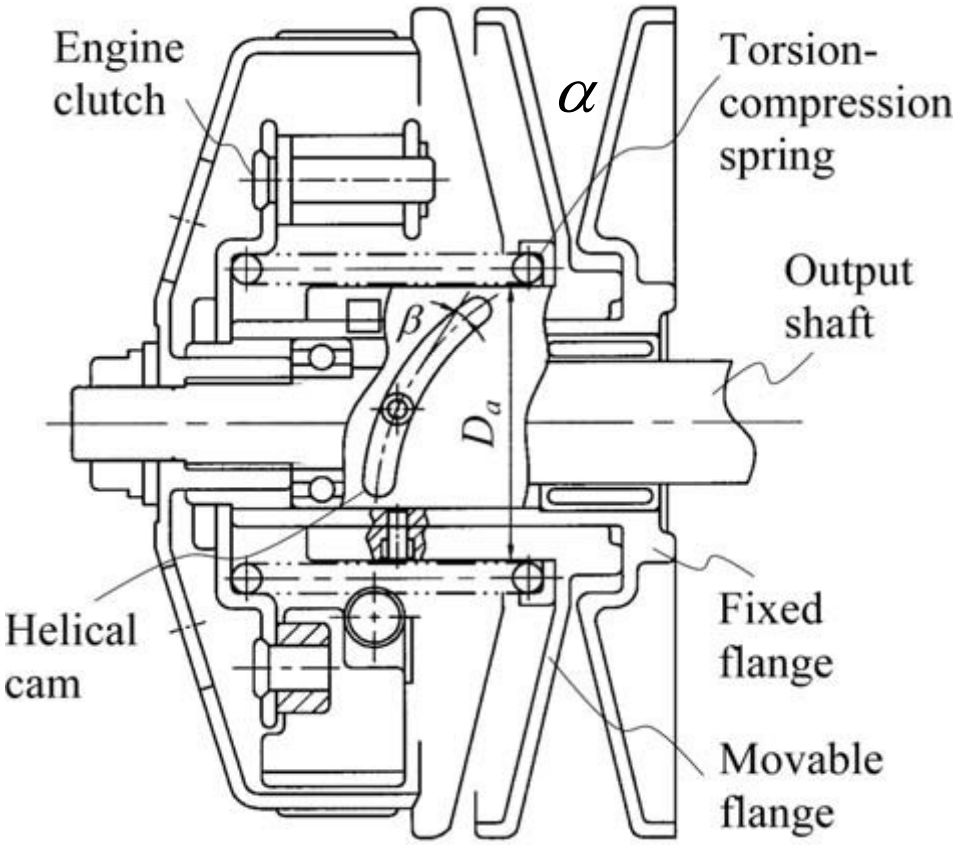


Figure 3.13: Driven pulley mechanism [99]

where β is the angle between the helical cam surface of the torque sensing mechanism and the shaft center line, D_a is the diameter of the helical cam, D_{no} is the minimum pitch diameter of the driven pulley, F_p is the compression preload of the spring, K_n is the spring constant of the torsion compression spring, α_g is the groove angle of the pulley, μ_a is the coefficient of the friction on the helical cam, D_n is the pitch diameter and $(F_1 - F_2)$ is the belt tension difference. The increase of F_{vn} results in increase of D_n for a constant drive shaft speed (i.e. constant ω_e). The road load acting on the driven pulley can be expressed as

$$T_{vn} = \frac{T_w}{R_f \eta_f}. \tag{3.37}$$

The belt tension difference can be expressed as

$$F_1 - F_2 = \frac{T_{vn}}{\frac{D_n}{2}}. \tag{3.38}$$

The belt applies an axial force on the pulley and it is derived as below [93–97]

$$F_{vn} = (F_1 - F_2)\left[\frac{\cos(\alpha_g/2) - \mu \sin\phi \sin(\alpha_g/2)}{2\mu \cos\phi}\right] \tag{3.39}$$

where μ is the coefficient of friction between belt and pulley, ϕ is the friction angle. The expression of D_n can be derived using (3.36), (3.37), (3.38) and (3.39):

$$D_n = \frac{C_1 - \sqrt{{C_1}^2 - 4T_w K_n \tan(\alpha_g/2) C_2}}{2K_n \tan(\alpha_g/2)} \tag{3.40}$$

where

$C_1 = \frac{T_w}{D_a}\frac{\cos\beta - \mu_a \sin\beta}{\sin\beta + \mu_a \cos\beta} + F_p + K_n D_{no} \tan(\alpha_g/2)$

$C_2 = \frac{\cos(\alpha_g/2) - \mu \sin\phi \sin(\alpha_g/2)}{2\mu \cos\phi}$

In (3.40), other than the friction angle ϕ, all the parameters can be measured from the

CVT component drawing. The D_n term can be expressed as

$$D_n = f(T_w, \phi, \mathbf{A}) \tag{3.41}$$

where $\mathbf{A}$ is the set of all measurable dimensional parameters of the CVT. The unknown parameter friction angle (ϕ) can be determined by solving (3.40) for the operating range of known road load T_w and maximum and minimum values of D_n. The maximum and minimum values of D_n together with other geometrical parameters for a CVT are provided by TVS Motor Company. The range of T_w can be found out by analyzing multiple drive cycle data. The first plot of Figure 3.14 shows the operating points of the CVT powertrain extracted from Indian Drive Cycle (IDC) and City Drive Cycle (CDC) adopted by TVS Motor Company. Certain operating points indicate negative road loads which implies braking operation by the chasis dynamometer. The operating region for friction angle is shown in the second plot of Figure 3.14. The operating area (the red box in the second plot of Figure 3.14) is selected based on the maximum and minimum values of D_n. Although the friction angle varies within a small range, it is considered to be a constant value for simplification.

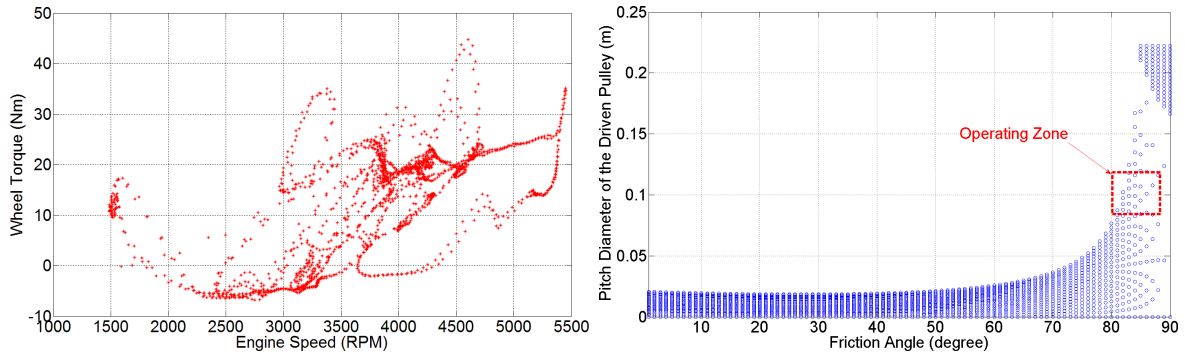


Figure 3.14: (a) Operating zone of CVT (b) Friction angle determination

3.4.2 Drive pulley system

The drive system consists of multiple centrifugal rollers which are placed inside a circular housing as shown in Figure 3.15. Once the input shaft starts rotating, the roller mass creates force on the housing which is balanced by the force exerted by the rubber belt on the pulley.

The axial force F_{cl} generated by the movement of the centrifugal masses can be expressed as [93, 99]

$$F_{cl} = \frac{m_{roller} y_m {\omega_e}^2}{\left(\frac{\cos\gamma + \mu_h \sin\gamma}{\sin\gamma - \mu_h \cos\gamma}\right) + \left(\frac{\sin\delta + \mu_b \sin\delta}{\cos\delta - \mu_b \sin\delta}\right)} \tag{3.42}$$

where μ_h and μ_b denotes the coefficient of friction between the roller and roller back plate and the roller housing respectively, m_{roller} is the mass of the roller, δ is the angle between the roller back contact plate and the perpendicular line on the shaft center line, γ is the contact angle of the housing and the centrifugal roller and ω_e is the input shaft speed i.e engine speed. The force F_{cl} is balanced by the force F_{vr}, which is exerted by the belt tension [93–97]:

$$F_{vr} = \frac{F_1 \theta_r}{2} \left[\frac{1 - \mu \tan(\alpha_g/2)}{\mu + \tan(\alpha_g/2)}\right] \tag{3.43}$$

where θ_r is the wrap angle of the driver pulley. The above equation shows that F_{vr} is a function of tension for F_1 (not on F_2). This is due to the fact that both the forces F_1 and F_2 are related to each other by the geometrical dimensions of CVT components. The relation can be expressed as

$$\frac{F_1}{F_2} = exp\left[\frac{\mu\theta_r \cos\phi}{\mu \sin\phi \cos(\frac{\alpha_g}{2}) + \sin(\frac{\alpha_g}{2})}\right]. \tag{3.44}$$

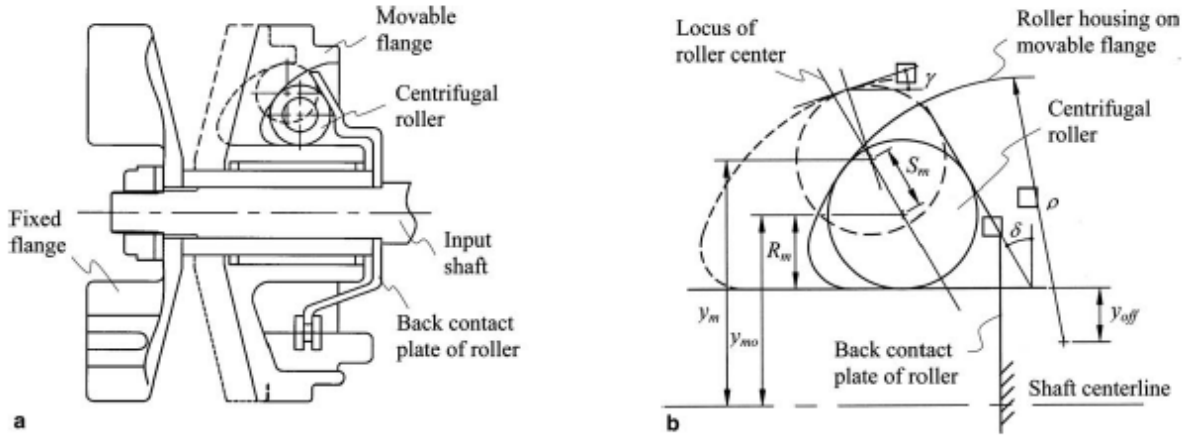


Figure 3.15: Drive pulley system [99]

The distance between the center of the roller and center-line of the shaft (which is given

as y_m in (3.42)) can be expressed as

$$y_m = y_{mo} - S_m \cos\delta \tag{3.45}$$

where y_{mo} is the distance between the roller center and the center-line of the shaft when the shaft is stationary and S_m is the travel along the roller center loci. The housing angle γ can be expressed as

$$\cos\gamma = \frac{R_m - y_{off} - S_m \cos\delta}{\rho - R_m} \tag{3.46}$$

where ρ is the radius of the curvature of the roller housing, R_m is the radius of the centrifugal roller, and y_{off} is the distance between the center point of the roller housing and shaft surface. The parameters γ and S_m vary with the operating points of the drive pulley. Both the parameters are related with a non linear function (3.47) and have dimensional limits. The axial distance traveled by the movable flange can be expressed by

$$(D_r - D_{rminimum}) \tan(\alpha_g/2) = D_1 - D_2 + S_m sin\delta \tag{3.47}$$

where

$D_1 = \sqrt{(\rho - R_m)^2 - (R_m + y_{off})^2}$

$D_2 = \sqrt{(\rho - R_m)^2 - (R_m + y_{off} + S_m cos\delta)^2}$.

D_r and $D_{rminimum}$ are the pitch and minimum pitch diameter of the drive pulley. The system

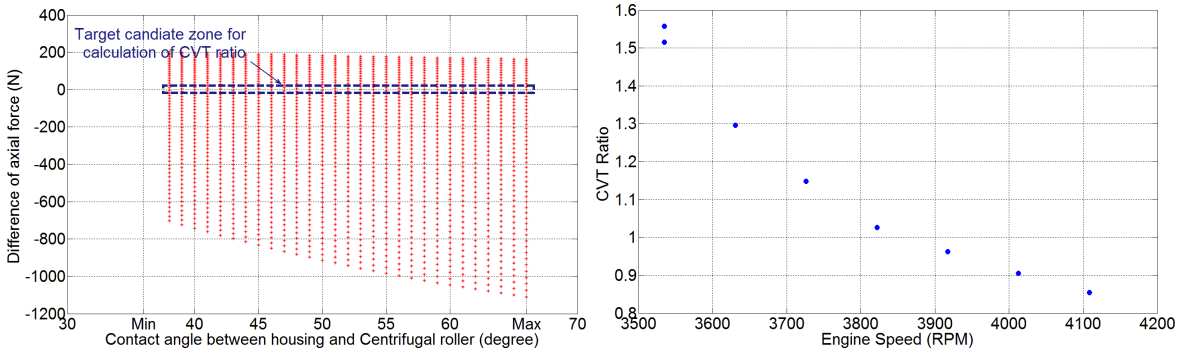


Figure 3.16: (a) Variation of Axial force w.r.t Gamma angle for a particular operating point (b) Variation of calculated CVT ratio for the Target candidate zone mentioned in figure (a)

parameters of the drive pulley systems are measured from the geometrical drawing of the CVT system. The working range of the angle γ can be determined using (3.47) and loci information of the S_m. The range of angle γ and S_m are crucial information for the calculation of CVT ratio for different operating points of the powertrain. If (3.42), (3.43), (3.45) and (3.47) are observed carefully, it can be concluded that the difference of both the axial forces (ie. F_{cl} and F_{vr}) is a function of γ, ω_e and F_1. F_1 is function of T_w and D_n as shown in (3.37) and (3.38). The force F_{vr} can be calculated based on F_1. Now, F_{cl} which is the counter balancing force of F_{vr} can be calculated based on different values of engine speed ω_e and γ. The differences of F_{cl} and F_{vr} are monitored for all the different values of γ. If the difference is less than a predefined band, respective values of S_m are accepted for the next step of calculation. The left hand side of Figure 3.16 shows the differences of F_{cl} and F_{vr} as a function of γ for a particular constant value of F_1. The target values of γ are used for calculation of CVT ratios for different values of ω_e and a particular value of F_1. The calculated values of CVT ratio are shown in the Figure 3.16. The out of range CVT ratios (for this iteration) are rejected. The same methodology is used in different operating points of the powertrain to build the CVT ratio map shown in Figure 3.17. The CVT maintains an overdrive CVT ratio at the high engine speed zone. This map can be used as a simplified CVT ratio control map in the CVT dynamic model. A first-order dynamics can be included in the derived CVT ratio control [98, 100] as

$$\frac{dR_N}{dt} + aR_N = aR_N^{Target} \tag{3.48}$$

where $\frac{1}{a}$ is the time constant of the ratio actuation system in the order of 200 msec [100] and aR_N^{Target} is the target CVT ratio based on the operating zone of the vehicle.

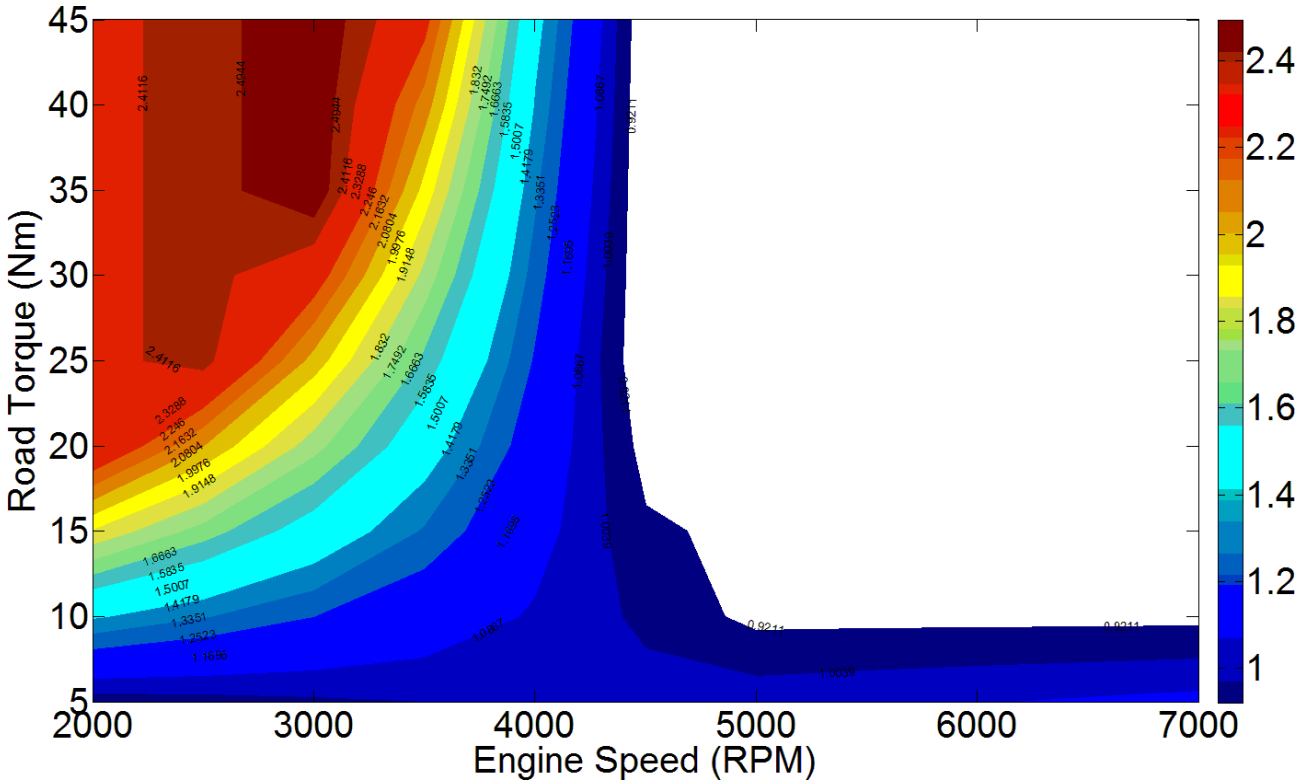


Figure 3.17: Predicted CVT Ratio

3.4.3 Dynamic model for power transfer

The dynamic model for the power transfer can be derived from (3.34) and (3.35). The equation can be expressed as

$$\left(J + \frac{mR_w^2\eta_{NS}}{R_N^2R_f^2\eta_N\eta_f}\right)\dot{\omega}_e + B_e\omega_e + \left(\frac{R_w^3\eta_{NS}^2C_n}{R_N^3R_f^3\eta_N\eta_f}\right)\omega_e^2 = T_e - \frac{R_w}{R_NR_f\eta_N\eta_f}\left(\mu_r mg\cos(\theta) + mg\sin(\theta) + F_b\right) \quad (3.49)$$

where η_{NS} is the slip loss of the centrifugal clutch. Experimental results show that the efficiencies of the centrifugal clutch, belt and complete CVT are function of the drive speed (i.e. ω_e) [101]. The engine speed and vehicle speed are related by

$$\omega_e = v\frac{R_NR_f}{R_w\eta_{NS}}. \quad (3.50)$$

The efficiency plot is shown in Figure 3.18. The centrifugal clutch can be considered as a

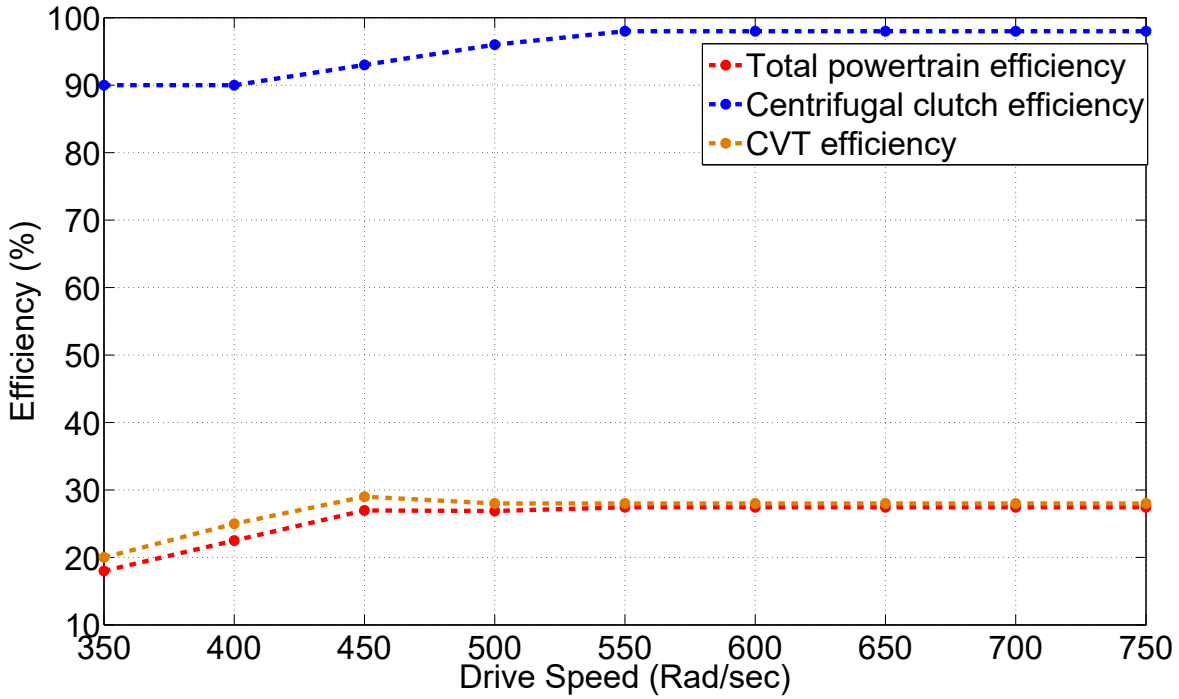


Figure 3.18: Efficiency of CVT with respect to drive speed (ω_e) [101]

speed-sensing device that consists of a inner disc driven by the driven shaft, several centrifugal shoes mounted on the inner disc and an outer wheel which is connected to the the final drive gear. The centrifugal clutch works in three modes: disengagement, slipping and engagement. Since the duration of the slipping mode is very small, compared to other modes (for drive cycle simulation), the centrifugal clutch is assumed to work in two modes i.e disengagement and engagement. The slipping mode is represented by the term η_{NS} [98]. The test results of [101] shows that once the centrifugal clutch reaches synchronization speed, the η_{NS} becomes unity.

3.4.4 Simulation results

In this section, the dynamic response of the CVT system is shown for a step change of road load and throttle. The drive cycle simulation is not covered here as it will be discussed during vehicle level simulation in a subsequent chapter. The simulation is based on the model developed using the dynamic (3.34), (3.35), (3.48) and (3.49). The plots are expressed in per unit to hide the

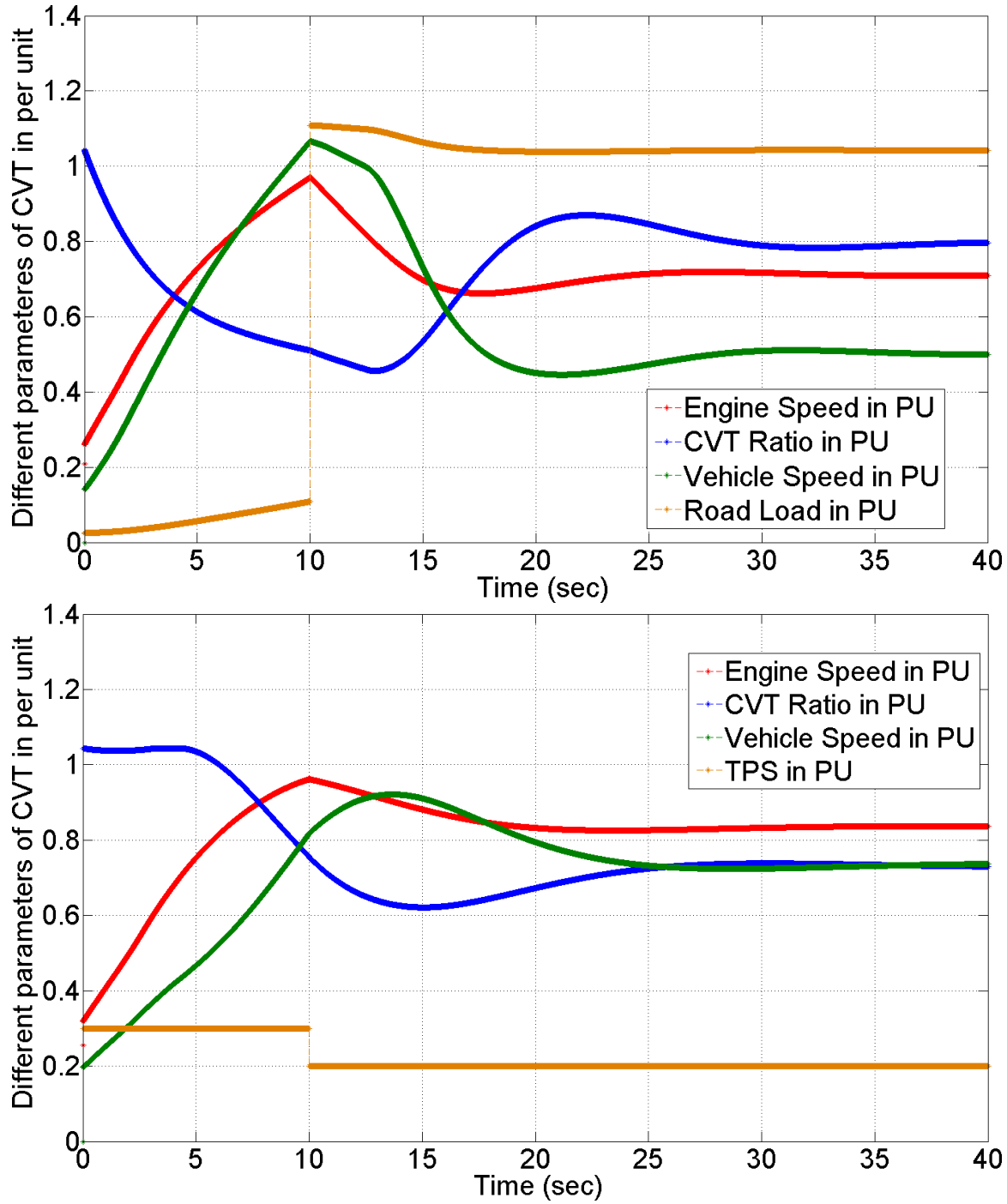


Figure 3.19: (a) Dynamic response of CVT for step Load change (b) Dynamic response of CVT for step TPS change

absolute range.

In the first plot of Figure 3.19, the CVT gear ratio starts decreasing for constant throttle request and it starts increasing once the powertrain is loaded with a step road load. The engine speed decreases due to this step load and CVT ratio moves towards the upper left segment in Figure 3.17. Therefore the powertrain operates at a larger CVT ratio to support more load torque. In the second plot of Figure 3.19, the CVT ratio moves towards the middle of the Figure 3.17.

3.5 Dynamic model for the Manual Transmission (MT)

The manual transmission consists of a clutch system with frictional plates and manual gear system as shown in Figure 3.20. The clutch system couples/decouples the engine with the road load during vehicle launch and gear shift operation. The clutch system consists of a frictional

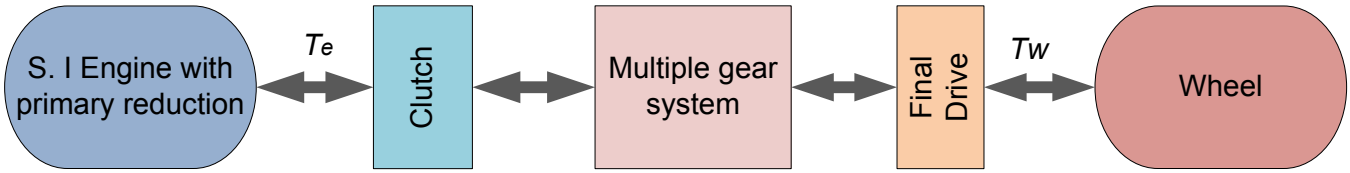


Figure 3.20: Schematic for manual transmission (MT) system

plate assembly actuated by a spring load system [102]. The dynamic model of the MT system consists of three modes depending on the three phases of the clutch, i.e disengaged, slipping and engaged. Several models of the friction clutch system are proposed in previous work. All of the models simulate torque transfer between engine and transmission system based on different principles. Some of the models are hyperbolic tangent model, Karnopp model, Reset-Integrator model, Dahl model, Bristle Model and LuGre model [103]. In this work, the clutch model is developed using the hyperbolic tangent model. This model can simulate the torque transfer with a continuous mathematical function. The disengaged model for the transmission can be expressed by (3.51) and (3.52). The engine speed ω_e and wheel speed v are decoupled in this

mode and given by the relations

$$J_e\dot{\omega}_e + B_e\omega_e = T_e, \tag{3.51}$$

$$m\dot{v} = -C_n v^2 - \mu_r mg\cos(\theta) - mg\sin(\theta) - F_b. \tag{3.52}$$

The symbols of these equations are defined previously in (3.34) and (3.35).

The slipping mode for the transmission system can be expressed by (3.53) and (3.54)

$$J_e\dot{\omega}_e + B_e\omega_e = T_e - T_{clutch}, \tag{3.53}$$

$$m\dot{v} = T_{clutch} - C_n v^2 - \mu_r mg\cos(\theta) - mg\sin(\theta) - F_b. \tag{3.54}$$

The torque T_{clutch} is expressed with the hyperbolic tangent model for clutch friction. The hyperbolic tangent model replaces the sign function of the Coulomb frictional model, with a numerically stable hyperbolic tangent function. The hyperbolic tangent function behaves as other clutch friction models [103, 104]. The clutch torque can be expressed as

$$T_{clutch} = 2\mu_{clutch} r_c F_n \tanh(\omega_{slip}) \tag{3.55}$$

where μ_{clutch} is the coefficient of friction of the clutch, r_c is the radius of the clutch frictional plate, F_n is the normal force exerted by the clutch spring assembly and ω_{slip} is the slip speed between both sides of clutch plates [102–104].

During the engaged condition, the powertrain unit works as a combined unit. Therefore the clutch torque term T_{clutch} disappears from the dynamic equation. The dynamic equations for the engaged powertrain unit can be expressed by (3.49) and (3.50) with the term μ_{NS} equal to unity.

3.6 Conclusions

This chapter presented dynamic mathematical models of

- An SI engine capable of simulating torque generation, fuel consumption and NOx emission.
- A Powertrain transmission capable of simulating gear-less transmission (CVT) and geared transmission (MT).

The SI engine model was validated and calibrated using available test data for a 110 cc production engine. The transmission model was simulated for dynamic response of the system. The presented work is the foundation for the following chapters.

Chapter 4

Objective analysis of the CVT and MT powertrain

4.1 Introduction

The objective analysis of certain characteristics of the gear-less transmission (CVT) and geared transmission (MT) for a low-powered powertrain is very much essential. The objective analysis is a powerful tool for providing essential information about both the powertrains using simulation methodology.

The main aim of this chapter is to derive an objective matrix for certain characteristics using the simulation model of the powertrain. The parameters that are very crucial for evaluating characteristics of a powertrain configuration are fuel consumption and NOx emission. The automotive industry for a low-powered powertrain in India, evaluates both the criteria using drive cycle tests. In this chapter the simulation methodology is proposed to capture the fuel consumption and NOx emission characteristics for a drive cycle test. The developed models in Chapter 3 are integrated together with a respective longitudinal driver model for simulating the chosen drive cycle, which is the Indian Drive Cycle (IDC) [105].

4.2 Simulation of the complete powertrain model for CVT vehicle

In this section, a suitable model is developed for evaluating the CVT-based powertrain for the above-mentioned two criteria. The drive cycle simulation is carried out in conjunction with a driver model. There are different approaches proposed for driver models [106], [107], [108], [109], [110], [111]. [106] presents an approach towards predicting the future velocity profile using a gain scheduled driver model together with a longitudinal vehicle model. The parameters of the driver model are estimated during vehicle operation using recursive least squares identification. Assuming repeated operation of the vehicle on the same route, the driver model is supplied with the desired velocity at a particular position and outputs the predicted velocity trajectory. The driver model presented in [107] uses fixed gains with a simple gain scheduling based on the vehicles speed. It presents a combined longitudinal-lateral controller that is regulating the steering angle and throttle/brake levels by previewing the path ahead of the vehicle. The structure of the model presented in [108] derives from the linear optimal discrete time preview control theory but it is non-linear. Its parameter values are obtained by heuristic methods, using insight gained from the linear optimal control theory. This study presented in [109] firstly analyses the drivers manipulation behaviour and relates the different components of the driver model. Then, a model controlling the driver directions is built according to the prediction-follower theory with the aim of improving the point search algorithm.the driver longitudinal speed control model was established by implementing feed-forward PID feedback. In [110], an integrated driver/direct yaw moment control (DYC) control system is presented that regulates the steering angle and yaw moment, considering driver previewed path. Thus, the driver previewed distance, the heading error and the lateral deviation between the vehicle and desired path are used as inputs. A PID controller with optimized gains is used for the control of integrated driver/DYC system. Genetic Algorithm as an intelligent optimization method is utilized to adapt PID controller gains for various working situations. A genetic algorithm procedure is proposed in [111] in order to adapt a set of optimized controller parameters suitable for various

driving styles, road conditions and the initial errors of vehicle position and orientation.

In this objective analysis, the driver model needs to follow the reference vehicle speed trajectory as mentioned in the drive cycle. As this process is equivalent to a controlled experiment, it can be achieved by a longitudinal driver model. The proposed longitudinal driver model ensures velocity trajectory tracking by controlling the throttle and braking force of the powertrain. The top level structure of the CVT-based powertrain is shown in Figure 4.1 The

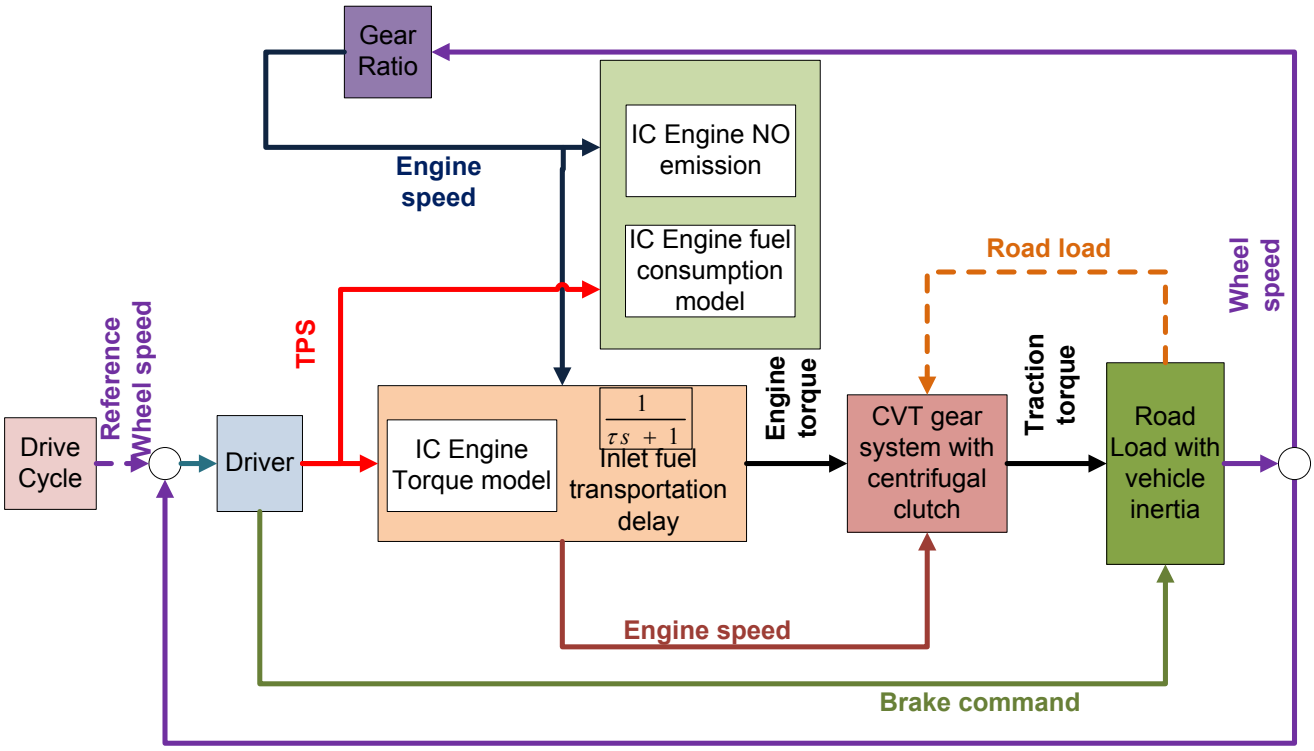


Figure 4.1: Powertrain model for drive cycle simulation for CVT vehicle

reference vehicle speed is generated from the drive cycle. The driver corrects the throttle and brake force based on the vehicle speed error. The driver model presented in this model is implemented using a PI controller with back calculation based anti-windup loop. The signal diagram for the driver model is presented in Figure 4.2. The output of the driver controller is manipulated using two different limiters as shown in Figure 4.2. Due to these limiters the throttle and brake request signals act in mutually exclusive manner. The brake request signal is manipulated with another negative gain as this signal is applied to the wheel (term F_b in (3.49)). Although there is scope for applying model-based preview control for the driver model, it is decided to apply a PI control-based driver model due to restricted development time. The

different constants of the driver model are tuned to reduce the RMS error of the vehicle speed during the drive cycle simulation. The integrator output of the model is corrected during saturation phase continuously by monitoring the error (caused by saturation) and correcting using back calculation mode. This mode ensures fast recovery for change of error sign during saturation. The IDC consists of 15% duration of time in idling. The drive model therefore consists of an idling speed control loop which maintains engine speed at desired idle speed. The IC

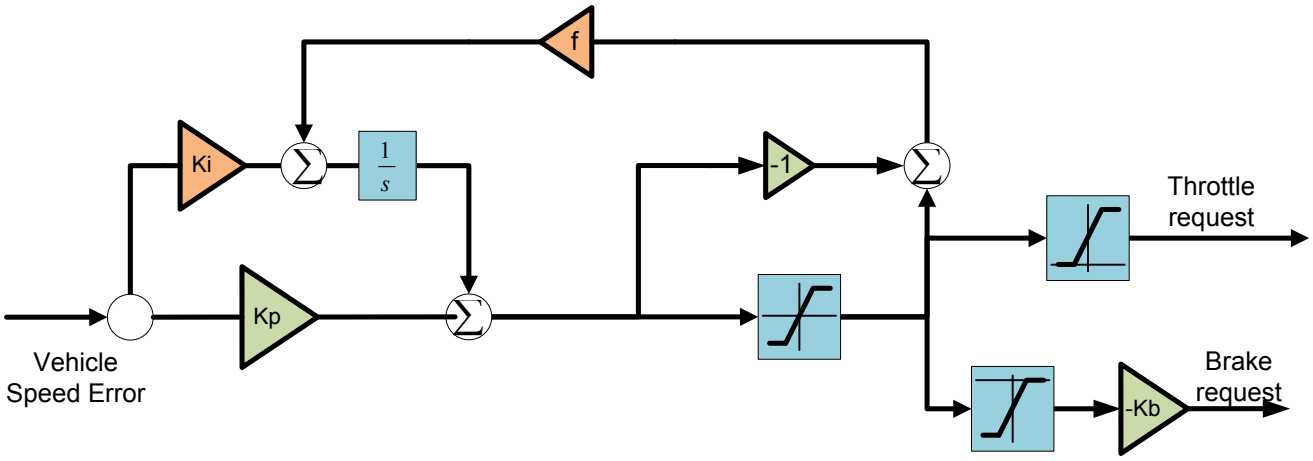


Figure 4.2: Driver model with back calculation-based anti-windup loop

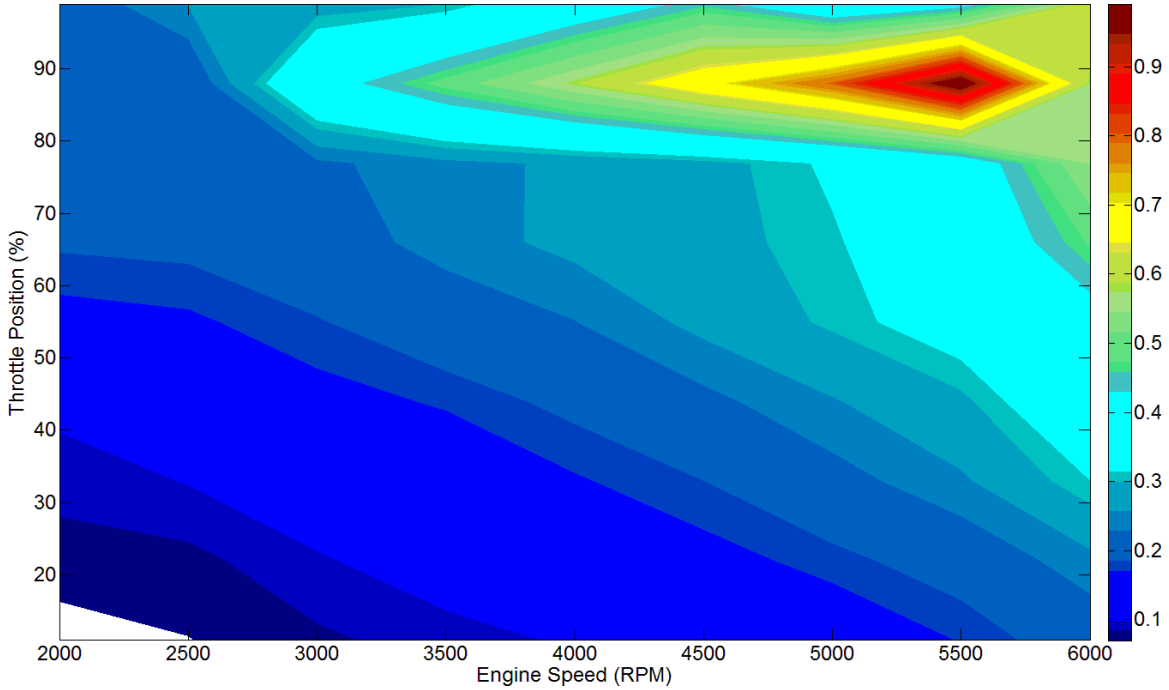


Figure 4.3: Feedforward model for the normalised engine fuel consumption

engine model mentioned in Figure 4.1 is the simplified model of the detailed model from the previous chapter. The simplified model includes a look-up table-based model (or feedforward model) of IC engine torque, IC engine fuel consumption and IC engine NO emission. These three models are derived from the steady state point simulation of the dynamic models of SI engine and NOx generation presented in the previous chapter. The plots of the feedforward models of the IC engine fuel consumption and IC engine NO emission are shown in Figures 4.3 and 4.4 respectively. The mean engine torque T_e is expressed as a function of TPS (throttle position) and ω_e. The manifold fuel transportation delay can be simulated by a first order delay with a 2 seconds time constant [11]. The absolute values of both the plots are converted to ratios of the maximum values of the corresponding plots to maintain confidentiality of the data. The white colored zones for both of the above plots are without any data. Therefore the operating points inside the zone with white color are represented with the values of nearest color data points. In Figure 4.4, it can be observed that the operating zone with low throttle and high engine speed has more $[NOx]$. This can be attributed to the value of AFR (which is near to 15) in this operating zone.

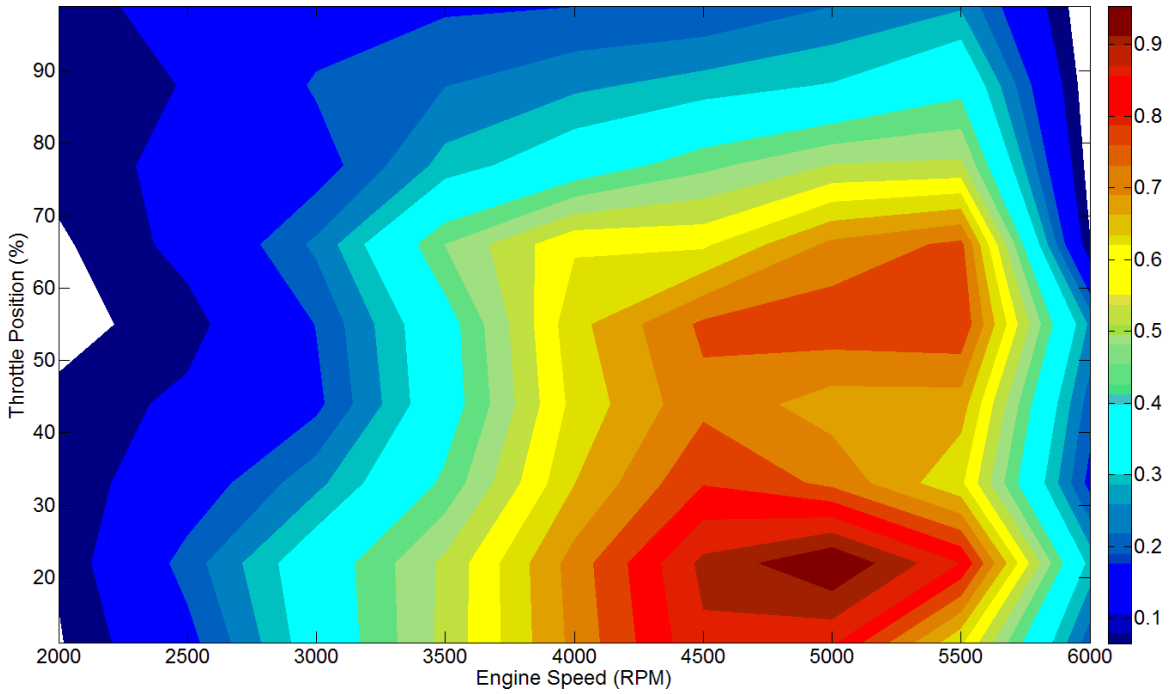


Figure 4.4: Feedforward model for the normalised NOx emission

4.3 Simulation of the complete powertrain model for manual transmission-based vehicle

In this section, a suitable model is presented for evaluating the MT-based powertrain for the two criteria mentioned in the objective matrix development section. The drive cycle simulation is carried in conjunction with a driver model which controls the throttle, braking force, clutch actuation and gear shift. The top level structure of the MT-based powertrain is shown in Figure 4.5. The IC engine torque model, NOx emission model and fuel consumption model are identical to the models integrated in the CVT powertrain model. The driver model is different compared to the driver model discussed for the CVT powertrain due to two reasons:

- The driver model needs to schedule the gains with respect to the stepped change of gear ratios [106].
- The driver model needs to schedule the operation of gear shift with coordination of clutch and throttle.

The first issue is solved by applying a bump-less transfer scheme with anti-windup protection discussed in [112]. Figure 4.6 shows the driver model with bump-less control scheme. As suggested in [112], the gains $f1$ and $f2$ are kept at a high value (1000) for smooth transition of internal states of the plant. The second issue is solved by applying a time-dependent function for clutch and throttle transition as proposed in [102]. In this research, the second issue is addressed by using a switch with bump-less transfer scheme.

4.4 Drive cycle simulation results

The Figures 4.7 and 4.9 show the tracking of drive cycle reference vehicle speed with the actual vehicle speed of CVT and MT powertrain respectively. It can be observed that, both the driver models (Figures 4.2 and 4.6) are working satisfactorily. The tracking error is acceptable since it is comparable with actual drive cycle tests conducted on a chassis dynamometer. There is

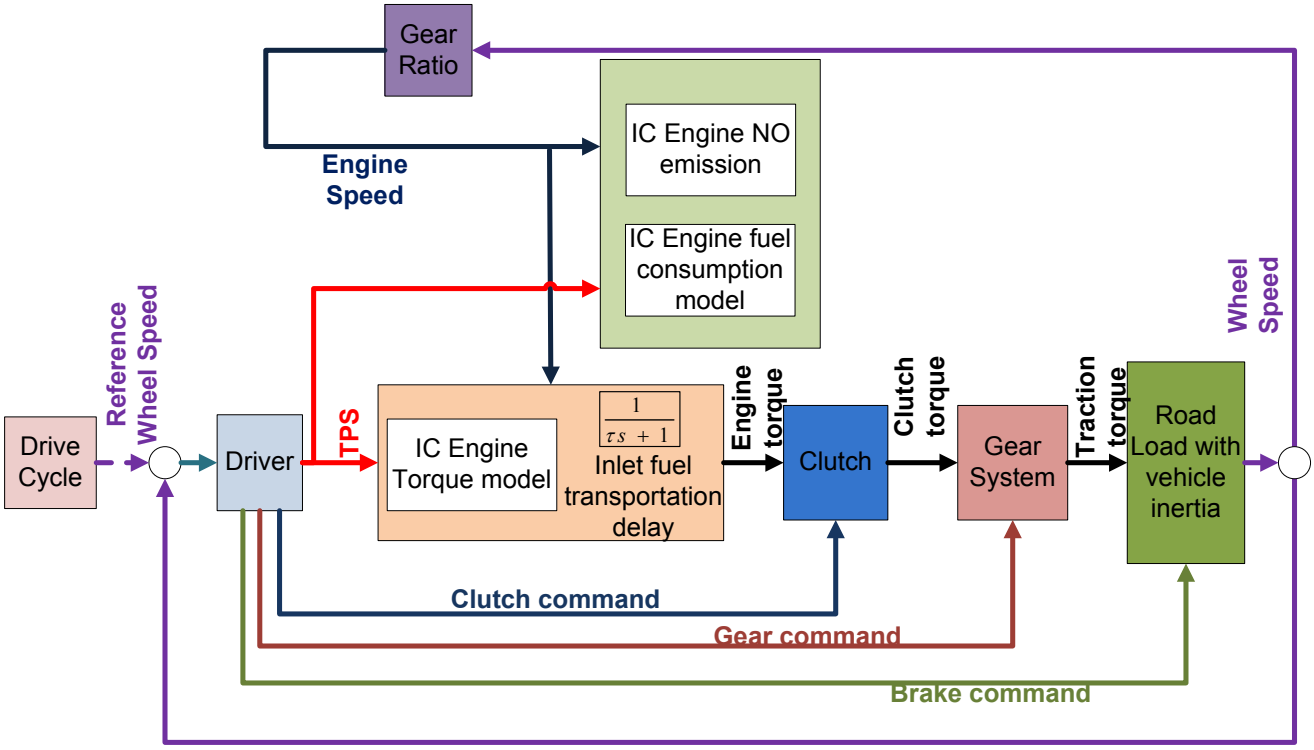


Figure 4.5: Powertrain model for drive cycle simulation for MT vehicle

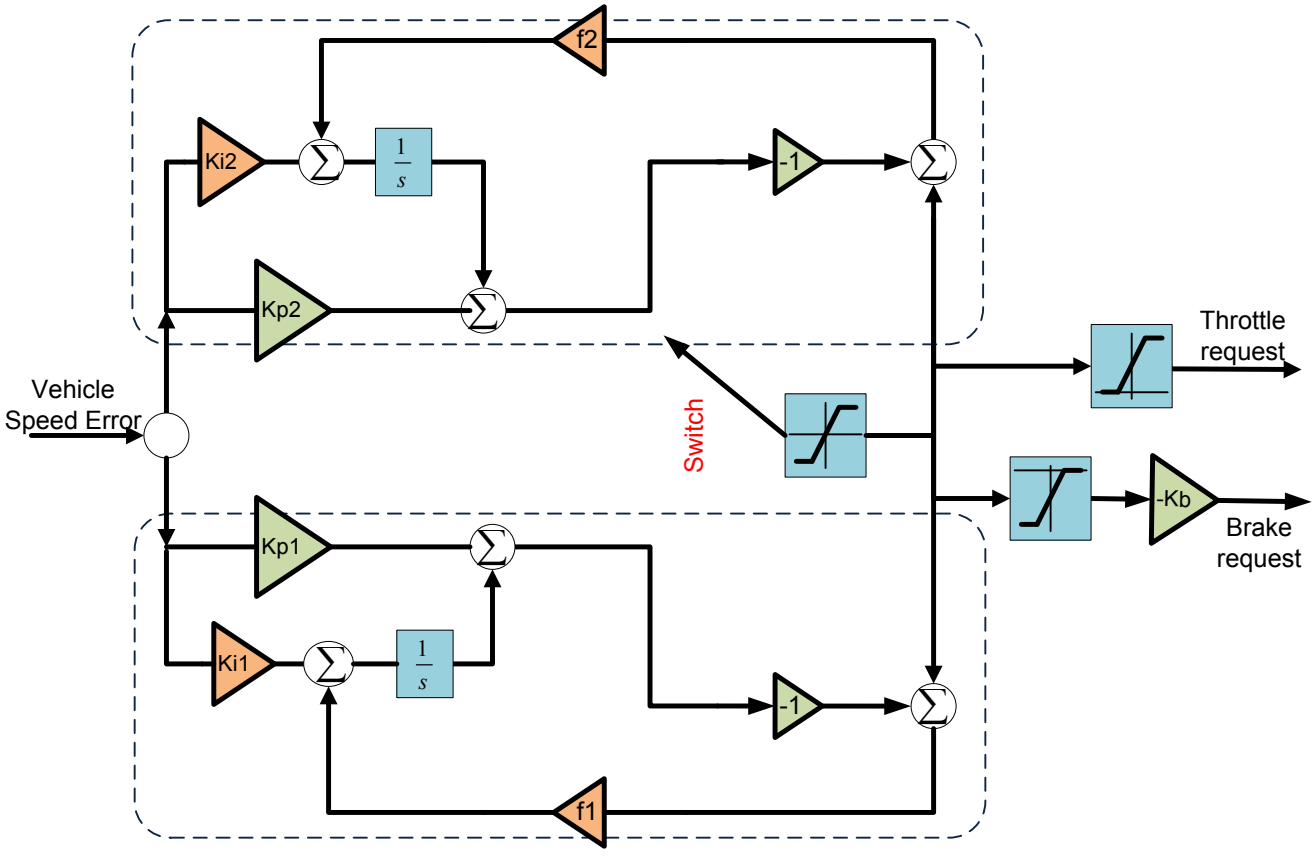


Figure 4.6: Driver model with bump-less transfer scheme with anti-windup loop

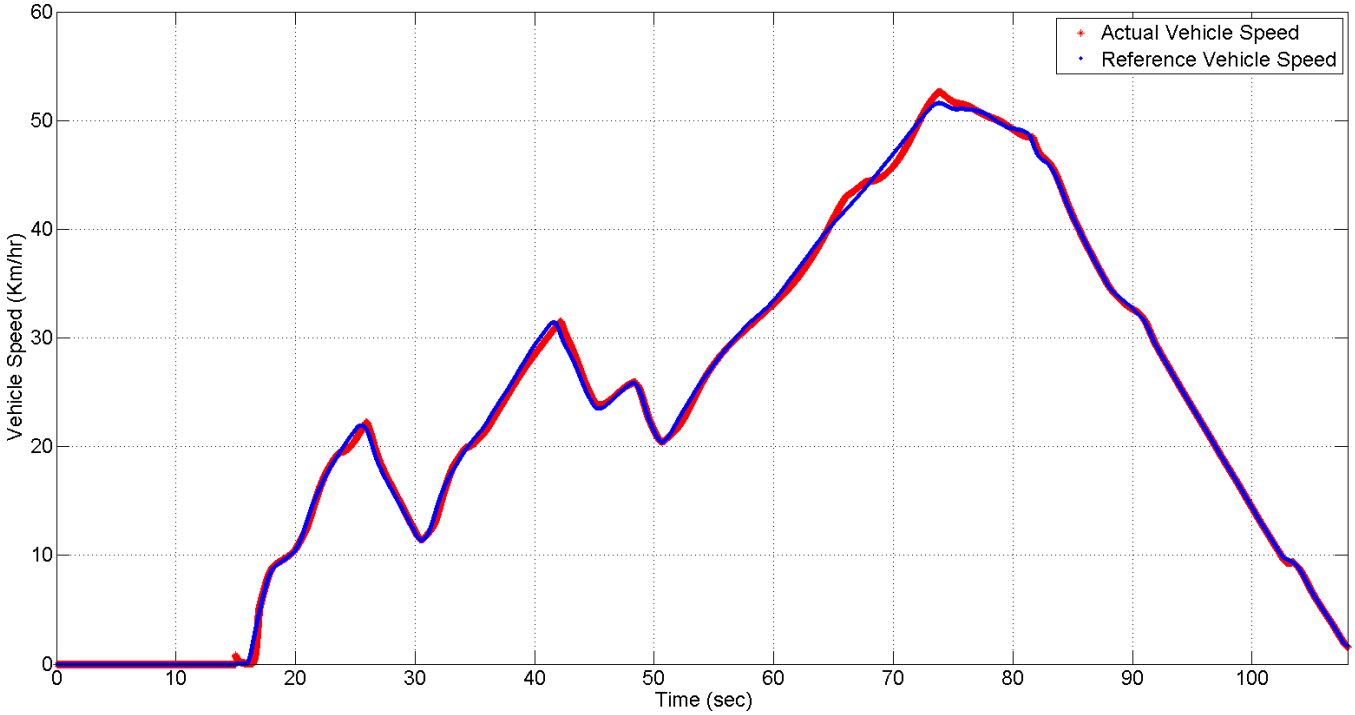


Figure 4.7: Vehicle speed and reference vehicle speed for CVT powertrain during drive cycle simulation

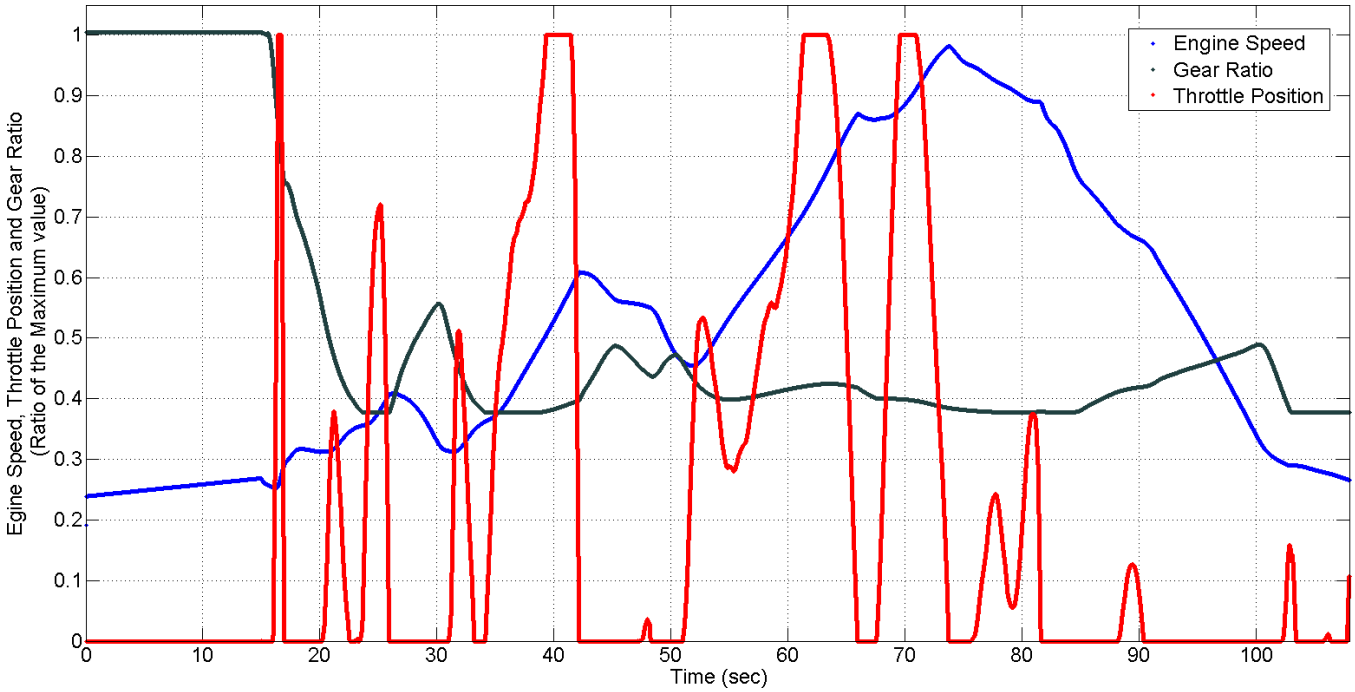


Figure 4.8: Variation of engine speed, throttle position and gear ratio during drive cycle testing for CVT Powertrain

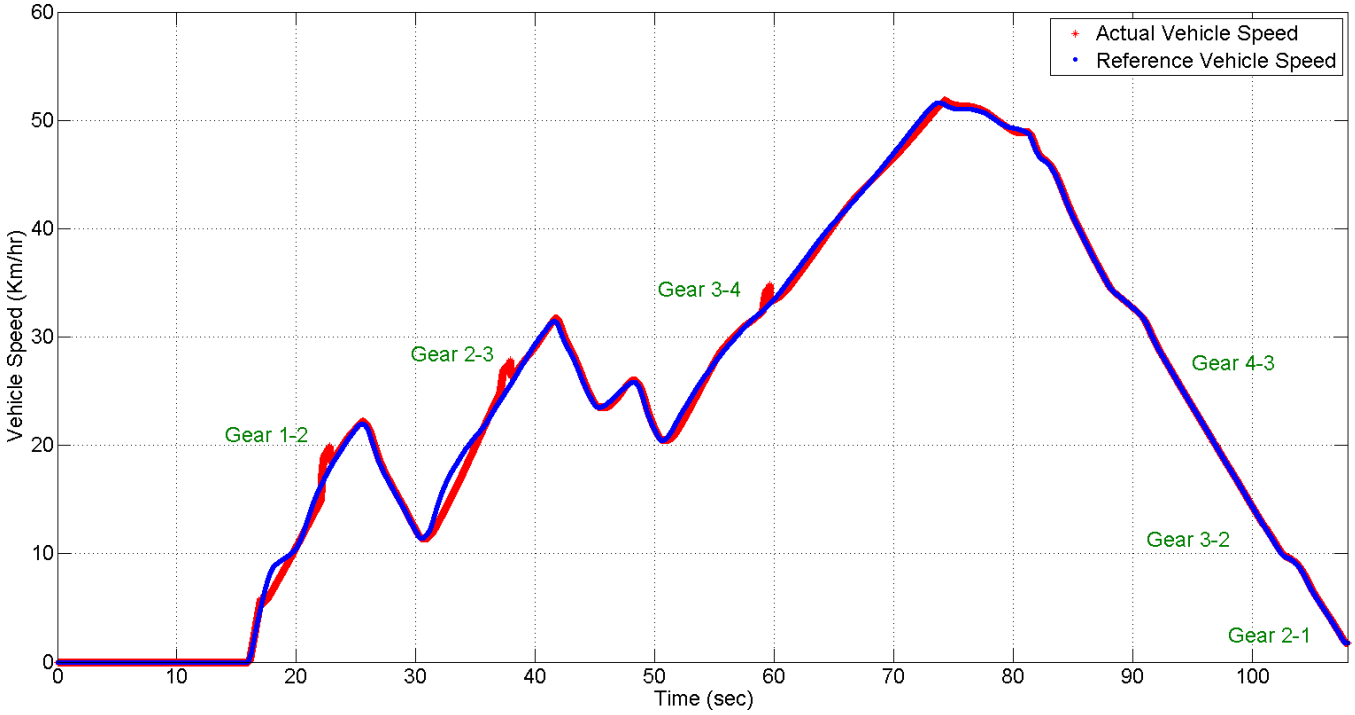


Figure 4.9: Vehicle speed and reference vehicle speed for MT powertrain during drive cycle simulation

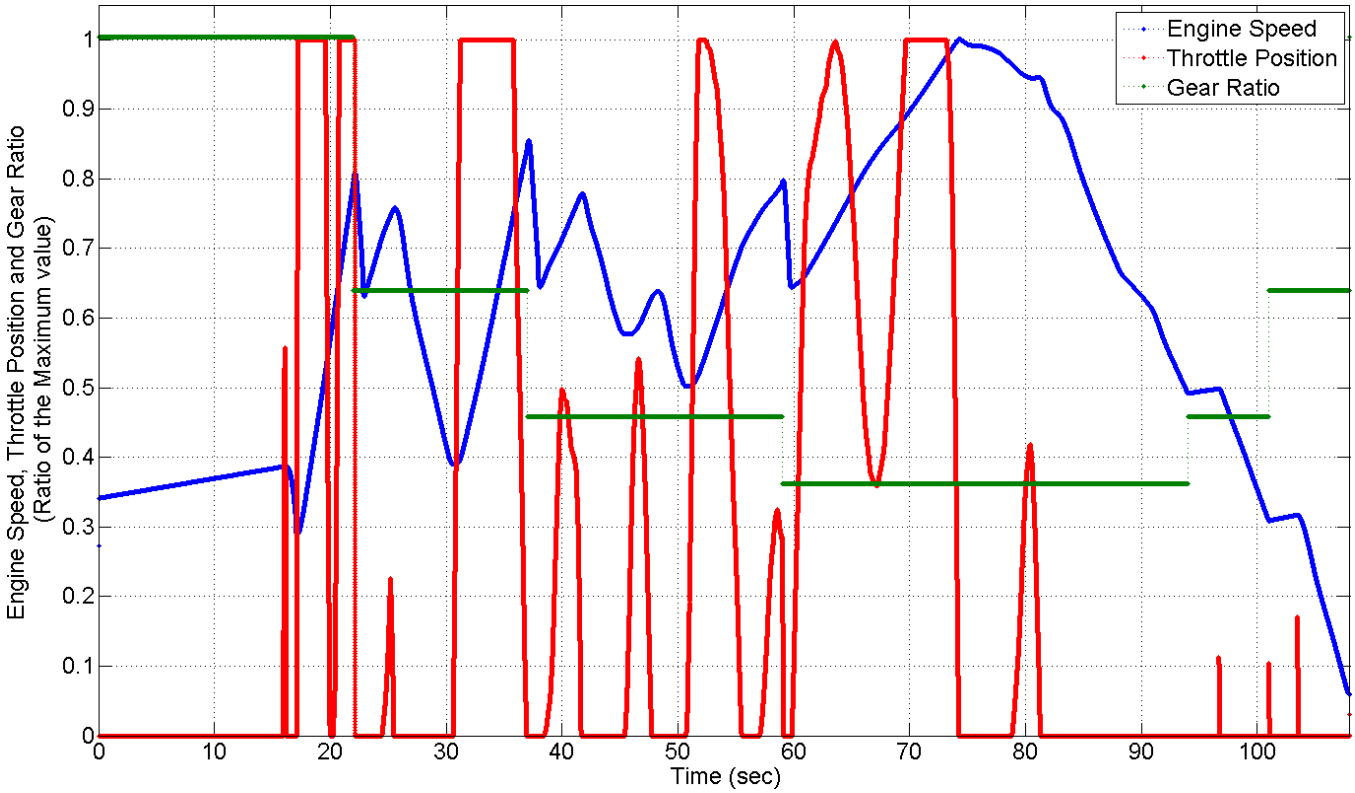


Figure 4.10: Variation of engine speed, throttle position and gear ratio during drive cycle testing for MT Powertrain

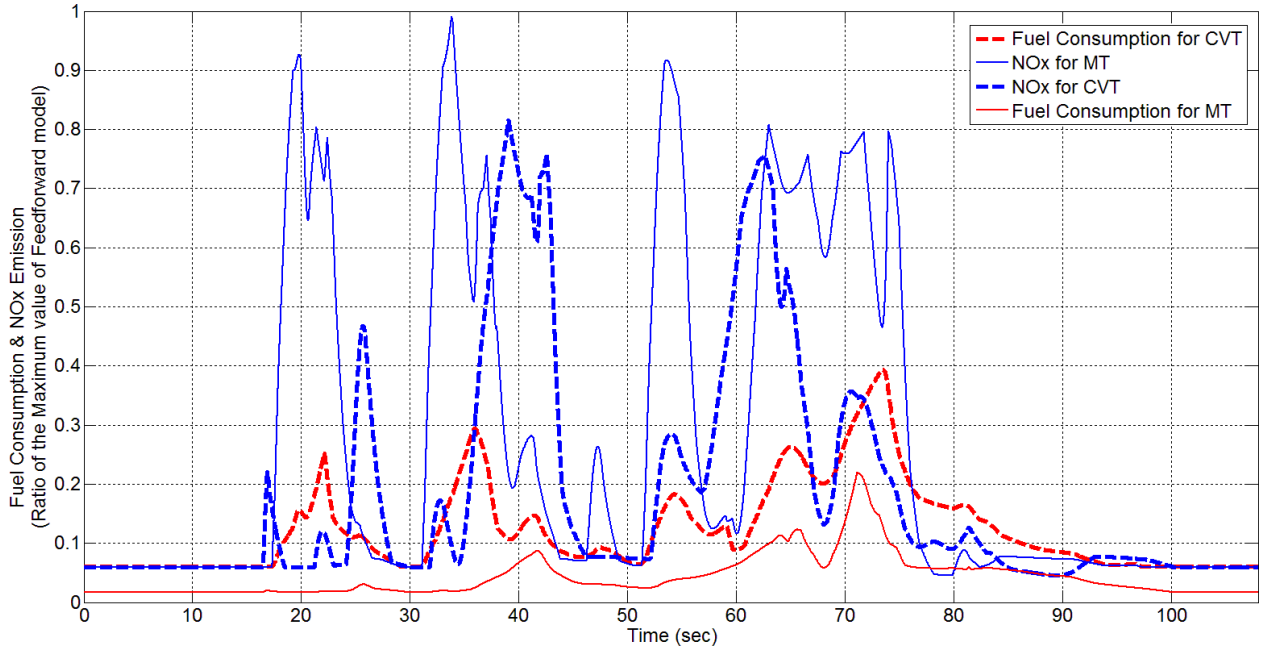


Figure 4.11: Variation of fuel mass rate and NOx emission during drive cycle testing for CVT and MT Powertrain

a scope of further reduction of tracking error using an advanced driver model applying the preview control method [113]. The gear shift events show local tracking error (Figure 4.9). The tracking error is minimized effectively by the bump-less transfer scheme proposed. Figures 4.8 and 4.10 show the variation of engine speed, throttle position and total gear ratio for the entire drive cycle for CVT and MT powertrain respectively. The variation of gear ratio of CVT vehicle allows the engine to operate at a lower operating speed region compared to the MT-based vehicle. The fuel consumption for the CVT-based powertrain is observed to be 25% more than the MT-based powertrain. The main reason is the different operating speed region of the engine for the drive cycle. The NOx emission is observed to be 44% more for the MT vehicle compared to the CVT vehicle. This is due to the unique distribution of NOx emission as shown in Figure 4.4 where NOx emission is more for the low throttle high speed region.

4.5 Conclusions

This chapter presents dynamic mathematical models of

- a vehicle with gear-less transmission (CVT) with a low-powered powertrain integrated

with a longitudinal driver.

- a vehicle with geared transmission (MT) with a low-powered powertrain integrated with a longitudinal driver.

The fuel consumption and NOx emission is simulated for both dynamic models. The vehicle models are useful for the drivability evaluation work presented in next chapter.

Chapter 5

Drivability characteristics assessment

5.1 Introduction

The proposed motor-integrated powertrain needs to be coupled with a suitable transmission selected from gear-less transmission (CVT) or geared transmission (MT) systems. The fuel consumption analysis conducted in the previous chapter provides some comparative information of the two transmission systems. The objective evaluation of the drivability characteristics between both type of powertrains is essential at this stage of the research work, as drivability is one of the critical and subjective parameters that influences the perception of a two-wheeler vehicle for urban customers in India. The objective evaluation of a subjective parameter, such as drivability for a two wheeler vehicle provides great challenges. In this chapter, a simulation-based methodology for the objective evaluation of the drivability for both types of powertrains is discussed. The powertrain model proposed in Chapter 3 consisting of an SI engine with CVT and MT system is adopted for this evaluation. However the expression for the centrifugal clutch is presented in this chapter.

5.2 Drivability characteristics

Drivability is defined as the longitudinal dynamic behavior of a vehicle in response to driver inputs, in a comprehensive range of driving situations, and the related driver subjective perception of that behavior [35]. Traditionally the drivability for low-power two-wheeled vehicles in India is assessed subjectively. Although there is no literature available for subjective assessment for this vehicle segment, the full subjective drivability analysis for a car involves evaluating around 300 parameters [36].

It is shown in previous works that all the subjective parameters can be linked to objective parameters such as the delay in response, stumble, oscillations and overshoot [36–42]. As the powertrain in the present work is powered by a carburettor fuel metering system, the interaction between SI engine and drivetrain becomes more challenging during transient operation due to poor acceleration enrichment capability. The parameters delay time, peak negative acceleration, peak positive acceleration and significant peaks of acceleration are considered in this work for objective assessment, as shown in Figure 5.1. These parameters are considered carefully with the consultations from the expert test riders of TVS Motor Company as well as with previous published works. It is evident from Figure 5.1 that the longitudinal acceleration is a second-order response, which can therefore be characterized by the parameters mentioned above.

Two wheelers in India are mainly used for city driving in high density traffic conditions. Therefore it is more meaningful to consider vehicle launch and tip in scenarios to characterize drivability of both powertrain configurations. Figure 5.2 shows the dynamic behavior of all the significant parameters of the CVT powertrain for the two scenarios. The dynamic behavior of the MT powertrain is similar to Figure 5.2. The left hand side of the plot captures the vehicle launch whereas the right hand side of the plot shows the tip in stage. The launch and tip in stages can be identified by observing the throttle signal. The clutch synchronization phases are visible (by observing the rotational speeds of input and output sides of the clutch plate, $\omega_{clutch_{ip}}$ and $\omega_{clutch_{op}}$ respectively) in both the instances of launch and tip in. The synchronization phase between $\omega_{clutch_{ip}}$ and $\omega_{clutch_{op}}$ affects the drivability during vehicle launch. The dip in engine

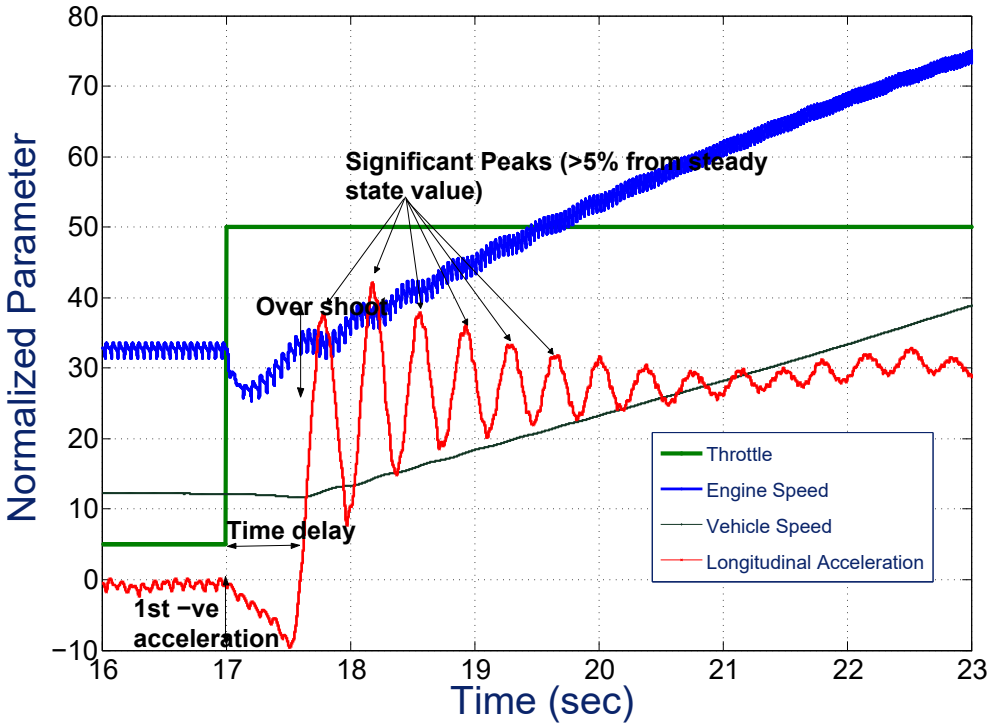


Figure 5.1: Objective assessment parameters for two wheeler drivability (from simulation)

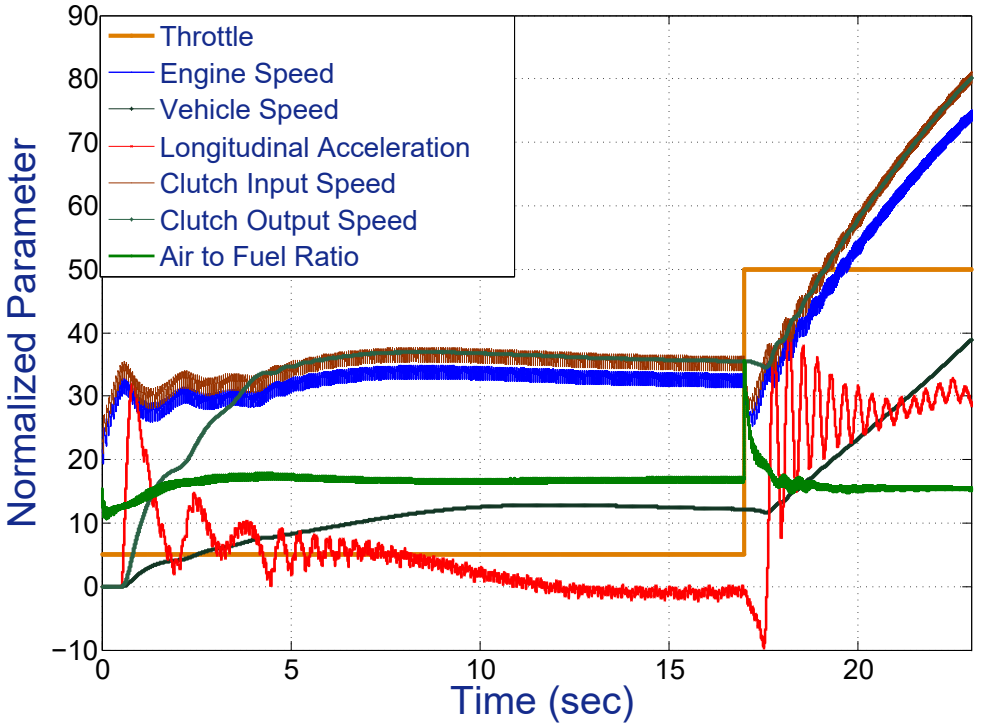


Figure 5.2: Drivability assessment for vehicle launch (left side) and tip in (right side)

speed (as well as $\omega_{clutch_{ip}}$) during tip in can be attributed to the AFR dynamics. The vehicle speed and longitudinal acceleration are also influenced by the AFR dynamics during tip in. The oscillations observed with longitudinal acceleration can be attributed to the clutch synchronization as well as AFR dynamics. The $\omega_{clutch_{ip}}$ term is directly dependent on crank shaft torque. The driver applies more throttle during vehicle launch for certain driving conditions (road with gradient, driving with more vehicle load etc). Therefore it is decided to test the vehicle launch for both powertrain configurations with different throttle openings.

The tip in response is strongly influenced by the torque dip generated by the AFR dynamics. Therefore it is essential to capture the tip in response for the significant operating zones of the SI engine. It is also very much necessary to investigate the tip in response for the significant operating zones of the vehicle. The vehicle operating zone is mapped with respect to longitudinal speed of the vehicle v and wheel torque $\mathbf{T}_{wheel}$. It is useful to select this zone based on drive cycles. In this work, the Indian drive cycle and a customized drive cycle (which is internally used in TVS Motor Company) are used to identify the dominant operating zone for city driving. Figure 5.3 shows the frequency of occurrence of vehicle operating points for both drive cycles. It is evident that the frequency of operation is high for ($15\,km/h < v < 30\,km/h$) and ($15\,Nm < \mathbf{T}_{wheel} < 25\,Nm$). The color bar on the right hand side of Figure 5.3 indicates the frequency of operation in each region for a sampling time of 1 s.

5.3 Transmission model

A two-wheeler transmission consists of a clutching device and gear system. The clutching system isolates the SI engine from the wheel load during the cranking and idling operating zones where the engine does not produce enough traction power. The gear system allows the engine to operate in a suitable torque-speed zone according to the wheel torque requirement. The mathematical model for the drive train can have a different degree of complexity based on the requirements. Since this model is a control-oriented model, the high frequency driveline phenomena can be excluded without sacrificing the accuracy of the model. [114] proposed

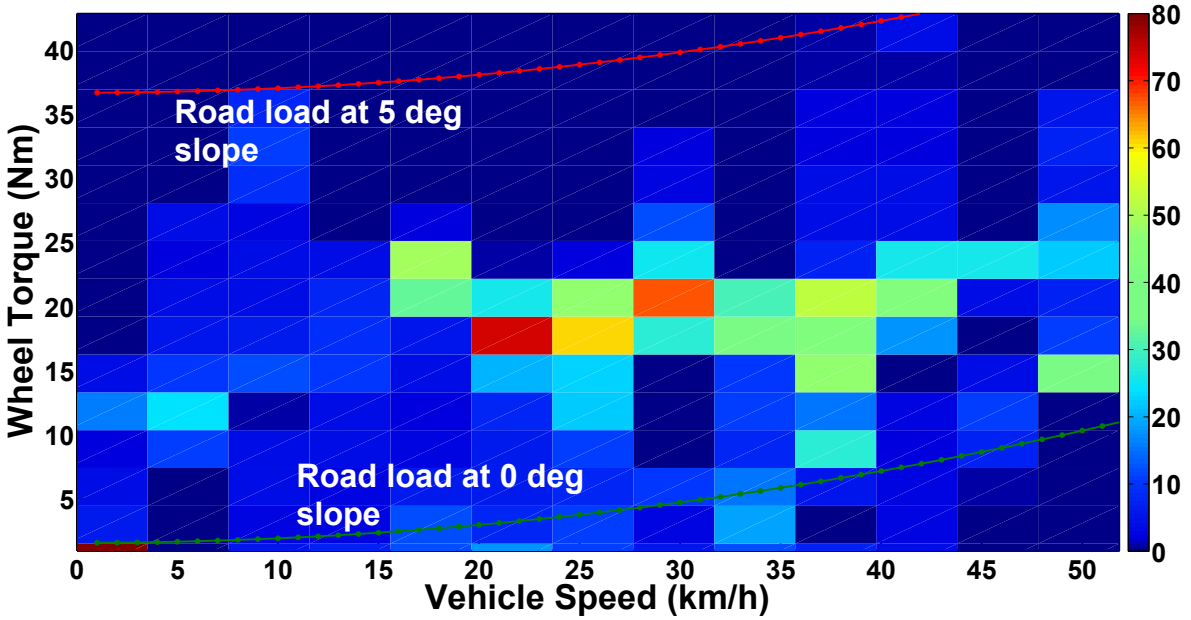


Figure 5.3: Significant operating zone for city driving conditions

different complexities of powertrain models and compared their results. The models of the two wheeler transmission developed for this work are inspired by the above-mentioned work. The wheel torque $\mathbf{T}_{wheel}$ is expressed in previous chapter as

$$m_{vehicle}\dot{v} = \frac{\mathbf{T}_{wheel}}{R_{wheel}} - C_n v^2 - \mu_r m_{vehicle} g\cos(\theta) - m_{vehicle} g\sin(\theta) - F_{brake} \tag{5.1}$$

where $m_{vehicle}$ is the mass of the vehicle, v is the linear velocity of the vehicle, R_{wheel} is the dynamic radius of the wheel, C_n is the equivalent air drag term, μ_r is the rolling friction coefficient, g is the gravitational acceleration constant, θ is the road inclination and F_{brake} is the braking force. $\mathbf{T}_{wheel}$ can be expressed as a function of the clutch torque $\mathbf{T}_{clutch}$

$$\mathbf{T}_{clutch} = \frac{\mathbf{T}_{wheel}}{R_N R_f \eta_N \eta_f} \tag{5.2}$$

where R_N is the gear ratio, R_f is the final gear ratio, η_N is the efficiency of the gear and η_f is the efficiency of the final ratio. The moment of inertia and stiffness properties of the drivetrain are neglected in this control-oriented model as contributions of these properties towards the drivability of the vehicle are not significant.

5.3.1 CVT transmission with centrifugal clutch

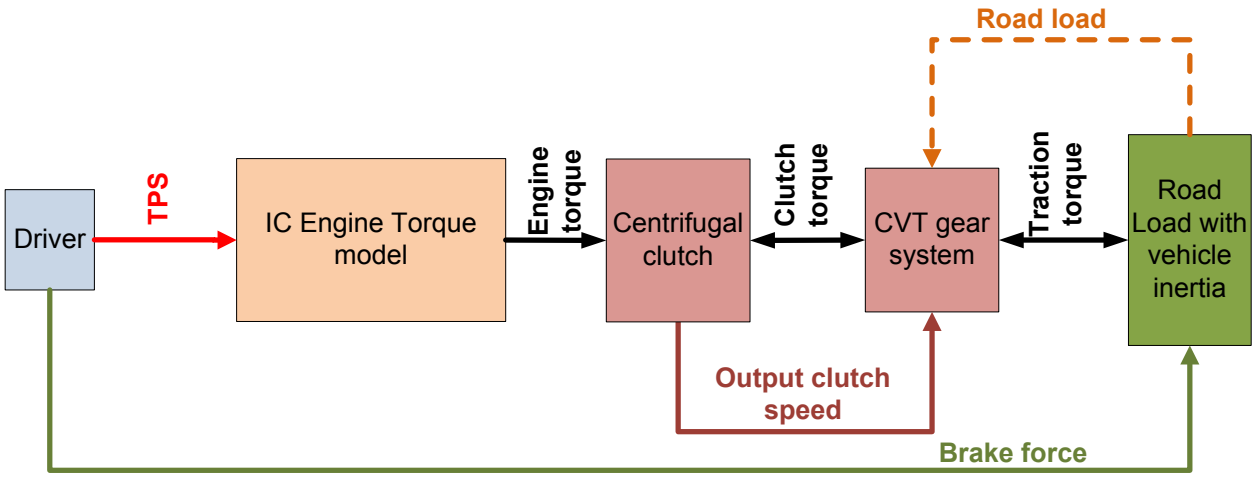


Figure 5.4: Functional diagram of CVT powertrain

The functional block diagram of a CVT-based powertrain is shown in Figure 5.4. The IC engine model, which is discussed in the previous section, is coupled with a centrifugal clutch by a speed reduction gear. The centrifugal clutch can be considered as a speed sensing device that consists of an inner disc driven by the driven shaft, several centrifugal shoes mounted on the inner disc and an outer wheel which is connected to the the final drive gear. The centrifugal shoes when rotated beyond a threshold angular speed of input shaft, they move radially outwards until the clutch is engaged. The threshold angular speed is termed as clutch engagement speed ($\omega_{clutch_{eng}}$). The effect of shoe radial motion on the clutch friction can be expressed as a hyperbolic function of the difference of angular speed between input shaft ($\omega_{clutch_{ip}}$) and $\omega_{clutch_{eng}}$. The clutch torque transfer can be modeled in several ways, some of which make use of appropriate friction models. Some of the torque transfer models are hyperbolic tangent, Karnopp, Reset-Integrator, Dahl, Bristle and LuGre models as mentioned by [115]. In this work, the clutch model is developed using a hyperbolic tangent function of clutch slip speed. This model can simulate the torque transfer with a continuous mathematical function which is essential for a control-oriented model. The torque transferred by the centrifugal clutch can be expressed as

$$\mathbf{T}_{clutch} = e^{(\psi(\omega_{clutch_{ip}} - \omega_{clutch_{eng}}))} \times \tanh(\varphi(\omega_{clutch_{ip}} - \omega_{clutch_{op}})) \tag{5.3}$$

where $\omega_{clutch_{op}}$ is the angular speed of the output shaft. ψ and φ are calibration constants. The centrifugal clutch isolates the engine from the drivetrain if the $\omega_{clutch_{ip}}$ falls below $\omega_{clutch_{eng}}$. The modeldoes not allow full engine braking due to this decoupling.

The CVT system consists of a pair of pulleys with rubber belt and pulley actuation system. The radius of the drive pulley is controlled by the force balance between the rubber belt and centrifugal masses placed on the actuation system. The force balance equation between the forces is expressed in [116–120]. This system is essentially a speed sensing system. The driven pulley diameter is controlled by a spring with mechanical cam-based system [116–120] which is essentially a torque sensing system. Due to the complexity of the above-mentioned systems, the equations are not included in the dynamic model of the CVT. Instead, the ratio of the CVT, R_N^{Target} can be expressed as a static function of engine speed and wheel torque as

$$R_N^{Target} = f(\omega_e, \mathbf{T}_{wheel}). \tag{5.4}$$

The relation is discussed in Chapter 3 and is shown in Figure 5.5. This map can be used as a

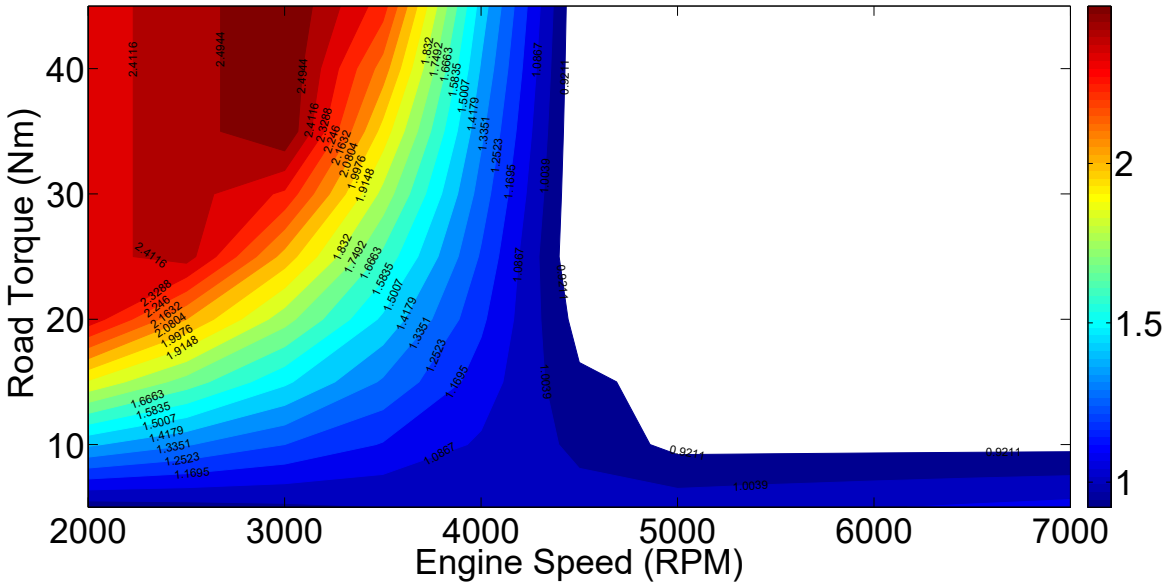


Figure 5.5: CVT Ratio for the two wheeler vehicle (presented in the previous chapter)

simplified CVT ratio control map in the CVT dynamic model. The dynamics of the CVT are

represented by a first order lag [121, 122] as

$$\frac{dR_N}{dt} + aR_N = aR_N^{Target} \tag{5.5}$$

where $\frac{1}{a}$ is the time constant of the ratio actuation system in the order of 200 ms [122] and R_N^{Target} is the target CVT ratio according to the operating zone of the vehicle.

5.3.2 MT transmission with clutch

The functional block diagram of the MT-based powertrain is shown in Figure 5.6. This model is simpler than a CVT model explained above as it does not involve a centrifugal clutch mechanism and automatic gear shift mechanism. The clutch and gear ratio are controlled by the driver. The clutch torque transfer is modeled using a hyperbolic tangent function of clutch slip speed

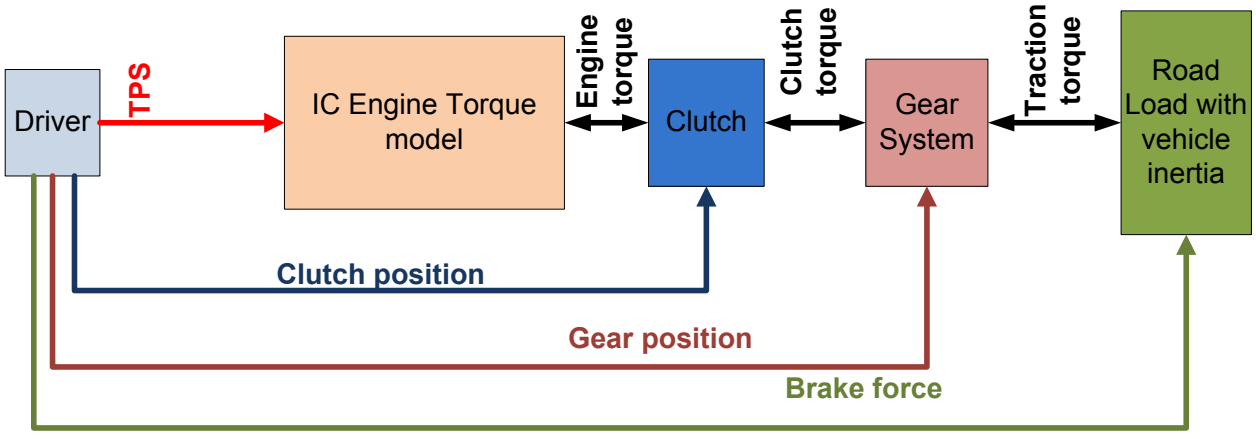


Figure 5.6: Functional diagram of MT powertrain

similar to the centrifugal clutches mentioned in the previous section. F_{clutch} is the normal force exerted by the spring mechanism on the clutch friction plates. It is linearly related to the clutch pedal position which is controlled by the driver. Since the driver controls the clutch pedal, it is necessary to express the clutch position as a function of time during clutch engagement phase. A normal driver applies the clutch with a very slow ramp (approximately 10 %/s) whereas an aggressive driver can apply clutch with a slope of 30 %/s. In the drivability simulation, it is decided to simulate the clutch profile for an aggressive driver. The torque transferred by the

clutch can be expressed as

$$\mathbf{T}_{clutch} = F_{clutch} \tanh(\varphi(\omega_{clutch_{ip}} - \omega_{clutch_{op}})) \tag{5.6}$$

where φ is a calibration constant. The gear ratio model is expressed as a static value. The gear shift dynamics for a MT powertrain (which is termed as gear shift feeling) is not considered in this research.

5.4 Simulation results

In this section simulation results for drivability tests of CVT and MT powertrains are presented. The results are subdivided into tip in and launch simulations. Tip in simulations are conducted for the significant engine and vehicle operating zones. The tip in simulations for the significant engine operating zone are conducted assuming the vehicle is driven on a flat road. These operating points are on the green line shown in Figure 5.3. The tip in simulations for the significant vehicle operating zones are conducted for selected operating points with high frequency of occurrence in city driving as presented in Figure 5.3. The gear ratio for the CVT powertrain automatically changes for the above-mentioned tests. The MT powertrain consists of a 4 speed gear system. The first gear ratio is 56 % higher than the second gear ratio. Moreover the first gear is only used for stationary vehicle. In order to reflect actual driver usage, tip in simulations are conducted for the second gear of the MT powertrain.

5.4.1 Tip in simulation for significant engine operating zones

In these simulations, both the powertrains are operated at certain steady state vehicle operating points along the green line in Figure 5.3 up to 40 km/h which corresponds to unique operating points of the IC engine. Five engine speed cases are considered for testing (2100 rpm, 2500 rpm, 3100 rpm, 4000 rpm, 5000 rpm) and for each engine speed case, throttle is stepwise increased to specific values to simulate tip in. For the CVT powertrain throttle is increased respectively,

10 %, 20 %,... 100 % and for the MT powertrain, 10 %, 20 %,... 70 %. Higher than 70 % cases of throttle opening for the MT are excluded due to very long simulation times. Time delay, negative and acceleration peaks and acceleration oscillation values for each tip in simulations are calculated and presented as contour diagrams for each transmission with all the speed-throttle test points in the remaining of this section.

The time delay parameter in seconds is shown in Figures 5.7 and 5.8 for the CVT and MT powertrains respectively. The delay time for the CVT powertrain for $\omega_e < 4000$ rpm and throttle opening< 50 % is significantly more (3 times) than that of MT powertrain. This is due to the smaller gear ratio of the CVT powertrain compared to MT ratio which gets adjusted according to the function mentioned in (5.4). The gear ratio of the MT powertrain remains constant whereas it dynamically changes to a smaller ratio for the CVT powertrain. The operating region mentioned above ($\omega_e < 4000$ rpm and throttle opening< 50 %) is very important for the city driving condition in which frequent acceleration/deceleration requests from the driver is a standard requirement. In these circumstances, it is more desirable to have reasonably high delay time (similar to the CVT powertrain) which can act as a low pass filter for the driver torque request. This is one of the unique requirements from customers of scooter vehicles with a lower cc (< 125 cc) engine. It is important to mention that the low delay time (similar to the MT powertrain) is preferred in other operating regions as otherwise the driver will not be able to execute kick-down operation (overtaking during cruising mode). The negative acceleration peak can contribute to the pulling back feeling during driving. It is therefore desirable to have a minimum value for it. Figures 5.9 and 5.10 show the values of negative peak accelerations in m/s^2 for the significant engine operating zones of both types of powertrain. The negative acceleration can be attributed to the torque dip due to the AFR leaning phase during sudden throttle opening. The lower values of gear ratio for the CVT powertrain contribute to the less negative peak acceleration values compared to the MT powertrain for $\omega_e < 3000$ rpm. The torque dip duration is more prominent for the mid engine operating region due to lean AFR tuning of the engine. The positive acceleration peak can contribute towards the sudden push feeling during driving. Although positive acceleration is desirable for the driver, the acceleration

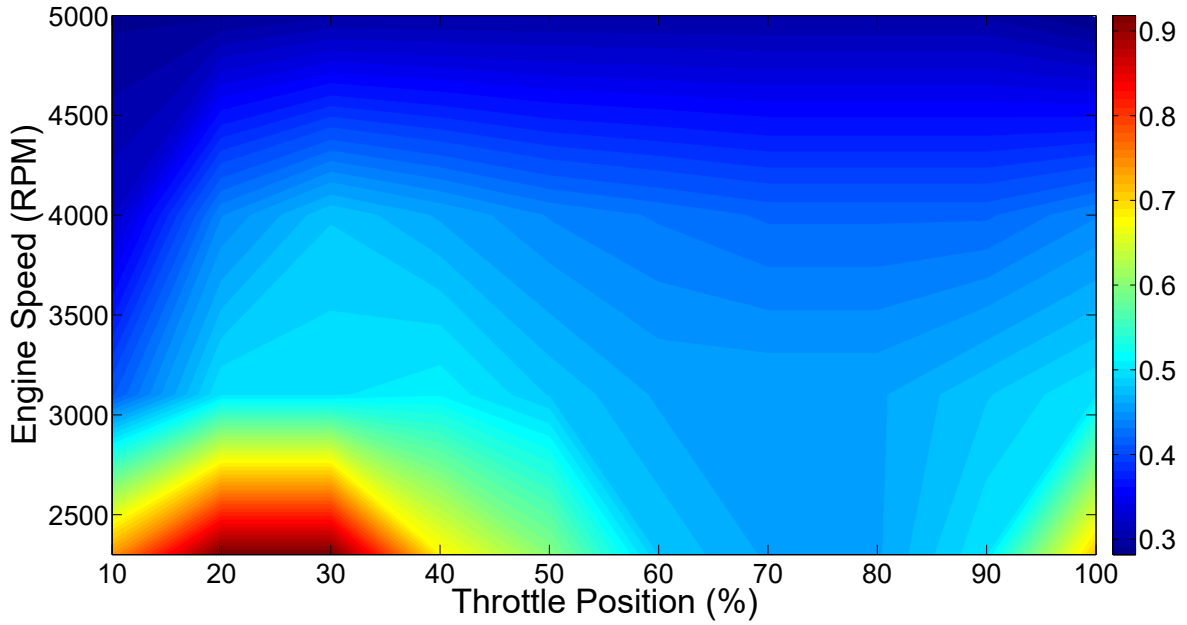


Figure 5.7: Delay for CVT Powertrain

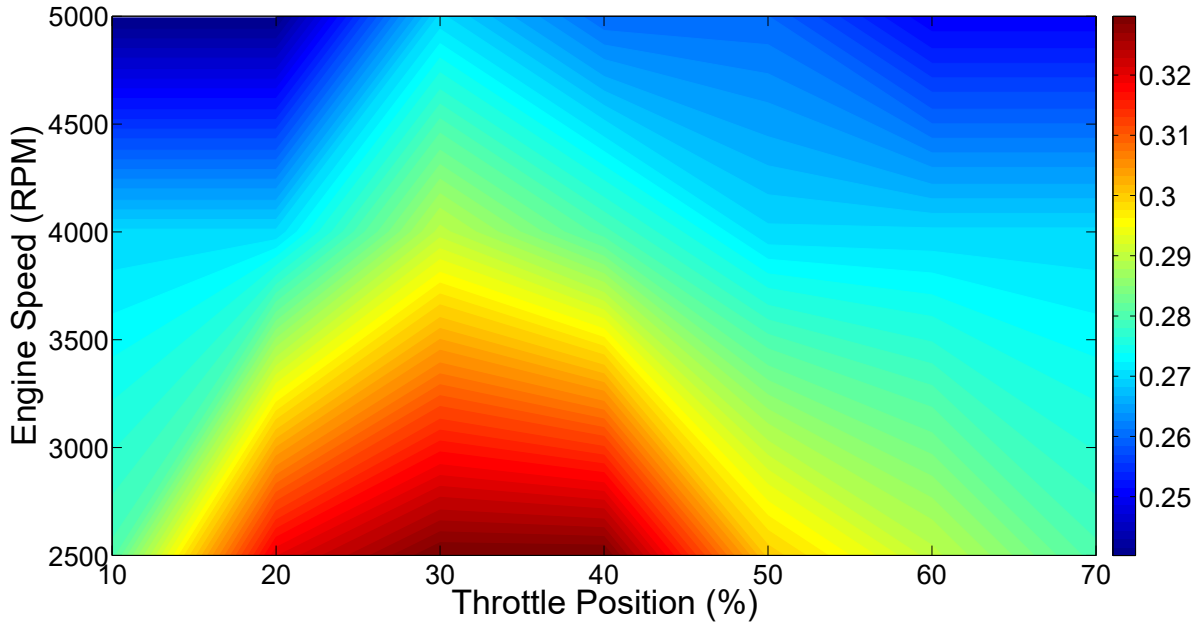


Figure 5.8: Delay for MT Powertrain

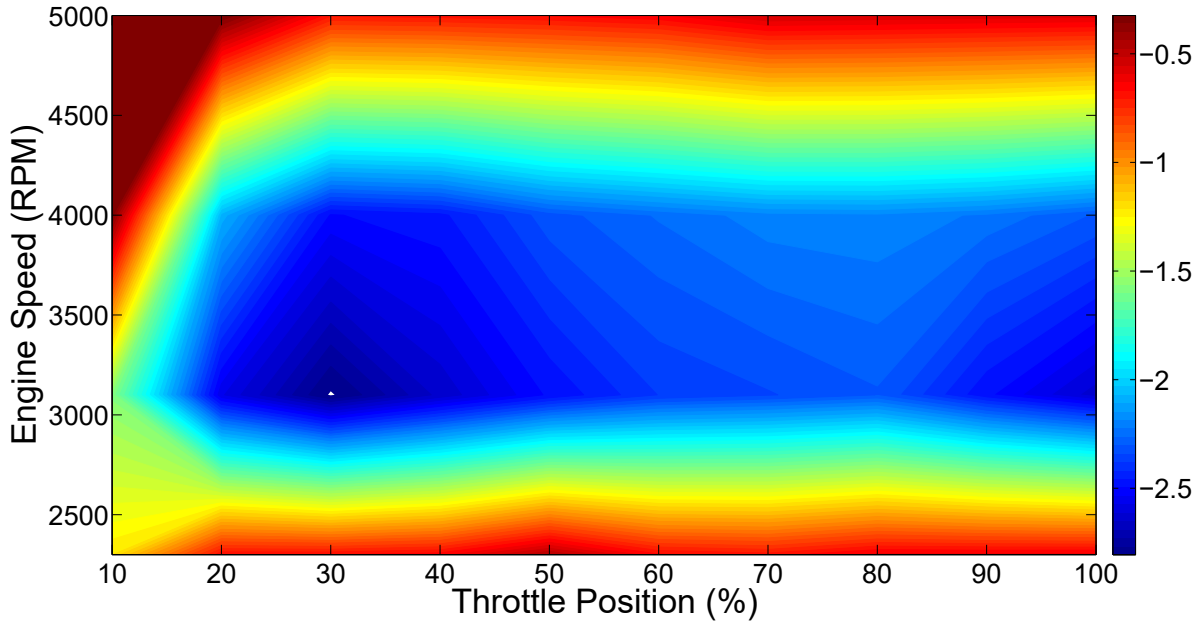


Figure 5.9: Negative acceleration peak (m/s^2) for CVT Powertrain

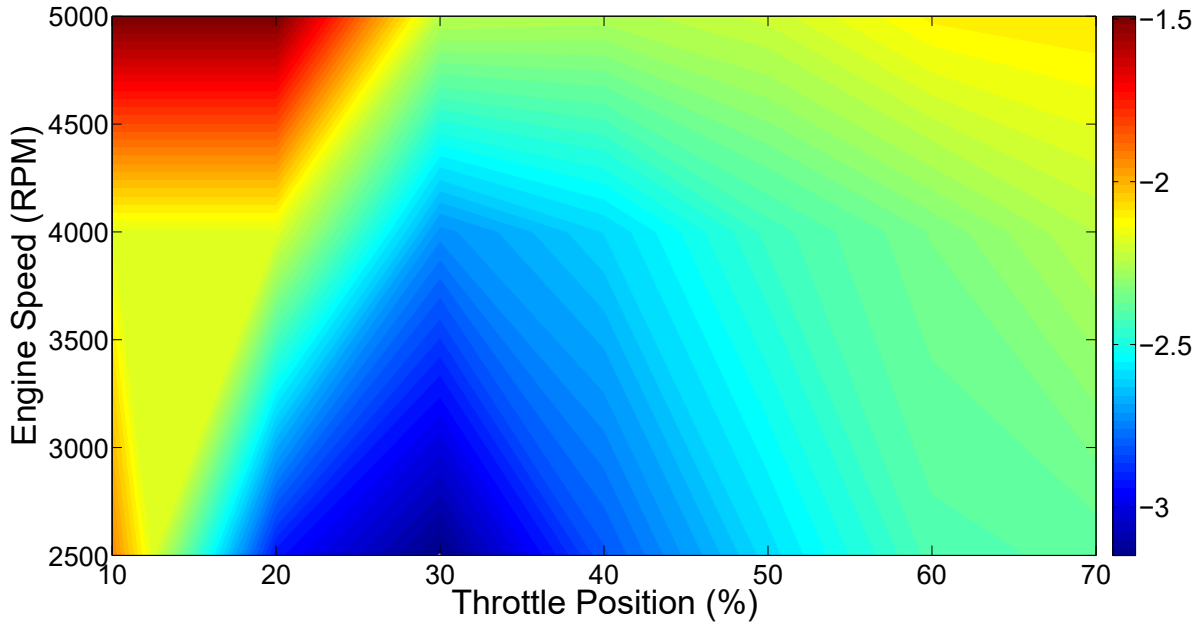


Figure 5.10: Negative acceleration peak (m/s^2) for MT Powertrain

peak is not desirable as it contributes to the jerk feeling (rate of change of acceleration). Figures 5.11 and 5.12 show the values of positive peak accelerations in m/s^2 for significant engine operating zones of both types of powertrain. The positive acceleration values are observed higher for higher throttle as in those cases the SI engine generates more torque output. The overall characteristics can be attributed to AFR tuning (shown in Figure 3.7).

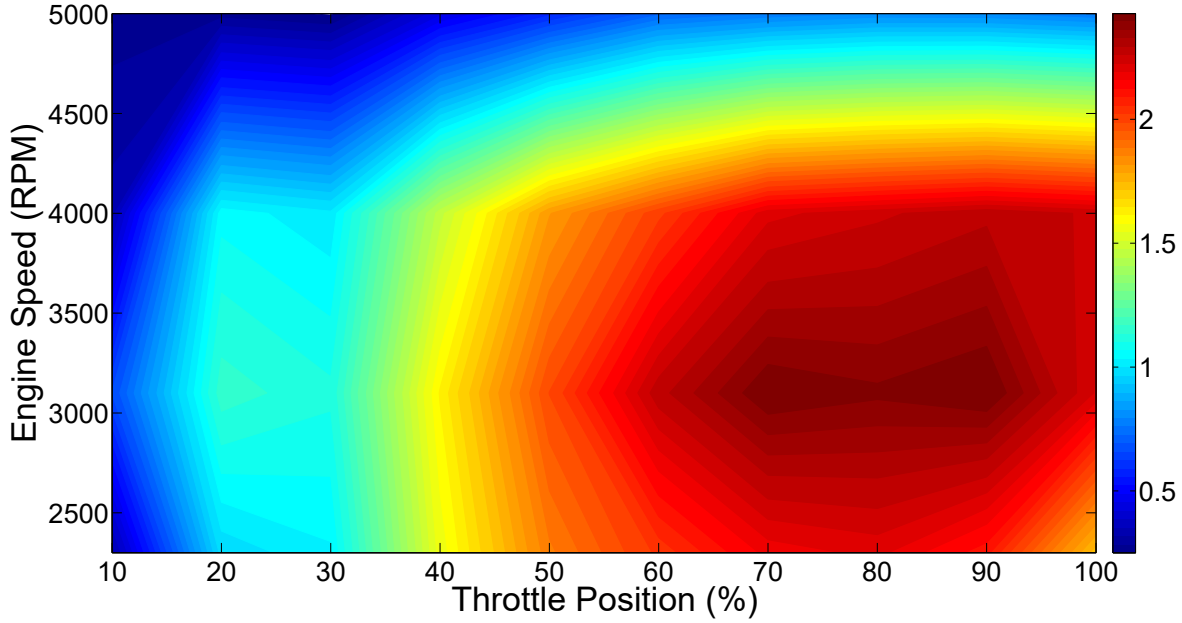


Figure 5.11: Positive acceleration peak (m/s^2) for CVT Powertrain

The acceleration oscillation (shown in Figure 5.1) can cause uncomfortable sensation due to the jerk pulses. Figures 5.13 and 5.14 show the distribution of the number of significant oscillations for the significant engine operating zones for both types of powertrain. The CVT powertrain shows significantly less numbers of oscillations due to smaller gear ratios compared to the MT powertrain for those operating points.

5.4.2 Tip in simulation for significant vehicle operating zones

In this section the tip in simulation is conducted with both types of powertrain configurations for two significant operating zones of the vehicle. The zones specified are selected from Figure 5.3.

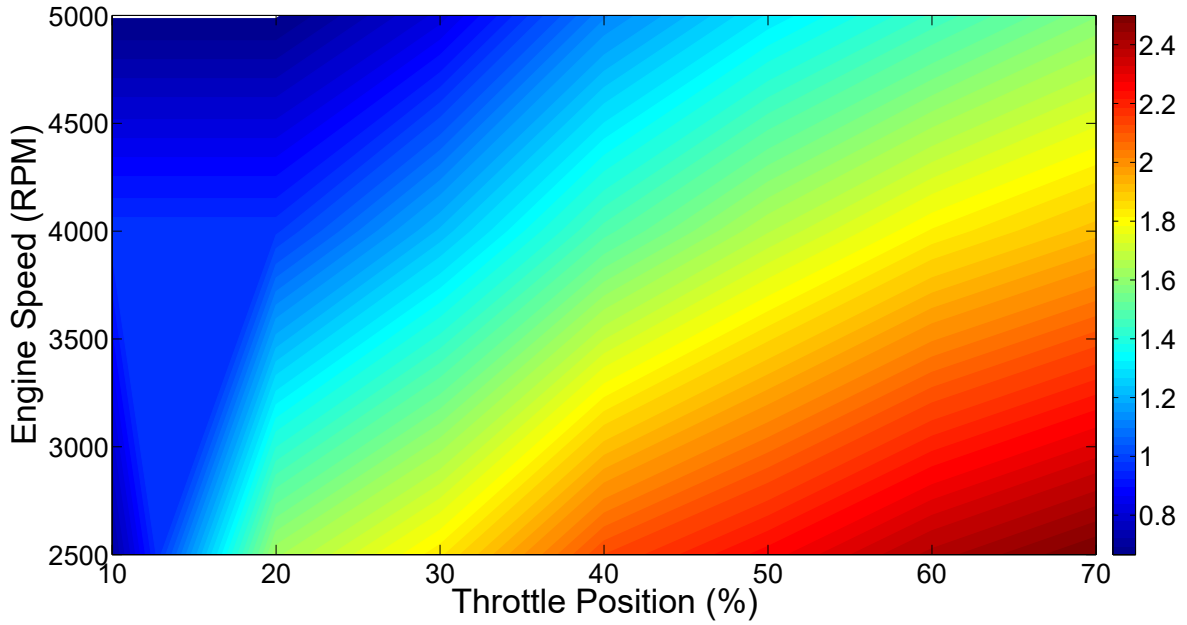


Figure 5.12: Positive acceleration peak (m/s^2) for MT Powertrain

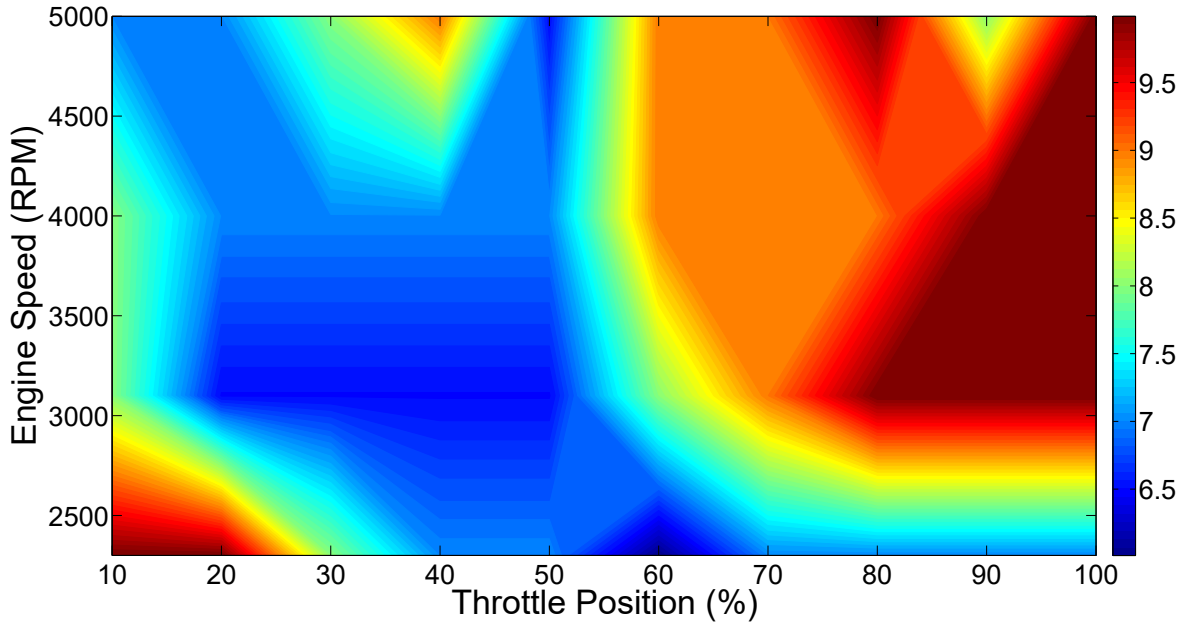


Figure 5.13: Acceleration oscillation for CVT Powertrain

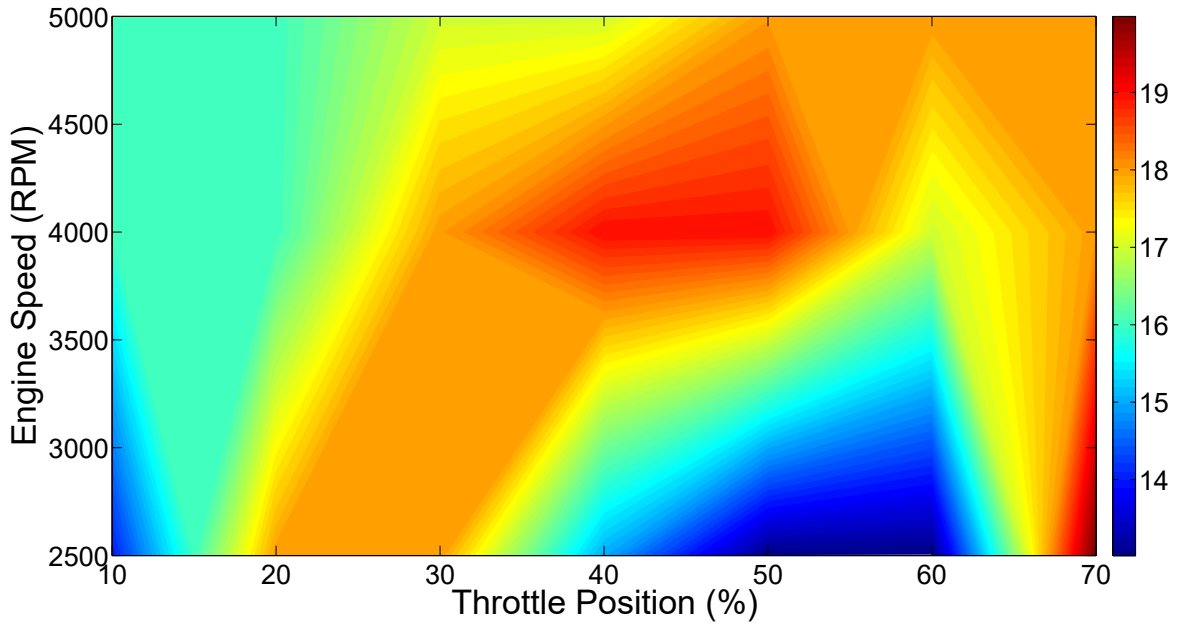


Figure 5.14: Acceleration oscillation for MT Powertrain

- zone 1 ($20\,\mathrm{km/h} < v < 24\,\mathrm{km/h}$) and ($15\,\mathrm{Nm} < \mathbf{T}_{wheel} < 20\,\mathrm{Nm}$)
- zone 2 ($24\,\mathrm{km/h} < v < 28\,\mathrm{km/h}$) and ($15\,\mathrm{Nm} < \mathbf{T}_{wheel} < 20\,\mathrm{Nm}$)

Figure 5.15 shows variation of four measurable parameters for drivability analysis. The most important observation is the significant reduction of the delay time compared to the tip in simulation explained in the previous section. This is due to the change of operating zone of the IC engine. In the previous section's tip in simulation, the engine torque requirement was low (green line in Figure 5.3). Therefore, the previous test could not cover all the operating points of the engine. As discussed in the previous section, the delay is caused by the manifold dynamics. The engine is operating in the mid throttle region for zone 1 and zone 2 ($\approx 45\,\%$) and it is calibrated with richer AFR (≈ 13). Since the delay time is insignificant ($\leq 50\,\mathrm{ms}$), the first negative acceleration is not exhibited and therefore it is not considered for drivability analysis. Instead of the first negative acceleration, the difference of the first positive peak and first negative peak acceleration is considered. The values of all three parameters (positive peak acceleration, peak to peak acceleration and number of significant oscillations) are higher for MT powertrain compared to CVT powertrain. The lower values of the three parameter imply better drivability as discussed in the previous section. The lower values of parameters for the

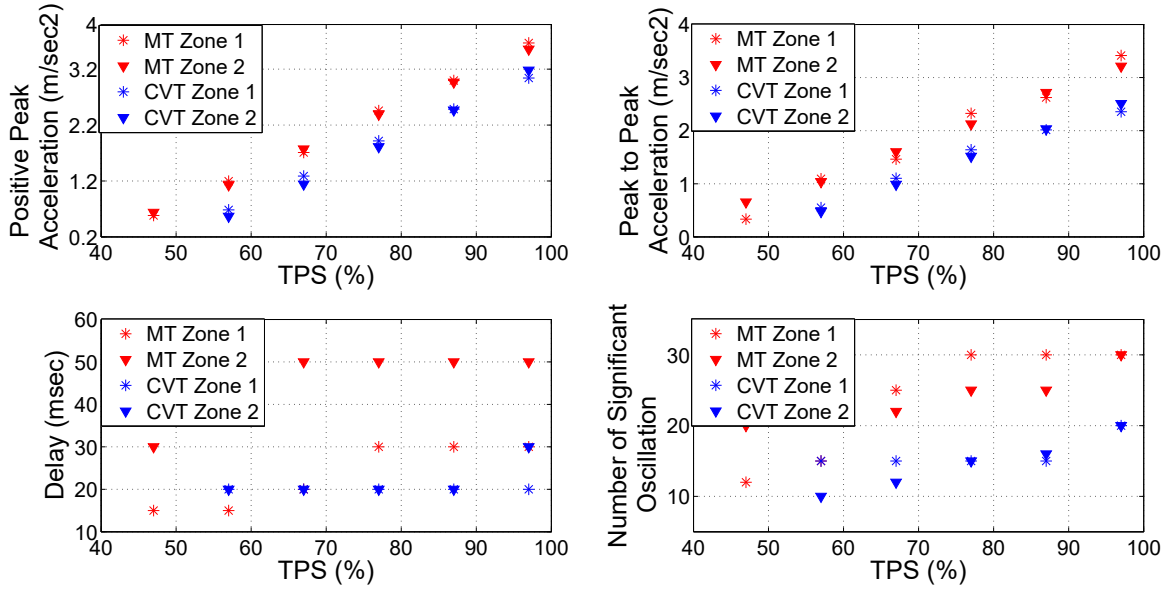


Figure 5.15: Drivability parameters for two significant operating zones of the vehicle

CVT can be attributed to its dynamic change of gear ratio to lower value (compared to the gear ratio values of the MT) during tip in.

5.4.3 Vehicle launch test

The vehicle launch simulation tests are conducted by opening different throttle openings (10 %, 20 %,... 80 %) while initially the vehicle is stationary and the IC engine is idle (throttle opening $\approx$ 5 %). For the MT powertrain, the clutch is initially disengaged, throttle is then opened to the tested amount and the clutch is then engaged according to the aggressive drive profile mentioned in Section 5.3.2 to launch the vehicle. For the MT (CVT) powertrain, the parameters are measured from the moment the clutch (centrifugal clutch) is engaged and vehicle starts moving. Therefore the launch tests are not influenced by the inlet manifold dynamics (leaning of AFR) of the IC engine. This operation is not a step torque request test unlike tip in, therefore it is not justified to consider the delay time parameter. Since the vehicle is stationary before starting of the test, the first negative peak acceleration does not exist in this operation. Therefore the positive peak acceleration and the number of significant oscillations are considered for evaluation of both powertrains. Figure 5.16 shows the variation of both parameters with

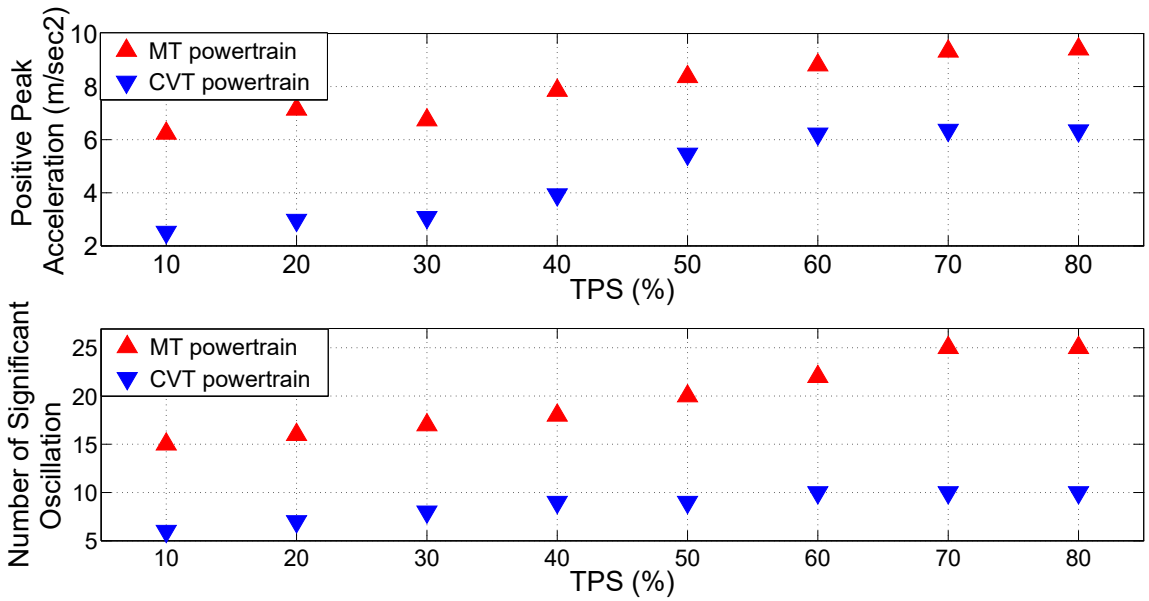


Figure 5.16: Drivability parameters for vehicle launch

different throttle openings. It is clearly evident from this figure that positive peak acceleration values and number of significant oscillations are less for CVT compared to MT which infers that the launch feeling for the CVT powertrain is better than the MT powertrain. This can be attributed to the working of the centrifugal clutch and dynamic change of gear ratio during vehicle launch for the CVT powertrain.

5.5 Conclusions

The chapter presents an objective drivability analysis for two types of existing powertrains by making use of the control-oriented model developed in Chapter 3. The control-oriented model consists of a mean value SI engine model capable of simulating in cylinder as well as crankshaft dynamics. The CVT and MT-based powertrain models are objectively analyzed for tip in and launch operation of the vehicle. The analysis shows that the CVT powertrain is more suitable for city driving conditions. Hence, the CVT system is considered for further works in multi-objective optimization and optimal control.

Chapter 6

Mathematical model of the electric machine and battery

6.1 Introduction

It is very essential to focus on the electric traction components of the motor-integrated powertrain. As mentioned in the previous chapter, the development of mathematical models of the powertrain components has far-reaching benefits for further work. The main components of electric traction are the electric drive system and battery. There are several types for both components. However, the brush-less direct current (BLDC) motor drive type and Li-Ion battery type are selected for this research, considering acceptance of both by the automotive industry [123]. In this chapter, the control-oriented models of the BLDC motor and Li-Ion battery are discussed in appropriate detail. Both the models are calibrated and tuned with experimental and simulation data from TVS Motor Company.

6.2 BLDC motor drive

The BLDC motor drive is very popular in the two wheeler automotive industry due to the following reasons [24]:

- Long operating life
- High dynamic response
- High efficiency
- Noiseless operation
- High speed range
- High torque-weight ratio
- Low cost-power ratio

BLDC motors are basically permanent magnet synchronous motors, which are driven by a DC voltage with the commutation achieved by solid state devices. The commutation instants are determined either by sensor or sensor-less techniques [25]. The BLDC motors can be compared with an inside-out DC motor because the armature is in the stator with the magnets in the rotor and their operating characteristics are similar to a DC motor [26]. The BLDC motors are subdivided into two types, based on the shape of the back EMFs: trapezoidal type and sinusoidal type. The shape of the back EMF depends on the shape of the rotor magnets and stator winding distribution. The trapezoidal and sinusoidal type BLDC motors should be supplied with quasi-square currents and sinusoidal type currents respectively for ripple free torque production. The trapezoidal type BLDC motor is selected for this research due to the following reasons [24–26]:

- a high resolution position sensor is not required
- simple construction
- lower price
- higher efficiency

The three-phase BLDC motor is operated by keeping two phases on, which produces

highest torque, with the third phase off. The phases are energized based on rotor position. The simplified scheme of the BLDC drive is shown in Figure 6.1.

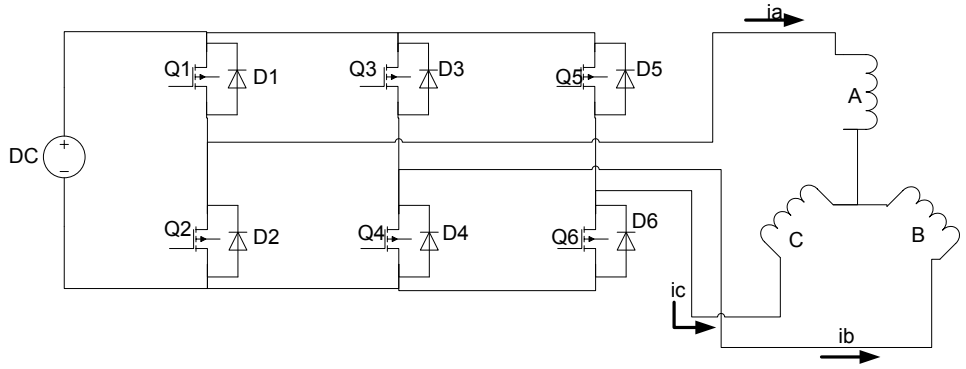


Figure 6.1: Simplified scheme of a BLDC drive system

6.2.1 Mathematical model of the BLDC motor

The three-phase star-connected BLDC motor can be described by the following dynamic equations

$$v_{ab} = R\left(i_a - i_b\right) + L\frac{d(i_a - i_b)}{dt} + e_a - e_b \tag{6.1}$$

$$v_{bc} = R\left(i_b - i_c\right) + L\frac{d(i_b - i_c)}{dt} + e_b - e_c \tag{6.2}$$

$$v_{ca} = R\left(i_c - i_a\right) + L\frac{d(i_c - i_a)}{dt} + e_c - e_a \tag{6.3}$$

$$T_e = k_f\omega_{motor} + J_{motor}\frac{d\omega_{motor}}{dt} + T_{load} \tag{6.4}$$

where v, i and e denote the phase to phase voltages, phase currents and phase back EMFs respectively for three phases a, b and c. The phase resistance R, phase inductance L, electrical torque T_e, load torque T_{load}, rotor inertia J_{motor}, friction constant k_f and rotor speed ω_{motor} are the other symbols used in the above equations. The back EMFs can be represented as

$$e_a = \frac{k_e}{2}\omega_{motor}F\left(\theta_e\right) \tag{6.5}$$

$$e_b = \frac{k_e}{2}\omega_{motor}F\left(\theta_e - \frac{2\pi}{3}\right) \tag{6.6}$$

$$e_b = \frac{k_e}{2}\omega_{motor} F\left(\theta_e - \frac{4\pi}{3}\right) \tag{6.7}$$

$$T_e = \frac{k_t}{2}\left[F\left(\theta_e\right) i_a + F\left(\theta_e - \frac{2\pi}{3}\right) i_b + F\left(\theta_e - \frac{4\pi}{3}\right) i_c\right] \tag{6.8}$$

The back EMF constant k_e, torque constant k_t, electrical angle θ_e are the symbols used in the above equations. The function $F\left(\cdot\right)$ gives the trapezoidal waveform of the back EMF. One period of $F\left(\cdot\right)$ can be expressed as

$$F\left(\theta_e\right) \approx \begin{cases} 1 & 0 \leq \theta_e < \frac{2\pi}{3} \\ 1 - \frac{6}{\pi}\left(\theta_e - \frac{2\pi}{3}\right) & \frac{2\pi}{3} \leq \theta_e < \pi \\ -1 & \pi \leq \theta_e < \frac{5\pi}{3} \\ -1 + \frac{6}{\pi}\left(\theta_e - \frac{5\pi}{3}\right) & \frac{5\pi}{3} \leq \theta_e < 2\pi \end{cases} \tag{6.9}$$

The dynamic equations (6.1), (6.2), (6.3) and (6.4) can be written in state space form for dynamic simulation. The number of equations can be reduced by using the following equilibrium relationship:

$$i_a + i_b + i_c = 0. \tag{6.10}$$

The dynamic equations (6.1), (6.2), (6.3) and (6.4) can be written as

$$v_{ab} = R\left(i_a - i_b\right) + L\frac{d(i_a - i_b)}{dt} + e_a - e_b, \tag{6.11}$$

$$v_{bc} = R\left(i_a + 2i_b\right) + L\frac{d(i_a + 2i_b)}{dt} + e_b - e_c. \tag{6.12}$$

The model can be expressed as

$$\begin{bmatrix} \dot{i_a} \\ \dot{i_b} \\ \dot{\omega_{motor}} \\ \dot{\theta_{motor}} \end{bmatrix} = \begin{bmatrix} -\frac{R}{L} & 0 & 0 & 0 \\ 0 & -\frac{R}{L} & 0 & 0 \\ 0 & 0 & -\frac{k_f}{J} & 0 \\ 0 & 0 & 1 & 0 \end{bmatrix} \begin{bmatrix} i_a \\ i_b \\ \omega_{motor} \\ \theta_{motor} \end{bmatrix} + \begin{bmatrix} \frac{2}{3L} & \frac{1}{3L} & 0 \\ -\frac{1}{3L} & \frac{1}{3L} & 0 \\ 0 & 0 & \frac{1}{J} \\ 0 & 0 & 0 \end{bmatrix} \begin{bmatrix} v_{ab} - e_{ab} \\ v_{bc} - e_{bc} \\ T_e - T_{load} \end{bmatrix} \tag{6.13}$$

$$\begin{bmatrix} i_a \\ i_b \\ i_c \\ \omega_{motor} \\ \theta_{motor} \end{bmatrix} = \begin{bmatrix} 1 & 0 & 0 & 0 \\ 0 & 1 & 0 & 0 \\ -1 & -1 & 0 & 0 \\ 0 & 0 & 1 & 0 \\ 0 & 0 & 0 & 1 \end{bmatrix} \begin{bmatrix} i_a \\ i_b \\ \omega_{motor} \\ \theta_{motor} \end{bmatrix} \tag{6.14}$$

The mathematical models of the electric machines are often transformed to a rotating frame of reference to reduce the computational load. There is no benefit for using this method here since the supply voltage is non sinusoidal [24–26].

6.2.2 Inverter

The inverter is an integral part of the BLDC drive system since it ensures commutation of the armature current. It can be implemented as a function of rotor position, the value of back EMF and whether the phase current is zero or non-zero [27]. Equation 6.13 shows that the inverter function needs to calculate the values of $v_{ab} - e_{ab}$ and $v_{bc} - e_{bc}$ which are inputs to the BLDC motor model. A detailed analysis was performed in [27] to derive the values of $v_{ab} - e_{ab}$ and $v_{bc} - e_{bc}$, which are expressed in Table 6.1. V_s represents DC voltage.

6.2.3 Simulation

The above-mentioned models of the BLDC motor and inverter were simulated. Since the physical prototypes of the particular motor is not available, the model is compared and calibrated

Table 6.1: Inverter Output Voltages [27]

θ_e	Diode Current	$v_{ab} - e_{ab}$	$v_{bc} - e_{bc}$
$0^o - 60^o$	$i_c \neq 0$	$V_s - e_a + e_b$	$-e_b + e_c$
	$i_c = 0$	$V_s - e_a + e_b$	$0.5(-V_s + e_a - e_b)$
$60^o - 120^o$	$i_b \neq 0$	$-e_a + e_b$	$V_s - e_b + e_c$
	$i_b = 0$	$0.5(V_s - e_a + e_c)$	$0.5(V_s - e_a + e_c)$
$120^o - 180^o$	$i_a \neq 0$	$-V_s - e_a + e_b$	$V_s - e_b + e_c$
	$i_a = 0$	$0.5(-V_s + e_b - e_c)$	$V_s - e_b + e_c$
$180^o - 240^o$	$i_c \neq 0$	$-V_s - e_a + e_b$	$-e_b + e_c$
	$i_c = 0$	$-V_s - e_a + e_b$	$0.5(V_s - e_a + e_b)$
$240^o - 300^o$	$i_b \neq 0$	$-e_a + e_b$	$-V_s - e_b + e_c$
	$i_b = 0$	$0.5(-V_s - e_a + e_c)$	$0.5(-V_s - e_a + e_c)$
$300^o - 360^o$	$i_a \neq 0$	$V_s - e_a + e_b$	$-V_s - e_b + e_c$
	$i_a = 0$	$0.5(V_s + e_b - e_c)$	$-V_s - e_b + e_c$

with the simulated data available from TVS Motor Company. The simulated data is generated using 3D motor simulation packages. Figure 6.2 shows the comparison between the torque output generated by the developed model with the above-mentioned simulation data. The model shows good correlation with the data.

Figure 6.3 shows the efficiency contour of the BLDC machine in the first quadrant operation. The efficiency contour is the same for the second quadrant operation. Since the machine is mounted on two wheeler vehicle, it never operates in the other two quadrants. The motor efficiency decreases considerably in the full load condition due to higher copper losses. The motor operation is not stable for low speed operation (< 500 RPM). The operating area provides information about the feasible values of primary gear ratio for vehicle application.

6.3 Li-Ion Battery

Li-Ion battery is very popular for two wheeler traction applications compared to the lead-acid battery type due to the following reasons:

- Long operating life
- Higher ratio of energy to weight
- High efficiency during charging and discharging (approximately 95%)

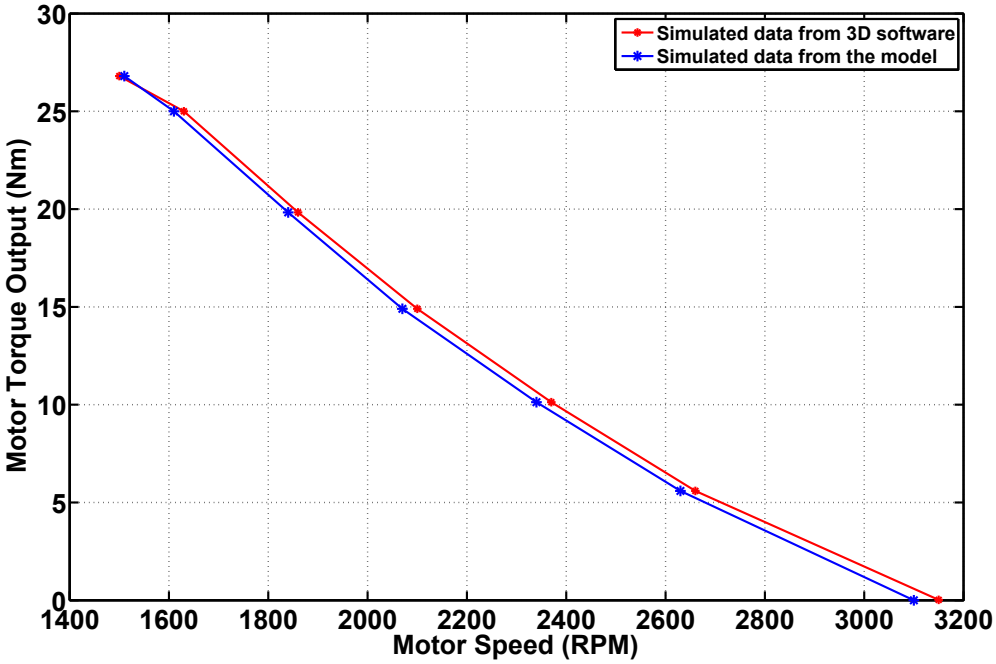


Figure 6.2: Comparison of peak torque output data between developed model and simulation data available from TVS Motor Company

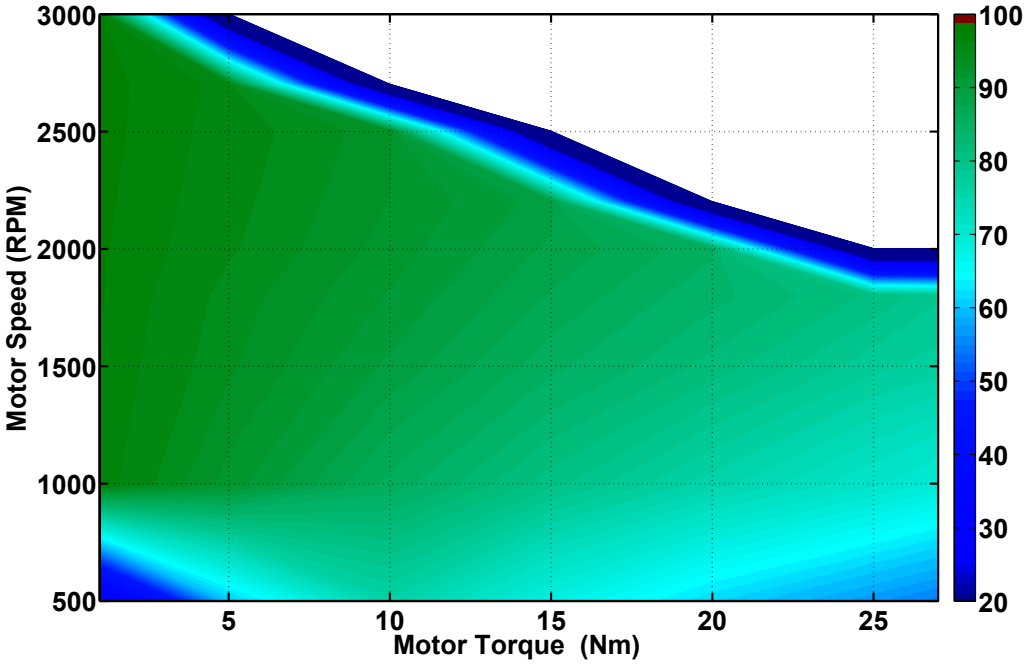


Figure 6.3: Efficiency η_{EM} contour for the BLDC motor in first quadrant

- Better time constant

The other battery technologies were not considered in consultations with TVS Motor Company due to unavailability of cost-effective production-ready technologies. Although the lead-acid battery type has lower price and lower sensitivity to temperature compared to Li-Ion battery, the overall advantages of Li-Ion battery make it more suitable for future two wheeler traction application.

6.3.1 Mathematical model

Significant works have been done for the development of control-oriented mathematical models for batteries [28–34]. The battery models can broadly divided into three categories:

- Experimental
- Electrochemical
- Electric circuit-based

It has been noted that the experimental and electrochemical models are not suitable for representing the cell dynamics for SOC calculation for the present work due to computational issues. Shepherd developed an equation to describe the electrochemical behavior of a battery directly in terms of terminal voltage, open circuit voltage, internal resistance, discharge current and state-of charge [28, 29, 31], and this model is applied for discharge as well as for charge. A modified version of the Shepherd model has been used in [28, 29]. This modification consists on using a polarisation voltage instead of a polarisation resistance in order to remove the algebraic loop problem [28–34].

6.3.2 Expressions for Li-Ion battery model

The battery model can be subdivided in charging and discharging model [28–34]. The discharge model for Li-Ion battery can be expressed as below [28, 29]. This model is the modified version

of the Shepherd model, namely

$$V_{batt} = E_0 - R \cdot i_{batt} - K\frac{Q}{Q - i_{batt}t} \cdot (i_{batt}t + i^*) + A\exp(-B \cdot i_{batt}t). \tag{6.15}$$

Battery voltage V_{batt}, battery constant voltage E_0, polarization constant K, battery capacity Q, actual battery charge $i_{batt}t$ ($\int i_{batt}dt$), exponential zone amplitude A, exponential zone time constant inverse B, internal resistance R, battery current i_{batt} and filtered battery current i^* are the parameters used in (6.15)

Similarly the charging model can be expressed as [28, 29]

$$V_{batt} = E_0 - R \cdot i_{batt} - K\frac{Q}{-0.1 \cdot Q + i_{batt}t} \cdot i^* - K\frac{Q}{Q - i_{batt}t} \cdot (i_{batt}t + A\exp(-B \cdot i_{batt}t). \tag{6.16}$$

6.3.3 Simulation results

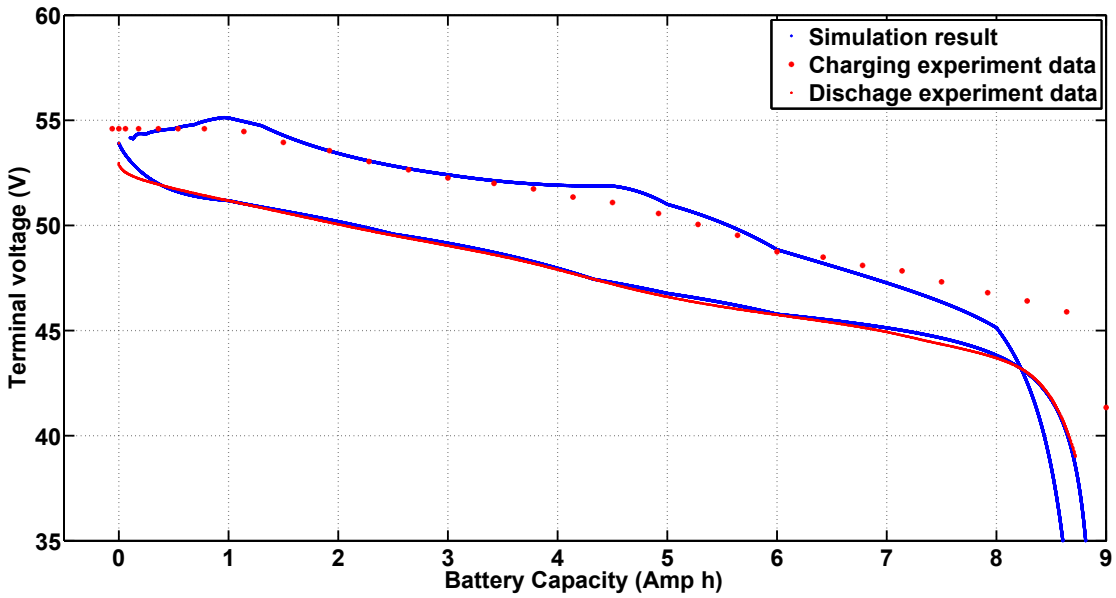


Figure 6.4: Charge and Discharge plot for Li-Ion Battery

The above model is implemented and calibrated using test data on a 48 V, 9 Ah battery from TVS Motor Company. Figure 6.4 shows the comparison of discharge and charge test data with simulation results. The battery is discharged with constant current of $9A$ and charged

with 0.5 A. The charging current of 0.5 A is the maximum allowable charging current specified by the manufacturer. The Figure 6.4 shows close a relation between test and simulation results for most of the operating area of the battery.

6.4 Conclusions

This chapter presented dynamic mathematical models of

- a BLDC motor with inverter.
- a Li-Ion battery.

Both of these models are very crucial for optimal control and multi-objective optimization presented in subsequent chapters.

Chapter 7

Integrated simulation for parallel hybrid configuration

7.1 Introduction

The proposed motor-integrated powertrain can be realized in multiple configurations with respect to the location of the electric machine inside the powertrain. Two possible placement location possibilities of the electric machine suitable for the two wheeler platform are:

- integration of a low torque and high speed electric machine on the crankshaft of the SI engine;
- integration of a high torque and low speed electric machine on the wheel hub of the vehicle.

Although this research targets the scooter platform of a two-wheeled vehicle, it is essential to consider design constraints for the motor cycle platform for future hybridization. In the case of the second option, the possible integration on a motor cycle platform is challenging due to the wheel construction. Moreover, with the first option, the same electric machine may be used as an integrated starter and generator for the vehicle. Hence, it is logical to choose the first option for this research. This chapter discusses some of the initial results of the integrated simulation

of the motor-integrated powertrain with the first option for CVT and MT transmissions. The simulation is performed for IDC keeping different levels of electric traction assist to understand the response of different parameters. The BLDC motor is integrated in-between the primary gear and clutch system since it allows the BLDC motor to operate in its operating zone (as shown in Figure 6.3) during IDC simulation. The simulation assumes that the Li-Ion battery is fully charged externally. The equivalent fuel consumption for the battery discharge is not considered during this simulation.

7.2 Parallel hybrid configurations with CVT and MT powertrains

The parallel hybrid configurations are shown in Figures 7.1 and 7.2 for CVT and MT transmissions respectively. The BLDC machine is integrated directly over the power-flow path without any other arrangement due to packaging constraints of the powertrain. The placement of the primary gear is very much crucial as otherwise the BLDC machine could not be operated in its feasible operating area. Initially the BLDC motor is connected directly on the engine crankshaft, which results in deterioration of fuel consumption of the hybrid configurations w.r.t. to the original powertrain. This is due to the mismatch of the operating zone of the BLDC machine. Hence, the BLDC machine is placed after the primary gear. Both the powertrains are subjected with three different levels of motor assist during this simulation (10 %, 50 % and 90 %) for the full duration of the IDC drive simulation. The driver model which has been explained in Chapter 4 controls the throttle, brake and gears (in the case of the MT powertrain) as shown in Figures 7.1 and 7.2.

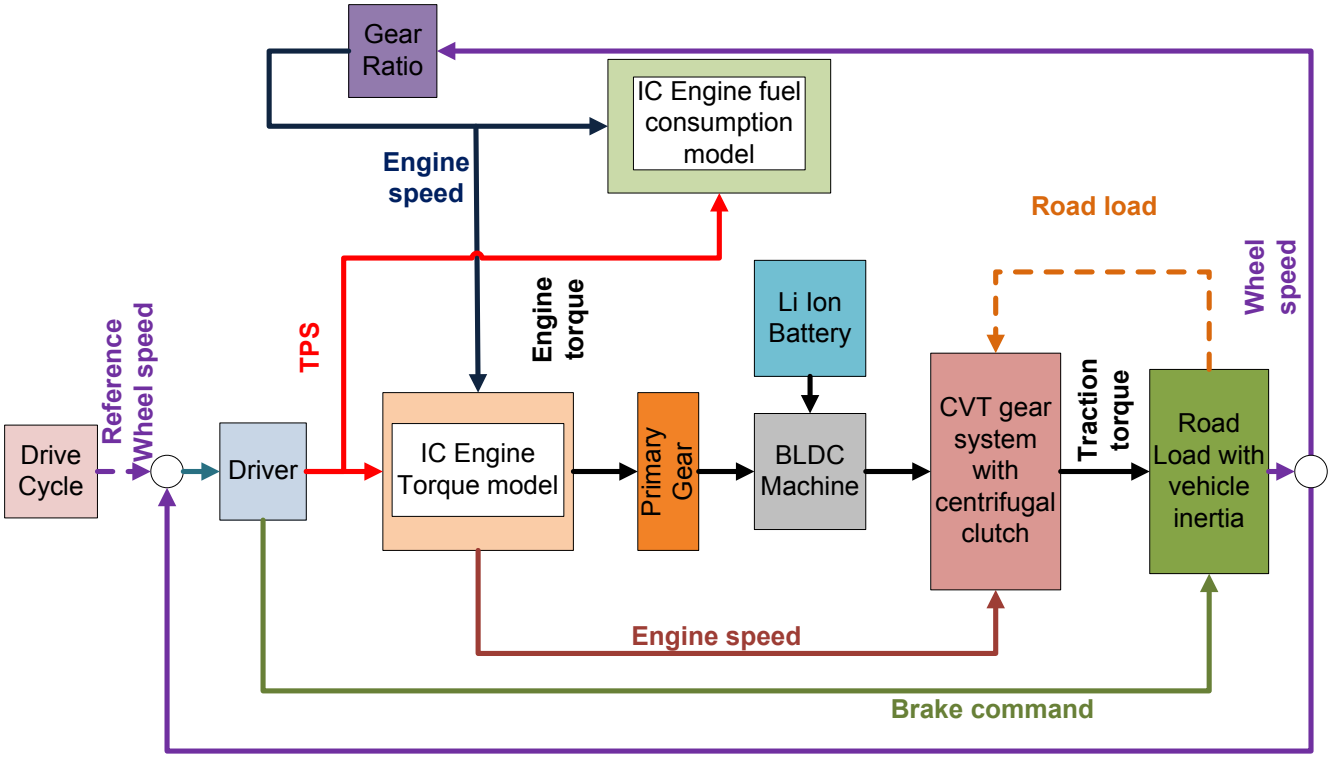


Figure 7.1: Block diagram of Parallel hybrid vehicle with CVT

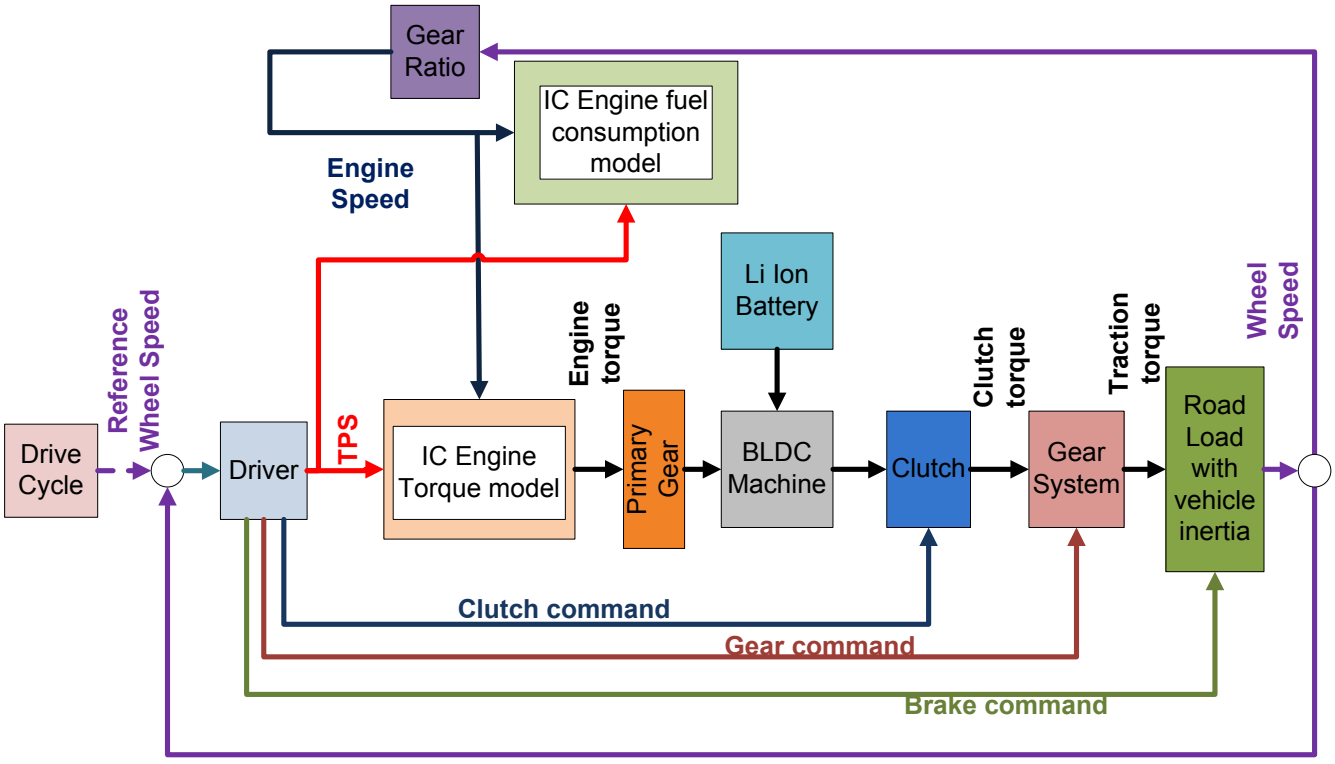


Figure 7.2: Block diagram of Parallel hybrid vehicle with MT

7.3 Simulations of the CVT powertrain

Figures 7.3 - 7.7 show variations of engine speed, fuel consumption, throttle position, brake position and CVT gear ratio during the IDC simulations. The most promising is the fuel consumption. The simulation shows that the fuel consumption decreases by 71 % by integrating the BLDC motor and fully charged Li-Ion battery. This can be realized by observing the throttle opening for different conditions in Figure 7.5. This parameter controls the fuel flow inside the IC engine. It can be observed that the required throttle openings are almost zero for 50 % and 90 % assist of the BLDC motor which means that the propulsion power is provided by the BLDC motor. Since the BLDC motor is coupled mechanically to the IC engine, the engine speed parameter is influenced by the torque output of the BLDC motor rather than the IC engine. The higher brake force (for 50 % and 90 % assist) from Figure 7.6 shows that the available power from the BLDC machine is more than the required wheel force for the IDC. The CVT ratio is influenced by the brake force (for 50 % and 90 % assist) rather than the wheel torque. This is due to the fact that the CVT ratio is the function of input speed and wheel torque.

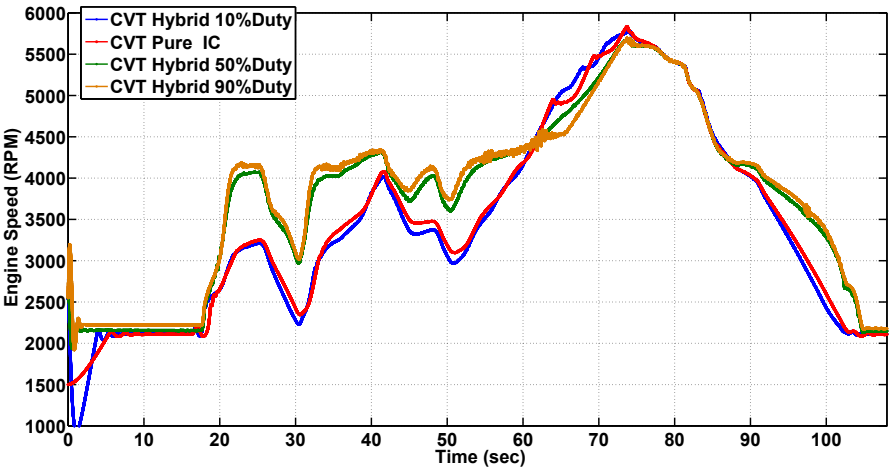


Figure 7.3: Engine speed variation for different hybrid assist in IDC

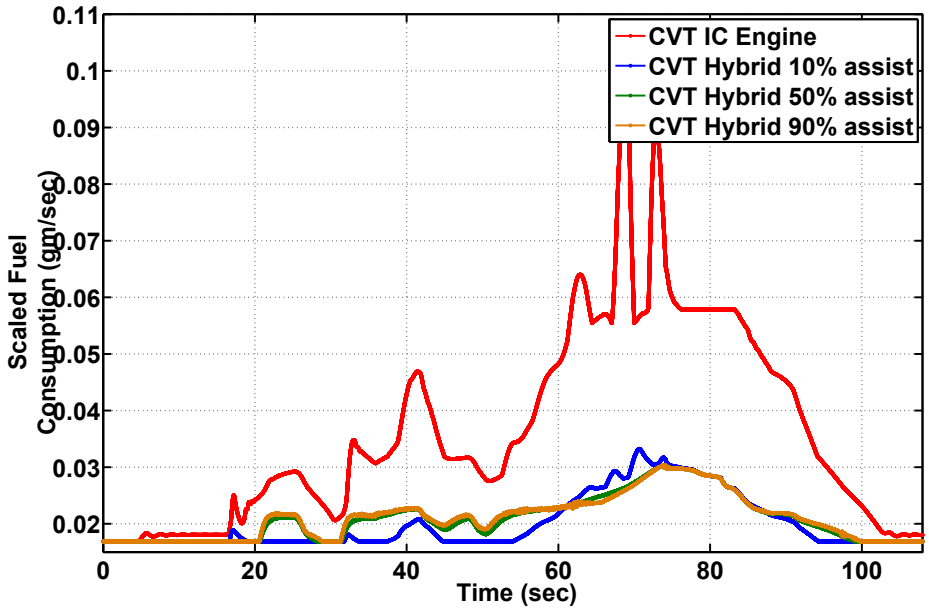


Figure 7.4: Fuel consumption variation for different hybrid assist in IDC

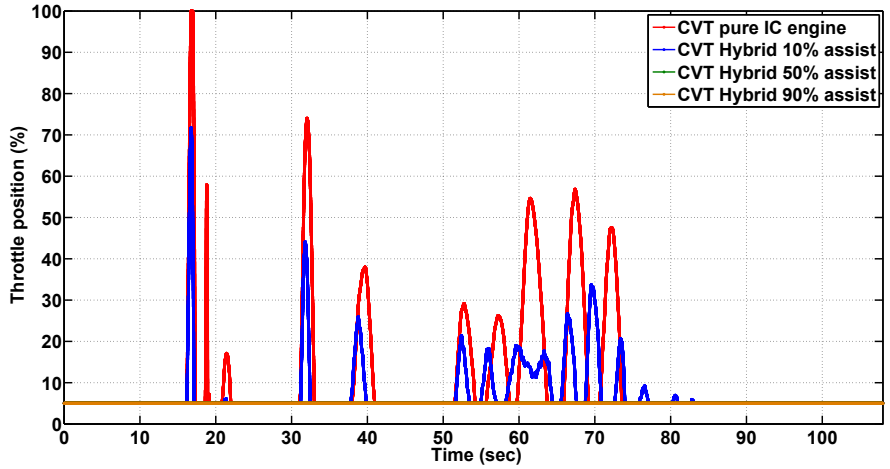


Figure 7.5: Throttle opening variation for different hybrid assist in IDC

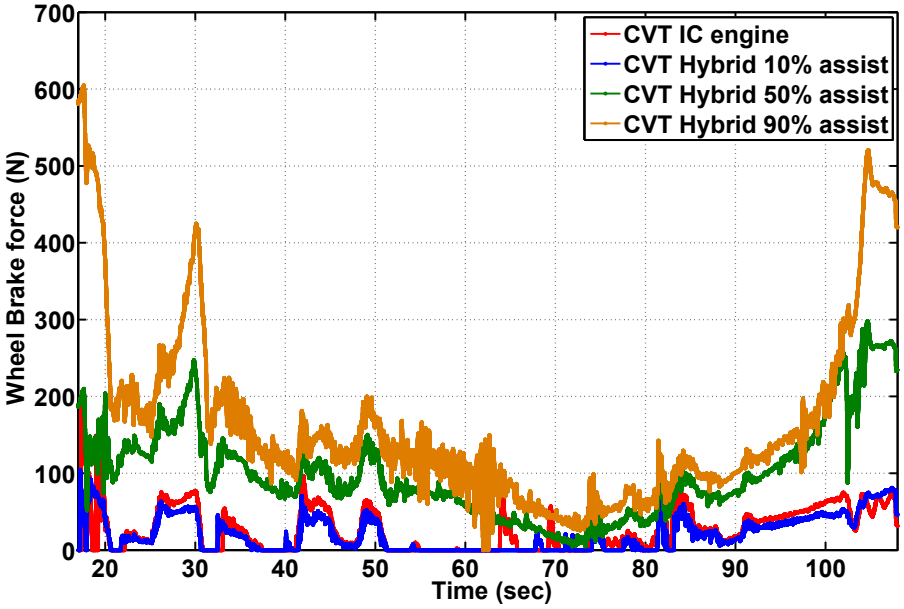


Figure 7.6: Brake force variation for different hybrid assist in IDC

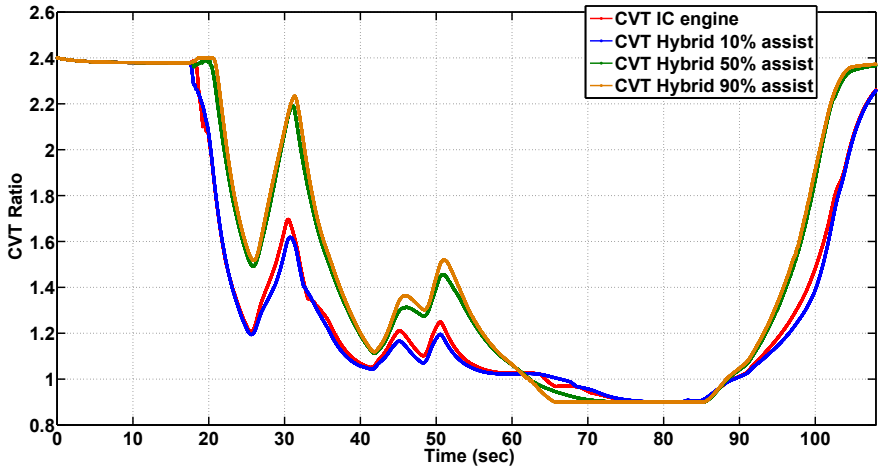


Figure 7.7: CVT ratio variation for different hybrid assist in IDC

7.4 Simulations of the MT powertrain

The Figures 7.8 - 7.11 show variations of engine speed, fuel consumption, throttle position and brake position during the IDC simulations. However, the simulation lags a rule based driver model to identify different operating region of the drive cycle (for example, the vehicle idle condition). Hence, it would be logical to consider the fuel consumption results during non-idle driving condition only. The simulation shows that the fuel consumption decreases by 71 % by integrating the BLDC motor and fully charged Li-Ion battery for non-idle driving condition. This can be realized by observing the throttle opening for different conditions in Figure 7.10. The throttle and brake signals show a lot of variations during the gear change due to the structure of the driver model. If the throttle signal is observed closely, it can be observed that the average value of throttle decreases with BLDC motor assist.

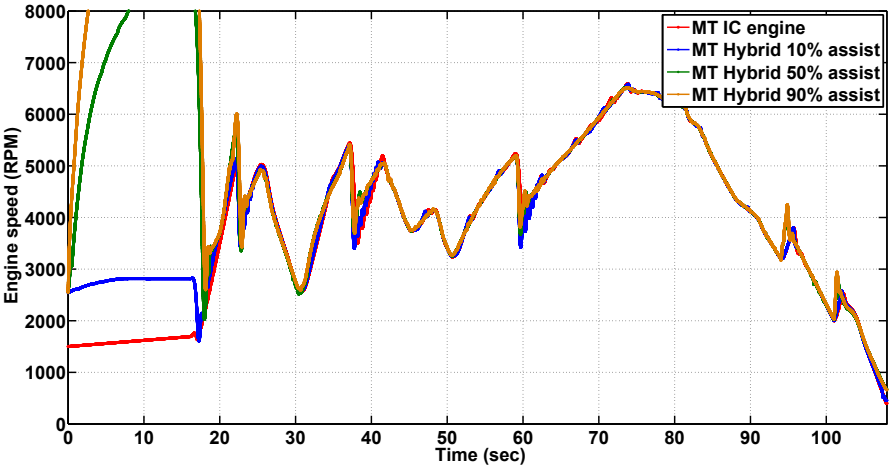


Figure 7.8: Engine speed variation for different hybrid assist in IDC

It can be observed that the required throttle openings are almost zero (except during gear shift) for 50 % and 90 % assist of the BLDC motor which means that the greater part of the propulsion power is provided by the BLDC motor. Since the BLDC motor is coupled mechanically to the IC engine, the engine speed parameter is influenced by the torque output of the BLDC motor rather than the IC engine (in case of 50 % and 90 % assist of the BLDC motor). The engine speed reaches a very high value during neutral gear position (initial 16 sec of the drive cycle) as the BLDC motor was operating during this period. Since the IC engine

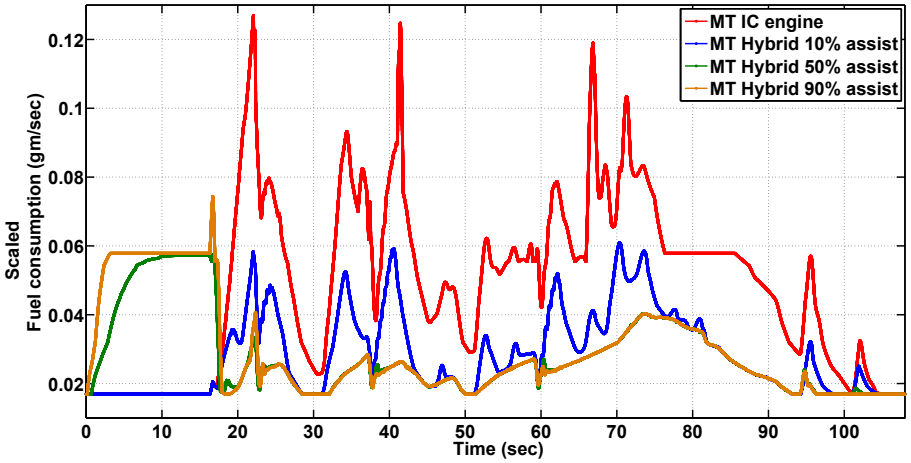


Figure 7.9: Fuel consumption variation for different hybrid assist in IDC

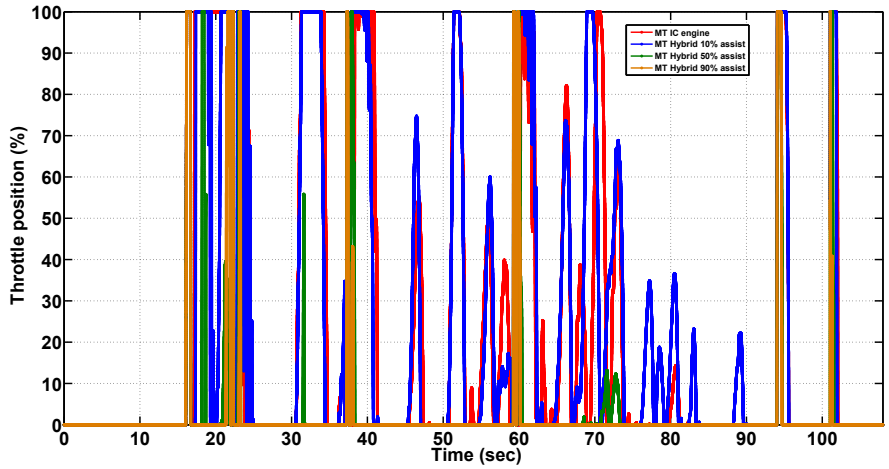


Figure 7.10: Throttle opening variation for different hybrid assist in IDC

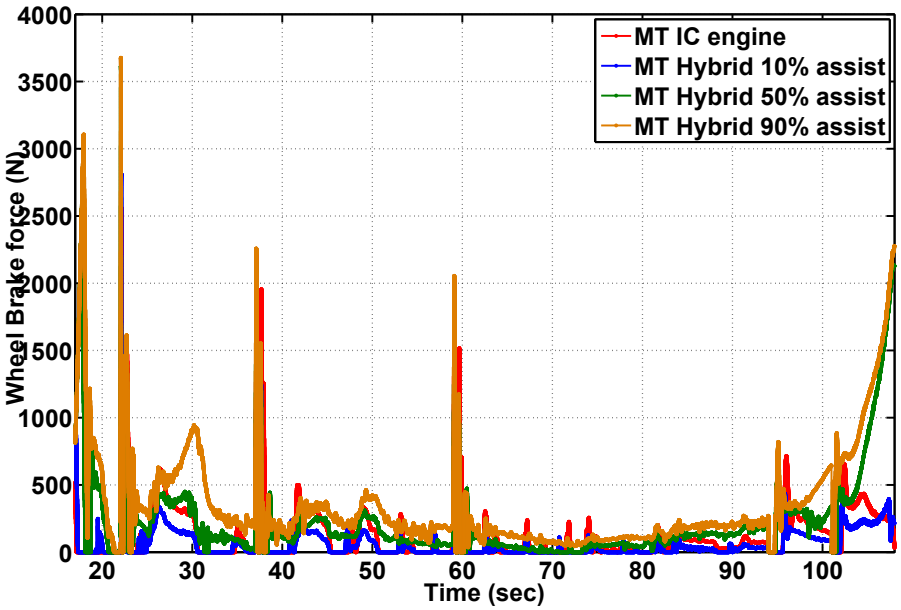


Figure 7.11: Brake force variation for different hybrid assist in IDC

fuel metering is achieved by the carburetor, the fuel consumption increases during this initial 16 sec duration of the drive cycle. The brake signals from Figure 7.11 show that the available power from the BLDC machine is excessive (for 50 % and 90 % assist) for the IDC.

7.5 Conclusions

The above simulations shows the interaction of different powertrain parameters which gives good confidence about the full hybrid powertrain in terms of stable simulation. The improvement of the fuel consumption can be calculated considering the equivalent fuel consumption for battery discharge with the electric assist. Since the power rating of the existing BLDC machine (approximately 60 % of the peak power of IC engine) is quite high for this application, the fuel consumption shows a very drastic improvement. This drastic improvement cannot be considered as a final result without considering the equivalent fuel consumption. Moreover, integration of this machine may not be feasible in the actual powertrain prototype. The total powertrain model can be used for the formulation of an optimal control problem for the optimal sizing of the electric traction components.

Chapter 8

Control-oriented model for optimal control

8.1 Introduction

The previous chapters presented detailed models for the motor-integrated powertrain. However, these models are very complex and not suitable for numerical optimal control and multi-objective optimization. Hence, it is very important to simplify the models. These control-oriented models ensure that the respective mathematical functions are continuous and differentiable. The models presented in the earlier chapters are adopted to generate the necessary characteristics for the control-oriented models.

8.2 Dynamic model for the vehicle powertrain

The dynamic model for the proposed motor-integrated powertrain incorporates the following features:

- A BLDC machine coupled to the IC engine crankshaft powered by a Li Ion battery.
- A CVT system coupled with the IC engine / BLDC machine. The gear actuation system

for the CVT system is considered to be controlled by the controller. This would ensure an additional control variable for the optimal control of the motor-integrated powertrain.

Figure 7.1 represents the block diagram of the parallel hybrid powertrain that is considered in this work. The proposed control-oriented model is simplified version of one in Figure 7.1 to reduce the resources of calculation.

The dynamic model for the power transfer can be expressed from first principles,

$$\left[\left(J_w + m_{vehicle}R_w^2 + G^2(J_{engine} + J_{rotor})\right)\right]\dot{\omega_w} = G(T_{ICE} + T_{EM}) - (m_{vehicle}\dot{v} + C_{aerodynamic}v^2 + C_{rollingfriction} + F_{Brake})R_w \quad (8.1)$$

$$\Rightarrow \left(J_w + m_{vehicle}R_w^2 + G^2(J_{engine} + J_{rotor})\right)\frac{\dot{v}}{R_w} = G\left[\frac{P_{ICE} + P_{EM}}{\omega_{engine}}\right] - (m_{vehicle}\dot{v} + C_{aerodynamic}v^2 + C_{rollingfriction} + F_{Brake})R_w \quad (8.2)$$

$$\Rightarrow \dot{v} = \frac{R_w^2}{J_w + 2m_{vehicle}R_w^2 + G^2(J_{engine} + J_{rotor})}\left[\frac{P_{ICE} + P_{EM}}{v} - (C_{aerodynamic}v^2 + C_{rollingfriction} + F_{Brake})\right] \quad (8.3)$$

where J_w is the moment of inertia of the wheel, $m_{vehicle}$ is the mass of the vehicle, R_w is the dynamic radius of the wheel, G is gear ratio, J_{engine} is the moment of inertia of the IC engine, J_{rotor} is the moment of inertia of the electric machine, ω_w is the rotational speed of the wheel, T_{ICE} is the IC engine torque, T_{EM} is the electric machine torque, v is the linear vehicle speed, $C_{aerodynamic}$ is the parameter for air drag loss, $C_{rollingfriction}$ is the parameter for rolling friction loss, F_{Brake} is the brake force, P_{ICE} is the IC engine power and P_{EM} is the electric machine power.

8.2.1 Battery

The electrochemical models for a Li-Ion battery as proposed by [28–30] are very much suitable for system level simulation. However, these models are not suitable for optimal control design because they involve a discontinuous mathematical function. The Li-Ion battery can be modeled as an open circuit voltage source with and internal resistance [124]. The $S\dot{O}C$ can be expressed as follows:

$$S\dot{O}C = -\frac{U_0 - \sqrt{{U_0}^2 - 4R_i\frac{P_{EM}}{\eta_{EM}}}}{2R_iQ_{Battery}} \tag{8.4}$$

$$\Rightarrow S\dot{O}C = -\frac{U_0 - U_0\sqrt{1 - 4R_i\frac{P_{EM}}{{U_0}^2\eta_{EM}}}}{2R_iQ_{Battery}} \tag{8.5}$$

Using test data from TVS Motor Company, $\frac{4R_i}{{U_0}^2\eta_{EM}} = 8.66*10^{-5}$ guaranteeing $\left|\frac{4R_i}{{U_0}^2\eta_{EM}}P_{EM}\right| < 1$. Therefore using a Taylor expansion

$$\Rightarrow S\dot{O}C = -\frac{U_0 - U_0(1 - 2R_i\frac{P_{EM}}{{U_0}^2\eta_{EM}})}{2R_iQ_{Battery}} \tag{8.6}$$

$$\Rightarrow S\dot{O}C = -\frac{P_{EM}}{\eta_{EM}U_0Q_{Battery}} \tag{8.7}$$

where SOC is the state of charge of the battery, U_0 is the open circuit voltage of the battery, R_i is the internal resistance of the battery, η_{EM} is the electric machine efficiency and $Q_{Battery}$ is the battery capacity. The Taylor expansion is limited to first order, as the values of the higher order terms for $\left|\frac{4R_i}{{U_0}^2\eta_{EM}}P_{EM}\right|$ would be negligible. η_{EM} is derived from the detailed model presented in Chapter 6 according to Figure 6.3.

8.2.2 IC Engine

The detailed mathematical model for an IC engine consists of many mathematical discontinuities. The IC engine model can be simplified using the Willans line approach [124, 125]. This describes an approximate linear relationship between brake mean effective pressure and fuel consumption of an IC engine. The Willans line model can be modified to represent the IC

engine power with the fuel consumption as

$$\dot{m}_f = \frac{V_d p_{mi} \omega_{engine}}{4\pi H_v \eta_{combustion}} + \frac{P_{ICE}}{H_v \eta_{combustion}} \tag{8.8}$$

where m_f is mass flow of fuel inside the IC engine, V_d is the displacement volume of the IC engine cylinder, ω_{engine} is the rotational speed of the engine, H_v is the lower heating capacity of gasoline, $\eta_{combustion}$ is the combustion efficiency and p_{mi} is the frictional loss of the IC engine.

Figures 8.1 and 8.2 provide information of $\eta_{combustion}$ and p_{mi} for the full operating zone of

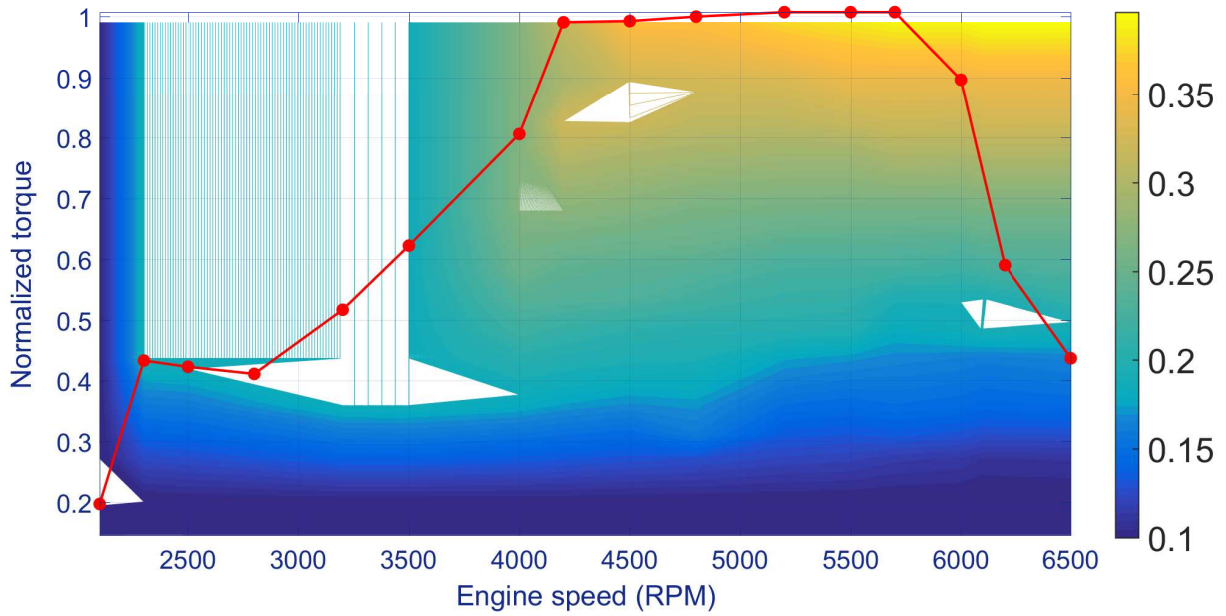


Figure 8.1: $\eta_{combustion}$ as a function of ω_{engine} and T_{ICE} with the maximum torque line (in red colour). The white colour region is without data

the IC engine. The maximum produced torque information is embedded into Figure 8.1, which serves as one of the bounds in the optimization framework. This information is derived from the detailed model presented in Chapter 3.

8.2.3 Reference vehicle speed

The reference vehicle speed is a horizon trajectory with respect to which the optimal control problem is solved. In this work, the reference vehicle speed is considered from a drive cycle. The

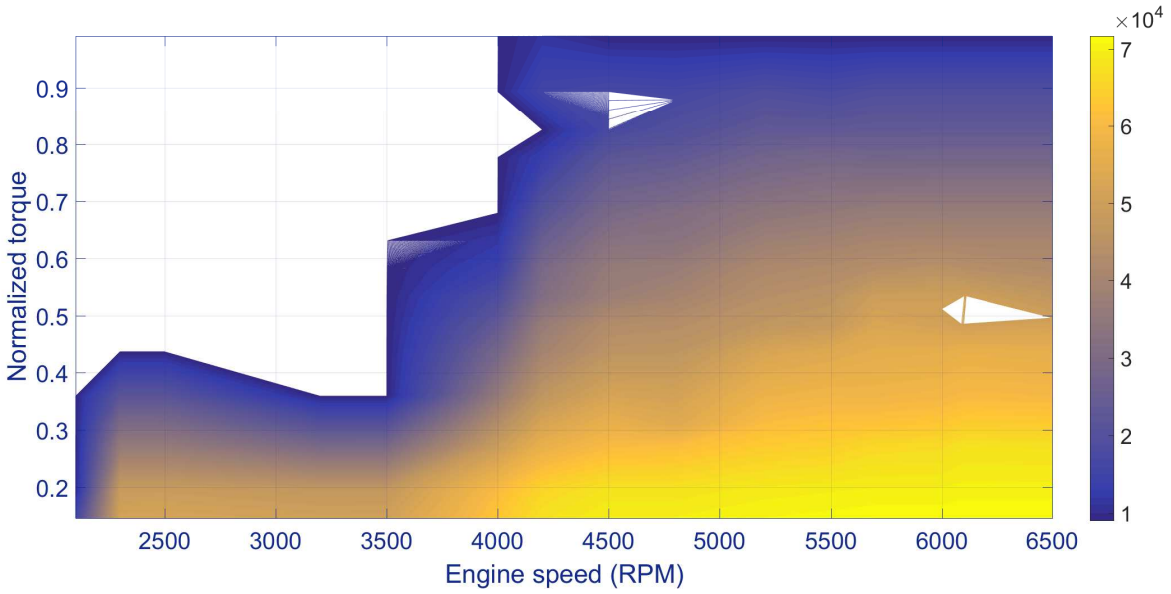


Figure 8.2: p_{mi} as a function of ω_{engine} and T_{ICE}

error between the reference vehicle speed and actual vehicle speed is considered as a state:

$$v_{error} = v_{drivecycle} - v \tag{8.9}$$

where $v_{drivecycle}$ is the reference vehicle speed and v_{error} is the error between actual vehicle speed and reference vehicle speed.

8.2.4 Gear shift and engine speed

The powertrain is coupled with a CVT system due to the benefit in drivability as observed in Chapter 5. The complex model of the CVT is simplified with a first-order delay system with a control variable G_{set}, which is the reference gear position and state G (as defined in (8.1)):

$$\dot{G} = \frac{1}{\tau_{Geardelay}}(G_{set} - G) \tag{8.10}$$

where $\tau_{Geardelay}$ is the delay caused by the CVT system. The dynamic equation for the state ω_{engine} can be expressed as a function of v and G. It is very much essential that the feasible area for optimal control is also dependent on the bounds of the variable ω_{engine}. Hence the

variable ω_{engine} is defined as a state in the formulation

$$\dot{\omega}_{engine} = \frac{1}{R_w}(v\dot{G} + G\dot{v}). \tag{8.11}$$

8.3 State and Control vector for optimal control problem formulation

The dynamic equations (8.3), (8.7), (8.8), (8.9), (8.10) and (8.11) can be collected together to represent the states X and control signals U for the dynamic system in vector format:

$$X = \begin{bmatrix} v \\ SOC \\ m_f \\ v_{error} \\ G \\ \omega_{engine} \end{bmatrix}, U = \begin{bmatrix} G_{set} \\ P_{ICE} \\ P_{EM} \\ F_{Brake} \end{bmatrix}. \tag{8.12}$$

The above-mentioned dynamic models are suitable for the further work on optimal control design to minimize fuel consumption or/and exhaust emission or/and battery charge sustainability. The higher order dynamics of the powertrain are not essential to consider during the design, since the design objective does not intend to address them (for example engine knocking reduction, crankshaft torque oscillation reduction, drive-shaft oscillation reduction, vehicle jerk reduction etc). The vectors (8.12) can be very demanding in terms of computational resources during the dynamic programming procedure due to the higher order. It is worth mentioning that the dynamic programming methodology is cursed by the number of states of the dynamic system. Hence it is advisable to reduce the number of states of the dynamic system by possible assumptions. Since the optimal sizing of the powertrain needs to be performed w.r.t. a reference drive cycle, some of the members of the vectors (8.12) can be converted as exogenous

signals. The optimal control procedure for the hybrid scooter powertrain is performed con-

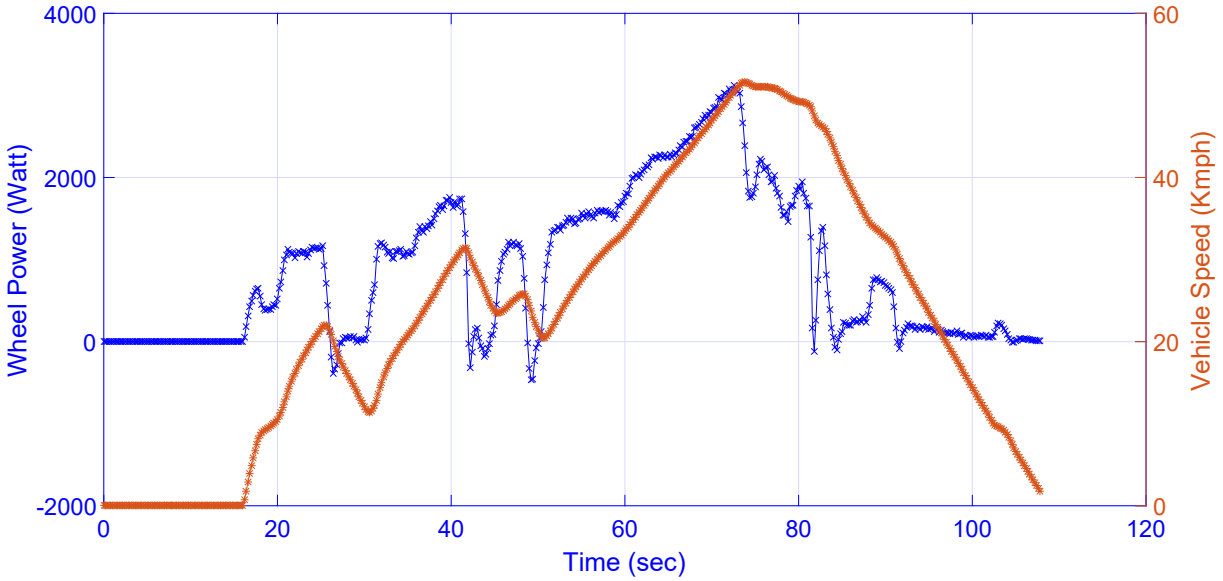


Figure 8.3: Wheel power and vehicle speed during IDC

sidering the reference drive cycle as the Indian drive cycle (IDC) [105]. Figure 8.3 shows the trajectory of v for the horizon of the one sub-cycle of the IDC. The full IDC consists of six repetitions of the sub-cycle shown in Figure 8.3. The figure also shows the corresponding wheel power for the IDC. Hence, from the information of Figure 8.3, the values of v and P_{ICE} can be deduced if v_{error} is set to zero, which is the desired value for v_{error} for the full time horizon. It is assumed that F_{Brake} can be incorporated by P_{EM}, since the wheel power information is available a priori. Since the research work aims to design the optimal powertrain and controller w.r.t. a known drive cycle, the prior information helps to simplify the dynamic system with reduced state and control. However, if the prior information is not available, the simplification of state and control vector is not feasible. The simplification does not effect the dynamics of the system nor the optimal trajectory as the physics of the dynamic system is not violated.

The above argument simplifies the vectors (8.12) to

$$X = \begin{bmatrix} SOC \\ m_f \\ G \\ \omega_{engine} \end{bmatrix}, U = \begin{bmatrix} G_{set} \\ P_{EM} \end{bmatrix}. \tag{8.13}$$

The continuous time model presented above needs to be discretized as the software functions used for optimal control design accepts discrete time dynamic model only. Although there are advanced & more accurate methods are available for discretization of the continuous time model, the forward Euler method is selected for discretization due to the simplicity of the method. However, in future the discretization would be achieved by multiple stage method. The error expected by single step discretization can be negated by a appropriate mesh size. The above system with lower number of states and control signals is discretized for implementing numerical optimal control with sampling time Ts=0.2 sec. The selected sampling time ensures a feasible simulation mesh for the full drive cycle of 628 sec. Most of the powertrain dynamics that can influence drivability of the vehicle are slower than the selected Ts.

$$\omega_{engine}(k+1) = \left\{ \frac{1}{R_w} \frac{1}{\tau_{Geardelay}} (G_{set}(k) - G(k)) v(k) \right\} Ts + \frac{1}{R_w} a(k) G(k) Ts + \omega_{engine}(k) \tag{8.14}$$

$$SOC(k+1) = -(\frac{P_{EM}(k)}{\eta_{EM} U_0 Q_{Battery}}) Ts + SOC(k) \tag{8.15}$$

$$m_f(k+1) = \left\{ \frac{V_d p_{mi} \omega_{engine}(k)}{4\pi H_v \eta_{combustion}} \right\} Ts + \left\{ \left[\frac{P_{wheel}(k)}{\eta_{gear}} - P_{EM}(k) \right] / H_v \eta_{combustion} \right\} Ts + m_f(k) \tag{8.16}$$

$$G(k+1) = \frac{1}{\tau_{Geardelay}} (G_{set}(k) - G(k)) Ts + G(k) \tag{8.17}$$

The values of velocity $v(k)$, longitudinal acceleration $a(k)$ and wheel power P_{wheel} are derived from drive cycle data as mentioned in Figure 8.3. In (8.16), η_{gear} is the efficiency of the CVT system which is assumed to be constant.

8.4 Conclusions

This chapter presented the control-oriented mathematical models for the motor-integrated powertrain which are coupled with a CVT system. The models are simplified versions of the detailed powertrain model developed in Chapters 3, 4 and 6. It should be noted that the AFR for the SI engine is pre-calibrated, independent of the coupled electric machine. This is essential, since the optimal controller intend to minimize the target cost function (for example fuel consumption or/and exhaust emission or/and maintain battery charge sustainability) by following a unique trajectory of power-sharing between SI engine and electric machine each time during operation. Hence, it would be desirable to consider the tuning of SI engine and electric machine independently. The model formulation is in discretized form and it is useful for numerical optimal control.

Chapter 9

Single function multi-objective optimization for component sizing

9.1 Introduction

The preceding chapters present work on the mathematical model development of the motor-integrated powertrain coupled with a CVT system. However, the work does not provide any information about

- the optimized size of each component of the powertrain with respect to a fuel consumption reduction, financial cost impact and weight impact;
- an optimal controller which can minimize the fuel consumption with battery charge sustainability.

The above requirements are very critical for the design of the motor-integrated powertrain suitable for two wheeler application. These design objectives are quite challenging due to the nature of the multi-objective requirements. In this chapter, the multi-objective optimal control design problem for the two-wheeled hybrid powertrain is addressed with a nested methodology of concurrent design of optimal controller and optimized powertrain component sizing. The nested methodology utilizes particle swarm optimization algorithm along with dynamic

programming.

9.2 Multi-objective optimization

The method of multi-objective optimization can be broadly sub-divided into two groups:

- Single function-based multi-objective optimization. Using the domain level information a weight vector transforms the multi-objective problem to a single-objective optimization. Another approach is to convert some of the objectives as constraints. The objective function can be solved using different methods of optimal control [44–51].
- Multiple objective functions, where a set of solutions in the form of multi-dimensional trade off plots and a suitable solution is chosen by the designer [126–131]. The main objective is to converge to a set of solutions by simultaneous optimization as close as possible to true pareto-optimal set. However, diversity in the obtained Pareto-Optimal set is the second objective specific to multi-objective problems. It is essential to include more diverse set of solutions that covers all parts of Pareto-front in the search space.

The design objectives mentioned in the previous section can be achieved by both of the above-mentioned multi-objective optimization methods. In this chapter, the first method is evaluated whereas the second method is evaluated in the following chapter.
The preferred method for optimization is stochastic optimization over classical optimization method due to the following reasons [130–132]:

- A stochastic optimization method evaluates a population of solutions from the design space in each iteration whereas classical optimization algorithms update one solution in each iteration. As the design optimization problem of the motor-integrated powertrain needs to search in a multi-domain design space, population search would be a superior approach than a single solution approach. A population search method has a number of advantages: (i) the stochastic optimization method can use parallel processing power achieving a computationally quick overall search, (ii) the stochastic optimization method

can find multiple optimal solutions, thereby facilitating the solution of multi-modal and multi-objective optimization problems, and (iii) the stochastic optimization method can normalize decision variables (as well as objective and constraint functions) within an evolving population using the population-best minimum and maximum values.

- The classical optimization method uses pre-determined rules and methods for search, whereas stochastic optimization methods tend to achieve a desired effect by using higher probabilities towards desirable outcomes.

Hence, in this research, the multi-objective optimization is performed using a stochastic method which can guarantee a global solution. However, the fitness function which needs to be evaluated by the multi-objective optimization procedure should be evaluated using a numerical optimal control method. This nested methodology of optimization with numerical optimal control can help achieve the design objectives with a mathematically guaranteed global optimal design.

9.3 Particle Swarm Optimization algorithm

The Particle Swarm Optimization (PSO) algorithm, proposed in [133] is a numerical optimization method discovered through simulations of a social model inspired by cognitive, social and stochastic learning method adopted by a bird flock [133, 134]. The global gradient-free stochastic search method is very much suitable for vast types of optimization problems. The common goal of all group members (swarms) is to find the best value of the fitness function $f(\cdot)$ within a specified search space at their corresponding location. Each member determines its movement in the specified search space by combining some aspects of its own current and best locations (corresponding to the best value of the fitness function $f(\cdot)$ with those of one or more members of the group. This algorithm is best suitable for the following type of problem [134]

$$\min_x f(x) \tag{9.1}$$

$$\begin{aligned} \text{subject to: } Ax &\leq b \\ A_{eq}x &= b_{eq} \\ c(x) &\leq 0 \\ c_{eq} &= 0 \\ l_b \leq x &\leq u_b \end{aligned} \tag{9.2}$$

where x, b, b_{eq}, l_b and u_b are vectors and A and A_{eq} are matrices. The fitness function $f(\cdot)$ quantifies the performance of x. The constraints are expressed with $c(x)$, c_{eq}, lb and ub. The functions $f(x)$, $c(x)$ and $c_{eq}(x)$ may be nonlinear.

The PSO algorithm is not very complex to express. The following intuitive formulation is proposed after several modifications [133–135]:

$$v_j^{m+1} = \phi^k v_j^m + \alpha_1 \left[\gamma_{1,j} \left(P_j - x_j^m\right)\right] + \alpha_2 \left[\gamma_{2,j} \left(G_{best} - x_j^m\right)\right] \tag{9.3}$$

$$x_j^{m+1} = x_j^m + v_j^{m+1} \tag{9.4}$$

The vectors x_j^m and v_j^m are the current position and velocity of the j-th member of the group in the m-th generation. The group consists of M members, i.e., $j = 1, 2, ..., M$. P_i is the personal best position of each member of the group and G_{best} is the global best position observed among all members up to the current generation. The parameters $\gamma_{1,2} \in [0, 1]$ are uniformly distributed random values, $\alpha_{1,2}$ are acceleration constants and ϕ works as inertia of the member which gives rise to certain momentum which influences it's trajectory in the search horizon. Equations 9.3 and 9.4 can be easily represented in vector diagram to visualize the PSO algorithm in a two-dimensional space [134], [133], [135]. This research uses the PSO algorithm proposed in [134]. The particular PSO algorithm handles the constraints (9.2) with three different ways, (i) penalize, (ii) absorb and (iii) nearest.

The first method is based on increasing the value of the objective function to penalize the particular member with a value higher than the highest attainable value in the feasible area in case the new position of the member violates any constraint. This forces the member

to re-enter the feasible area in the search region. The second method absorbs the member in the boundary imposed by the constraints and evaluates the objective function at the boundary loci. The third method allows the member to travel outside the feasible area and retracts it to the nearest loci on the constraint boundary.

9.4 Deterministic dynamic programming algorithm

It is essential to build an optimal policy which can guarantee global optimal behaviour for an optimal control problem. The global optimal control policy may be non-causal. The deterministic dynamic programming tool is very much suitable for the non-causal optimal control problem. The solution of this approach can be used for (i) component level design optimization and (ii) realization of a benchmark control policy which can be compared with a causal optimal control policy.

The term "Dynamic Programming" is coined by Richard E. Bellman who proposed the principle of optimality. The principle of optimality suggests sequential solving of the optimal control problem, by solving all the "tail sub-problems" for the known time horizon, using the solutions of the "tail sub-problems" of shorter time length [66]. The deterministic dynamic programming requires [66] (i) an underlying discrete time dynamic system and (ii) a cost function which is additive over time.

Let the discrete time dynamic system with N discrete time steps be

$$x_{k+1} = F_k(x_k, u_k), k = 0, 1, 2, ...N - 1 \tag{9.5}$$

where x_k is the state variable, $x_k \in \Phi_k$ and u_k is the control signal, $u_k \in \Psi_k$.

If $\psi = u_0, u_1, ...u_{N-1}$ is the control signal for the whole time horizon, the discrete cost

function can be expressed as

$$J_{\psi}(x_0) = g_N(x_N) + \Phi_N(x_N) + \sum_{k=0}^{N-1} h_k(x_k, u_k(x_k)) + \Phi_k(x_k) \tag{9.6}$$

where $g_N(x_N) + \Phi_N(x_N)$ is the final cost and $h_k(x_k, u_k(x_k))$ is the cost of applying control u_k at x_k. The penalty function $\Phi_k(x_k)$ is added for the state constraints $x_k \in \Phi_k$ for $k = 0, 1, 2, ...N-1$. The optimal control signal $\psi^o = u_0^o, u_1^o, ...u_{N-1}^o$ is defined as the set which ensures the minimum value of J_{ψ}

$$J^o_{(x_0)} = \min J_{\psi}(x_0) \tag{9.7}$$

The algorithm for the dynamic programming can be expressed as [136]

1. Step 1: Final cost function calculation for the discrete state points (x^i are the unique nodes of the whole grid of state space)

$$T_N(x^i) = g_N(x^i) + \Phi_N(x^i) \tag{9.8}$$

2. Step 2: Calculate intermediate cost function backwards for the whole time horizon

$$T_k(x^i) = \min_{u_k \in \Psi_k} h_k(x^i, u_k) + \Phi_N(x^i) + T_{k+1}(F_k(x^i, u_k)) \tag{9.9}$$

The optimal control signal $\psi^o = u_0^o, u_1^o, ...u_{N-1}^o$ is calculated based on the argument that minimizes the cost function expressed in (9.9). The output of the deterministic dynamic programming algorithm is an optimal control map, which is used to find the optimal control signal during forward simulation of the dynamic model (9.5) starting from the initial state x_0, to generate the optimal state trajectory [136].

9.5 Nested methodology for optimal sizing using PSO and DP

In this section, the nested method of optimal control is proposed and implemented where the PSO and DP algorithm work in tandem. Figure 9.1 explains the working of PSO and DP algorithm for solving the optimal control problem of sizing the components of the hybrid powertrain. The hybrid powertrain and problem formulation is explained in the next sections. The multi-objective fitness function is defined as a part of the optimal formulation. The members

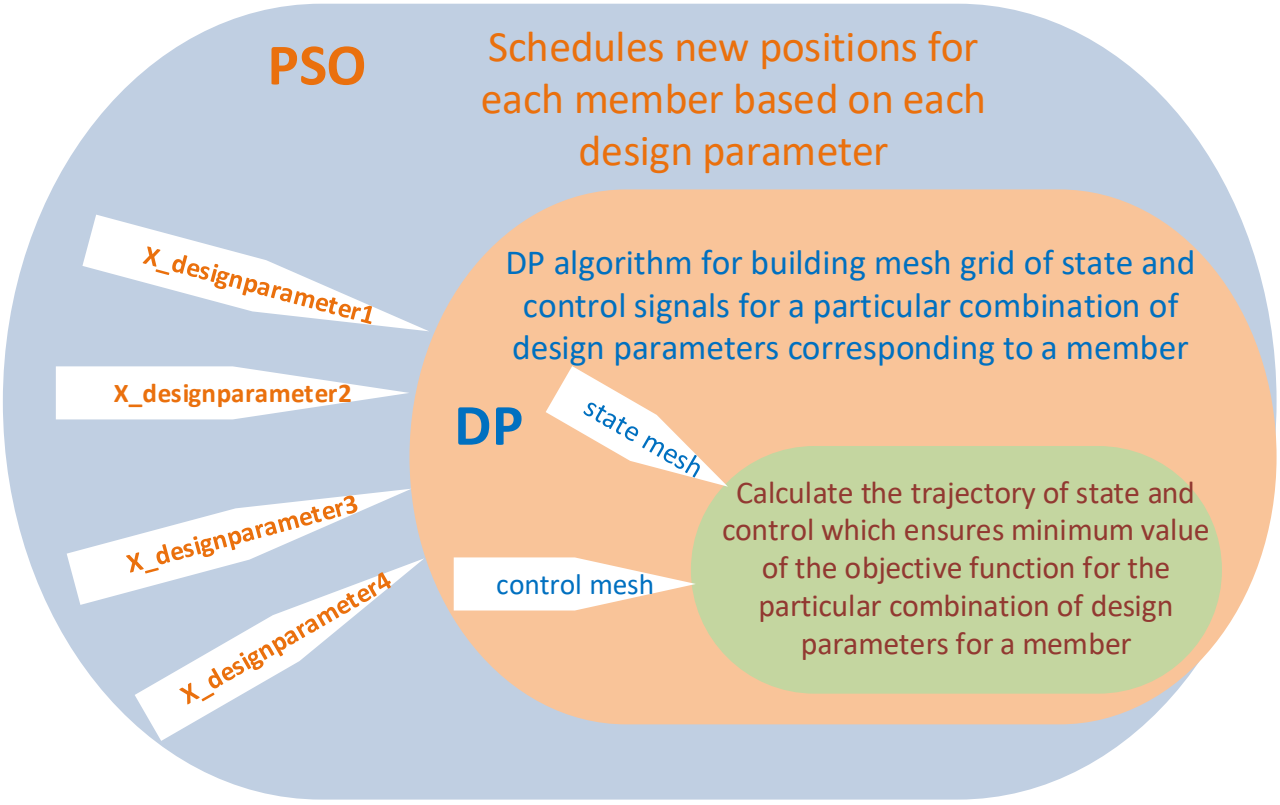


Figure 9.1: Top level diagram of Optimal design methodology

are initiated in PSO with different design parameters of the hybrid powertrain and each member deploys the DP algorithm, which ensures the global minimum of the objective function for the particular configuration proposed by the member. The above task of calculating the minimum value of the objective function can be deployed concurrently using parallel computing as each member does not use social interaction during evaluating the fitness function for a particular

iteration. Figure 9.2 explains the concurrent evaluation of the fitness function by each member

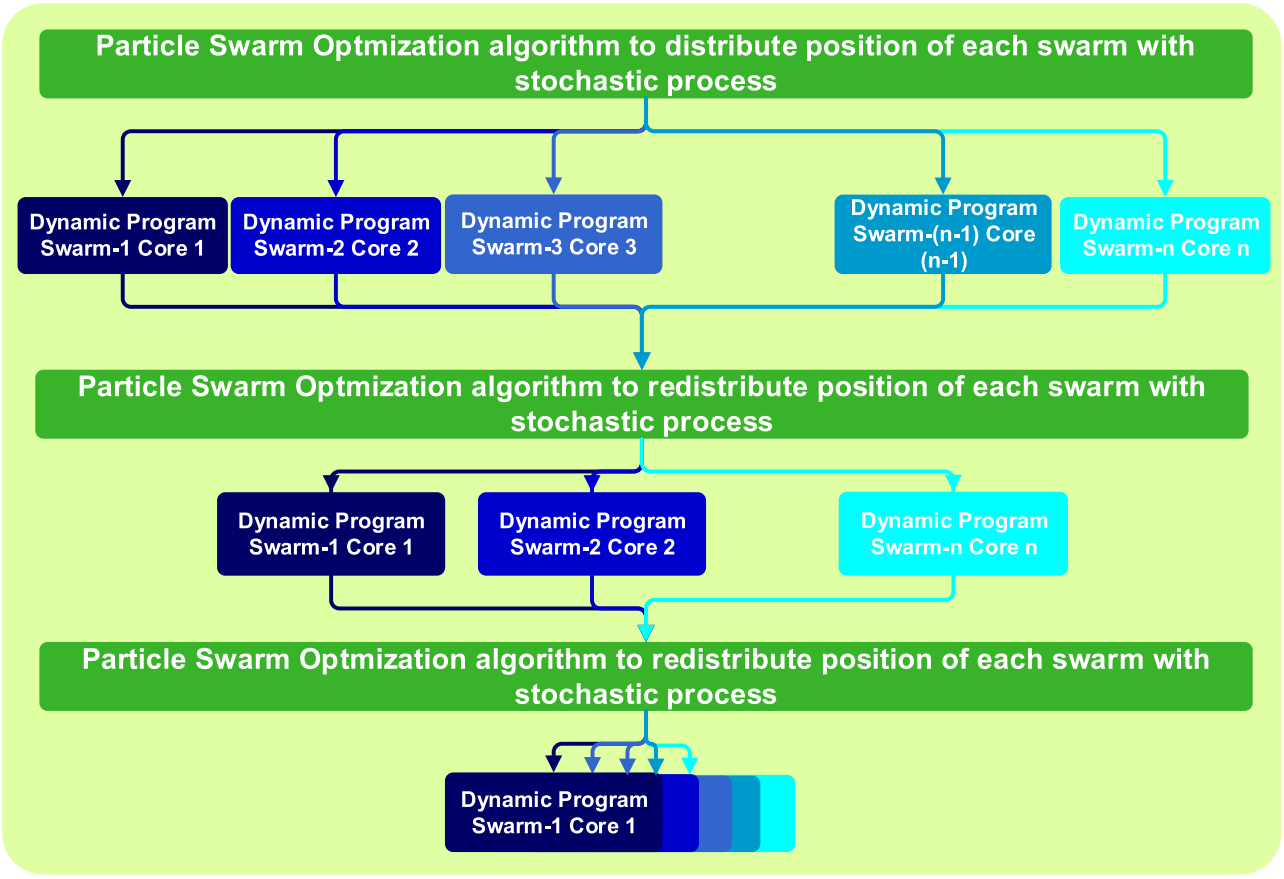


Figure 9.2: Execution of optimal methodology using parallel computing

initiated by the PSO algorithm. The fitness function evaluations of all members are deployed to independent cores of a multiple core computer. Each member uses a cognitive, social and stochastic learning method which helps to converge to the global optimal value of the fitness function by each member. The design parameters corresponding to the global optimal value of the fitness function are accepted as design parameters for the hybrid powertrain.

9.6 Optimal design problem formulation

The formulation of the optimal design is subdivided into two parts based on PSO and DP algorithms. The multi-objective fitness function is expressed as a single function with multiple

weighting factors. The vector for the design parameters which is formulated for the PSO algorithm (9.1), (9.2) is expressed as

$$X_{designparameter} = \begin{bmatrix} MaxPower_{electricmachine} \\ MaxCapacity_{battery} \\ GearRatio_{max} \\ GearRatio_{min} \end{bmatrix} \tag{9.10}$$

It is essential to propose the mathematical relation between the elements of $X_{designparameter}$. The electric components of the powertrain need to satisfy the energy balance between the electric machine and battery for a defined boundary of SOC. The upper limit and lower limit of the boundary can be defined as $SOC_{highthreshold}$ and $SOC_{lowthreshold}$ respectively. The battery should provide enough energy to the electric machine during the acceleration phase (corresponding time of T_{acc}) assuming the latter is operating in peak rating. In this case, initial battery SOC is assumed as $SOC_{highthreshold}$ and at the end of drive cycle it should not deplete beyond $SOC_{lowthreshold}$. Similarly, the battery should be able to recover the energy during the deceleration phase (corresponding time of T_{dec}) of the drive cycle. In this case, the initial battery SOC is assumed as $SOC_{lowthreshold}$ and at the end of the drive cycle it should not cross $SOC_{highthreshold}$. The above requirements result in the mathematical inequalities

$$MaxPower_{electricmachine} * T_{acc} < MaxCapacity_{battery} * (SOC_{highthreshold} - SOC_{lowthreshold}) * U_0 \tag{9.11}$$

$$MaxPower_{electricmachine} * T_{dec} < MaxCapacity_{battery} * (SOC_{highthreshold} - SOC_{lowthreshold}) * U_0 \tag{9.12}$$

In the case of Indian drive cycle, $T_{dec} < T_{acc}$, resulting in $a_{12} = MaxCapacity_{battery} * (SOC_{highthreshold} - SOC_{lowthreshold}) * U_0/T_{dec}$ in the following A matrix:

$$A = \begin{bmatrix} 1 & a_{12} & 0 & 0 \\ 0 & 0 & 1 & -1 \\ 0 & 0 & 1 & 0 \\ 0 & 0 & 0 & -1 \end{bmatrix}, b = \begin{bmatrix} 0 \\ 0 \\ b_{31} \\ b_{41} \end{bmatrix} \tag{9.13}$$

where b_{31} and b_{41} are the limits of $GearRatio_{max}$ and $GearRatio_{min}$ respectively. The matrix A and vector b correspond to the elements of the inequality constraints of (9.2). The fitness function is expressed as

$$J_{optimizeddesign} = \mu_1 l_1 + \mu_2 FinacialCost_{EV} + \mu_3 Weight_{EV} + \mu_4 (SOC - SOC_{desired})^2 \tag{9.14}$$

with

$$\sum_{i=1}^{4} \mu_i = 1 \tag{9.15}$$

and with

$$l_1 = o_1 m_f + o_2 (SOC - SOC_{desired})^2 \tag{9.16}$$

Equation (9.14) is the multi-objective single function proposed for the design optimization. The values of μ_i, o_1 and o_2 are of strategic importance for future products for TVS Motor Company and hence they are not disclosed in this work. The value of μ_4 in (9.14) is significantly less than the values of μ_1, μ_2 and μ_3. The expression of (9.16) serves as the cost function of the DP algorithm.

Financial cost ($FinacialCost_{EV}$) and weight ($Weight_{EV}$) for the electric traction components can be expressed as

$$FinacialCost_{EV} = (\kappa_1 MaxPower_{electricmachine} + \kappa_2 MaxCapacity_{battery} + \kappa_3 FinacialCost_{TotalPowertrain} + \kappa_4 \tag{9.17}$$

$$Weight_{EV} = (\nu_1 MaxPower_{electricmachine} + \nu_2 MaxCapacity_{battery} + \nu_3 Weight_{TotalPowertrain} + \nu_4) \tag{9.18}$$

where κ_1, κ_2, κ_3, κ_4, ν_1, ν_2, ν_3 and ν_4 are regression coefficients calculated using component pricing and weight information from TVS Motor Company.

The design parameters $MaxPower_{electricmachine}$, $GearRatio_{max}$ and $GearRatio_{min}$ mentioned in (9.10) are used as the limits for control signals and states in implementing the DP algorithm. As the parameter $MaxCapacity_{battery}$ does not appear as a control signal or state in system equations (8.14), (8.15), (8.16) and (8.17), it is handled as an exogenous signal for the dynamic model.

9.7 Results for optimal design and control

In this section, the simulation results for the PSO and DP algorithm deployed for optimal design and control are presented and discussed. It is essential to evaluate the multi-objective fitness function (9.14) which would help to determine the elements of the design matrix (9.10). Figure 9.3 shows the value of the multi-objective fitness function for the PSO algorithm as a

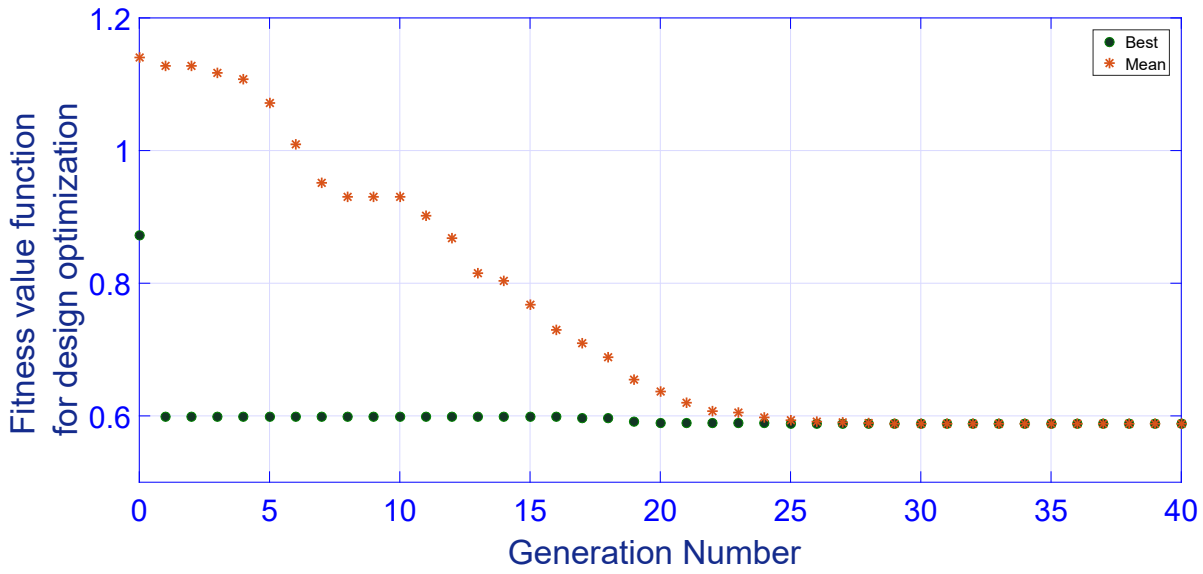


Figure 9.3: Fitness function evaluation with PSO algorithm

function of generations (or iterations). This figure can be linked with Figure 9.2 discussed in

the previous section. Figures 9.4 and 9.5 show the trajectories of the members of the swarm group during the PSO algorithm. Figures 9.3, 9.4 and 9.5 together explain the working of the PSO algorithm. Since the design vector (9.10) is a 4 dimensional vector, the trajectories of the

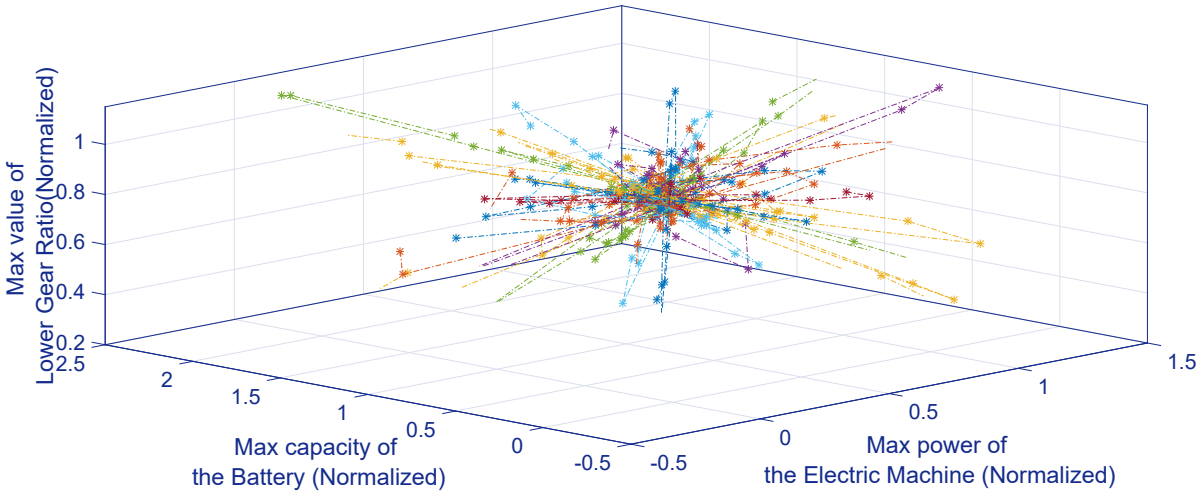


Figure 9.4: Trajectories of members of group in design space with first, second and third elements of vector (9.10)

members of the PSO algorithm are shown in segmented $3D$ design spaces in Figures 9.4 and 9.5. The number of members in the group is considered as 23 as discussed in [135].

The best values of the fitness function in each iteration of PSO (as shown in Figure 9.3) are the minimum values of the fitness function calculated by each of the members corresponding to their respective loci in the design space (as shown in Figures 9.4 and 9.5). The mean values of the fitness function in Figure 9.3 are the average values of the fitness function of the other 22 members. The mean value of the fitness function in Figure 9.3 converges to the best value due to the cognitive, social and stochastic learning capabilities of each member of the group ensuring the global optimal value of the fitness function. The optimal values of the elements of the vector (9.10) are calculated based on the above methodology. The absolute values of the vector elements are out of scope of the thesis due to confidentiality of the powertrain configuration.

Figures 9.6 and 9.7 show the trajectories of the control signal P_{EM} and G_{set} for the IDC.

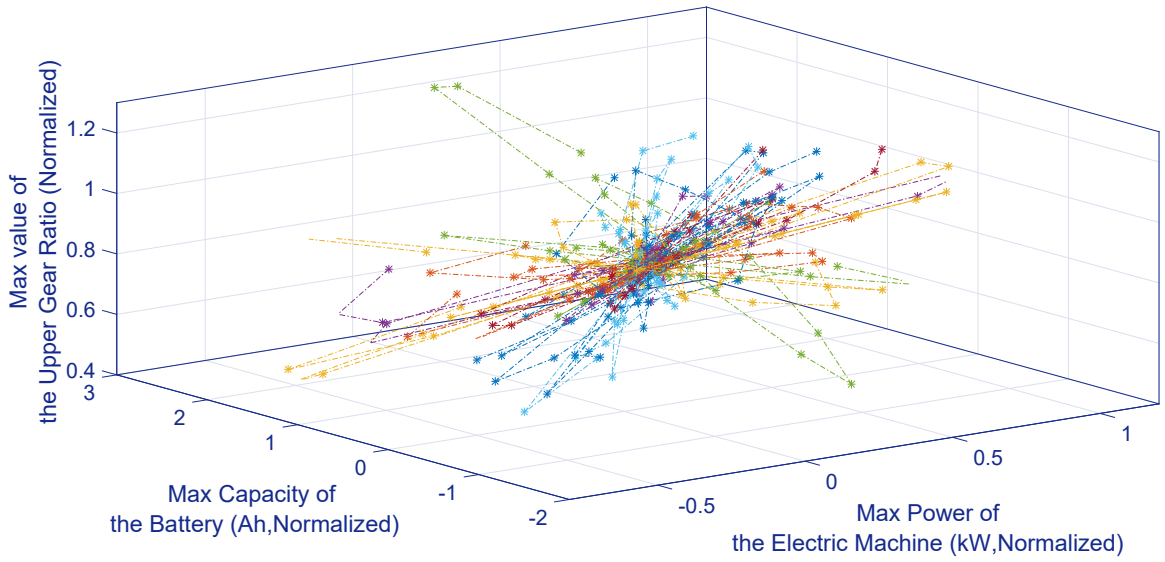


Figure 9.5: Trajectories of members of group in design space with first, second and fourth elements of vector (9.10)

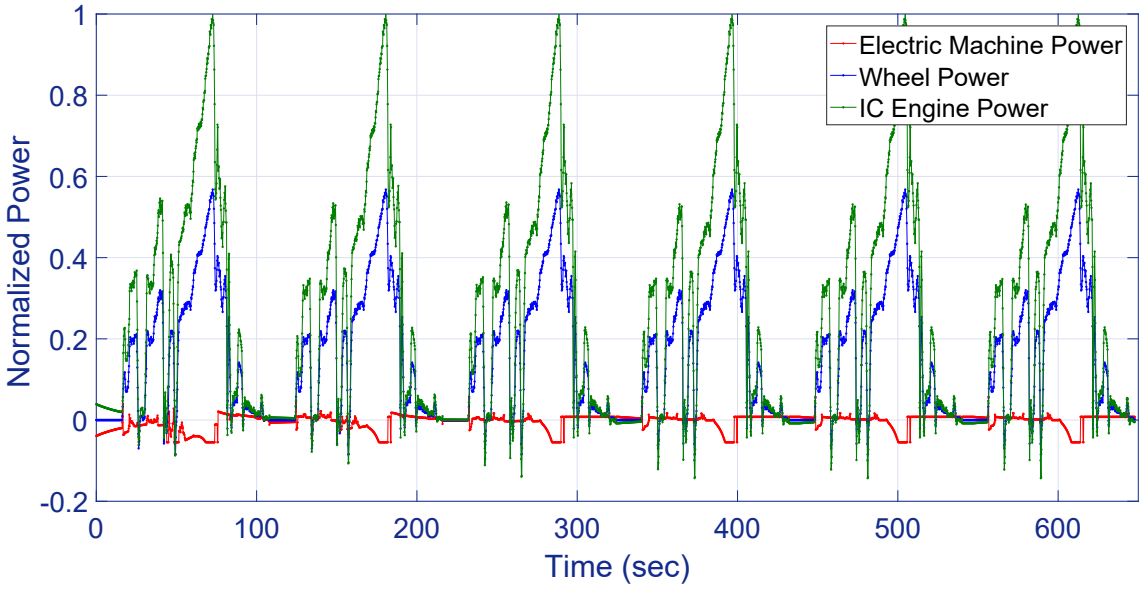


Figure 9.6: Wheel Power and Vehicle Speed during IDC

The trajectory of P_{wheel} is calculated as explained in the previous section. Figure 9.6 shows that the share of electric machine power is around 15% of the wheel power requirement. This is due to the higher value of $FinancialCost$ in (9.14) as well as weighting factors μ_2 and μ_3. The effect of μ_i can be explored with a Pareto analysis which is done in the next chapter. It can be argued from Figure 9.7 that the value of the $GearRatio_{max}$ is utilized for very short duration in IDC. As the higher value of $GearRatio_{max}$ is influenced by gradeability of a vehicle, it is usual to expect lower use of higher ratios of gear during drive cycle analysis. However, the range of the use of gear ratio is a function of the maximum allowable range of the engine speed. The $\tau_{Geardelay}$ is influencing G with a first order delay.

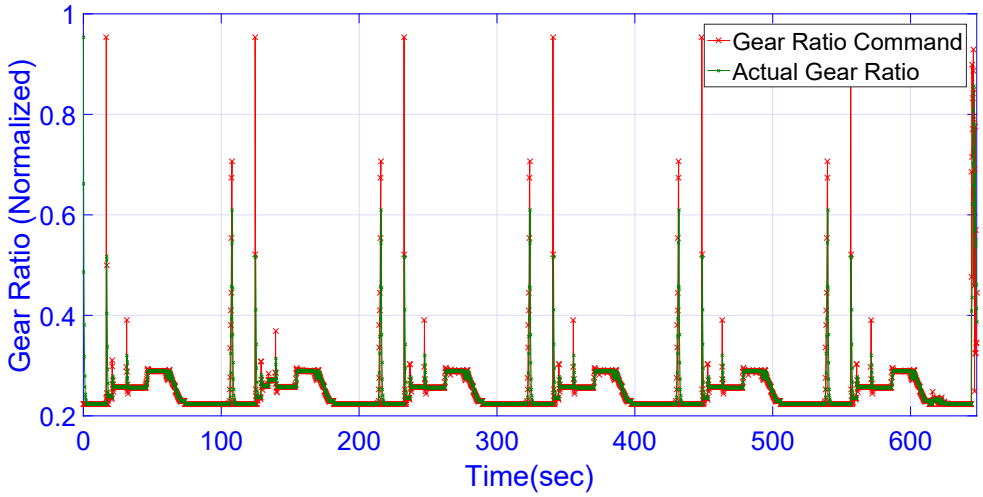


Figure 9.7: Gear Ratio Command and Actual Gear Ratio during IDC

Figures 9.8, 9.9 and 9.10 show the trajectories of states ω_{engine}, m_f and SOC respectively for the IDC. The trajectory of ω_{engine} shows the period of IC engine idling when the vehicle is stationary. As mentioned in the earlier section of problem formulation, one of the objectives is to design a charge sustainable hybrid EV system. The SOC trajectory shows that the optimal control system reaches the final desired SOC of 80%. It should be noted that the desired value of final SOC is chosen considering a charge sustaining system.

Figures 9.11 and 9.12 are derived from Figure 9.6. Figure 9.11 shows the power speed characteristics requirement for both energy sources. Similarly Figure 9.12 shows the torque speed characteristic requirement for the IC engine as well as the electric machine. Both of

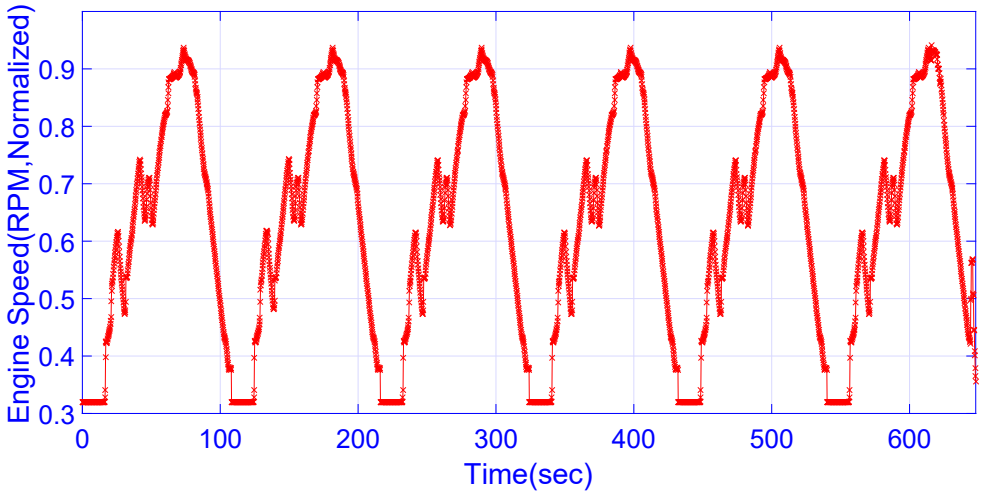


Figure 9.8: Engine Speed during IDC

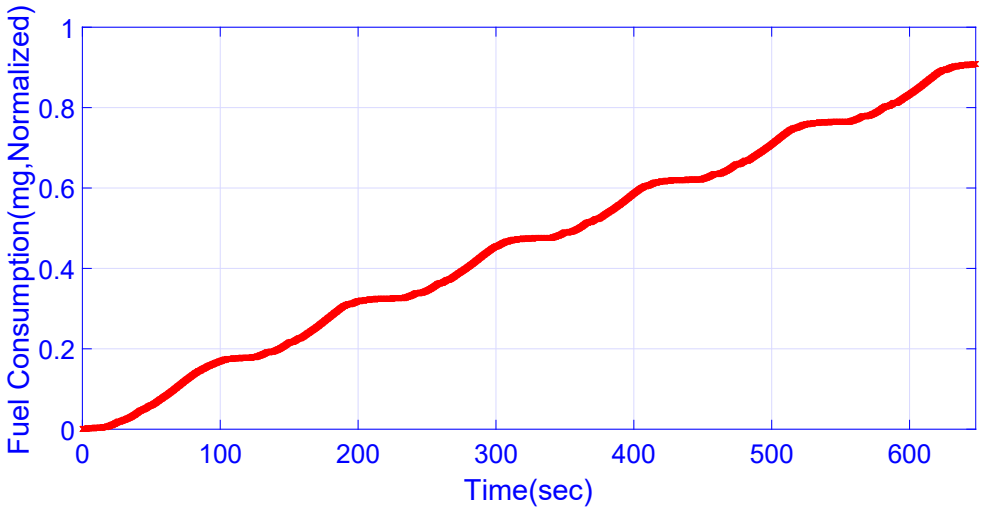


Figure 9.9: Fuel Consumption during IDC

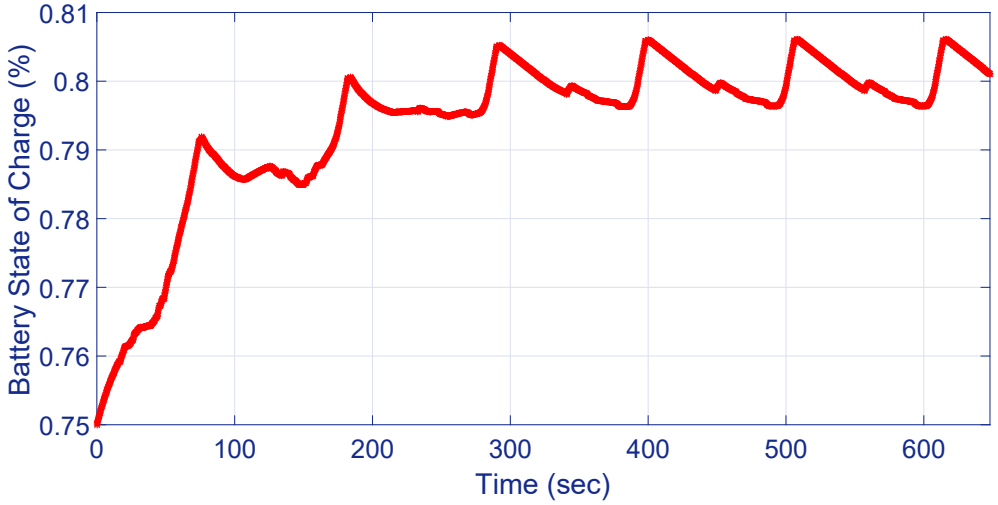


Figure 9.10: Battery SOC during IDC

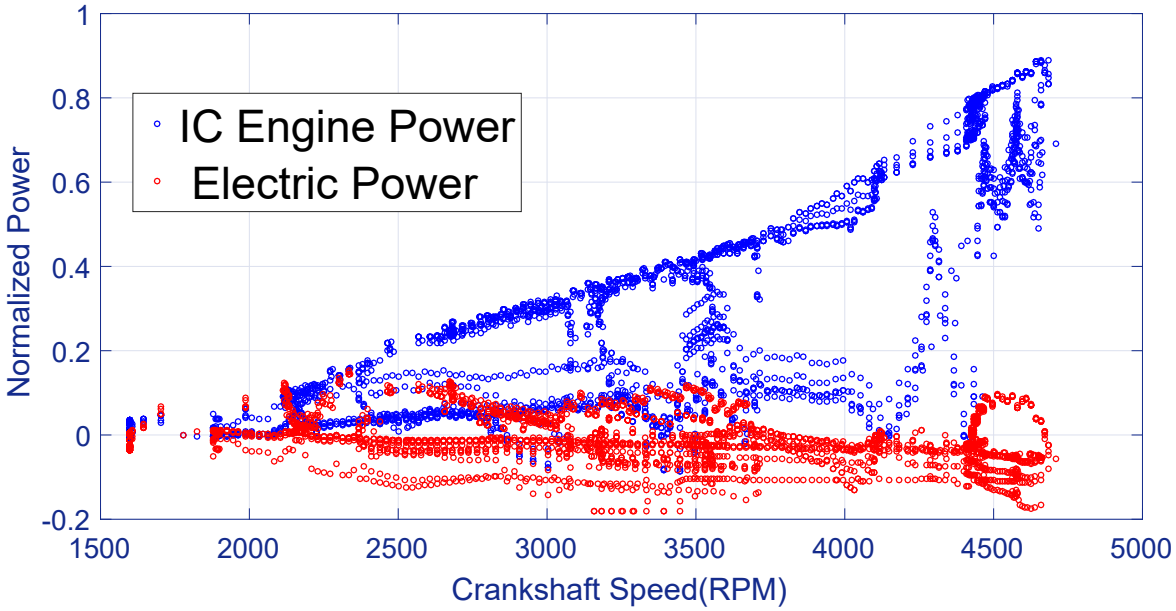


Figure 9.11: Power Speed characteristics for IC engine and Electric machine for IDC

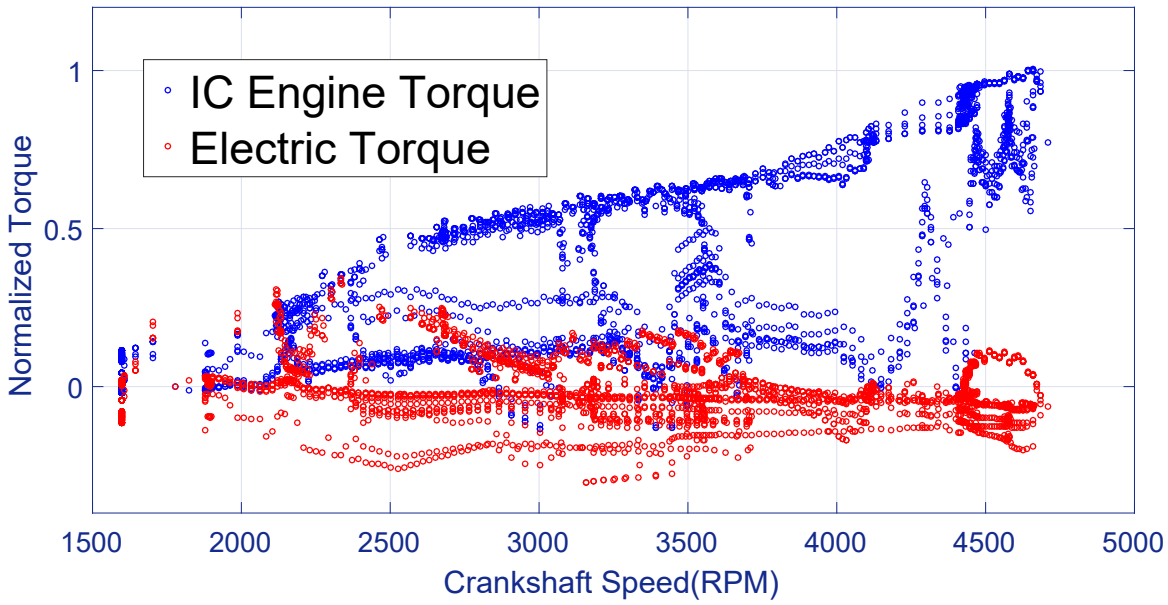


Figure 9.12: Torque Speed characteristics for IC engine and Electric machine for IDC

the figures are very significant in terms of design and tuning of the electric machine and IC engine.

9.8 Conclusions

In this chapter, a nested design methodology of optimal controller development and optimized powertrain component sizing for a parallel hybrid powertrain is proposed and implemented. The optimized sizing of different powertrain components (maximum power of the electric machine, maximum capacity of the Li-Ion battery pack, maximum gear ratio and minimum gear ratio) are determined using the algorithm, which can guarantee the global optimal performance of the objective function. The objective function is formed such that the single mathematical function can address multiple design objectives.

Chapter 10

Pareto-optimal multi-objective optimization for component sizing

10.1 Introduction

The single function-based multi-objective optimization is not adequate to provide information about Pareto-optimal solutions for the optimization problem. The previous chapter has laid the foundation of the multi-objective optimization without discussing details about Pareto-optimal design. It is very much essential to evaluate the Pareto-optimal front, which may provide more options for sizing of different components of the motor-integrated powertrain. The multi-objective optimization needs to consider the following objectives:

- to reduce fuel consumption of the IC engine
- not to allow deviation of battery SOC from a desired value to ensure battery charge sustainability
- to consider the cost rise of the vehicle due to the addition of electric machine, battery and inverter
- to consider increase in weight of the vehicle due to the addition of electric machine, battery and inverter

Previous research on optimal supervisory control has mostly considered single-objective optimization [44–51]. However the design optimization of the motor-integrated hybrid powertrain for optimal performance needs a different treatment due to

- multiple and conflicting objectives,
- a highly complex search space [126–131].

There is substantial research performed in the field of multi-objective optimization algorithms [126–131]. However, the researchers of design optimization of motor-integrated hybrid powertrains for the optimal performance task tend to overlook the challenges of a multi-objective optimization problem by converting it to single-objective optimization deploying certain weights.

There are several evolutionary optimization algorithms suitable for the multi-objective optimization task. Some research studies were conducted to determine the characteristics of particular algorithms and to compare them [130, 131, 137, 138]. The characteristics elements of an evolutionary optimization algorithm that need to be considered are

- fitness assignment
- diversity mechanism
- elitism
- external population.

The most representative, discussed and compared evolutionary algorithms are Elitist non-dominated sorting genetic algorithm (NSGA-II) [130], Strength pareto evolutionary algorithm (SPEA, SPEA2) [139, 140], Pareto archived evolution strategy (PAES) [141, 142] and Pareto enveloped-based selection algorithm (PESA, PESA II) [143, 144]. The above-mentioned comparative research studies perform numerical simulations on various test problems and conclude that NSGA-II and SPEA2 algorithms perform better in comparison to other algorithms. This research chooses the NSGA-II algorithm for the multi-objective optimization task of the motor-integrated hybrid powertrain.

10.2 Multi-objective optimization algorithm for Pareto-optimal solution

As mentioned earlier, a multi-objective optimization problem consists of more than one objective functions. The multi-objective optimization problem involves a number of constraints similar to the single-objective optimization problem. The constraints define the boundary for the feasible zone of the problem. The multi-objective optimization problem can be defined as

$$\min_{x} f(x) \tag{10.1}$$

$$\begin{aligned} \text{subject to: } g(x) &\geq 0 \\ h(x) &= 0 \\ l_b \leq x &\leq u_b \end{aligned} \tag{10.2}$$

where x is the vector of the decision variable and f is the multi-dimensional vector of the objective function. The fitness function vector $f(\cdot)$ quantifies the performance of x. The constraints are expressed with $g(x)$ and $h(x)$, and l_b and u_b are the variable bounds defining the feasible region. The functions $f(x)$, $g(x)$ and $h(x)$ may be non-linear functions. The vector space of the objective function is termed as the objective space, the solution is a vector of decision variables and a point is the corresponding objective vector. A particular solution is termed as dominating other solutions, provided the point of the particular solution is no worse than other points and at least one objective of the solution is better than the corresponding objective of the other solutions. All points which are not dominated by any other member of the set are called the non-dominated points or Pareto-optimal solutions. One property of any two such points is that deterioration of at least one objective can only results in the gain of an objective from one point to the other. This important relation between the non-dominated points emphasises the need of searching a wide variety of them before making a final choice. These points make up a front when viewed together on the objective space, hence the non-dominated points are often visualized to represent a non-domination front. The computational

resource required to select the points of the non-domination front from a set of N points is $N\log N$ for 2 and 3 objectives and $N\log^{M-2}N$ for $M > 3$ objectives [130, 131]. The multi-objective optimization should be able to perform the following task:

- capable of finding multiple solutions in the Pareto-optimal front
- capable of diversifying the solutions which can confidently represent the entire Pareto-optimal front

The chosen NSGA-II algorithm confirms the above-mentioned requirements [130, 131] by

- adapting the elitist principle
- adapting an explicit diversity preserving mechanism
- emphasizing the non-dominated solutions

The following section briefly explains the NSGA-II algorithm from [130]. The NSGA-II algorithm generates a random parent population in the feasible search space defined by (10.2) followed by sorting for non-dominated points from the initial population. In the next phase offspring population of the same size as the parent population is formed by using binary tournament selection, recombination and mutation operators. The elitism cannot be introduced in the first phase as the previous non-dominated points are not available at this stage. Then the combined population of the parent and offspring are sorted together for non-dominated fronts and ranked accordingly. In the next iteration, a population of the same size as the initial population is chosen based on the ranking of non-dominated fronts. The diversity among non-dominated solutions is introduced by using the crowding comparison procedure, which is used in the tournament selection and during the population reduction phase.

10.3 Nested methodology for fitness function evaluation

In this section the nested methodology adopted for multi-objective optimization is presented. It is very essential to calculate the objective space for every member of the population in each iteration of the NSGA-II algorithm, which ensures non-dominated sorting as explained in the

previous section. The detailed formulation of the problem as in (10.1) and (10.2) is presented in the next section. The first and second design objectives mentioned in the previous section state that the optimization should guarantee a battery charge sustainable system which consumes the least fuel without violating any system constraints. The mentioned requirement necessitates the need of a numerical optimal control methodology embodied inside the NSGA-II algorithm for global optimal behavior. The dynamic programming method is a numerical optimal control method which results in a global optimal control [8,46,66,136]. DP has been used with NSGA-II similarly to the case of the previous chapter when DP was used with PSO.

The dynamic programming technique needs to calculate the first and second design objectives for each member of the population independently. Hence the dynamic programming task for each member of the population can be implemented using parallel computing methodology. Figure 10.1 provides a comprehensive view of the implemented method of multi-objective optimization. The first step shows the initialization and off spring generation of the population using operators of the genetic algorithm. In the next step, the objective space for every member of the population is evaluated using independent cores of a multi-core computer.

In each evaluation of the objective space, the dynamic programming method calculates the trajectory of all control and state trajectories for the particular member of the population. This step can be visualized in Figure 10.2. The NSGA-II algorithm calculates the solutions, which constitute the values of multiple design parameters. The dynamic programming method creates the grids of the state and control signals based on the threshold limits of same, which may be functions of the design parameters for each of the solutions of the NSGA-II algorithm. The numerical optimal control method calculates the minimum cost function and corresponding control vector from the tail end of the known time horizon for each point of the grid in the time axis. This is followed by a forward simulation of the discrete dynamic model to calculate the state trajectories corresponding to the control signal calculated in the previous step. This phase generates the two elements of the objective space for the particular solution of the NSGA-II algorithm. The objective spaces of each of the members of the population are compared and sorted for the non-dominant front as shown in Figure 10.1. The process is repeated until a

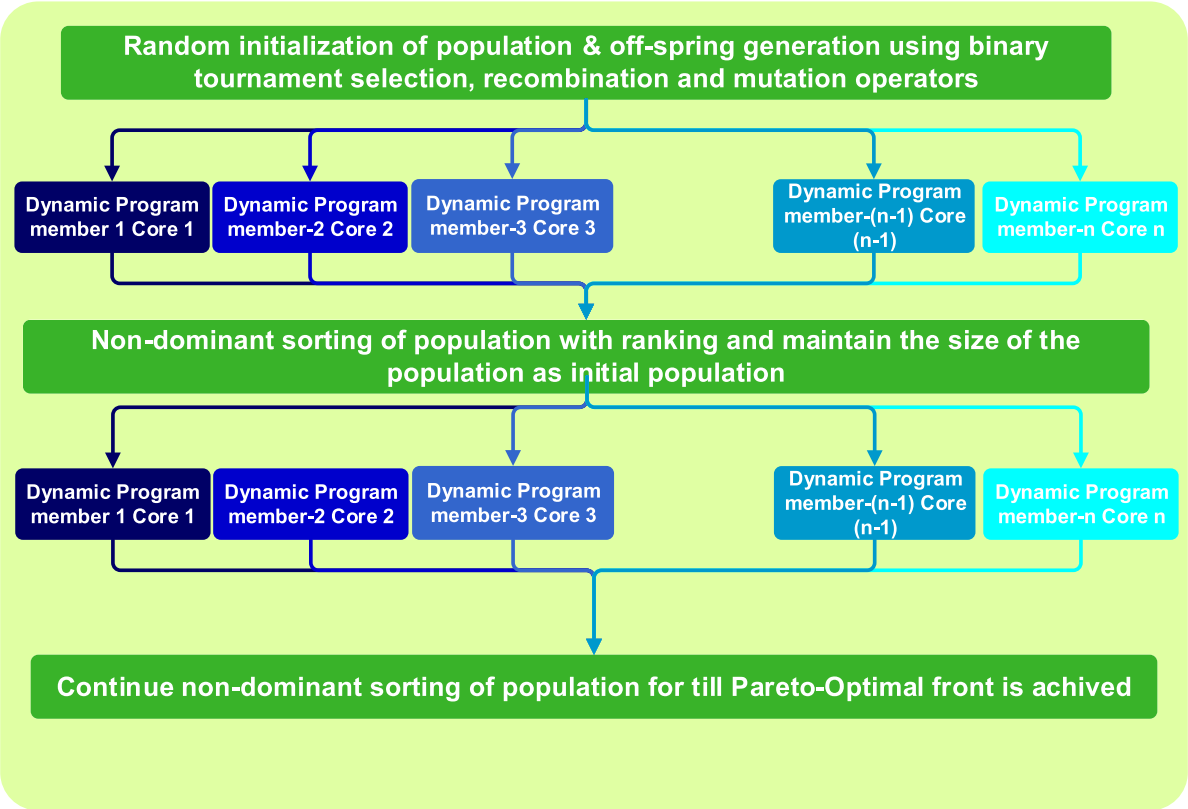


Figure 10.1: Top level diagram for the multi-objective optimization methodology

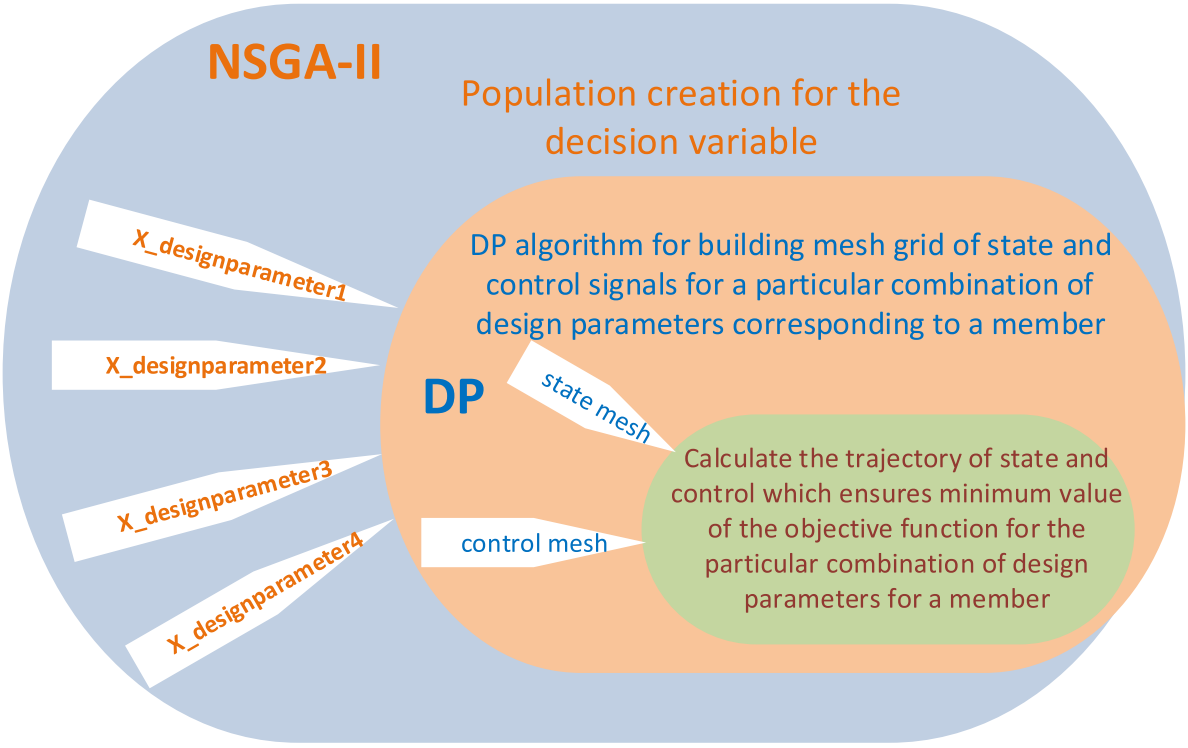


Figure 10.2: Nested methodology with NSGA-II and DP algorithm

Pareto-optimal front is achieved.

10.4 Optimal control problem formulation

The formulation of the optimal control is subdivided into two parts based on the NSGA-II and DP algorithm respectively. The multi-objective fitness function is expressed as a vector. The vector for the design parameters, which is formulated for the NSGA-II algorithm (10.1), (10.2) is expressed as

$$X_{designparameter} = \begin{bmatrix} MaxPower_{electricmachine} \\ MaxCapacity_{battery} \\ GearRatio_{max} \\ GearRatio_{min} \end{bmatrix}. \tag{10.3}$$

The constraints of the optimization problem are

$$A = \begin{bmatrix} 1 & a_{12} & 0 & 0 \\ 0 & 0 & 1 & -1 \\ 0 & 0 & 1 & 0 \\ 0 & 0 & 0 & -1 \end{bmatrix}, B = \begin{bmatrix} 0 \\ 0 \\ b_{31} \\ b_{41} \end{bmatrix}. \tag{10.4}$$

in which A and B are presented in equation (9.13). The constraint $g(x)$ from (10.2) can be expressed as

$$g(x) = Ax + B. \tag{10.5}$$

The fitness function $f(x)$ from equation (10.1) is expressed as

$$f(x) = \begin{bmatrix} j_1 \\ FinacialCost_{EV} \\ Weight_{EV} \end{bmatrix}. \tag{10.6}$$

with

$$j_1 = \mu_1 m_f + \mu_2 (SOC - SOC_{desired})^2. \tag{10.7}$$

Equation 10.6 is the multi-objective function proposed for design optimization. The values of μ_i are of strategic importance for future products for TVS Motor Company and hence they are not disclosed in this work. Equation 10.7 is calculated using the DP algorithm. The expression of (10.7) serves as the cost function of the DP algorithm.

Financial cost $FinancialCost_{EV}$ and weight $Weight_{EV}$ for the electric traction components can be expressed as

$$FinancialCost_{EV} = \kappa_1 MaxPower_{electricmachine} + \kappa_2 MaxCapacity_{battery} + \kappa_3 FinacialCost_{TotalPowertrain} + \kappa_4 \tag{10.8}$$

$$Weight_{EV} = \nu_1 MaxPower_{electricmachine} + \nu_2 MaxCapacity_{battery} + \nu_3 Weight_{TotalPowertrain} + \nu_4 \tag{10.9}$$

where κ_1, κ_2, κ_3, κ_4, ν_1, ν_2, ν_3 and ν_4 are regression coefficients calculated using component pricing and weight information from TVS Motor Company. The design parameters $GearRatio_{min}$, $GearRatio_{max}$ and $MaxPower_{electricmachine}$ mentioned in (10.3) are used as the boundary for control signals and states in implementing the dynamic programming algorithm. As the parameter $MaxCapacity_{battery}$ is not appearing as either control signal or state in the system equations (8.14), (8.15), (8.16) and (8.17), it is handled as an exogenous signal for the dynamic model.

10.5 Results and discussion

The following section presents the results of the multi-objective optimization with the results of the dynamic programming for a solution in the Pareto-optimal front. The multi-objective simulation is executed on the Matlab software platform in a multi-core computer (44 cores), 2.2

GHz processor with 128 GB RAM. The grid size of the control and state vector corresponding to (8.12) is kept as 8. The multi-objective simulation is executed for 100 numbers of iterations. The full simulation took around 120 hours of time with a parallel deployment of 35 cores of the computer. The size of the population for the NSGA-II algorithm is kept at 50.

The distribution of objective vectors for the first (represented by red colour dots) and final iterations (represented by blue colour dots) is shown in Figure 10.3. The findings indicate the stochastic distribution of the initial population converged to a confined zone after 100 iterations. The objective 1 (from (10.6)) is calculated by dynamic programming where as objective 2 and objective 3 are calculated by solving the linear equations (10.8) and (10.9), respectively. However, the loci of the objective vectors of the final iteration do not provide much information from this particular figure other than providing converging information.

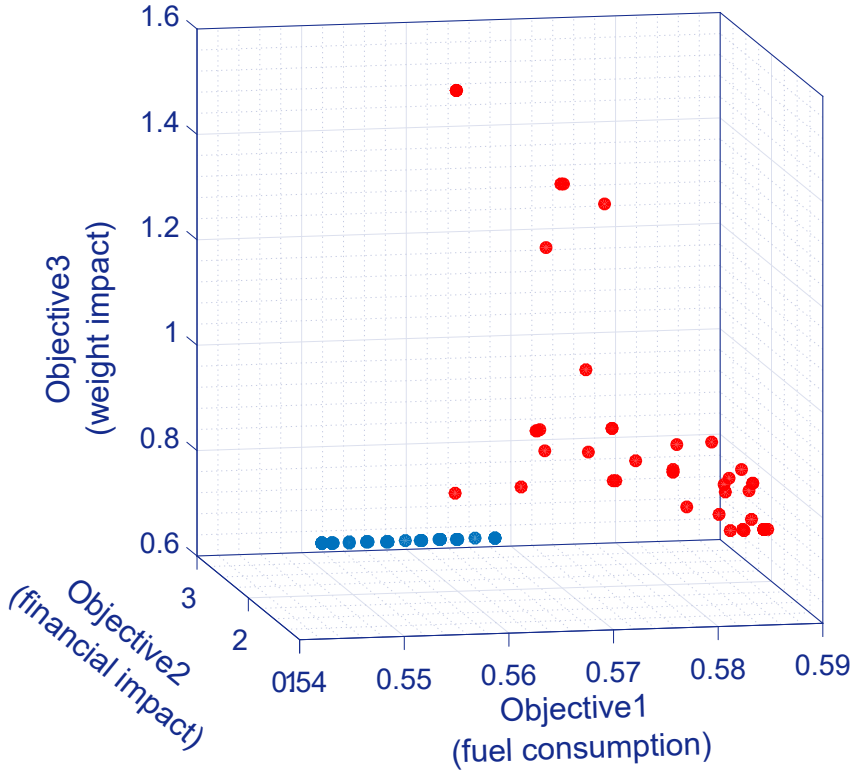


Figure 10.3: Loci of the objective vectors for the corresponding population of first (red colour) and final (blue colour) iteration

Figure 10.4 shows a zoomed view of the loci of the objective vectors of the final iteration. All of the points of the population do not belong to Pareto-optimal front. The Pareto-optimal

front (represented by red dots) constitutes around 32 % of the final population. However, it is observed that the points of the final iteration are more or less converged to a region. This observation is unusual since Pareto-optimal front was expected to be a big set. This can be attributed to the fact that the current prices and weights of the electric machine and battery form a significant portion of $FinancialCost_{EV}$ and $Weight_{EV}$ respectively for a low-powered two-wheeled vehicle. Hence, the multi-objective optimization tends to find a solution where $MaxPower_{electricmachine}$ and $MaxCapacity_{battery}$ are minimum. However, this situation need not be identical for a different segment vehicle where current prices and weights of electric machine and battery values do not form a significant portion of $FinancialCost_{EV}$ and $Weight_{EV}$ respectively.

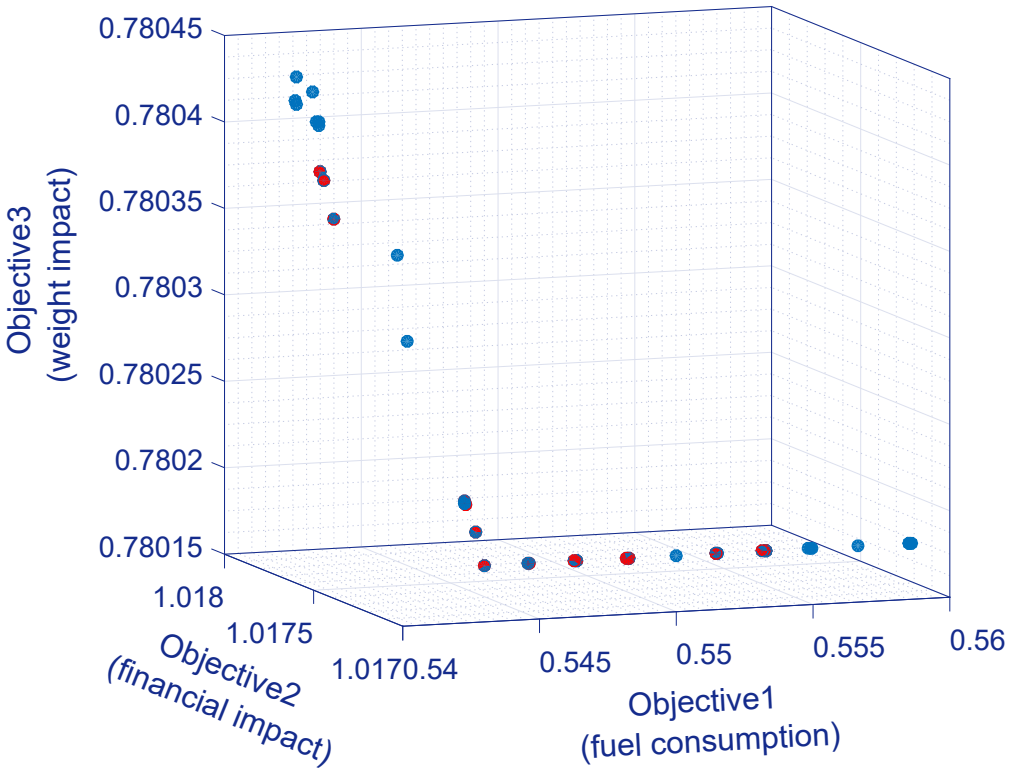


Figure 10.4: Loci of the objective vectors for the corresponding population of Pareto-optimal (red colour) and final (blue colour) iteration

Figures 10.5 - 10.7 provide a detailed 2-dimensional prospective of the Pareto-optimal front for the Figure 10.4. The Pareto-optimal points for the relations between objective 1 and objective 2 and objective 1 and objective 3 are very evident from the plot. This ensures that the

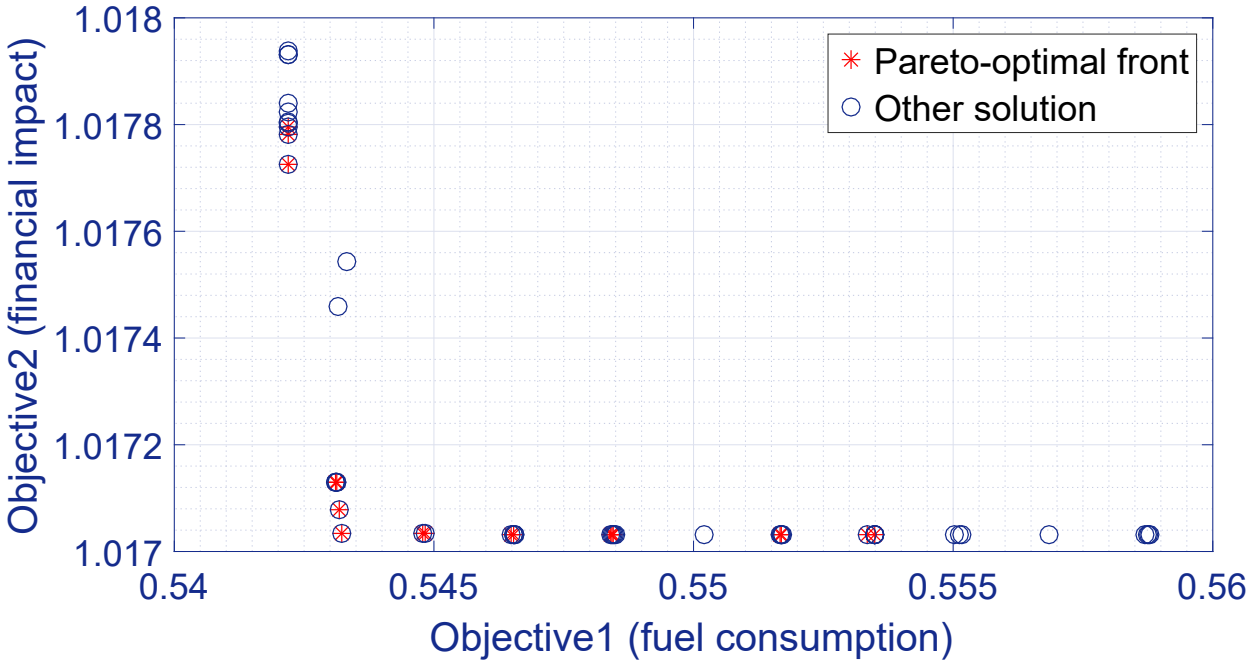


Figure 10.5: 2-dimensional prospective of the Pareto-optimal front between objective 1 and objective 2

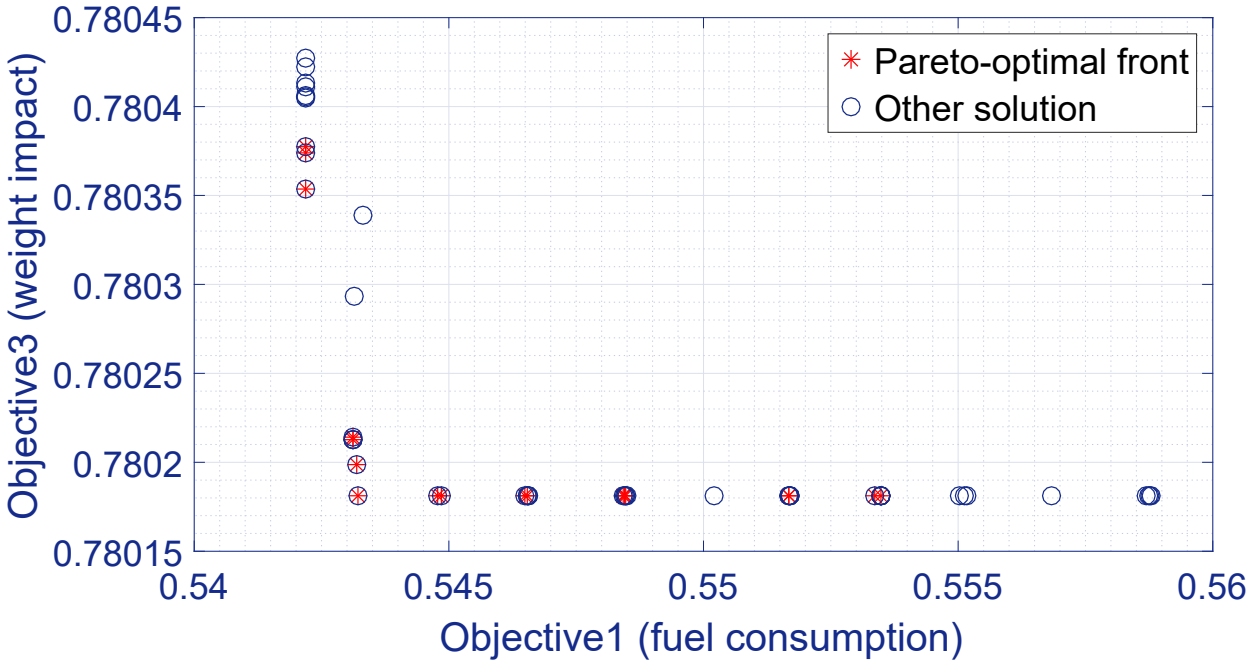


Figure 10.6: 2-dimensional prospective of the Pareto-optimal front between objective 1 and objective 3

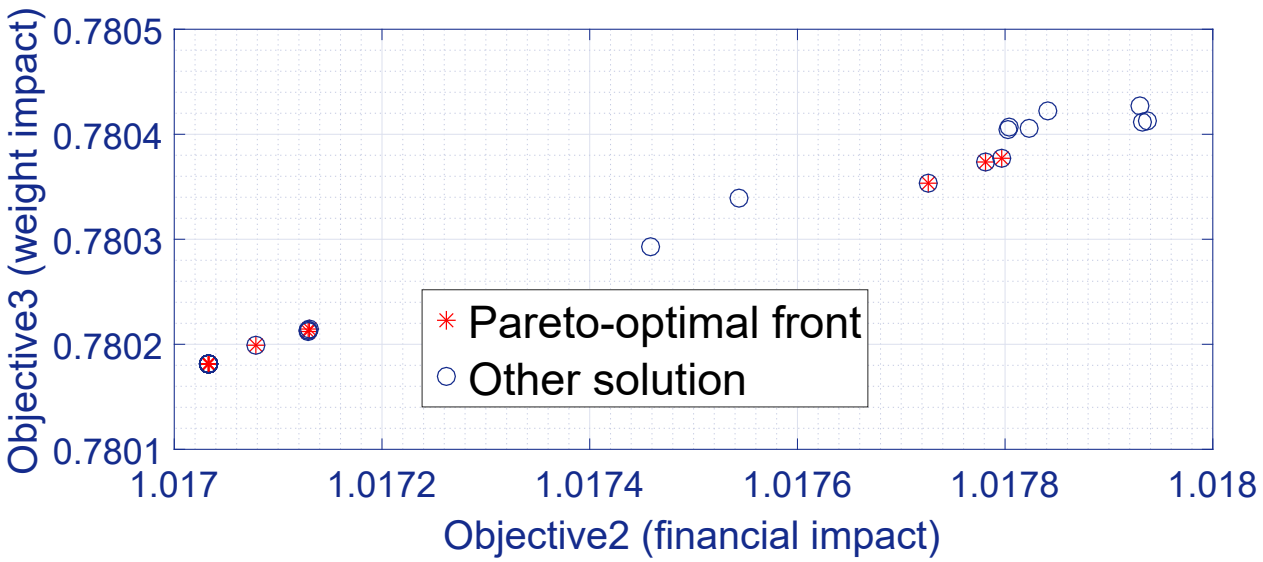


Figure 10.7: 2-dimensional prospective of the Pareto-optimal front between objective 2 and objective 3

charge sustainable configuration which consumes minimal fuel has an inverse relation with the financial cost as well the weight impact of the multi-objective design. The addition of a battery with more capacity and a more powerful electric machine would ensure lower fuel consumption and charge sustainability with more cost impact. This explains the presence of Pareto-optimal front points between objective 1 and objective 2 and objective 1 and objective 3. However, the points of Figure 10.7 do not provide us the expected Pareto-optimal front. This can be attributed to the possible relation between financial impact and weight impact objectives for the current motor-integrated powertrain. In general, these two objectives have a linear relationship between them, which can lead to the argument of combining them. However, in future powertrains, the cost of software (which would be a more dominating factor) need not have direct relation with the weight of the unit. Hence, both objectives are treated independently in this research work.

It is very important to observe the trajectory of the decision variables during the multi-objective optimization. Since the vector of the decision variable consists of 4 elements, the Figures 10.8 and 10.9 show the 3 dimensional views of the movement of the decision variables during the 100 iterations of the NSGA-II algorithm. It is clearly evident from both the figures that the decision variables are converging to zone minima from random initialization.

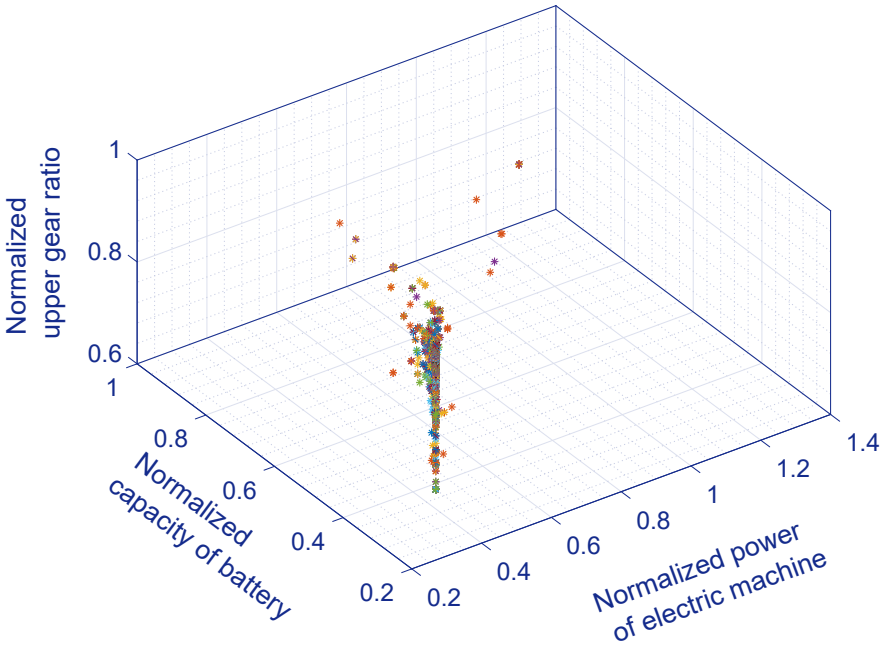


Figure 10.8: Loci of decision variables (electric machine power, battery capacity, upper gear ratio) for multi-objective optimization over 100 iterations

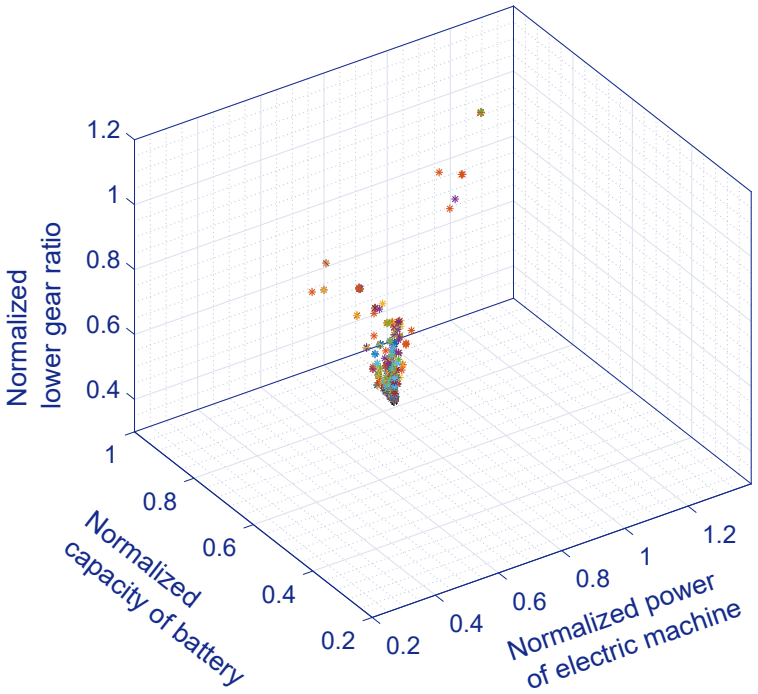


Figure 10.9: Loci of decision variables (electric machine power, battery capacity, lower gear ratio) for multi-objective optimization over 100 iterations

It is important to discuss the trajectories of dynamic programming simulation for a selected Pareto-optimal point. Since the decision variables converge to a zone rather than multiple zones, it would be correct to pick any configuration from the Pareto-optimal front. Since the decision variables converge to the point which is identical to the point found by the single function multi-objective optimization method in the previous chapter, the earlier discussion holds good here.

10.6 Conclusions

The chapter presented a multi-objective optimization coupled with a numerical optimal method for a motor-integrated hybrid powertrain. The NSGA-II algorithm is suitable for multi-objective optimization due to its inherent strength. The numerical optimal control method is implemented using the dynamic programming method and it is used for evaluation of part of the objective vector. The multi-objective simulation provides a Pareto-optimal front of possible sizes of different components of the motor-integrated powertrain. The decision variables of the multi-objective simulation are observed to converge to a feasible zone indicating the presence of a global optimal point for the design. The trajectories of state and control for a Pareto-optimal point indicate meeting the objective of fuel consumption minimization and battery charge sustainability of the powertrain.

Chapter 11

Optimal controller for the motor-integrated transmission using hp-adaptive collocation

11.1 Introduction

Various numerical methods based on optimization approaches have been developed to solve optimal problems with recent progress in numerical methods. Arguably the most powerful numerical methods for solving general optimal control problems are direct collocation methods [86, 89, 91]. A direct collocation method is a state and control parametrization method where the state and control are approximated using a specified functional form. However, there are very few references available which present optimal controllers based on the direct collocation method for motor-integrated powertrain applications. It is very important to realize a numerical method-based optimal controller since it provides the stepping stone for possible future real-time implementation. The research for motor-integrated powertrain can be integrated on future vehicles only if the controller can be implemented on a real-time platform.

The main aim of this chapter is to investigate an optimal controller based on a numerical

method which can:

1. reduce fuel consumption and maintain charge sustainability for the hybrid powertrain;
2. be considered for future real-time application.

In this research, the multi-objective optimal control design problem for the two-wheeled hybrid powertrain is addressed with a hp-adaptive direct collocation method.

11.2 Numerical methods for Optimal Control

The formulation for the optimal problem is presented in Chapter 2. The optimal problem mentioned in (2.1), (2.2), (2.3) and (2.4) can be solved using various numerical methods. The numerical methods should consist of the following sub modules

1. numerical solvers for differential and integration functions
2. numerical solver for solving a nonlinear optimization problem
3. numerical solver for nonlinear algebraic equations

Figure 2.1 shows the major types of numerical optimal control methodologies based on the above-mentioned modules. The direct method is the combination of numerical methods for differential equations with non-linear optimization whereas the indirect method is the combination of numerical methods for differential equations with numerical solution of systems of non-linear equations. Figure 2.2 gives a top level overview of different methods of solving a numerical optimal control problem. Overall, there are three numerical approaches which are predominantly used in optimal control research viz dynamic programming, the indirect method and direct method [86, 87, 89, 145]. Dynamic programming is based on the principle of optimality which states that any subarc of an optimal trajectory is also optimal. It calculates recursively backwards the values of control which can guarantee the minimum value of the cost function. If the time steps are decreased infinitely small, then dynamic programming leads to the Hamilton Jacobi Bellman (HJB) equation. The equation leads to a partial differential equa-

tion in state space which needs to be solved backwards numerically [146]. There are numerical methods that can solve HJB equations, however the numerical methods suffer from "curse of dimensionality". The main advantage of this method is that it searches the whole state space for finding the global minimum value. Hence this method is very much suitable for calculating the global optimal controller for benchmarking different sub-optimal controllers.

The Indirect methods use the necessary conditions of optimality of the problem which leads to a multiple point boundary-value problem (BVP). The necessary conditions of optimality are expressed as Pontryagin's Maximum Principle [147] and the indirect method requires the adjoint equation, control equation and all the transversality conditions (in case they exist). There are several methods for solving the indirect methods numerically [87, 89]. The basic method for this is the shooting method. In this method at one end of the boundary of the BVP, a guess for the control is made and the Hamilotonian ($\mathcal{H}$) is integrated until the other end (either from t_0 till t_f in forward direction or from t_f till t_0 in backward direction).

$$\dot{\mathbf{x}}(t) = \left[\frac{\partial \mathcal{H}}{\partial \lambda}\right], \dot{\lambda} = \left[\frac{\partial \mathcal{H}}{\partial \mathbf{x}}\right] \tag{11.1}$$

where

$$\mathcal{H}\left(\mathbf{x}, \lambda, \mu, \mathbf{u}, t\right) = \mathcal{L} + \lambda^T f - \mu^T C, \tag{11.2}$$

where $\mathcal{L}$ is the Lagrangian, $\lambda(t) \in R^n$ is the adjoint, $\mu(t) \in R^c$ is the Lagrange multiplier associated with the path constraints C, f is the dynamic constraint, $\mathbf{x}$ is the state vector and $\mathbf{u}$ is the control vector.

If the integrated terminal condition is different from the known terminal condition as expressed in (11.3) and (11.4) by a specified tolerance, the initial condition is modified followed by another integration. This iterative process is continued until the final condition falls inside the tolerance band:

$$\phi((\mathbf{x}(t_0), t_0, (\mathbf{x}(t_f), t_f) = 0 \tag{11.3}$$

$$\lambda(t_0) = -\frac{\partial \phi}{\partial \mathbf{x}(t_0)} + \nu^T \frac{\partial \phi}{\partial \mathbf{x}(t_0)}, \lambda(t_f) = \frac{\partial \phi}{\partial \mathbf{x}(t_f)} - \nu^T \frac{\partial \phi}{\partial \mathbf{x}(t_f)} \tag{11.4}$$

where ν is the Lagrange multiplier associated with the boundary conditions ϕ. The problem with the shooting method is the numerical difficulties caused by the dynamics of the Hamilotonian [89, 147]. Multiple shooting is a modified method, which is developed to overcome the numerical difficulties of the shooting method. In the multiple shooting method, the time duration between t_0 and t_f is segmented into multiple sub-intervals. The above-mentioned shooting method is then applied in each segment $[t_i, t_{i+1}]$ with state and adjoint of the interior intervals unknown. The following continuity condition needs to be satisfied in multiple shooting methods:

$$\begin{bmatrix} \mathbf{x}(t_i^-) \\ \lambda(t_i^-) \end{bmatrix} = \begin{bmatrix} \mathbf{x}(t_i^+) \\ \lambda(t_i^+) \end{bmatrix}. \tag{11.5}$$

Indirect methods satisfy the necessary condition for local optimality. However the solution of multiple shooting methods are sensitive to the guess of the costate elements $\mathbf{x}(t)$ and $\lambda(t)$.

The direct methods are inspired by non-linear programming (NLP) [87,89,147] techniques. The state and/or control are discretized based on the technique that has been selected followed by optimization. If the control is discretized the approach is named as control parametrization. There are two approaches for control parametrization as shown in Figure 2.2, direct shooting and direct multiple shooting. Direct shooting is conducted by converting the control to the functional form [87, 89, 147]

$$\mathbf{u}(t) \approx \sum_{i=1}^{m} a_i \psi_i(t). \tag{11.6}$$

with discrete controls $\mathbf{u}(t)$ on the fixed grid $t_0 = t_1 < t_2 < ... < t_m = t_f$ and states $\mathbf{x}(t)$ as dependent variables for the duration $[t_0, t_f]$. In the expression for $\mathbf{u}(t)$, $\psi_i(t)$s are known mathematical functions and a_is are the parameters that need to be determined after optimization. The trajectories of of states are calculated using numerical integration as a function of $\mathbf{u}(t)$ and t. The NLP is obtained after the control discretization and numerical integration is solved with a finite dimensional optimization solver. Multiple shooting for the direct method follows the same process as multiple shooting for the indirect method. The interval $[t_0, t_f]$ is subdivided into multiple segments and the above-mentioned direct shooting method is deployed in each

segment enforcing continuity for states as [148]

$$\mathbf{x}(t_i^-) = \mathbf{x}(t_i^+). \tag{11.7}$$

The other direct method is a state and control parametrization method. Another name for this method is direct collocation method. There are two sub methods under direct collocation method, as shown in Figure 2.2; local collocation and global collocation. The local collocation method is similar to the above-mentioned control parametrization method. The method is subdivided into two methods based on the discretization scheme. Implicit/explicit integration is implemented using the Runga-Kutta method, whereas the orthogonal collocation can be realized using collocation points, which are roots of the used orthogonal polynomial. The final method of numerical optimal control is global collocation, which is commonly known as pseudospectral collocation. The above-mentioned local collocation methods solve the problem piece by piece, whereas the pseudospectral collocation approximates the entire problem with a Lagrange polynomial which is approximated by a quadrature rule such as Gauss, Gauss-Lobatto, etc.

The research presented in this thesis is based on the sub-interval pseudospectral method, named the Legendre-Gauss-Radau (LGR) collocation method. The total time interval of the optimal problem $[t_i, t_f]$ is split into subintervals $[t_k, t_{k+1}]$ and every subinterval is solved by using an independent pseudospectral collocation method. This method is superior to other methods due to the fact that it provides highly accurate states, controls, and costate approximations while maintaining a relatively low-dimensional approximation of the continuous-time problem. The time variable t is converted to an independent variable $\tau \in [-1, +1]$ where

$$t = \frac{t_f - t_0}{2}\tau + \frac{t_f + t_0}{2}. \tag{11.8}$$

The optimal control problem is expressed in terms of τ now. The time interval $[t_i, t_f]$ is split into K subintervals with $k = 1, 2, ..., K$ and $(\tau_1^{(k)}, ..., \tau_{N_{(k)}}^{(k)})$ are the LGR collocation points in the mesh interval k defined in the subinterval $\tau^k \in [t_{k-1}, t_k)$. The continuous approximations

of state and control are expressed as

$$\mathbf{x}^{(k)}(\tau) = \sum_{j=1}^{N_{(k)}+1} \mathbf{X}_j^{(k)} l_j^{(k)}(\tau) \tag{11.9}$$

$$\mathbf{u}^{(k)}(\tau) = \sum_{j=1}^{N_{(k)}+1} \mathbf{U}_j^{(k)} l_j^{(k)}(\tau) \tag{11.10}$$

where l_j^k with $k = 1, 2, ..., K$ and $j = 1, 2, ..., N_{(k)} + 1$ is a basis of Lagrange polynomial (11.11) for the k^{th} subinterval of $[t_i, t_f]$:

$$l_j^k(\tau) = \prod_{l=1, l\neq j}^{N_{(k)}+1} \frac{\tau - \tau_l^{(k)}}{\tau_j^{(k)} - \tau_l^{(k)}}. \tag{11.11}$$

The $\mathbf{X}$ and $\mathbf{U}$ of (11.9) and (11.10) are the approximation of the state and control for the optimal control problem. The derivative for the state with respect to τ can be represented as

$$\frac{d\mathbf{x}^{(k)}(\tau)}{d\tau} = \sum_{j=1}^{N_{(k)}+1} \mathbf{X}_j^{(k)} \frac{dl_j^{(k)}(\tau)}{d\tau}. \tag{11.12}$$

The cost function expressed in (2.1) can be shown as

$$J = \Phi\left[\mathbf{X}_1^{(1)}, t_0, \mathbf{X}_{N_K+1}^{(K)}, t_f, \mathbf{q}\right] \tag{11.13}$$

with

$$\mathbf{q} = \frac{t_f - t_0}{2} \int_{-1}^{+1} \mathcal{L}\left(\mathbf{x}(\tau), \mathbf{u}(\tau), \tau\right) d\tau. \tag{11.14}$$

The dynamic equations (2.2) and (11.12) can be expressed as a dynamic constraint

$$\sum_{j=1}^{N_{(k)}+1} \mathbf{X}_j^{(k)} \frac{dl_j^{(k)}(\tau)}{d\tau} - \frac{t_f - t_0}{2} f\left(\mathbf{X}_i^{(k)}, \mathbf{U}_i^{(k)}, \tau_i^{(k)}\right) = 0 \tag{11.15}$$

where $(i = 1, .., N_k)$. Equations 11.14 and 11.15 with path constraints (2.3) and boundary conditions (2.4) can be treated as an NLP. The NLP is solved based on the KKT condition of the NLP and the collocation is redone in case the convergence of the solution is not achieved.

The flowchart for the above-mentioned LGR collocation method is shown in Figure 11.1.

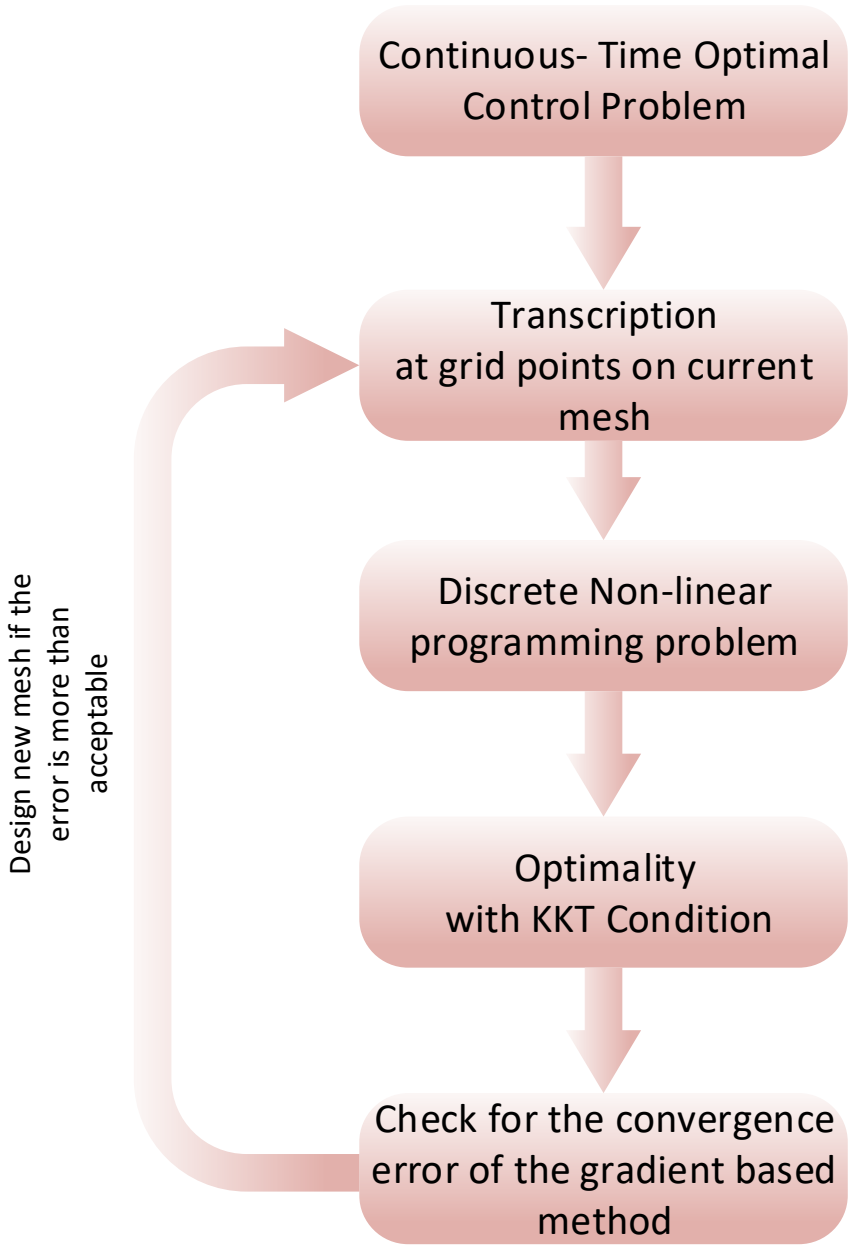


Figure 11.1: Flowchart of pseudospectral collocation method

The mesh mentioned in the second step of the flowchart is an important part of this method. The mesh refinement can be implemented by two different variable-order methods. In this research, the hp-adaptive mesh refinement method is adopted. This method increases the order of the polynomial (p) when the solution is smooth and the convergence rate is small, and

also splits the problem into further sub-intervals (h) when the solution changes rapidly thus improving computational efficiency of solving the NLP. The integration of the h method with the p method allows different segmentation rates and orders of the polynomial interpolation in every subinterval. hp-adaptive collocation is an iterative method and the stop condition is given when a suitable error or a bounded iteration is achieved. These features ensure this method has a desirable adaptation to any optimization problem and better convergence rate for most of the problems. On the other hand, this is an iterative method and, depending on the problem, the convergence of the solution may be not achieved in a suitable limit of iteration. One of the drawbacks of adapting the above method is its inherent weakness with non-smooth functions. Considering all the numerical optimal control methods, hp-adaptive collocation provides more flexibility in designing the optimal controller. Hence this method is adopted for further work.

11.3 Optimal control problem formulation

The objective of the optimal control is to reduce fuel consumption of the IC engine considering the battery SOC level should not deviate from a pre-determined level. The multi-objective cost function is expressed as a single function with equal weighting factors as in equation (11.13)

$$J = \Phi\left[\mathbf{X}_1^{(1)}, t_0, \mathbf{X}_{N_K+1}^{(K)}, t_f, \mathbf{q}\right]$$

where

$$\mathbf{q} = \dot{m}_f * \omega_1 + \frac{d\left((SOC - SOC_{target})^2\right)}{dt} * \omega_2 \tag{11.16}$$

in which ω_1 and ω_2 are different weighting factors for both the objectives of the cost function. In this particular research both of these factors are kept the same ($\omega_1 = \omega_2 = 0.5$) . The dynamics of the system is expressed in (8.13), (8.14), (8.15), (8.16) and (8.17). The exact boundary conditions of the problem are not expressed in this thesis due to confidentiality of the limits. The initial guess of the problem is very crucial as this method is not a global optimal control

method. The initial guess of the trajectories of states $\mathbf{X}$ and controls $\mathbf{U}$ of (11.9) and (11.10) respectively are calculated by solving the dynamic equation for the system with known control signal before starting the LGR collocation method as shown in Figure 11.1. In this chapter, the hp-collocation method is compared with the DP method, which was presented in Chapter 9. The cost function for the DP method is formulated as in (9.16).

11.4 Mathematical tools for hp-adaptive collocation method and dynamic programming

The explained LGR or hp-adaptive collocation method are implemented using the commercially available MATLAB software program called GPOPS-II [148]. An adaptive mesh refinement method is implemented in the software that determines the number of mesh intervals and the degree of the approximating polynomial within each mesh interval to achieve a specified accuracy. The software can be interfaced with either quasi-Newton (first derivative) or Newton (second derivative) NLP solvers, and all derivatives required by the NLP solver are approximated using sparse finite-differencing of the optimal control problem functions. In this research the NLP software package IPOPT [149] is used to solve the NLP resulting from the above-mentioned collocation. The NLP solver package IPOPT requires to obtain the solution of sparse, symmetric, indefinite linear systems by using the linear solver MA57 [150].

The dynamic programming simulation is conducted using the MATLAB software function presented in [136].

11.5 Results and discussion

In this section simulation results of the hp-adaptive collocation method is presented and compared with the simulation results of the dynamic programming method. The dynamic program method ensures a global optimal control which works as a benchmark design for the perform-

ance of the hp-adaptive collocation method for the motor-integrated hybrid powertrain. The simulation is conducted on the motor-integrated powertrain as shown in Figure 7.1 with the motor, IC engine, Battery and CVT gear box presented in Chapter 8. The problem formulation, starting condition, end condition and boundary conditions for both the methods are kept identical. The simulation is conducted for the Indian drive cycle as shown in Figure 8.3 in a computer with operating system Windows 10 and Intel Xenon CPU E5-2699 (2.20 GHz , 44 core, 128 GB RAM) processor. The entire simulation takes around 140 hours of time for the hp-adaptive collocation method. The simulation is conducted for six iterations of mesh. The initial three mesh iterations results in infeasible solutions followed by optimal solution as reported by GPOPS2 software program. The simulation results for the hp-adaptive collocation method are presented for each mesh calculation which provides more insight into the method. The dynamic programming method is conducted on same computer with the mesh size of control and state of twelve each. The dynamic programming method takes around twenty four hours of time for the simulation.

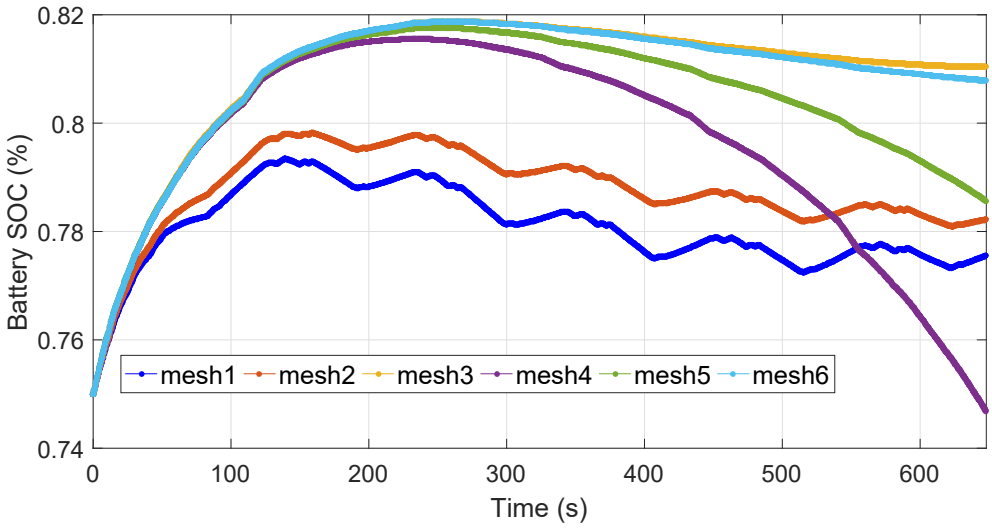


Figure 11.2: Battery SOC during IDC with hp-adaptive collocation method

Figures 11.2 and 11.3 show the trajectory of the state SOC for the hp-adaptive collocation method and dynamic programming method respectively. The objective function mentioned in equation (11.16) provides importance on maintaining the SOC on a target value. The trajectories of different mesh iterations with the hp-adaptive collocation method indicate that

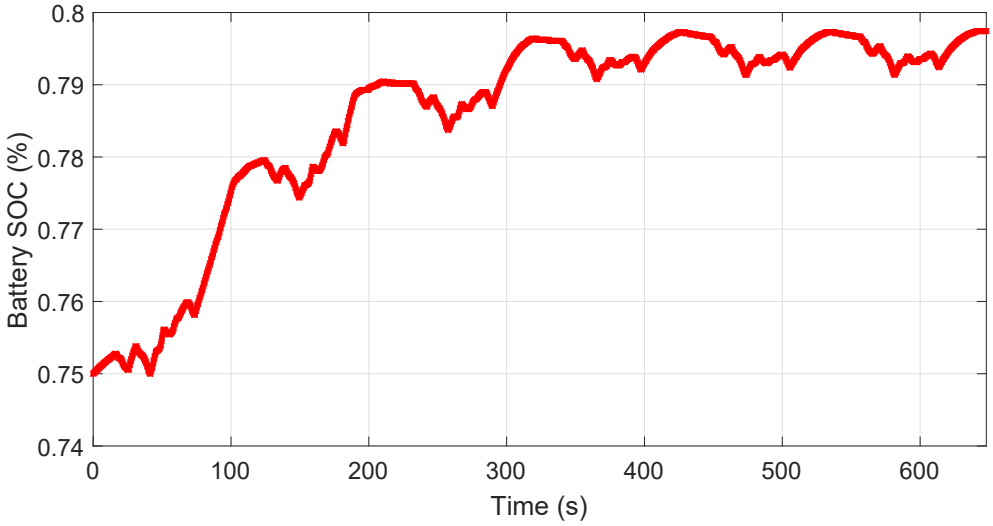


Figure 11.3: Battery SOC during IDC with dynamic programming method

the optimal control provides more importance of maintaining charge sustainability from the first cycle of the drive cycle whereas the dynamic programming method follows a different strategy to maintain charge sustainability.

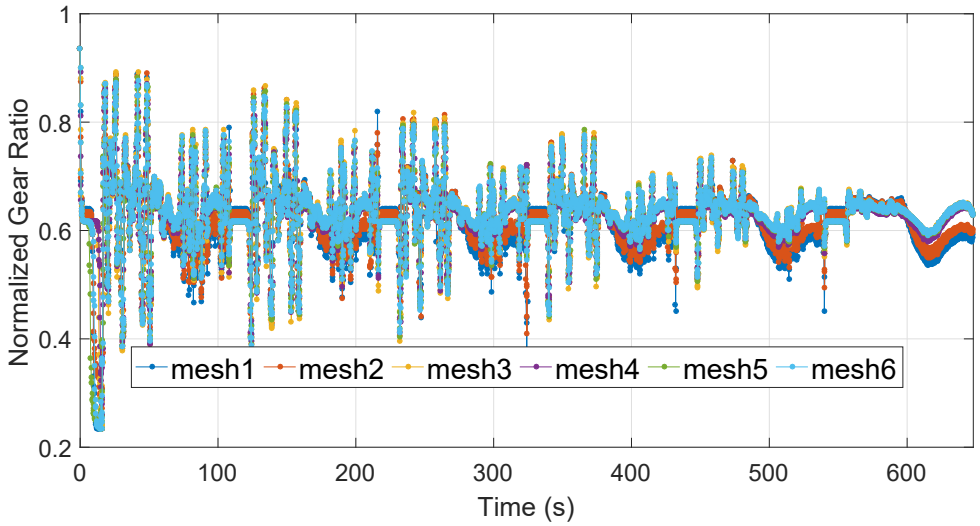


Figure 11.4: Normalized Gear Ratio during IDC with hp-adaptive collocation method

The trajectory of the CVT gear ratio control signal in Figures 11.4 and 11.5 provides the clear perspective of the difference of both the numerical optimal control methods. Figure 11.4 constitutes several higher frequency components which necessitates the need of zoomed Figures 11.6, 11.7 and 11.8 corresponding to the first, third and sixth sub-cycle of the complete drive cycle. The hp-adaptive collocation method maintains a higher gear ratio compared to

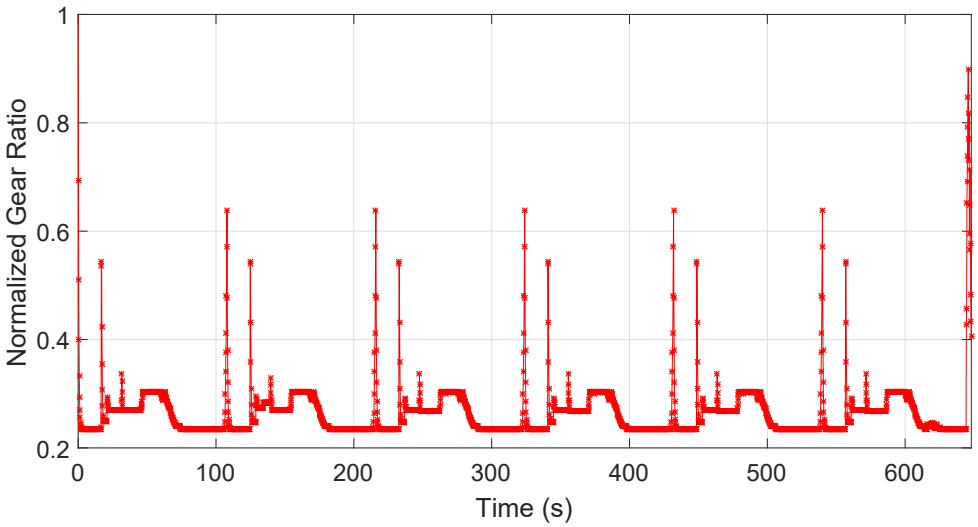


Figure 11.5: Normalized Gear Ratio during IDC with dynamic programming method

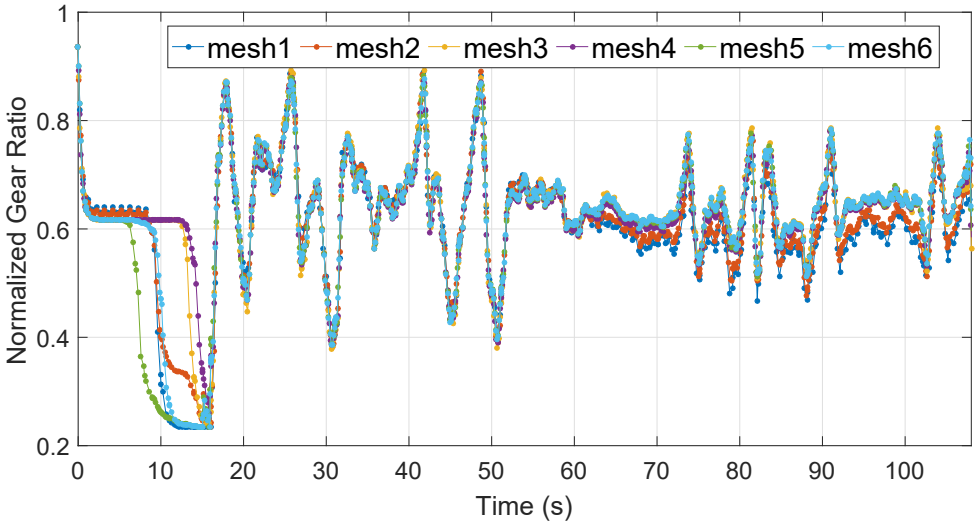


Figure 11.6: Normalized Gear Ratio during first cycle of IDC with hp-adaptive collocation method

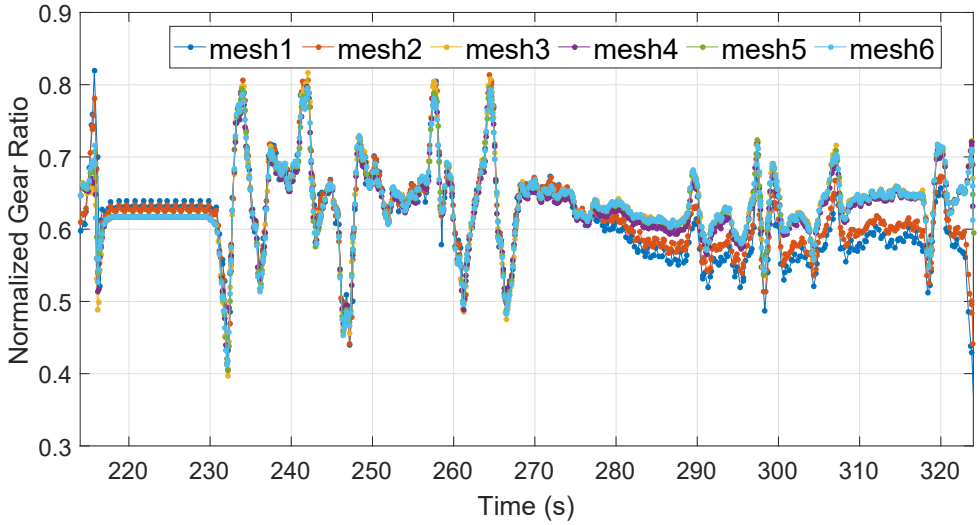


Figure 11.7: Normalized Gear Ratio during third cycle of IDC with hp-adaptive collocation method

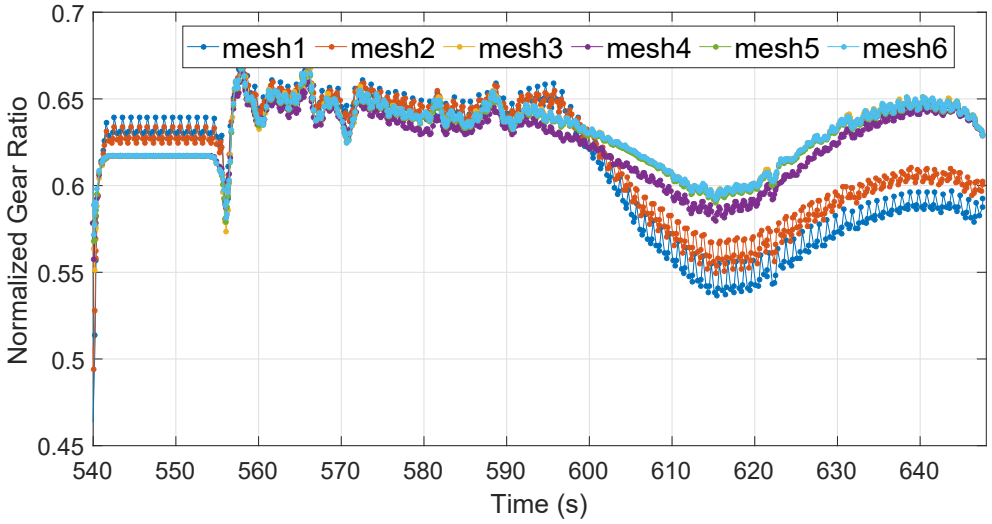


Figure 11.8: Normalized Gear Ratio during sixth cycle of IDC with hp-adaptive collocation method

DP and the gear control trajectory tends to control the CVT gear ratio for meeting the wheel torque requirement. The relations between gear ratio control in Figures 11.6, 11.7 and 11.8 and corresponding trajectories of engine speed in Figures 11.11, 11.12 and 11.13 in hp-adaptive collocation method are worth noticing. In the case of the first sub cycle of the drive cycle, the CVT gear control is performed dynamically so that the reference vehicle speed trajectory is followed. The CVT gear control increases the gear ratio for wheel acceleration requirements and vice versa. The same trajectory is repeated for the third sub cycle, however the same can not be said for the sixth sub cycle. This observation can be only attributed towards the battery charge sustaining strategy followed by the hp-adaptive collocation method. In the case of dynamic programming the CVT gear control shown in Figure 11.5, does not follow the wheel torque requirement.

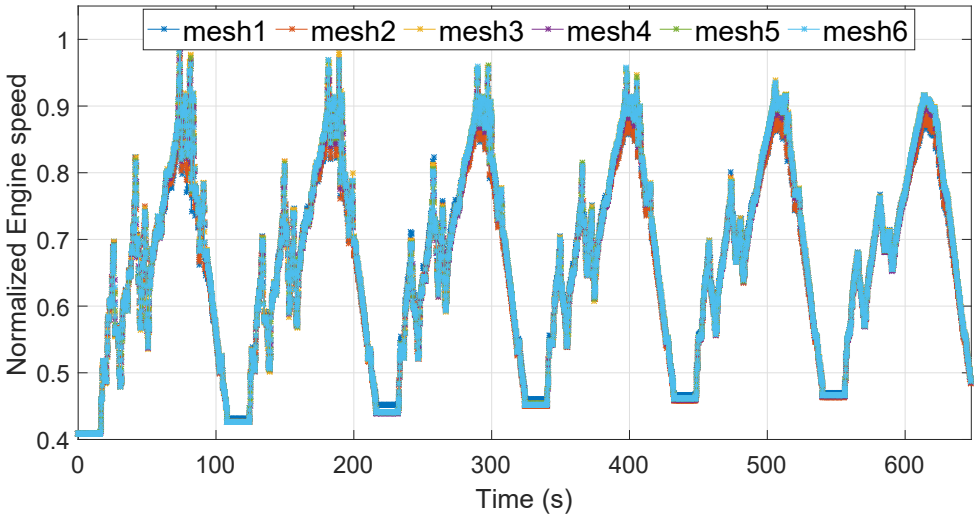


Figure 11.9: Normalized Engine Speed during IDC with hp-adaptive collocation method

In that case, the wheel power requirement is met by the supply of power by the electric machine as shown in Figure 11.15. The control of electric torque adopted by the dynamic programming method is reflected in battery SOC trajectory shown in Figure 11.3. The trajectory of electric power by the hp-adaptive collocation method, shown in Figure 11.14 is very interesting. The results of the initial mesh simulations tries to control the electric machine power during the acceleration phase of the drive cycle. The impact of the electric machine power control trajectory is visible in initial mesh iterations of battery SOC in Figure 11.2. However,

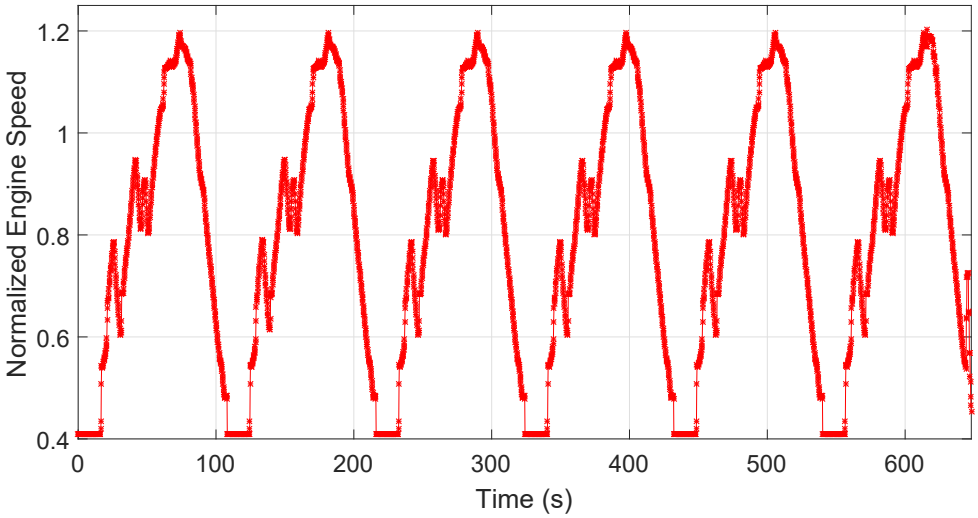


Figure 11.10: Normalized Engine Speed during IDC with dynamic programming method

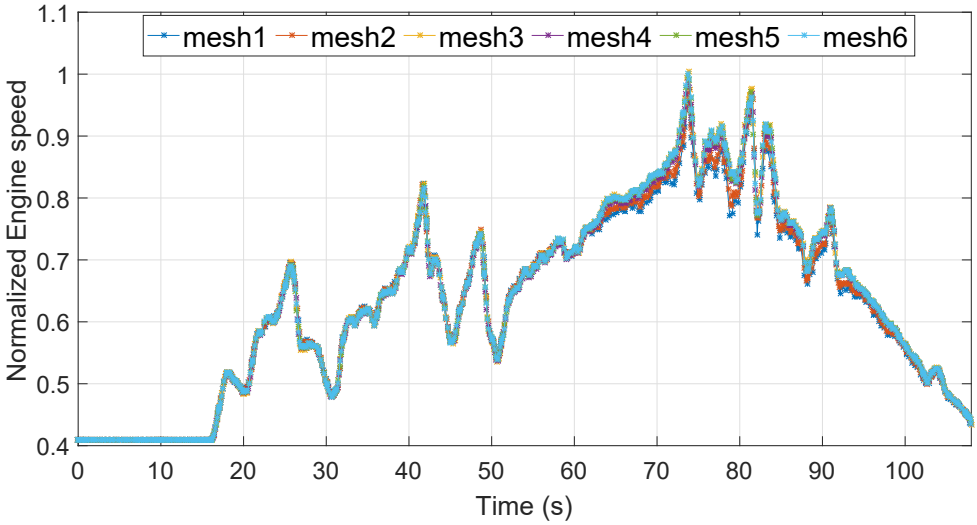


Figure 11.11: Normalized Engine Speed during first cycle of IDC with hp-adaptive collocation method

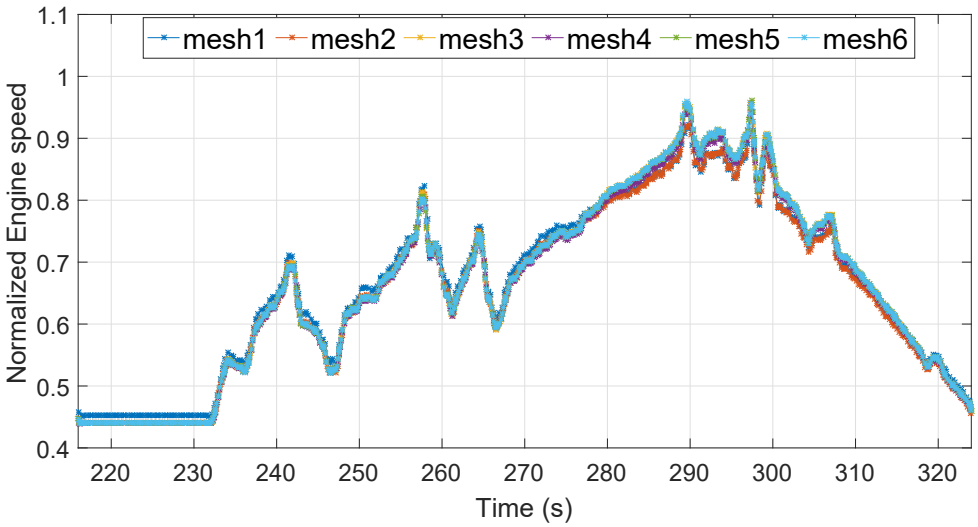


Figure 11.12: Normalized Engine Speed during third cycle of IDC with hp-adaptive collocation method

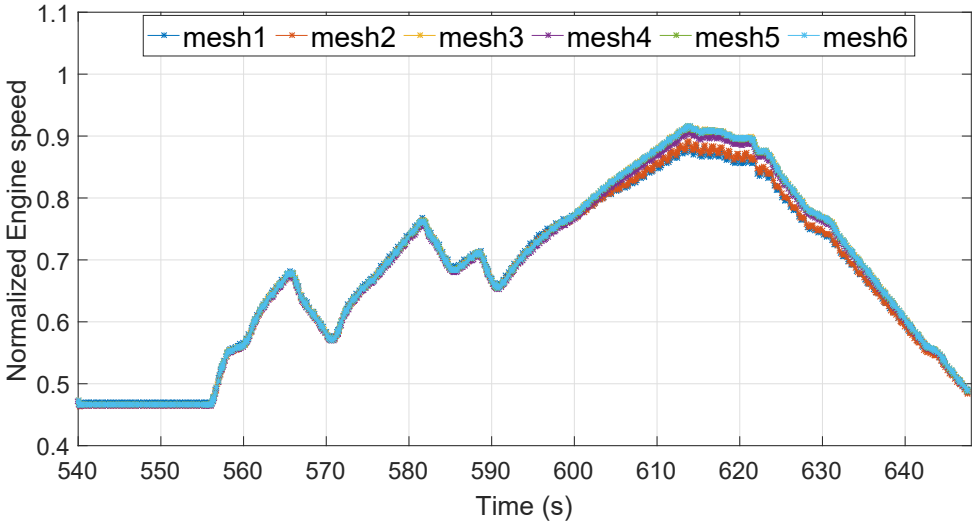


Figure 11.13: Normalized Engine Speed during sixth cycle of IDC with hp-adaptive collocation method

the mesh results suggest that the restoration phase for these iterations is unsuccessful. However due to these results the number of collocation points are increased to solve the problem, which results in a trajectory for the electric machine power control which indicates a battery SOC conservative strategy. The use of the term "conservative" is justified by the tendency of the methods to maintain the battery SOC level at a predefined a target value. In the case of the dynamic programming method, the battery charging and discharging is synchronized with acceleration and deceleration of the drive cycle.

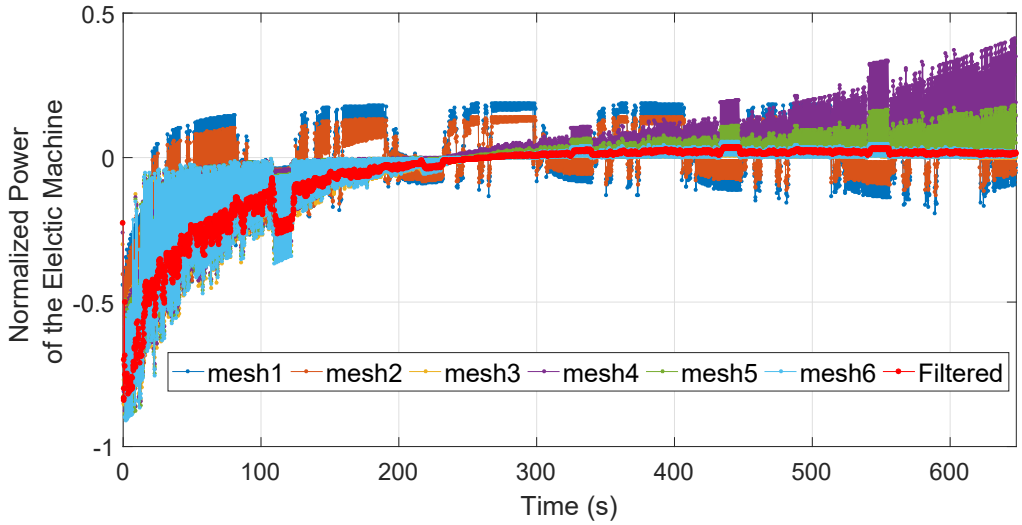


Figure 11.14: Normalized power of the electric machine during IDC with hp-adaptive collocation method

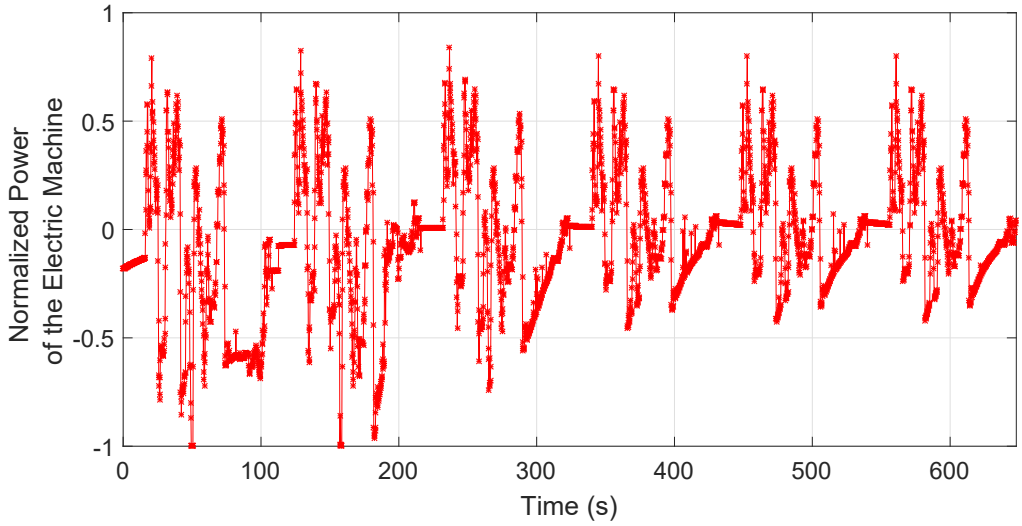


Figure 11.15: Normalized power of the electric machine during IDC with dynamic programming method

As mentioned in earlier discussion, the hp-adaptive collocation method gives priority to

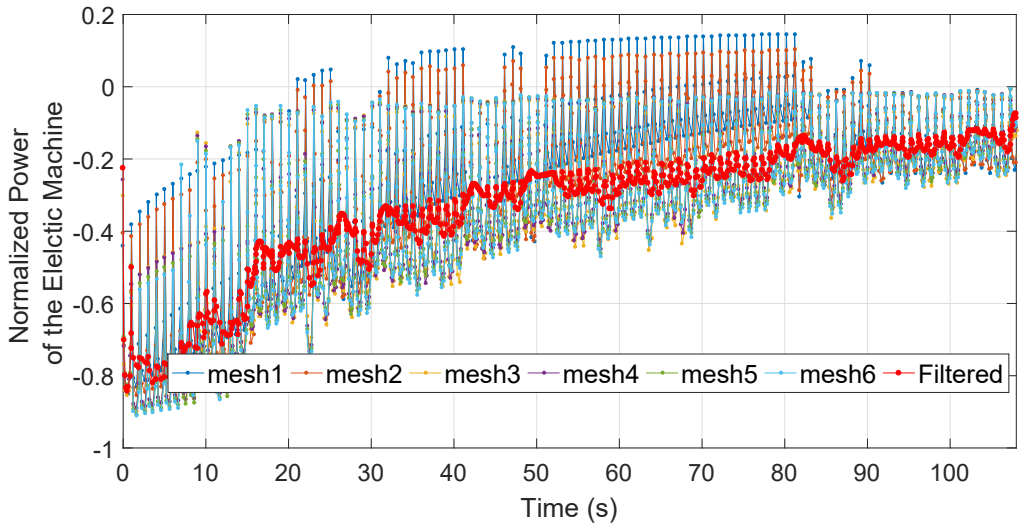


Figure 11.16: Normalized power of the electric machine during first cycle of IDC with hp-adaptive collocation method

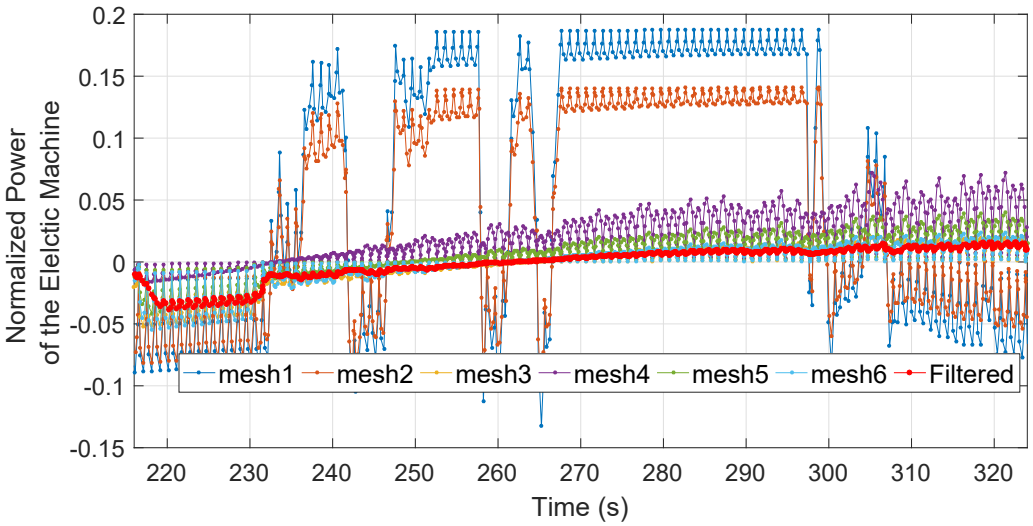


Figure 11.17: Normalized power of the electric machine during third cycle of IDC with hp-adaptive collocation method

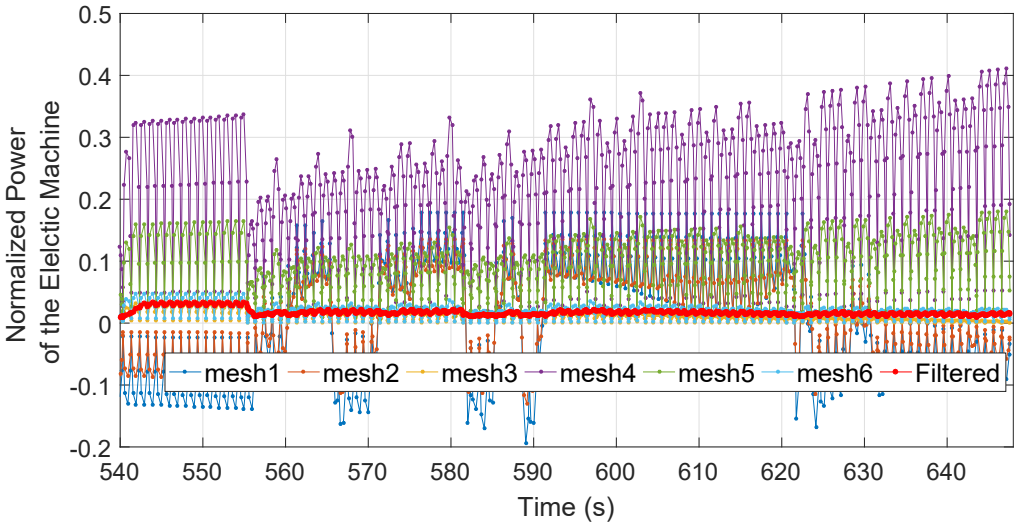


Figure 11.18: Normalized power of the electric machine during sixth cycle of IDC with hp-adaptive collocation method

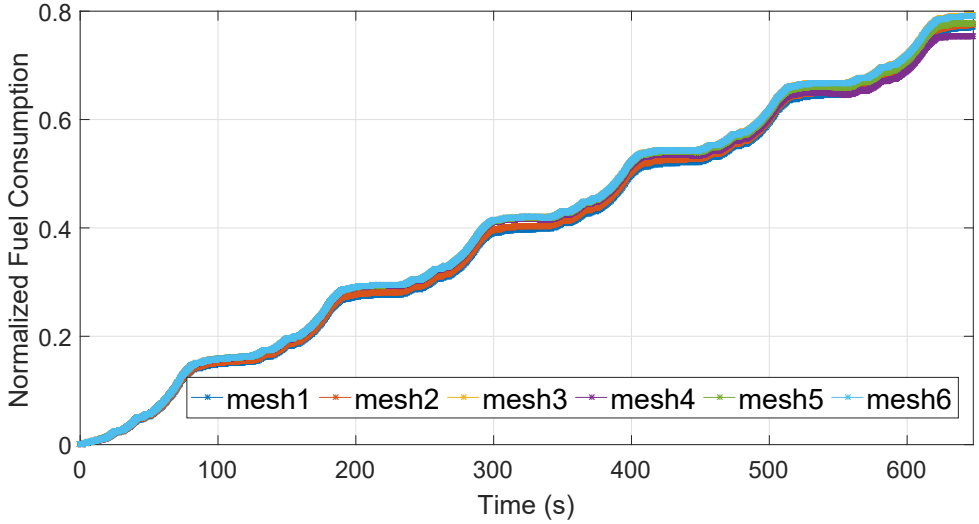


Figure 11.19: Normalized fuel consumption during IDC with hp-adaptive collocation method

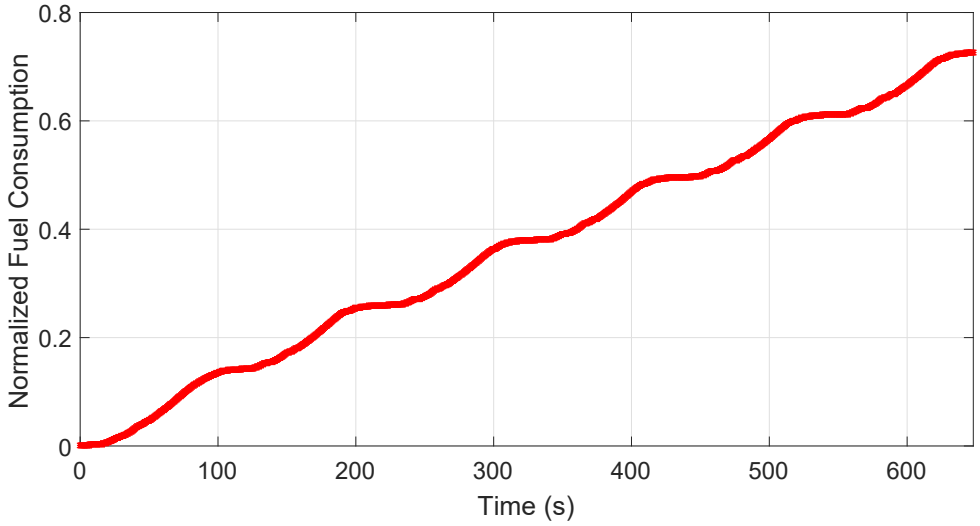


Figure 11.20: Normalized fuel consumption during IDC with dynamic programming method

maintaining the battery SOC at a target level which results in more fuel consumption compared to the dynamic programming method. Figures 11.19 and 11.20 show the fuel consumption during the drive cycle simulation. The trajectory of the fuel consumption for different mesh iterations for the hp-adaptive collocation looks consistent during the first, second and third sub-cycle of the drive cycle in Figure 11.19. However, the mentioned trajectories start deviating from each other due to the change of use of the electric machine by the optimal control method. The fuel consumption for the hp-adaptive collocation method is around 11% more than the dynamic programming method.

11.6 Conclusions

The chapter presented an overview about different numerical optimal methods. The hp-adaptive collocation method was chosen in this work due to its advantages over the other numerical optimal control methods. The objective function of the optimal control problem is formulated with equal weightage towards minimizing the fuel consumption and maintaining the battery SOC near a pre-defined level. The minimization of fuel consumption definitely results in reduction in exhaust gas emissions and the second objective ensures charge sustainability of the vehicle, which is very much essential for a two-wheeled vehicle used for personal

transportation in an urban city. The control and state trajectories of the hp-adaptive collocation method are compared with the corresponding trajectories determined using the dynamic programming method. The hp-adaptive collocation and dynamic programming methods give different importance to the elements of the control vector. The fuel consumption of the hp-adaptive collocation method is 11% more than the dynamic programming method. However, the hp-adaptive collocation method can be explored further for real-time implementation with shorter future horizon.

Chapter 12

Conclusions and Future Work

The work presented in the thesis provides a detailed insight into the optimal control of a motor-integrated hybrid powertrain for a two wheeler application particularly suitable for a scooter platform.

The prerequisite for an optimal control methodology is a control-oriented mathematical model of the motor-integrated hybrid powertrain. Hence, the initial section of the thesis is dedicated to the dynamic model development of the powertrain. The task of first principle-based dynamic model development of the powertrain is chosen over using commercially available models, due to possible future flexibility of developing unconventional powertrains, as well as to have full transparency of the models. The proposed dynamic model of the SI engine is based on the mean value approach, as well as the crank angle approach. The mean value approach is suitable for slower dynamics of the SI engine model, whereas the crank angle-based model is suitable for in-cylinder dynamics. The experimental data from the production SI engine is very crucial to calibrate and verify the dynamic model of the SI engine. The model needs to couple with a suitable transmission model which is very much essential for the powertrain configuration. The challenges due to unavailability of full information about the gear-less transmission can be tackled by an analytical method which is inspired by the physics of the system. The comparison of the fuel consumption and NOx emission from a gear-less powertrain and a geared powertrain is important for choosing the suitable transmission. The mathematical

model provides a sound and suitable platform for conducting drive cycle simulation to evaluate both the powertrains. However, it is concluded that evaluation of fuel consumption and NOx emission is not sufficient to choose the suitable transmission.

The other characteristic for choosing a suitable transmission is inspired by the very important customer requirement of smooth drivability. The drivability evaluation is traditionally subjective for the low-powered two wheeler application. The subjective evaluation can be converted to an objective evaluation by proposing a suitable methodology. The proposed methodology identified several parameters from the longitudinal drive characteristics of the vehicle and drivability simulation is conducted for the tip in and launch scenarios. It is concluded from the simulation results that gear-less transmission is suitable for the motor-integrated hybrid powertrain. The components for the electric traction system are selected based on commercially feasible options in automotive industry. The BLDC motor drive with Li Ion battery is selected for the proposed motor-integrated hybrid powertrain. The selection of a suitable mounting position of the electric motor is influenced by possible future applications in other types of two wheeler platforms. The electric motor was coupled to the crankshaft of the SI engine.

The combined dynamic model of the motor-integrated hybrid powertrain provides a suitable platform for optimization and optimal control. Since the design requirement for the motor-integrated hybrid powertrain is multi-objective, an appropriate nested methodology is adapted to perform the design optimization. The multiple objectives for the optimization are:

- to optimize size of each component of the powertrain with respect to a fuel consumption reduction, financial cost impact and weight impact;
- to design an optimal controller that can minimize the fuel consumption with battery charge sustainability.

The nested methodology is proposed using particle swarm optimization and dynamic programming methods. The main intention of the methodology is to determine certain design parameters of the motor-integrated hybrid powertrain using a single function-based multi-objective optimization methodology. The methodology provides information about the design paramet-

ers and an optimal controller, however it does not provide information about multiple feasible combinations of the design parameters. This necessitates the need of investigation for a Pareto-Optimal design. The Pareto-Optimal design solved the multi-objective optimization and the front converges to the design parameters combination determined by the previous method. The finding provides confidence on the design parameters combination.

It is important to design the optimal controller based on numerical methods for future possible deployment in a real-time platform. Such an optimal controller was developed using the hp-adaptive collocation method, which provides insight on the working of numerical optimal control method. The hp-adaptive collocation method is chosen in this work due to its advantages over the other numerical optimal control methods. The objective function of the optimal control problem is formulated with equal weightage towards minimizing the fuel consumption and maintaining the battery SOC near a pre-defined level. The minimization of fuel consumption definitely results in reduction of exhaust gas emissions and the second objective ensures charge sustainability of the vehicle which is very much essential for a two-wheeled vehicle used for personal transportation in an urban city. The control and state trajectories of the hp-adaptive collocation method were compared with the corresponding trajectories determined using the dynamic programming method. The hp-adaptive collocation method and dynamic programming method give different importance to the elements of the control vector. The fuel consumption of the hp-adaptive collocation method is 11% more than the dynamic programming method. However, the hp-adaptive collocation method can be explored further for real-time implementation with a shorter horizon.

The future work for the research project could focus on real-time implementation of the numerical optimal controller. It is very much essential to have information about the future time horizon for certain states of the optimal controller. This necessitates the need for an intelligent driver model which can predict certain future states. The driver model may possibly use a cloud platform for calculation, otherwise it may be non-feasible to do this calculation on the real-time platform available on-board. In the case of cloud-based driver model, it is necessary to have a robust cellular network connectivity. Otherwise, the on-board control unit

can compute a simple data driven model. Another research direction would be to develop and compare different optimal control methods suitable for real-time implementation. Future research work could be conducted on a vehicle platform from TVS Motor Company.

Bibliography

[1] F. Posada, F. Kamakate, and A. Bandivadekar, *Sustainable Management of Two and Three-Wheelers in Asia*. The International Council of Clean Transportation, 2011.

[2] S. Ray, *Indian Two-Wheeler Industry*. ICRA Research Services, 2014.

[3] A. Sciarretta and L. Guzzella, "Control of hybrid electric vehicles," *IEEE Control Systems*, vol. 27, no. 2, pp. 60–70, April 2007.

[4] C. Zhang and A. Vahid, "Real-time optimal control of plug-in hybrid vehicles with trip preview," *Proceedings of the 2010 American Control Conference*, pp. 6917–6922, June 2010.

[5] C. Zhang, A. Vahidi, X. Li, and D. Essenmacher, "Role of trip information preview in fuel economy of plug-in hybrid vehicles," *Proceedings of the ASME 2009 Dynamic Systems and Control Conference*, pp. 253–258, 2009.

[6] K. B. Wipke, M. R. Cuddy, and S. D. Burch, "Advisor 2.1: a user-friendly advanced powertrain simulation using a combined backward/forward approach," *IEEE Transactions on Vehicular Technology*, vol. 48, no. 6, pp. 1751–1761, Nov 1999.

[7] A. Kleimaier and D. Schroder, "An approach for the online optimized control of a hybrid powertrain," *7th International Workshop on Advanced Motion Control. Proceedings (Cat. No.02TH8623)*, pp. 215–220, July 2002.

[8] L. Guzzella and A. Sciarretta, *Vehicle Propulsion Systems:Introduction to Modeling and Opitmization*. Springer-Verlag Berlin Heidelberg, 2005.

[9] J. Dhinagar. and D. Himadri., "Integrated unit for motor integrated hybrid transmission control and engine control," Nov. 14 2013, wO Patent App. PCT/IN2013/000,307. [Online]. Available: http://www.google.com/patents/WO2013168183A1?cl=en

[10] L. Guzzella and C. H. Onder, *Introduction to Modelling and Control of Internal Combustion Engine Systems.* Springer-Verlag Berlin Heidelberg, 2001.

[11] J. B. Heywood, *Internal Combustion Engines Fundamentals.* McGraw-Hill Education, 1988.

[12] U. Kiencke and L. Nielsen, *Automotive Control Systems for Engine, Driveline and Vehicle.* Springer-Verlag Berlin Heidelberg, 2001.

[13] B. Sendyka and J. Filipczyk, "Simulation of the characteristic of a carburettor of an internal combustion engine," *SAE Technical Paper*, 02 1995. [Online]. Available: https://doi.org/10.4271/950987

[14] G. A. Alla, "Computer simulation of a four stroke spark ignition engine," *Energy Conversion and Management*, vol. 43, no. 8, pp. 1043 – 1061, 2002. [Online]. Available: http://www.sciencedirect.com/science/article/pii/S0196890401000929

[15] S. H. Chan and J. Zhu, "Modelling of engine in-cylinder thermodynamics under high values of ignition retard," *International Journal of Thermal Sciences*, vol. 40, no. 1, pp. 94 – 103, 2001. [Online]. Available: http://www.sciencedirect.com/science/article/pii/S129007290000274X

[16] M. H. S. A.H.Kakaee and J.Zareei, "Sensitivity and effect of ignition timing on the performance of a spark ignition engine: An experimental and modeling study," *Journal of Combustion*, vol. 2011, no. 678719, 2011.

[17] C. R. Ferguson and A. T. Kirkpatrick, *Internal Combustion Engine Systems.* John Wiley Sons, Inc, 2015.

[18] H. J. Lavoie, G.A. and K. J.C., "Experimental and theoretical study of nitric oxide formation in internal combustion engines," *Combustion Science and Technology*, vol. 1,

pp. 313–326, 1970.

[19] C. T. Bowman, "Kinetics of pollutant formation and destruction in combustion," *Prog. Energy Combust Sci*, vol. 1, pp. 33–45, 1975.

[20] H. A. A. Dashti Mehrnoosh and M. A. Asghar, "Thermodynamic model for prediction of performance and emission characteristics of si engine fuelled by gasoline and natural gas with experimental verification," *Journal of Mechanical Science and Technology*, vol. 7, pp. 2213–2225, 2012.

[21] C. P. Ivan Arsie and G. Rizzo, "Models for the prediction of performance and emissions in a spark ignition engine- a sequentially structured approach," *SAE World Congress*, 02 1998. [Online]. Available: https://doi.org/10.4271/980779

[22] D. G. Miller R and L. G, "A super-extended zel'dovich mechanism for nox modeling and engine calibration," *SAE World Congress*, 02 1998. [Online]. Available: https://doi.org/10.4271/980781

[23] R. Miller, S. Russ, C. Weaver, E. Kaiser, C. Newman, G. Davis, and G. Lavoie, "Comparison of analytically and experimentally obtained residual fractions and nox emissions in spark-ignited engines," *SAE World Congress 1998*, 10 1998. [Online]. Available: https://doi.org/10.4271/982562

[24] P. Yedamale, *Brushless DC Motor Fundamentals*. Microchip Technology, 2003. [Online]. Available: http://ww1.microchip.com/downloads/en/AppNotes/00885a.pdf

[25] R. Krishnan, *Electric Motor Drives Modeling, Analysis and Control*. Prentice Hall, 2001.

[26] P. Sen, *Electric Machines and Power Electronics*. John Wiley Sons,Inc, 1997.

[27] S. Baldursson, *BLDC Motor Modelling and Control- A Matlab/Simulink Implementation- MSc Thesis*. Chalmers University, 2005.

[28] O. Tremblay and L.-A. Dessaint, "Experimental validation of a battery dynamic model for ev applications," *World Electric Vehicle Journal*, vol. 3, no. 2, pp. 289–298, 2009.

[Online]. Available: http://www.mdpi.com/2032-6653/3/2/289

[29] O. Tremblay, L. A. Dessaint, and A. I. Dekkiche, "A generic battery model for the dynamic simulation of hybrid electric vehicles," *2007 IEEE Vehicle Power and Propulsion Conference*, pp. 284–289, Sept 2007.

[30] A. A. H. Hussein and I. Batarseh, "An overview of generic battery models," *2011 IEEE Power and Energy Society General Meeting*, pp. 1–6, July 2011.

[31] C. M. Shepherd, "Design of primary and secondary cells: 2. an equation describing battery discharge," *Journal of The Electrochemical Society*, vol. 112, no. 7, pp. 657–664, 1965. [Online]. Available: http://jes.ecsdl.org/content/112/7/657.abstract

[32] M. Drr, A. Cruden, S. Gair, and J. McDonald, "Dynamic model of a lead acid battery for use in a domestic fuel cell system," *Journal of Power Sources*, vol. 161, no. 2, pp. 1400 – 1411, 2006. [Online]. Available: http://www.sciencedirect.com/science/article/pii/S0378775306000401

[33] E. Kuhn, C. Forgez, P. Lagonotte, and G. Friedrich, "Modelling ni-mh battery using cauer and foster structures," *Journal of Power Sources*, vol. 158, no. 2, pp. 1490 – 1497, 2006. [Online]. Available: http://www.sciencedirect.com/science/article/pii/S0378775305014096

[34] P. Mauracher and E. Karden, "Dynamic modelling of lead/acid batteries using impedance spectroscopy for parameter identification," *Journal of Power Sources*, vol. 67, no. 1, pp. 69 – 84, 1997, proceedings of the Fifth European Lead Battery Conference. [Online]. Available: http://www.sciencedirect.com/science/article/pii/S0378775397024981

[35] E. Cacciatori, "Evaluating the impact of driveability requirements on the performance of an energy management control architecture for a hybrid electric vehicle," in *2006 2nd IEE Conference on Automotive Electronics*, March 2006, pp. 297–320.

[36] P. Schoeggi and E. Ramschak, "Vehicle driveability assesement using neural networks for development, calibration and quality tests," *SAE World Congress*, 2000.

[37] P. Liu, T. Zhang, and X. Zhao, "Vehicle drivability evaluation and pedal-acceleration response analysis," *Advances in information Sciences and Services Sciences*, vol. 5, no. 6, 2013.

[38] X. Wei and G. Rizzoni, "Objective metrics of fuel economy, performance and driveability a review," *SAE World Congress*, 2004.

[39] J. Persson, *Integrated Powertrain Control-a Literature Survey on Longitudinal Vibrations, Drivability Aspects and Future Challenges.* Chalmers University of Sweden, 2004.

[40] R. E. Dorey and E. J. Martin, "Vehicle driveability- the development of an objective methodology," *SAE World Congress*, 2000.

[41] R. E. Dorey and C. B. Holmes, "Vehicle driveability- its characterisation and measurement," *SAE World Congress*, 2000.

[42] H. O. List and P. Schoeggi, "Objective evaluation of vehicle driveability," *SAE World Congress*, 1998.

[43] B.Jager, T. Keulen, and J. Kessels, *Optimal control of hybrid vehicles.* Springer-Verlag Berlin Heidelberg, 2013.

[44] P. Pisu and G. Rizzoni, "A comparative study of supervisory control strategies for hybrid electric vehicles," *IEEE Transactions on Control Systems Technology*, vol. 15, no. 3, pp. 506–518, May 2007.

[45] S. G. Wirasingha and A. Emadi, "Classification and review of control strategies for plug-in hybrid electric vehicles," *IEEE Transactions on Vehicular Technology*, vol. 60, no. 1, pp. 111–122, Jan 2011.

[46] C. M. Martinez, X. Hu, D. Cao, E. Velenis, B. Gao, and M. Wellers, "Energy management in plug-in hybrid electric vehicles: Recent progress and a connected vehicles perspective," *IEEE Transactions on Vehicular Technology*, vol. 66, no. 6, pp. 4534–4549, June 2017.

[47] J. Torres, R. Gonzalez, A. Gimenez, and J. Lopez, "Energy management strategy for plug-in hybrid electric vehicles. a comparative study," *Applied Energy*, vol. 113, no. Supplement C, pp. 816 – 824, 2014. [Online]. Available: http://www.sciencedirect.com/science/article/pii/S0306261913006429

[48] A. Sciarretta, L. Serrao, P. Dewangan, P. Tona, E. Bergshoeff, C. Bordons, L. Charmpa, P. Elbert, L. Eriksson, T. Hofman, M. Hubacher, P. Isenegger, F. Lacandia, A. Laveau, H. Li, D. Marcos, T. Nesch, S. Onori, P. Pisu, J. Rios, E. Silvas, M. Sivertsson, L. Tribioli, A.-J. van der Hoeven, and M. Wu, "A control benchmark on the energy management of a plug-in hybrid electric vehicle," *Control Engineering Practice*, vol. 29, no. Supplement C, pp. 287 – 298, 2014. [Online]. Available: http://www.sciencedirect.com/science/article/pii/S0967066113002323

[49] P. Zhang, F. Yan, and C. Du, "A comprehensive analysis of energy management strategies for hybrid electric vehicles based on bibliometrics," *Renewable and Sustainable Energy Reviews*, vol. 48, no. Supplement C, pp. 88 – 104, 2015. [Online]. Available: http://www.sciencedirect.com/science/article/pii/S1364032115002464

[50] M. M. Sabri, K. Danapalasingam, and M. Rahmat, "A review on hybrid electric vehicles architecture and energy management strategies," *Renewable and Sustainable Energy Reviews*, vol. 53, no. Supplement C, pp. 1433 – 1442, 2016. [Online]. Available: http://www.sciencedirect.com/science/article/pii/S1364032115010060

[51] C. M. Wenzhong Gao, "Hybrid vehicle design using global optimisation algorithms," *International Journal of Electric and Hybrid Vehicles*, vol. 1, no. 1, pp. 57–70, January 2007.

[52] Y. Zou, H. Shi-jie, L. Dong-ge, G. Wei, and X. Hu, "optimal energy control strategy design for a hybrid electric vehicle"," *Discrete Dynamics in Nature and Society Volume 2013, Article ID 132064*, 2013.

[53] N. Al-Aawar and A. Arkadan, "optimal control strategy for hybrid electric vehicle power-train"," *IEEE Journal of emerging and selected topics in power electronics, Vol. 03, No.*

2, 2015.

[54] N. Kim, S. Cha, , and H. Peng, "Optimal control of hybrid electric vehicles based on pontryagins minimum principle," *IEEE Transactions on Control systems technology, Vol 19, No 5, September 2011*, 2011.

[55] D. Sinoquet, G. Rousseau, and Y. Milhau, "Design optimization and optimal control for hybrid vehicles," *Optimization engineering, Springer Science and Businees Media, 2009*, 2009.

[56] T.Kim, C.Manzie, and R.Sharma, "optimal control of a parallel hybrid vehicle with a traffic preview"," *J Automobile Engineering 2014, Vol. 228*, 2014.

[57] M. Nechyba and Y. Xu, "human control strategy abstraction, verification and replication"," *IEEE Control systems 1997*, 1997.

[58] Y. Gao and M. Ehsani, "Design and control methodology of plug-in hybrid electric vehicles," *IEEE Transactions on Industrial Electronics*, vol. 57, no. 2, pp. 633–640, Feb 2010.

[59] J. Gonder and T. Markel, "Energy management strategies for plug-in hybrid electric vehicles," in *SAE Technical Paper*. SAE International, 04 2007. [Online]. Available: https://doi.org/10.4271/2007-01-0290

[60] L. Tribioli, M. Barbieri, R. Capata, E. Sciubba, E. Jannelli, and G. Bella, "A real time energy management strategy for plug-in hybrid electric vehicles based on optimal control theory," *Energy Procedia*, vol. 45, no. Supplement C, pp. 949 – 958, 2014, aTI 2013 - 68th Conference of the Italian Thermal Machines Engineering Association. [Online]. Available: http://www.sciencedirect.com/science/article/pii/S1876610214001015

[61] A. Rousseau, S. Pagerit, and D. W. Gao, "Plug-in hybrid electric vehicle control strategy parameter optimization," *Journal of Asian Electric Vehicles*, vol. 6, no. 2, pp. 1125–1133, 2008.

[62] C. Sun, S. J. Moura, X. Hu, J. K. Hedrick, and F. Sun, "Dynamic traffic feedback data enabled energy management in plug-in hybrid electric vehicles," *IEEE Transactions on Control Systems Technology*, vol. 23, no. 3, pp. 1075–1086, May 2015.

[63] P. Tulpule, V. Marano, and G. Rizzoni, "Effects of different phev control strategies on vehicle performance," in *2009 American Control Conference*, June 2009, pp. 3950–3955.

[64] Z. Chen, C. C. Mi, J. Xu, X. Gong, and C. You, "Energy management for a power-split plug-in hybrid electric vehicle based on dynamic programming and neural networks," *IEEE Transactions on Vehicular Technology*, vol. 63, no. 4, pp. 1567–1580, May 2014.

[65] C. Hou, M. Ouyang, L. Xu, and H. Wang, "Approximate pontryagins minimum principle applied to the energy management of plug-in hybrid electric vehicles," *Applied Energy*, vol. 115, no. Supplement C, pp. 174 – 189, 2014. [Online]. Available: http://www.sciencedirect.com/science/article/pii/S0306261913008945

[66] D. P. Bertsekas, *Dynamic Programming and Optimal Control Volume 1.* Athena Scientific, 2005.

[67] A. Lew and H. Mauch, *Dynamic Programming: A Computational Tool*, ser. Studies in Computational Intelligence. Springer Berlin Heidelberg, 2006. [Online]. Available: https://books.google.co.in/books?id=IzlsCQAAQBAJ

[68] H. Khayyam and A. Bab-Hadiashar, "Adaptive intelligent energy management system of plug-in hybrid electric vehicle," *Energy*, vol. 69, no. Supplement C, pp. 319 – 335, 2014. [Online]. Available: http://www.sciencedirect.com/science/article/pii/S0360544214002825

[69] S. Koziel and X. Yang, *Computational Optimization, Methods and Algorithms*, ser. Studies in Computational Intelligence. Springer Berlin Heidelberg, 2011. [Online]. Available: https://books.google.co.in/books?id=HOHwCAAAQBAJ

[70] J. P. F. Trovo, V. D. N. Santos, P. G. Pereirinha, H. M. Jorge, and C. H. Antunes, "A simulated annealing approach for optimal power source management in a small ev," *IEEE*

Transactions on Sustainable Energy, vol. 4, no. 4, pp. 867–876, Oct 2013.

[71] S. Hui, "Multi-objective optimization for hydraulic hybrid vehicle based on adaptive simulated annealing genetic algorithm," *Engineering Applications of Artificial Intelligence*, vol. 23, no. 1, pp. 27 – 33, 2010. [Online]. Available: http://www.sciencedirect.com/science/article/pii/S0952197609001250

[72] K. Chen, Y. Deng, F. Zhou, G. Sun, and Y. Yuan, "Control strategy optimization for hybrid electric vehicle based on particle swarm and simulated annealing algorithm," in *2011 International Conference on Electric Information and Control Engineering*, April 2011, pp. 2054–2057.

[73] Z. Chen, C. C. Mi, R. Xiong, J. Xu, and C. You, "Energy management of a power-split plug-in hybrid electric vehicle based on genetic algorithm and quadratic programming," *Journal of Power Sources*, vol. 248, no. Supplement C, pp. 416 – 426, 2014. [Online]. Available: http://www.sciencedirect.com/science/article/pii/S0378775313015917

[74] S. Bashash, S. J. Moura, J. C. Forman, and H. K. Fathy, "Plug-in hybrid electric vehicle charge pattern optimization for energy cost and battery longevity," *Journal of Power Sources*, vol. 196, no. 1, pp. 541 – 549, 2011. [Online]. Available: http://www.sciencedirect.com/science/article/pii/S0378775310011390

[75] M. Montazeri-Gh, A. Poursamad, and B. Ghalichi, "Application of genetic algorithm for optimization of control strategy in parallel hybrid electric vehicles," *Journal of the Franklin Institute*, vol. 343, no. 4, pp. 420 – 435, 2006, modeling, Simulation and Applied Optimization. [Online]. Available: http://www.sciencedirect.com/science/article/pii/S0016003206000329

[76] D. R. Jones, *Direct global optimization algorithm.* Boston, MA: Springer US, 2001, pp. 431–440. [Online]. Available: https://doi.org/10.1007/0-306-48332-7_93

[77] M. Bjorkman and K. Holmstrom, "Global optimization using the direct algorithm in matlab," *Advanced Modeling and Optimization*, vol. 1, no. 2, 1999.

[78] M. Osborne and A. Rubinstein, *A Course in Game Theory*, ser. A Course in Game Theory. MIT Press, 1994. [Online]. Available: https://books.google.co.in/books?id=5ntdaYX4LPkC

[79] A. H. Mohsenian-Rad, V. W. S. Wong, J. Jatskevich, R. Schober, and A. Leon-Garcia, "Autonomous demand-side management based on game-theoretic energy consumption scheduling for the future smart grid," *IEEE Transactions on Smart Grid*, vol. 1, no. 3, pp. 320–331, Dec 2010.

[80] L. Cigler and B. Faltings, "Decentralized anti-coordination through multi-agent learning," *CoRR*, vol. abs/1402.0583, 2014. [Online]. Available: http://arxiv.org/abs/1402.0583

[81] C. Dextreit and I. V. Kolmanovsky, "Game theory controller for hybrid electric vehicles," *IEEE Transactions on Control Systems Technology*, vol. 22, no. 2, pp. 652–663, March 2014.

[82] Q. Gong, Y. Li, and Z. R. Peng, "Trip-based optimal power management of plug-in hybrid electric vehicles," *IEEE Transactions on Vehicular Technology*, vol. 57, no. 6, pp. 3393–3401, Nov 2008.

[83] L. Wu, P. Shi, and X. Su, *Sliding Mode Control of Uncertain Parameter-Switching Hybrid Systems*, ser. Wiley Series in Dynamics and Control of Electromechanical Systems. Wiley, 2014. [Online]. Available: https://books.google.co.in/books?id=RHnnAwAAQBAJ

[84] S. Boyd and L. Vandenberghe, *Convex Optimization*, ser. Berichte über verteilte messysteme. Cambridge University Press, 2004. [Online]. Available: https://books.google.co.in/books?id=mYm0bLd3fcoC

[85] B. Egardt, N. Murgovski, M. Pourabdollah, and L. J. Mardh, "Electromobility studies based on convex optimization: Design and control issues regarding vehicle electrification," *IEEE Control Systems*, vol. 34, no. 2, pp. 32–49, April 2014.

[86] J. Asprion, O. Chinellato, and L. Guzzella, "Optimal control of diesel engines: Numerical methods, applications, and experimental validation," *Mathematical Problems in Engin-*

eering, vol. 2014, no. 286538, p. 21, 2014.

[87] M. Diehl, H. Bock, H. Diedam, and P.-B. Wieber, *Fast Direct Multiple Shooting Algorithms for Optimal Robot Control*. Berlin, Heidelberg: Springer Berlin Heidelberg, 2006, pp. 65–93. [Online]. Available: https://doi.org/10.1007/978-3-540-36119-0_4

[88] J. T. Betts, "Survey of Numerical Methods for Trajectory Optimization," *Journal of Guidance, Control, and Dynamics*, vol. 21, no. 2, pp. 193–207, Mar. 1998. [Online]. Available: http://dx.doi.org/10.2514/2.4231

[89] A. Rao, "A survey of numerical methods for optimal control," *Advances in the Astronautical Sciences*, vol. 135, January 2010.

[90] B. A. Conway, "A survey of methods available for the numerical optimization of continuous dynamic systems," *Journal of Optimization Theory and Applications*, vol. 152, no. 2, pp. 271–306, Feb 2012. [Online]. Available: https://doi.org/10.1007/s10957-011-9918-z

[91] D. Garg, M. Patterson, W. W. Hager, A. V. Rao, D. A. Benson, and G. T. Huntington, "A unified framework for the numerical solution of optimal control problems using pseudospectral methods," *Automatica*, vol. 46, no. 11, pp. 1843 – 1851, 2010. [Online]. Available: http://www.sciencedirect.com/science/article/pii/S0005109810002980

[92] Benson, Annand, and Barua, "A simulation model including intake and exhaust systems for a single cylinder four-stroke cycle spark ignition engine," *International Journal for Mechanical Science*, vol. 17, pp. 97–124, 1975.

[93] W.-M. H. T.-S. W. K.-B. Sheu, S.-T. Chiou and H.-S. Yan, "New automatic hybrid transmissions for motorcycles," *Proc. Natl. Sci. Counc. ROC(A)*, vol. 6, pp. 716–727, 1999.

[94] D. L. Keller and R. E. Wilson, "Torque sensing variable speed v-beit drive," *SAE World Congress*, 1972.

[95] J. E. S. Larry R. Oliver, K. G. Hornung and H. N. Shapiro, "Design equations for a speed and torque controlled variable ratio v-beit transmission," *SAE World Congress*, 1973.

[96] L. R. Oliver and D. D. Henderson, "Design and development of a high horsepower torque sensing variable speed drive," *National Combined Farm, Construction Industrial Machinery and Powerplant Meetings Milwaukee, Wis.*, 1972.

[97] W. S. Worley, "Designing adjustable-speed v-belt drives for farm implements," *SAE National Tractor Meeting, Milwaukee, Wis., Sept. 16, 1954*, 1955.

[98] Y.-T. L. Chyuan-Yaw Tseng, Li-Wen Chen and J.-Y. Li, "A hybrid dynamic simulation model for urban scooters with a mechanical-type cvt," *Proceedings of the IEEE International Conference on Automation and Logistics Qingdao, China September 2008*, 2008.

[99] K.-B. Sheu and T.-H. Hsu, "Design and implementation of a novel hybrid-electric-motorcycle transmission," *Applied Energy*, vol. 83, p. 959974, 2006.

[100] T. Kim and H. Kim, "Integrated engine-cv't control considering powertrain response lag in acceleration," *KSME International Journal*, vol. 14, pp. 764–772, 2000.

[101] S. Phandis, "Dynamic simulation of continuous variable transmission,msc thesis," 2008.

[102] P. J. Dolcini, "Contribution to the clutch comfort,phd thesis," 2007.

[103] M. Marius, Andrei and Nicolae, "Automotive clutch model for real time simulation," *Proceedings of the Romanian Academy*, vol. 12, pp. 109–116, 2011.

[104] S. Andersson and Bjorklund, "Friction models for sliding dry, boundary and mixed lubricated contacts," *Tribology International*, vol. 40, pp. 580–587, 2006.

[105] ARAI, "Indian emissions regulations limits,regulations measurement of exhaust emissions and calculation of fuel consumption," 2011.

[106] U. Bender and Sawodny, "An adaptive driver model for driving cycle prediction in the intelligent truck," *The International Federation of Automatic Control Cape Town, South Africa.*, 2014.

[107] C. I. Chatzikomis and K. N. Spentzas, "A path-following driver model with longitudinal and lateral control of vehicle's motion," *Forschung im Ingenieurwesen*, vol. 73, no. 4, p. 257, Nov 2009. [Online]. Available: https://doi.org/10.1007/s10010-009-0112-5

[108] R. Sharp, D. Casanova, and P. Symonds, "A mathematical model for driver steering control, with design, tuning and performance results," *Vehicle System Dynamics*, vol. 33, no. 5, pp. 289–326, 2000. [Online]. Available: https://www.tandfonline.com/doi/abs/10.1076/0042-3114%28200005%2933%3A5%3B1-Q%3BFT289

[109] J. Wang, W. Li, J. Li, Y. Liu, B. Song, and H. Gao, "Modeling a drivers directional and longitudinal speed control based on racing track features," *Shock and Vibration*, vol. 2018, 2018. [Online]. Available: https://www.hindawi.com/journals/sv/2018/7487295/cta/

[110] B. Mashadi, M. Mahmoudi-Kaleybar, P. Ahmadizadeh, and A. Oveisi, "A path-following driver/vehicle model with optimized lateral dynamic controller," *Latin American Journal of Solids and Structures*, vol. 11, pp. 613 – 630, 08 2014. [Online]. Available: http://www.scielo.br/scielo.php?script=sci_arttext&pid=S1679-78252014000400004&nrm=iso

[111] B. Mashadi, M. Mahmoodi-K, A. H. Kakaee, and R. Hosseini, "Vehicle path following control in the presence of driver inputs," *Proceedings of the Institution of Mechanical Engineers, Part K: Journal of Multi-body Dynamics*, vol. 227, no. 2, pp. 115–132, 2013. [Online]. Available: https://doi.org/10.1177/1464419312469755

[112] Green and Limebeer, *Linear Robust Control*. Prentice Hall, 2012.

[113] K. Takaba, "A tutorial on preview control systems," *SICE Annual Conference in Fuhi*, 2003.

[114] O. Hayat, M. Lebrun, and E. Domingues, "Powertrain drivability evaluation : Analysis and simplification of dynamic models," *SAE World Congress*, 2003.

[115] Marius, M. Andrei, and Nicolae, "Automotive clutch model for real time simulation," *Proceedings of the Romanian Academy*, vol. 12, pp. 109–116, 2011.

[116] W. S. Worley, "Designing adjustable-speed v-belt drives for farm implements," *SAE National Tractor Meeting, Milwaukee, Wis., Sept. 16, 1954*, 1955.

[117] D. L. Keller and R. E. Wilson, "Torque sensing variable speed v-beit drive," *SAE World Congress*, 1972.

[118] L. R. Oliver and D. D. Henderson, "Design and development of a high horsepower torque sensing variable speed drive," *National Combined Farm, Construction and Industrial Machinery and Powerplant Meetings Milwaukee, Wis.*, 1972.

[119] L. R. Oliver, K. G. Hornung, J. E. Swenson, and H. N. Shapiro, "Design equations for a speed and torque controlled variable ratio v-beit transmission," *SAE World Congress*, 1973.

[120] K. B. Sheu, S.-T. Chiou, W. M. Hwang, T. S. Wang, and H. S. Yan, "New automatic hybrid transmissions for motorcycles," *Proc. Natl. Sci. Counc. ROC(A)*, vol. 6, pp. 716–727, 1999.

[121] C.-Y. Tseng, L.-W. Chen, Y.-T. Lin, and J.-Y. Li, "A hybrid dynamic simulation model for urban scooters with a mechanical-type cvt," *Proceedings of the IEEE International Conference on Automation and Logistics Qingdao, China September 2008*, 2008.

[122] T. Kim and H. Kim, "Integrated engine-cv't control considering powertrain response lag in acceleration," *KSME International Journal*, vol. 14, pp. 764–772, 2000.

[123] T. A. P. Centre, "Electric machines and power electronics: Uk opportunities electric machines and power electronics working group : September 2013," *APC report*, 2013.

[124] X. Wei, L. Guzzella, V. I. Utkin, and G. Rizzoni, "Model-based fuel optimal control of hybrid electric vehicle using variable structure control systems," *Journal of Dynamic Systems, Measurement, and Control*, vol. 129, no. 13, 2007.

[125] G. Rizzoni, L. Guzzella, and B. M. Baumann, "Unified modeling of hybrid electric vehicle drivetrains," *IEEE/ASME Transactions on Mechatronics*, vol. 4, no. 3, pp. 246–257, Sep 1999.

[126] C. A. C. Coello, G. B. Lamont, and D. A. V. Veldhuizen, *Evolutionary Algorithms for Solving Multi-Objective Problems (Genetic and Evolutionary Computation)*. Secaucus, NJ, USA: Springer-Verlag New York, Inc., 2006.

[127] S. Buerger, B. Lohmann, M. Merz, B. Vogel-Heuser, and M. Hallmannsegger, "Multi-objective optimization of hybrid electric vehicles considering fuel consumption and dynamic performance," in *2010 IEEE Vehicle Power and Propulsion Conference*, Sept 2010, pp. 1–6.

[128] L. Fang, S. Qin, G. Xu, T. Li, and K. Zhu, "Simultaneous optimization for hybrid electric vehicle parameters based on multi-objective genetic algorithms," *Energies*, vol. 4, no. 3, pp. 532–544, 2011. [Online]. Available: http://www.mdpi.com/1996-1073/4/3/532

[129] C. M. Fonseca and P. J. Fleming, "An overview of evolutionary algorithms in multiobjective optimization," *Evolutionary Computation*, vol. 3, no. 1, pp. 1–16, 1995.

[130] K. Deb, A. Pratap, S. Agarwal, and T. Meyarivan, "A fast and elitist multiobjective genetic algorithm: Nsga-ii," *Trans. Evol. Comp*, vol. 6, no. 2, pp. 182–197, Apr. 2002. [Online]. Available: http://dx.doi.org/10.1109/4235.996017

[131] K. Deb, *Multi-objective Optimisation Using Evolutionary Algorithms: An Introduction*. London: Springer London, 2011, pp. 3–34. [Online]. Available: https://doi.org/10.1007/978-0-85729-652-8_1

[132] D. E. Goldberg and J. H. Holland, "Genetic algorithms and machine learning," *Machine Learning*, vol. 3, no. 2, pp. 95–99, Oct 1988. [Online]. Available: https://doi.org/10.1023/A:1022602019183

[133] J. Kennedy and R. Eberhart, "Particle swarm optimization," *Neural Networks, IEEE International Conference*, 1995.

[134] P. K. Soren Ebbesen and L. Guzzella, "A generic particle swarm optimization matlab function," *2012 American Control Conference*, 2012.

[135] R. Poli, J. Kennedy, and T. Blackwell, "Particle swarm optimization," *Swarm Intelligence*, vol. 1, no. 1, pp. 33–57, Jun 2007. [Online]. Available: https://doi.org/10.1007/s11721-007-0002-0

[136] O. Sunderstrom and L. Guzzella, "A generic dynamic programming matlab function," *18th IEEE International conference on Control Applications*, 2009.

[137] A. Konak, D. W. Coit, and A. E. Smith, "Multi-objective optimization using genetic algorithms: A tutorial," *Reliability Engineering System Safety*, vol. 91, no. 9, pp. 992 – 1007, 2006, special Issue - Genetic Algorithms and Reliability. [Online]. Available: http://www.sciencedirect.com/science/article/pii/S0951832005002012

[138] E. Zitzler, K. Deb, and L. Thiele, "Comparison of multiobjective evolutionary algorithms: Empirical results," *Evol. Comput.*, vol. 8, no. 2, pp. 173–195, Jun. 2000. [Online]. Available: http://dx.doi.org/10.1162/106365600568202

[139] E. Zitzler and L. Thiele, "An Evolutionary Algorithm for Multiobjective Optimization: The Strength Pareto Approach," ETH Zurich, Zurich, TIK-Report 1, May 1998, see also URL https://doi.org/10.3929/ethz-a-004284029.

[140] E. Zitzler, M. Laumanns, and L. Thiele, "SPEA2: Improving the Strength Pareto Evolutionary Algorithm," ETH Zurich, Zurich, Working paper 1, May 2001, see also URL https://doi.org/10.3929/ethz-a-004284029.

[141] J. Knowles and D. Corne, "The pareto archived evolution strategy: a new baseline algorithm for pareto multiobjective optimisation," in *Proceedings of the 1999 Congress on Evolutionary Computation-CEC99 (Cat. No. 99TH8406)*, vol. 1, 1999, p. 105 Vol. 1.

[142] J. D. Knowles and D. W. Corne, "Approximating the nondominated front using the pareto archived evolution strategy," *Evol. Comput.*, vol. 8, no. 2, pp. 149–172, Jun. 2000. [Online]. Available: http://dx.doi.org/10.1162/106365600568167

[143] D. W. Corne, N. R. Jerram, J. D. Knowles, and M. J. Oates, "Pesa-ii: Region-based selection in evolutionary multiobjective optimization," in *Proceedings of the 3rd Annual*

Conference on Genetic and Evolutionary Computation, ser. GECCO'01. San Francisco, CA, USA: Morgan Kaufmann Publishers Inc., 2001, pp. 283–290. [Online]. Available: http://dl.acm.org/citation.cfm?id=2955239.2955289

[144] D. W. Corne, J. D. Knowles, and M. J. Oates, *The Pareto Envelope-Based Selection Algorithm for Multiobjective Optimization*. Berlin, Heidelberg: Springer Berlin Heidelberg, 2000, pp. 839–848. [Online]. Available: https://doi.org/10.1007/3-540-45356-3_82

[145] D. A. Benson, G. T. Huntington, T. P. Thorvaldsen, and A. V. Rao, "Direct trajectory optimization and costate estimation via an orthogonal collocation method," *Journal of Guidance, Control and Dynamics*, vol. 29, no. 6, p. 6, November - December 2006.

[146] P. Lions, *Generalized solutions of Hamilton-Jacobi equations*, ser. Research notes in mathematics. Boston : Pitman Advanced Pub. Program, 1982.

[147] H. S. Rodrigues, M. T. T. Monteiro, and D. F. M. Torres, *Generalized solutions of Hamilton-Jacobi equations*, ser. Systems Science Series (Series Editor: Francisco Miranda). nova science publishers, 2014. [Online]. Available: https://www.novapublishers.com/catalog/product_info.php?products_id=49649

[148] M. A. Patterson and A. V. Rao, "Gpops ii: A matlab software for solving multiple-phase optimal control problems using hp-adaptive gaussian quadrature collocation methods and sparse nonlinear programming," *ACM Transactions on Mathematical Software*, vol. 41, no. 1, p. 37, October 2014.

[149] A. Wächter and L. T. Biegler, "On the implementation of an interior-point filter line-search algorithm for large-scale nonlinear programming," *Mathematical Programming*, vol. 106, no. 1, pp. 25–57, Mar 2006. [Online]. Available: https://doi.org/10.1007/s10107-004-0559-y

[150] I. S. Duff, "Ma57—a code for the solution of sparse symmetric definite and indefinite systems," *ACM Trans. Math. Softw.*, vol. 30, no. 2, pp. 118–144, Jun. 2004. [Online].

Available: http://doi.acm.org/10.1145/992200.992202